Synthesis, Characterization, Analysis and Design of Porous Metal-Organic Frameworks for Charge Transport and Redox Activity

by

Joshua Patrick Dvorak

A dissertation accepted and approved in partial fulfillment of the

requirements for the degree of

Doctor of Philosophy

in Chemistry

Dissertation Committee:

Professor Ramesh Jasti, Chair

Professor Carl K. Brozek, Advisor

Professor Paul A. Kempler, Core Member

Professor Benjamín J. Alemán, Institutional Representative

University of Oregon

Fall 2025

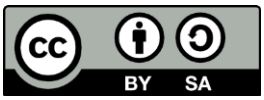

DISSERTATION ABSTRACT

Joshua Patrick Dvorak

Doctor of Philosophy in Chemistry

Title: Synthesis, Characterization, Analysis and Design of Porous Metal-Organic Frameworks for Charge Transport and Redox Activity

Conductive and redox active porous materials present an ideal platform for the fundamental study of charge transport and application in charge storage. Two- and three-dimensional architectures available support metal-organic frameworks as a highly tunable and well-defined systems that support electron and ion conductivity, accessibility of various redox states and bonding environments that can be tailored to specific need. The work presented in this thesis begins with the synthetic aspects of size and phase control of the most conductive 3D MOF as of the time of writing. The application of previously utilized "modulated" syntheses are employed and its limitations are demonstrated due to the complexity of phase selection. Chapter 2 presents a set of reaction conditions that result in size and phase control of $Fe_2(BDT)_3$.

The redox potential of trapped excited electrons in titanium-oxo material MIL-125 is shown to be size-dependent in chapter 3. Due to changing properties of materials with respect to particle size, especially in the nano-regime, this work presents an analysis that demonstrates increasingly negative redox potential of photodoped MIL-125 as nanoparticle size becomes smaller. Evidence of transfer hydrogenation between small organic substrates is demonstrated through the photodoping equilibrium, suggesting that previous considerations of photodoping limitations invoking hydrogen evolution may be an incomplete analysis.

Chapter 4 utilizes density functional theory to evaluate bond covalency in molecular analogues to 2-dimensional conductive MOFs. The identity of the heteroatom involved in metal-

ligand bonding in conductive MOFs has been linked to the materials ability to conduct electronically. Utilizing delocalization index, obtained from Atoms-In-Molecules analysis, Lowdin spin population and Mayer bond order analysis, this work proposes optimal parameters for design of ligands in conductive MOFs. Between the metal and heteroatom associated with bonding, a match of delocalization index, even distribution of spin, and a bond order of one-half is implicated in optimal parameters when comparing molecular analogues with reported conductivity of extended 2D sheets. Nucleus-independent chemical shift analysis was employed to determine a partial reduction in aromaticity of ligands is linked to materials with higher conductivity. The calculated parameters explored in this chapter predict that a material based on benzimidazolium N-heterocyclic dithiocarboxylate linkers will be conductive.

ACKNOWLEDGMENTS

This dissertation simply would not exist without the support of several creatures incredibly important to me. I say creatures because not all involved are of the human variation.

My sweet, protective, loving companion, Ellie, kept me sane for so many years during my time here. She was a high energy german shepherd who needed at least two long walks every day (and more that I wish I could have provided) who passed away in the final year of my Ph.D. She got me out of bed every morning, made sure I kept myself moving, gave me a reason to come home before ungodly hours of the night, and above all, provided me with such wonderful adoring love that felt undeserved, but kept me going through the darkest of times. She kept me alive. I can only hope that she is happy somewhere in the universe, playing forever with her sister.

My partners, Checkers Marshall and Cassandra Marxer, provided such love and support that I feel totally confident saying I would not be able to complete this journey without them. Checkers provided me, at all times, with unwavering love, support and scientific insight. They helped me discover who I was and remember to experience life while I survived through the academic experience. They are my scientific inspiration. I can only hope to be as cool as they are one day. Cassandra helped remind me that there is so much to talk about outside of the academic bubble that we Ph.D. students tend to live in. She made sure I was doing more than simply surviving. She was always ready to lend an ear, even if I was rambling about chemistry that was far outside of her usual realm of knowledge. Her consideration of life and philosophy has always been of a deep and thoughtful consideration that I think most scientists could learn from her perspective. Her small, sweet and patient tuxedo cat, Monday, was also a source of much needed non-human companionship.

Of course, no lab exists alone. My wonderful friends and coworkers helped me see the joy in lab on days when I struggled. Audrey Davenport is such a wonderful, bright source of joy and insight who always found ways to encourage me. Anyone would be fortunate to call her colleague and a friend, and I feel incredibly lucky to be among the people who can claim as such. Erik Svensson-Grape was always so giving with his time, energy and happiness that I know for certain that my experience would not be the same without him there. I hope that I can imitate even a fraction of his kindness and insight in my future endeavors. The rest of the lab is certainly not forgotten in my acknowledgements. I thank every member of the Brozek lab for such a positive atmosphere and a wonderful atmosphere of learning.

Professor Brozek, of course, deserves my deep gratitude for his mentorship and a place in his lab. When I was in need of a new advisor halfway through my journey, he accepted me into his group without hesitation. His perspective on science is one of a truly deep and thoughtful insight that has influenced my own perspective in ways that I am sure I will only be able to truly appreciate years from now.

The friends I had inside the department and outside of the university were instrumental in the enjoyment I found in the day-to-day. Ice skating, playing music, game nights, movie nights, late night chats and drives, and spinning fire kept me going and helped me remember what life was about. Shiva Moaven, Olivia and Gunnar Vulpin, Andy Davis, Willow Davis, Vi Baird, Will, Lucifer Anderson, Hannah, Delaney, Riley Brown and many more all deserve paragraphs of acknowledgement, but I will succinctly say that they all made my time here so much brighter than it would have been without them. I am eternally grateful to all of them and everyone else who made my pursuit of a Ph.D. feel like I wasn’t alone.

DEDICATION

This thesis is dedicated to fire and the one who helped me see it as both art and science. Fire was the first chemical reaction I was obsessed with, even if I didn't understand it that way.

TABLE OF CONTENTS

Chapter Page

ACKNOWLEDGMENTS 5
DEDICATION 7
TABLE OF CONTENTS 8
LIST OF FIGURES 10
CHAPTER I 21
INTRODUCTION AND MINI-REVIEW 21
General introduction 21
Background/Mini review 21
Types of conductivity 24
Early reports of conductive MOFs 26
Design aspects of 3D conductive MOFs 27
Design aspects of 2D conductive MOFs 28
Current benchmarks for conductive MOFs 29
CHAPTER II 33
SYNTHETIC CONTROL OF CONDUCTIVE IRON MOF $Fe_2(BDT)_3$ 33
Phase and nanoparticle size control of $Fe_2(BDT)_3$ 35
Synthetic considerations and modulator identity 42
CHAPTER III 46
SIZE-DEPENDENT REDOX POTENTIAL OF MIL-125 46
Size-dependent redox potential of MIL-125 nanoparticles 48
Side-reactivity in MIL-125 photodoping 54
CHAPTER IV 58
MODELING COVALENCY IN 2-DIMENSIONAL CONDUCTIVE MOFS 58
Modeling covalency and bonding in molecular analogues of 2D MOF sheets. 61
CHAPTER V 88
CONCLUDING REMARKS 88
APPENDIX A 90
SUPPLEMENTARY INFORMATION FOR CHAPTER 2 90

General unmodulated synthesis 91
General modulated syntheses 91
PXRD patterns of reactions with varied synthetic parameters 93
SEM Images 113
APPENDIX B 118
SUPPLEMENTARY INFORMATION FOR CHAPTER 3 118
Synthesis 118
Powder x-ray diffraction patterns of MIL-125 materials 119
SEM images of MIL-125 particles 120
Spectra of photodoping experiments in NMR tubes 122
APPENDIX C 130
SUPPLEMENTARY INFORMATION FOR CHAPTER 4 130
General: 130
Computational: 130
Calculated Energies 134
Calculated HOMO/LUMOs 135
Select MO visualizations 137
AIM electrostatic potentials 143
AIM delocalization index 144
Lowdin Spin Population 147
Mayer Bond orders 148
Bond lengths 149
Mulliken Atomic Orbital analysis 150
Electrostatic Potential Maps 165
Integrated zNICS values 169
zNICS curve fits 170
Example Orca compound script 176
Optimized structure geometries 179
Single-crystal x-ray diffraction 209
REFERENCES 210

LIST OF FIGURES

Figure Page

Figure 1. a) Cartoon schematic of electron transport in typical densely packed semi-conductors. b) MOF structures and ionic bonding. Electron transport is shown through redox hopping pathways, host-guest interactions and through bond conductivity. 22

Figure 2. a) Representations of energy states in redox hopping and b) band-type conductivity.....25

Figure 3. a) The linker and two perspectives of the $Cu[Cu(pdt)_2]$ crystalline lattice and b) a chemdraw of $Ni_3(HITP)_2$. 27

Figure 4. A schematic representation of particle packing in MOF samples. Measured conductivity as MOF particles become smaller and more densely packed.....28

Figure 5. Synthesis of $Fe_2(BDT)_3$ as reported in literature. The structure of $Fe_2(BDT)_3$-X isomers are displayed on the right, with properties such as iron spin state, conductivity and solvent system reported to produce the corresponding phase. 34

Figure 6. Reaction scheme of the modulated synthesis of $Fe_2(BDT)_3$. Equivalents of 1-mIm, x = 0, 0.26, 1.3, 2.6, 12.9 and 25.8.....36

Figure 7. chemdraw reaction over a stacked pxrd of all the first and last reactions in each series. SS1 and SS2. 38

Figure 8. reaction scheme with $FeCl_24H_2O$, structure of modulators, varied temp and mod. graph of varied sizes from scherrer size with octylamine.....40

Figure 9. a) Chemdraw representation of modulators and Scherrer size for successful syntheses. b) PXRD pattern of Fe2(BDT)3-2 synthesized with MeOH/MeCN at 80 °C. Fitting of peaks for Scherrer analysis is pictured. 42

Figure 10. a) Synthesis of MIL-125 with various Ti^{4+} precursors. b) a schematic of the photodoping process. VB = valence band and CB = conduction band. c) Chemdraw schematic of the MIL-125 Ti_8 cluster. The top half represents the photodoping reaction, consuming a sacrificial alcohol and producing an aldehyde as a Ti^{3+} center is formed. Pictured on the bottom is oxidation of the reduced MIL-125 from

atmospheric oxygen, producing water.....47

Figure 11. a) proposed reaction equilibria with included optical redox indicator, [Fc^*][BF_4] which is reduced to neutral Fc^*. b) Hydrogen evolution reaction represented as a combination of protons and electrons to form gaseous hydrogen. This occurs at -0.624 V vs Fc/Fc^+ in MeCN. 48

Figure 12. UV-Vis spectra of MIL-125 in MeCN before and after photodoping for 18 h. The extent of signal quenching at 778 nm is dependent on the size of the MIL-125 nanoparticles. On the right, the redox potential versus particle size is plotted relative to the Fc/Fc^+ redox couple. 50

Figure 13. a) reaction equilibrium proposed to form isopropanol from the addition of acetone into the photodoping process. b) NMR spectra of pre- and post-photodoping reactions in MeCN-d3 of both 32 nm and bulk MIL-125. Expanded view of the isopropanol $(CH_3)_2CHOH$ proton signal is shown in the box on the left. 52

Figure 14. a) reaction equilibrium including varied reductants and use of deuterated acetone to produce a proton signal that is not split from the neighboring -CD_3. N-butanol and 2-octanol pictured. b) NMR spectra of pre- and post-photodoping reactions in MeCN-d3 with 32 nm MIL-125 using n-butanol and 2-octanol. C2 protonated isopropanol-d6 signal is expanded in circles. Leftover DMF and newly formed acetamide are labelled. Peaks labelled with a star correspond to proton signals from original alcohol structure 53

Figure 15. chemdraw schemes of model compounds a) Carboxylate linker motif found in MOF-5 b) 2D sulfur-based conductive MOFs utilizing the dithiolene motif c) radical ligand complexes of palladium and nickel utilizing NHC-dithiocarboxylates d) A proposed triphenylene-based synthetic target e) carboxylate, dithiolene and NHC-dithiocarboxylate molecular analogues 61

Figure 16. Chemdraw representations of modeled complexes and their optimized structures. From left to right: the synthetic target where X = S, N,N'-dimethyl benzimidazolium dithiocarboxylate (or it's carboxylate analogue where X = O) labelled as $BICS_2$/$BICO_2$; the molecular analogue of M(BHT) materials – di(thi)olenes, also

known as catecholates labelled as DT/DO; the reduced diradical forms of di(thi)olenes, labelled as $DT^{2\bullet}/DO^{2\bullet}$; the (dithio)carboxylate models $PhCS_2/PhCO_2$. Below are both a chemdraw representation of a tris-coordinated $BICS_2$ complex and the modeled example. Pictured in the bottom right are electrostatic potentials of the nuclei in reduced copper bisdithiolene obtained from Atoms-in-Molecules analysis. *bis-cobalt complexes were not modeled with oxygen-based ligands or $PhCS_2$ 62

Figure 17. Calculated delocalization indices of the different modeled complexes. ΔESPn values in atomic units. a) Delocalization indices of modeled Ni complexes b) Delocalization indices of modeled Cu complexes. c) Delocalization indices of complexes of $BICS_2$, dithiolene and the reduced dithiolene of copper, nickel and cobalt. 65

Figure 18. Löwdin spin population of the metal d orbitals and p orbitals of the sulfur or oxygen heteroatoms. a) spin population of modeled nickel complexes. b) spin density of modeled copper complexes. c) spin density of copper, nickel and cobalt modeled with $BICS_2$, dithiolene or reduced dithiolene. d) spin density maps of nickel, copper and cobalt models. 70

Figure 19. Mayer bond orders of each model, including some long range bonding interactions. a) bond order of modeled nickel complexes. b) bond order of modeled copper complexes. c) spin density of copper, nickel and cobalt modeled with dithiolene or reduced dithiolene. Legend: gray circles represent carbon-carbon bond order between the CX_2 carbon and it's nearest carbon neighbor, or the double bond between carbons of di(thi)olene motifs directly bonded to heteroatoms. Red diamonds represent metal to heteroatom bond order. Hollow triangles represent heteroatom to heteroatom bonding interactions across the metal center in a trans configuration. Solid triangles represent bond orders of heteroatoms in a cis configuration relative to the metal center on the same ligand.....72

Figure 20. zNICS(SOM) aromaticity values relative to benzene modeled and calculated with the same theory and basis set as were used to optimize and calculate energies. The phenyl ring and imidazole ring of the $BICS_2/BICO_2$ models were evaluated separately, denoted as $BICO_2$-ph/im or $BICS_2$-ph/im. Values are in percentage of ratio of integrated value from 0 to 10 from exponential curves fit to data, *with the exception

of $NiBICS_2$-im which could not be fit, so the area of the data from 2 to 6 was used in lieu of an integrated value. In the structure of $MeBICS_2$ obtained from SCXRD, the ring labelled "Im" denotes to the imidazolium ring of the molecule and "Ph" denotes the phenyl ring where the zNICS scans were taken. Yellow spheres represent sulfur atoms, blue spheres represent nitrogen and grey represent carbon. Hydrogen atoms are not shown. 76

Figure 21. xy-NICS(SOM) scans taken at 2 Å above the plane of the ring. Chemical shifts calculated at the same level of theory as all other calculations. Yellow spheres represent sulfur atoms, blue spheres represent nitrogen and grey represent carbon. Hydrogen atoms are not shown. 78

Figure 22. Calculated data of bis- and tris-complexed models of $BICS_2$ for prediction of properties. Delocalization index, Lowdin spin population and Mayer bond order are plotted with Cu^{2+}, Ni^{2+}, Co^{2+}, Co^{3+}, Cr^{3+} and Sc^{3+}..... 82

Figure 23. PXRD patterns of $Fe_2(BDT)_3$ syntheses in solvent system 1. Varied sodium thiocyanate equivalents with all other parameters kept standard 93

Figure 24. PXRD patterns of $Fe_2(BDT)_3$ syntheses in solvent system 2. Varied sodium thiocyanate equivalents with all other parameters kept standard 94

Figure 25. PXRD patterns of $Fe_2(BDT)_3$ syntheses in solvent system 3. Varied sodium thiocyanate equivalents with all other parameters kept standard 95

Figure 26. PXRD patterns of $Fe_2(BDT)_3$ syntheses in solvent system 1. Varied equivalents of 1-methyl imidazole added as a modulator with all other parameters kept standard 96

Figure 27. PXRD patterns of $Fe_2(BDT)_3$ syntheses in solvent system 2. Varied equivalents of 1-methyl imidazole added as a modulator with all other parameters kept standard 97

Figure 28. PXRD patterns of $Fe_2(BDT)_3$ syntheses in solvent system 3. Varied equivalents of 1-methyl imidazole added as a modulator with all other parameters kept standard 98

Figure 29. PXRD patterns of $Fe_2(BDT)_3$ syntheses in solvent system 1. 0 equivalents of 1-methyl imidazole added as a modulator at varied reaction times. 99

Figure 30. PXRD patterns of $Fe_2(BDT)_3$ syntheses in solvent system 1. 0.25 equivalents of 1-

methyl imidazole added as a modulator at varied reaction times. 100

Figure 31. PXRD patterns of $Fe_2(BDT)_3$ syntheses in solvent system 1. 2.5 equivalents of 1-methyl imidazole added as a modulator at varied reaction times. 101

Figure 32. PXRD patterns of $Fe_2(BDT)_3$ syntheses in solvent system 1. 10 equivalents of 1-methyl imidazole added as a modulator at varied reaction times. 102

Figure 33. PXRD patterns of $Fe_2(BDT)_3$ syntheses in solvent system 2. 0 equivalents of 1-methyl imidazole added as a modulator at varied reaction times. 103

Figure 34. PXRD patterns of $Fe_2(BDT)_3$ syntheses in solvent system 2. 0.25 equivalents of 1-methyl imidazole added as a modulator at varied reaction times. 104

Figure 35. PXRD patterns of $Fe_2(BDT)_3$ syntheses in solvent system 2. 2.5 equivalents of 1-methyl imidazole added as a modulator at varied reaction times. 105

Figure 36. PXRD patterns of $Fe_2(BDT)_3$ syntheses in solvent system 2. 10 equivalents of 1-methyl imidazole added as a modulator at varied reaction times. 106

Figure 37. PXRD patterns of $Fe_2(BDT)_3$ syntheses in solvent system 1. Iron precursors used: $FeSO_4 \cdot 7H_2O$, $Fe(BF_4)_2 \cdot 6H_2O$, $FeCl_2 \cdot 4H_2O$ 107

Figure 38. PXRD patterns of $Fe_2(BDT)_3$ syntheses in solvent system 2. Iron precursors used: $FeSO_4 \cdot 7H_2O$, $Fe(BF_4)_2 \cdot 6H_2O$, $FeCl_2 \cdot 4H_2O$ 108

Figure 39. PXRD patterns of $Fe_2(BDT)_3$ syntheses in solvent system 1. Iron precursors used: $FeSO_4 \cdot 7H_2O$, $Fe(BF_4)_2 \cdot 6H_2O$, $FeCl_2 \cdot 4H_2O$ 109

Figure 40. PXRD patterns of $Fe_2(BDT)_3$ syntheses in varied solvent systems with modulators 1-methyl imidazole, octylamine or EDTA. Reactions run at 60 °C with $FeCl_2 \cdot 4H_2O$ precursor 110

Figure 41. PXRD patterns of $Fe_2(BDT)_3$ syntheses in varied solvent systems with modulators 1-methyl imidazole, octylamine or EDTA. Reactions run at 120 °C with FeCl2·4H2O precursor 111

Figure 42. PXRD patterns of $Fe_2(BDT)_3$ syntheses in varied mixtures of methanol and hexane. Reactions run at 160 °C with $FeSO_4 \cdot 7H_2O$ precursor 112

Figure 43. SEM images of $Fe_2(BDT)_3$ with 0 eq 1-mIm modulator 113

Figure 44. SEM images of $Fe_2(BDT)_3$ with 0.26 eq 1-mIm modulator 113

Figure 45. SEM images of $Fe_2(BDT)_3$ with 1.3 eq 1-mIm modulator 113

Figure 46. SEM images of $Fe_2(BDT)_3$ with 2.6 eq 1-mIm modulator 114

Figure 47. SEM images of $Fe_2(BDT)_3$ with 12.9 eq 1-mIm modulator 114

Figure 48. SEM images of $Fe_2(BDT)_3$ with 25.8 eq 1-mIm modulator 114

Figure 49. SEM images of $Fe_2(BDT)_3$ synthesized at 60 °C with octylamine as a modulator.....115

Figure 50. SEM images of $Fe_2(BDT)_3$ synthesized at 60 °C with octylamine as a modulator (2) 115

Figure 51. SEM images of $Fe_2(BDT)_3$ synthesized at 60 °C with octylamine as a modulator (3) 116

Figure 52. SEM images of $Fe_2(BDT)_3$ synthesized at 60 °C with octylamine as a modulator (4) 116

Figure 53. SEM images of $Fe_2(BDT)_3$ synthesized at 60 °C with octylamine as a modulator (5) 117

Figure 54. Powder x-ray diffraction patterns of MIL-125 119

Figure 55. SEM image of medium MIL-125 nanoparticles.....120

Figure 56. SEM image of large MIL-125 nanoparticles 121

Figure 57. Stacked NMR spectra of Pre- and Post-photodoping experiments of 32 nm MIL-125with ethanol and acetone. Bottom to top: pre-photodopoing, 20 hours, 36 hours of photodoping.....122

Figure 58. Stacked NMR spectra of Pre- and Post-photodoping experiments of 32 nm MIL-125 with ethanol and acetone. Scaled from 5 to 0 ppm. Bottom to top: pre-photodopoing, 20 hours, 36 hours of photodoping.....123

Figure 59. NMR of pre- and post-photodoping (96 h) of 32 nm MIL-125 with hexanal with ethanol. NMR in MeCN-d3 124

Figure 60. NMR of pre- and post-photodoping (96 h) of 32 nm MIL-125 with styrene with ethanol. NMR in MeCN-d3 125

Figure 61. Photo of 18 nm MIL-125 in acetonitrile with decamethyl ferrocenium tetrafluoroborate in solution after being photodoped. 126

Figure 62. Photo of 32 nm MIL-125 particles in a quartz teflon-capped NMR tube after being photodoped and allowed to settle. 126

Figure 63. GCMS trace of pure hexanal (top) and the post reaction mixture (bottom) after 32 nm MIL-125 photodoping reaction 127

Figure 64. GCMS trace of pure methyl phenyl ketone (top) and the post reaction mixture (bottom) after 32 nm MIL-125 photodoping reaction. Database-matched structure and similarity in percent are overlaid at peak positions. 128

Figure 65. GCMS trace of pure hexanal (top) and the post reaction mixture (bottom) after 32 nm MIL-125 photodoping reaction. Database-matched structure and similarity in percent are overlaid at peak positions. 129

Figure 66. ^{1}H NMR spectrum of N,N'-dimethyl benzimidazole. Left, full spectrum from -2.5 to 15.5 ppm. Right, enlarged spectrum. 132

Figure 67. ^{1}H NMR Spectrum of N,N'-dimethyl benzimidazolium dithiocarboxylate in DMSO. 133

Figure 68. HOMO-LUMO gaps of Nickel Complexes 136

Figure 69. HOMO-LUMO gaps of Copper Complexes 136

Figure 70. HOMO-LUMO gaps of tris complexes 136

Figure 71. Molecular orbitals of nickel-oxygen models 137

Figure 72. Molecular orbitals of nickel-sulfur models 138

Figure 73. Molecular orbitals of copper-oxygen models 139

Figure 74. Molecular orbitals of copper-sulfur models 140

Figure 75. Molecular orbitals of bis-cobalt-sulfur models 140

Figure 76. Molecular orbitals of tris-cobalt-BICS$_2$ models 141

Figure 77. Molecular orbitals of tris-chromium-BICS2 models..... 142

Figure 78. Molecular orbitals of tris-scandium-BICS2 models..... 142

Figure 79. Electrostatic potential maps of nickel complexes, plotted at 0.05 isosurface level, colormap from -0.1 to 0.0 to 0.1 a.u. (Red-Green-Blue). 165

Figure 80. Electrostatic potential maps of copper complexes, plotted at 0.05 isosurface level, colormap from -0.1 to 0.0 to 0.1 a.u. (Red-Green-Blue). 166

Figure 81. Electrostatic potential maps of nickel complexes, plotted at 0.1 isosurface level, colormap from -0.1 to 0.0 to 0.1 a.u. (Red-Green-Blue). 167

Figure 82. Electrostatic potential maps of copper complexes, plotted at 0.05 isosurface level, colormap from -0.1 to 0.0 to 0.1 a.u. (Red-Green-Blue). 168

Figure 83. zNICS exponential fit: Benzene..... 170

Figure 84. zNICS exponential fit: Benzimidazole dithiocarboxylate – phenyl ring..... 170

Figure 85. zNICS exponential fit: Benzimidazole dithiocarboxylate – imidazole ring..... 171

Figure 86. zNICS exponential fit: Nickel-Benzimidazole carboxylate – phenyl ring 171

Figure 87. zNICS exponential fit: Nickel-Benzimidazole carboxylate – imidazole ring 172

Figure 88. zNICS exponential fit: Nickel-Benzene carboxylate 172

Figure 89. zNICS exponential fit: Nickel-bisdiolene..... 173

Figure 90. zNICS exponential fit: reduced Nickel-bisdiolene..... 173

Figure 91. zNICS exponential fit: Nickel benzimidazole dithiocarboxylate – phenyl ring..... 174

Figure 92. zNICS exponential fit: Nickel benzimidazole dithiocarboxylate – phenyl ring..... 174

Figure 93. zNICS exponential fit: Nickel-bisdthiolene..... 175

Figure 94. zNICS exponential fit: reduced Nickel-bisdiolene..... 175

LIST OF TABLES

Table 1. A short list of terms commonly used in the study of MOFs and conductive porous materials. 22

Table 2. Resulting phases of Fe_2BDT_3-X from varied equivalents of sodium thiocyanate or 1-methyl imidazole. Phase is denoted as 1, 2 or 3, with X representing no product. The solvent system used is indicated as SS1, SS2 or SS3, corresponding to 3:1 iPrOH/cyclohexane, 8:1 iPrOH/water and 1.67:1 iPrOH/water respectively. 36

Table 3. Utilized iron precursor salts and added ionic salts as modulators/solubilizing agents. Resulting phase is reported as 1, 2 or 3, corresponding to $Fe_2(BDT)_3$-X. 39

Table 4. Unpaired electron count and single point energy of modeled complexes 134

Table 5. Calculated α and β HOMO and LUMO of Models. Calculated α and β HOMO/LUMO gap 135

Table 6. AIM-derived electrostatic potentials 143

Table 7. AIM Delocalization Index (total) of all complexes 144

Table 8. AIM Delocalization index (alpha) of all complexes 145

Table 9. Aim Delocalization Index (beta) of all complexes 146

Table 10. Lowdin Spin Population of all complexes 147

Table 11. Mayer Bond Orders of all complexes 148

Table 12. Select bond lengths/atomic distances in all complexes 149

Table 13. Mulliken Atomic Orbital Analysis - NiBICO2 150

Table 14. Mulliken Atomic Orbital Analysis - $NiPhCO_2$ 150

Table 15. Mulliken Atomic Orbital Analysis - NiBDO 151

Table 16. Mulliken Atomic Orbital Analysis - $NiBDO^{2\bullet}$ 152

Table 17. Mulliken Atomic Orbital Analysis - $NiBICS_2$ 152

Table 18. Mulliken Atomic Orbital Analysis - $NiPhCS_2$ 153

Table 19. Mulliken Atomic Orbital Analysis - NiBDT 154
Table 20. Mulliken Atomic Orbital Analysis - $NiBDT^{2\bullet}$ 154
Table 21. Mulliken Atomic Orbital Analysis - $CuBICO_2$.....155
Table 22. Mulliken Atomic Orbital Analysis - $CuPhCO_2$ 155
Table 23. Mulliken Atomic Orbital Analysis - CuBDO 156
Table 24. Mulliken Atomic Orbital Analysis - $CuBDO^{2\bullet}$.....157
Table 25. Mulliken Atomic Orbital Analysis - $CuBICS_2$ 157
Table 26. Mulliken Atomic Orbital Analysis - $CuPhCS_2$.....158
Table 27. Mulliken Atomic Orbital Analysis - CuBDT.....159
Table 28. Mulliken Atomic Orbital Analysis - $CuBDT^{2\bullet}$ 159
Table 29. Mulliken Atomic Orbital Analysis - $CoBICS_2$ 160
Table 30. Mulliken Atomic Orbital Analysis - CoBDT.....160
Table 31. Mulliken Atomic Orbital Analysis - $CoBDT^{2\bullet}$ 161
Table 32. Mulliken Atomic Orbital Analysis - Tris-$CoBICS_2$ 162
Table 33. Mulliken Atomic Orbital Analysis - Tris-$CrBICS_2$.....163
Table 34. Mulliken Atomic Orbital Analysis - Tris-$ScBICS_2$.....164
Table 35. xNICS fit values and integrations. Calulated data fit to exponential functions.....169
Table 36. Optimized geometry coordinates of $NiBICO_2$.....179
Table 37. Optimized geometry coordinates of $NiPhCO_2$.....181
Table 38. Optimized geometry coordinates of NiBDO 182
Table 39. Optimized geometry coordinates of $NiBDO^{2\bullet}$.....183
Table 40. Optimized geometry coordinates of $NiBICS_2$.....184
Table 41. Optimized geometry coordinates of $NiPhCS_2$ 186
Table 42. Optimized geometry coordinates of NiBDT.....187

Table 43. Optimized geometry coordinates of $NiBDT^{2\bullet}$ 188

Table 44. Optimized geometry coordinates of $CuBICO_2$ 189

Table 45. Optimized geometry coordinates of $CuPhCO_2$ 191

Table 46. Optimized geometry coordinates of CuBDO 192

Table 47. Optimized geometry coordinates of $CuBDO^{2\bullet}$ 193

Table 48. Optimized geometry coordinates of $CuBICS_2$ 194

Table 49. Optimized geometry coordinates of $CuPhCS_2$ 196

Table 50. Optimized geometry coordinates of CuBDT 197

Table 51. Optimized geometry coordinates of $CuBDT^{2\bullet}$ 198

Table 52. Optimized geometry coordinates of bis-$CoBICS_2$ 199

Table 53. Optimized geometry coordinates of CoBDT 201

Table 54. Optimized geometry coordinates of $CoBDT^{2\bullet}$ 202

Table 55. Optimized geometry coordinates of tris-$CoBICS_2$ 203

Table 56. Optimized geometry coordinates of $CrBICS_2$ 205

Table 57. Optimized geometry coordinates of $ScBICS_2$ 207

Table 58. Crystallographic details for $MeBICS_2$. SCXRD data were collected on a Bruker Apex2 diffractometer, using Cu Kα (λ = 1.54178 Å) radiation. 209

CHAPTER I

INTRODUCTION AND MINI-REVIEW

General introduction

Metal-organic frameworks (MOFs) have been identified for use in gas capture and storage, chemical separations, catalysis (photo-, electro-, heterogenous), semiconductors, batteries and capacitors, sensors, drug delivery and fundamental studies.[1–21] The synthetic tunability and modularity of MOFs is what enables the development of porous materials with advantageous properties versus their densely packed inorganic counterparts (Figure 1a). Even though MOFs have been explored for semiconducting and charge-transport related applications, the majority of MOFs are insulating due to small, hard ionic bonding interactions (Figure 1b) and a variety of transport mechanisms have been explored to circumvent this limitation.[22] Highly conductive MOFs have been synthesized through careful selection of architecture and bonding motifs that promote electronic transport, either by utilizing redox states, covalency or delocalized bonding.[23–26] A wide range of mechanisms for charge transport are known in these porous frameworks.

Background/Mini review.

Like all other fields of study, researchers who work with MOFs or conductive materials can take for granted that the terminology used frequently within the field may be used elsewhere in a different manner. For that reason, provided is a short table of terms that may be helpful to define here within the context of MOFs or conductive porous materials in general (Table 1). This list is by no means exhaustive but is hopefully a simple way to ensure clarity.

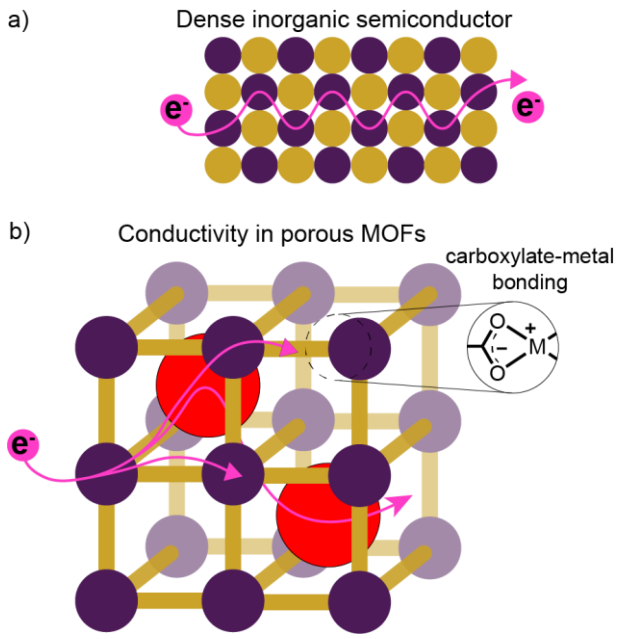

Figure 1. a) Cartoon schematic of electron transport in typical densely packed semi-conductors. b) MOF structures and ionic bonding. Electron transport is shown through redox hopping pathways, host-guest interactions and through bond conductivity.

Table 1. A short list of terms commonly used in the study of MOFs and conductive porous materials.

Terminology	Definition
Linker	An organic molecule that is functionalized at multiple points, allowing for bonding between multiple metals or inorganic clusters. One of the two components of metal-organic frameworks.
Secondary Building Unit (SBU)	Usually a metal cluster subunit that is a part of the structure that builds into a MOF. Sometimes the SBU includes portions of the organic linkers.
Modulator	An additional molecule added into the MOF synthesis to control the size or crystallite shape. This can be in an equilibrium of a bound and unbound form with the metal or SBU.
Conductivity	Defined as inverse resistance, usually in units of siemens per centimeter ($S \cdot cm^{-1}$).

Table 1. continued

Terminology	Definition
Insulator	Insulators or insulating materials are usually defined as having a band gap of greater than 4 eV. Typical conductivity values lie below 10^{-6} S·cm^{-1}
Semiconductor	Semi-conductors have a band gap less than 4 eV. Because there exists an energy gap between the conduction and valence band, increased thermal input typically results in increased conductivity. Conductivity values range greatly for this class of materials. 10^{-8} to 10^{2} S·cm^{-1} represent typical values.
Metallic conductor	Metallic conductors do not have a band gap, and instead features a continuum of energy states that allow for electron flow. Increased thermal input typically results in decreased conductivities due to thermal noise limiting the efficiency of electron transport. Usually very high conductivities of 10^{6} S·cm^{-1} but can vary.
Single crystal	A crystal of a given material that is a single crystalline domain throughout with no grain boundaries.
Redox hopping	Electrical transport between two species of different oxidation states. This is commonly seen in iron-containing MOFs with $Fe^{2+/3+}$ redox pairs.
Guest	A species that is introduced into a material that is not bonded to the structure, usually kept in place through intermolecular interactions. Guests are often intercalated into the pores of MOFs.
Dopant	A species that is introduced into a material that is included in the material itself. Electronic dopants typically take the form of additional electrons or holes introduced into semiconductors.

Table 1. continued

Terminology	Definition
Photodoping	The process of exciting electrons into the conduction band of a material with photoexcitation and trapping them there by quenching the hole left in the valence band.
NanoMOFs	In the context of MOFs, it is most useful to define nanoparticles or nanoMOFs as having total particle size of less than 500 nm, although practically, most differences are seen below 100 nm.
Bulk	Referring to MOF materials that are not made in the nano-regime. Typical particle sizes range from 0.5-10 μm or larger.
Phase	A crystalline lattice corresponding to a unique arrangement of a given set of metals/SBUs and linkers. The same combination of linker and metals can sometimes result in different phases.

Types of conductivity

There are several mechanisms of conductivity in MOFs and substantial effort has been put into increasing conductivity.[27] It is often difficult to elucidate exactly what mechanism is responsible for electron transport, but the types can be broken down into categories. The type of measurement used can also influence the reported value of conductivity, and single crystal measurements can be used to elucidate axial-dependence of conductivity as well.[28,29]

Redox Hopping: MOFs with metals or linkers of mixed oxidation states are primarily responsible for redox hopping mechanisms in materials (Figure 2a).[30] Iron is most commonly implicated in redox hopping mechanisms due to its accessible $Fe^{2+/3+}$ redox couple at mild conditions. MOFs like $Fe(TA)_2$ and $Fe_2(BDT)_3$ are well known for this behavior. Potential-dependent conductivity measurements are a powerful tool to determine if a material is participating

in redox hopping for charge transport.[31] In order for electrons to be shuttled across the material in this way, there must be a mixed population of a redox couple. If all species are oxidized or reduced, charge cannot effectively pass through because all potential charge carrying sites are either occupied or empty. When an external potential is applied at the potential of the redox couple, a mixed-valency state is induced, and optimal conditions are present for charge transport.

Band type: In materials that have a continuous pathway across the system in which to transport charge, it is considered band type (Figure 2b). Due to the highly ionic nature of many MOFs, this is less common and somewhat difficult to incorporate. Several examples of MOFs have been implicated in this type of conductivity, with sometimes difficult to determine conductive pathways. Conductive 2D sheet MOFs are often categorized as having band type conductive mechanisms, but directionality and crystal packing can influence the measured values to a large extent.

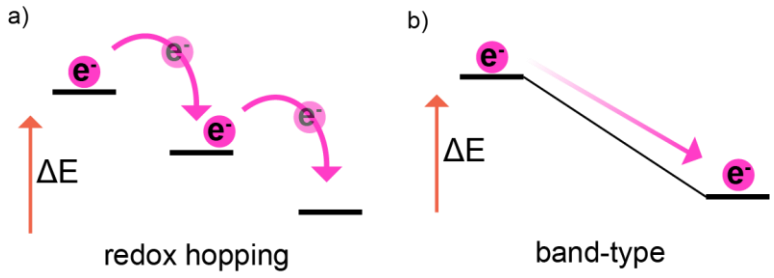

Figure 2. a) Representations of energy states in redox hopping and b) band-type conductivity

Through-bond: A subset of band type conductivity, when charge is directly passed through bonds in a material, it is called a through-bond pathway. Metals and ligands with high orbital overlap are required for electron transport with low resistivity in this category. Softer and larger metal-heteroatom pairs are typically utilized for through-bond transport like copper and sulfur.[32] Some redox-hopping materials are categorized as through-bond transport, especially when 1D rod-like SBUs are included in the structure.

Extended conjugation: Typically attributed to materials with aromatic π-systems, extended conjugation pathways transport charge through highly conjugated bonds. Like through-bond pathways, often times 2D sheets are active for electron transport with extended conjugation pathways. Large annulated aromatic cores of linkers are able to shuttle charge across their intrinsically delocalized orbitals quite like graphene and are often used to induce this type of charge transport. Annulated cores are not a requirement, however, and often redox non-innocent linkers are utilized with extended conjugation pathways that do not include graphene-like linkers.[33]

Through-space[34]: 2D stacked sheets or pillared materials are often examples of through-space charge transport, where overlapping π bonds or p-orbitals can pass charge from sheet to sheet. When extended-conjugation pathways are present, often there is a possibility for through-space transport as well. π-stacking and overlap between p or d orbitals of adjacent systems are able to move electrons in directions that are not always in line with the bonding motifs, enhancing conductivity along crystalline axes that may not otherwise be able to conduct.[35]

Guest promoted: Redox active additives or molecules that enable continuous pathways of electron transport are utilized in guest promoted conductivity. When a MOF is itself unable to shuttle charges in the lattice, incorporation of species with accessible redox couples can act as a substitute to promote redox hopping. Other guests provide a through-space transport mechanism such as tetracyanoquinodimethane (TCQN).[36,37] The architecture and redox active nature of the TCQN allows for electron mobility between metal centers that are otherwise electronically insulated from each other.[38,39]

Early reports of conductive MOFs

Although MOF-5 is not electrically conductive, it has been explored for its optoelectronic properties soon after its discovery in 1999.[40] In 2004, MOF-5 was identified as an analogue to zinc

oxide quantum dots and the study revealed charge transfer between organic linkers and the ZnO clusters closely mimicking the quantum dot analogue.[41] In 2008, a metal-organic framework was reported as conductive for the first time.[42] $Cu[Cu(pdt)_2]$ was reported with a conductivity of $6 \cdot 10^{-4}$ $S \cdot cm^{-1}$ consisting of 2,3-pyrazinedithiolate linkers complexed with copper (Figure 3a). While the measured conductivity is not particularly high compared to the range of known conductive materials, it did mark the start of metal-organic frameworks as viable targets for semiconductors and conductive porous materials. In 2014, $Ni_3(HITP)_2$ was reported as a 2-dimensional porous sheet with a remarkable conductivity of up to 40 $S \cdot cm^{-1}$ (Figure 3b).[43] The move towards the possibility of metallic conductors in MOFs continued to push development of 2D conductive materials.

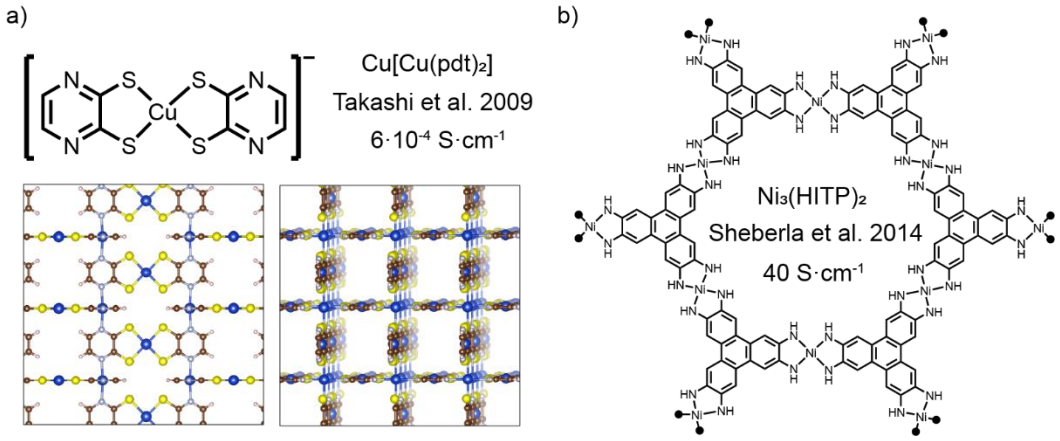

Figure 3. a) The linker and two perspectives of the $Cu[Cu(pdt)_2]$ crystalline lattice and b) a chemdraw of $Ni_3(HITP)_2$.

Design aspects of 3D conductive MOFs

3-dimensional MOFs have continued to garner interest with highly porous frameworks featuring large surface areas. The intrinsic challenge of introducing high conductivity to frameworks of high porosity makes the formation of conductive 3D MOFs a difficult prospect. The introduction of guest molecules has proven an effective strategy for tuning electrical properties, but

pore volume is intrinsically lost when guests are introduced, decreasing surface area. Many of the conductive 3D frameworks currently known feature redox active metals, SBUs or linkers and utilize redox hopping mechanisms. Precise control of mixed valency can prove to be difficult in some cases or instability to atmospheric oxidants such as O_2. Size control of resulting particles has been reported as an effective method of tuning conductivity, with nanoMOFs increasing thin-film conductivity as particle size decreases. It is hypothesized that dense packing of nanoMOF films contributes to increased conductivity.

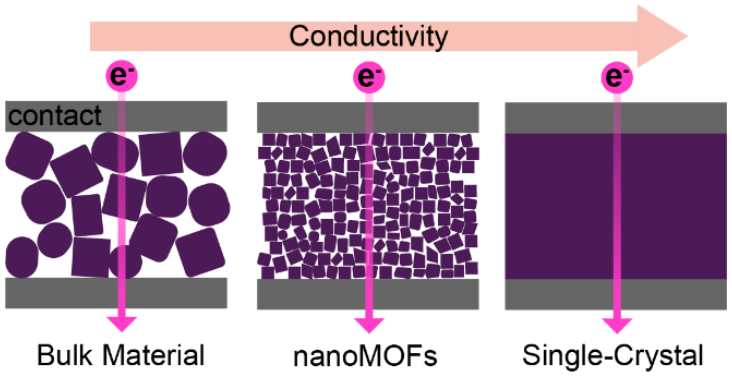

Figure 4. A schematic representation of particle packing in MOF samples. Measured conductivity as MOF particles become smaller and more densely packed.

Design aspects of 2D conductive MOFs

Synthetic conditions for the acquisition of highly crystalline 2D conductive frameworks have posed as the most challenging aspect of designing 2D conductive porous materials. Synthetic methods often rely on biphasic systems and formation of crystalline materials at the interface with slow growth. The crystal structure and packing of layers can highly depend on slow controlled growth. Often, it is useful to obtain single crystal conductivities along different axes in 2D sheet materials to deconvolute in-plane and inter-sheet charge transport efficiencies. Control of oxidation state is often important in 2D sheets, with external reductants or oxidants highlighting preferred oxidation states. The identity of the heteroatom responsible for metal-ligand bonding has also been

highly implicated for the extent of conductivity. While heteroatom identity affects resulting conductivity of 3D and 2D sheets, graphene-like MOFs are especially susceptible to heteroatom identity with through bond and extended conjugation pathways making covalency and conjugation an important design aspect.

Current benchmarks for conductive MOFs

Copper benzenehexathiolate ($Cu_3(BHT)$) stands as a MOF with the highest reported conductivity to date. Initially reported in 2015, and then again in 2018, the densely packed 2D sheets display conductivity of 2500 $S \cdot cm^{-1}$, even displaying superconductivity at low temperatures and metallic conductor-like behavior.[44,45] The structure features copper-sulfur bonds in a dense network with low porosity.

Nickel hexaiminotriphenylene ($Ni_3(HITP)_2$) holds the record for the highest conductivity of a framework with permanent porosity, first reported at 40 $S \cdot cm^{-1}$ and later at 150 $S \cdot cm^{-1}$ as a single crystal under vacuum.[43,46] The 2D sheets feature large hexagonal pores and unique stacking enabling both inter-sheet charge transport and through-sheet conductivity.

$Fe_2(BDT)_3$ has been reported as the most conductive 3D porous framework with conductivities up to 1.8 $S \cdot cm^{-1}$ after oxidation in ambient conditions.[47] With 1D rod-like SBUs, a through bond redox hopping mechanism is implicated with introduction of a mixed $Fe^{2+/3+}$ population. The conductivities reported are single crystal measurements taken from one of three possible phases of $Fe_2(BDT)_3$. While synthetically challenging to access, the report of this MOF presents a rather impressive benchmark for permanently porous 3D materials.

This thesis

Towards the advancement of conductive porous materials, several approaches are presented in this work. Chapter 2 presents a synthetic approach and consideration of 3D conductive

MOF $Fe_2(BDT)_3$. While $Fe_2(BDT)_3$ currently stands as the most conductive 3-dimensional MOF, consideration of this material has consisted of an analysis of single crystals.[47] Only one of the three reported phases provides a conductivity of 1.8 $S \cdot cm^{-1}$, whereas the other possible products display low conductivities and/or other interesting electronic phenomena, such as spin-crossover. The reported synthetic approach described includes high temperatures (160 °C), long times (3 days) and difficulty in phase selection.[48] In fact, the synthetic methods previously used for development do not reliable produce phase pure MOF powders, and often a mixture of two or all three phases are present and a single crystal is extracted for analysis. This work utilizes modulators in the synthetic approach to lower the temperature of formation, reliably increase phase purity and even control the nanoparticle size of two known phases. Control of phase purity was achieved using a modulator that demonstrated success previously in closely related iron-MOFs.[49] Size control of $Fe_2(BDT)_3$ nanoparticles was achieved with a surfactant-like modulator, with particle size as small as 11 nm.

Chapter 3 presents how the redox potential of electronically doped MOF MIL-125 can be tuned through nanoparticle size. The oxo-cluster based nature of MIL-125 makes meaningful comparison to non-porous metal-oxo materials possible. Importantly, metal-oxo materials are a group of materials that can be photodoped under the correct synthetic conditions.[50] Due to titanium's energetically low-lying d-orbitals and accessible band-gap, titanium-based materials are targets for stable, electronically dopable semiconductors. MIL-125 is a titanium-oxo cluster MOF that can readily undergo photodoping in anaerobic conditions.[51] To effectively trap electrons in the conduction band, sacrificial reductants donate electrons to quench valence-band holes. The extent of photodoping is highly dependent on the identity of the reductant, and proton-coupled electron transfer methods cannot fully reduce the material.[52,53] Although the reduction process has been

well-studied with MIL-125, the particle size-dependent nature of the process has only recently received study.[54] The size-dependent redox potential of MIL-125 was investigated here using optical redox indicators, monitored by ultraviolet-visible light absorbance spectroscopy. This work revealed that in non-aqueous and non-pH controlled conditions, the redox potential became increasingly negative as particle size decreased but did not reach that of the hydrogen evolution reaction. Experimental evidence of transfer hydrogenation from an organic sacrificial reductant to an acceptor carbonyl-containing molecule was observed. No hydrogen gas evolution was observed, meaning that the doping limit is not controlled by unwanted production of H_2 gas.

Chapter 4 presents a molecular analysis of 2D conductive MOFs through DFT and proposes synthetic design of new 2D or 3D materials using an NHC-dithiocarboxylate-based ligand. While 2D materials with high conductivities like Cu_3(BHT) have been realized, a lack of full understanding and difficulties in synthetic methodologies are still present that limit the development of new conductive materials. An increase in covalency through selection of sulfur-containing ligands has been implicated in increased electronic communication in conductive materials.[55] A majority of MOFs are made using carboxylate-based linkers – small, hard, ionic bonding motifs that lack covalency. When considering electronic trends in conductive materials and the identity of the heteroatom, we find that for a series of isostructural materials, sulfur tends to result in higher conductivities than nitrogen or oxygen. This depends on the crystal packing of the material, so direct analogy is not always possible. The common approach to modeling conductive properties tends to focus on band diagrams and models of the extended materials.[56] An analysis of specific molecular properties are missing from many of these studies that could be linked to emergent materials properties. Using delocalization index, derived from the Atoms-In-Molecules theory, Lowdin spin population analysis and Mayer bond order with a series of molecular

analogues, the covalency of metal-ligand environments were evaluated.[57–60] This work demonstrates that covalency of sulfur-containing models is indeed higher than in the oxygen-containing analogues, but comparison across sulfur-containing models with known literature properties of the extended materials, a similarity in delocalization index between the metal and heteroatom is necessary for conductivity. Using the calculated trends, a linker based on zwitterionic N-heterocyclic carbene dithiocarboxylate motifs is proposed as a synthetic target due to a good match between calculated properties and proposed optimal values. Copper is implicated as a metal that would pair well with the proposed ligand to optimize the parameters.

In this thesis, attempts to control the size of $Fe_2(BDT)_3$ nanoparticles led to insight on phase selection and synthetic aspects of the material. A low-temperature, phase-pure method was developed to form 2 of 3 known phases and preliminary results of nanosizing of phase 2 and 3 are demonstrated as well. Continuing with the idea of emergent size-dependent electrical properties, the variation of redox potential was observed using optical indicators in conjunction with MIL-125 nanoparticles. The limitations of the redox potential were investigated and experimental evidence of transfer hydrogenation in non-aqueous media was confirmed. Finally, the theoretical investigation of sulfur-based ligands for increased conductivity revealed that simple estimates of covalency are inadequate to predict conductive properties in extended materials. A similarity of delocalization, spin density and well distributed bonding is necessary for electron transport optimization. A new motif for MOF ligands was proposed based on NHC-dithiocarboxylate delocalized radicals.

CHAPTER II

SYNTHETIC CONTROL OF CONDUCTIVE IRON MOF $Fe_2(BDT)_3$

Introduction

The field of conductive porous materials has been vital to the development of technology in today's day and age with need for better batteries, semiconductors and electro/photocatalysts.[61] 3-dimensional porous conductive frameworks have been a high-interest target for both fundamental studies and application-based works. Metal-organic frameworks (MOFs) have seen attention in the last two decades as conductive porous materials due to their modularity and regularity of crystal structure.[62] The ability to consider charge transport mechanisms along molecularly defined pathways has enabled insight into charge transport dynamics in a way that is not easily attained with densely packed, traditional semiconductors.[63,64] The opportunity for intercalation of guests and modular design of frameworks has put MOFs at an advantage in this field. While it is easy to idealize the development of porous frameworks that are electrically, or ionically, conductive, in reality the synthesis and realization of materials with those properties can be quite difficult. The material that holds the place of most conductive permanently porous MOF is $Fe_2(H_{0.67}BDT)_3 \cdot 17(H_2O) \cdot 0.5(iPrOH)$ (H_2BDT = 5,5′-(1,4-phenylene)bis(1H-tetrazole)), simplified as $Fe_2(BDT)_3$.[65] While this MOF has a reported conductivity of 1.8 $S \cdot cm^{-1}$ at the maximum, it is not as simple to obtain as one might expect. With three different possible phases resulting from the same starting materials, all with varying conductivity and electronic properties, careful synthetic choices must be made in order to produce the phase of choice.[48] Specific phases of $Fe_2(BDT)_3$ will hereafter be referred to as $Fe_2(BDT)_3$-X, with X = 1, 2 or 3 to denote one of three previously reported phases. $Fe_2(BDT)_3$-1 has been reported as an iron(II) material with low spin behavior, $Fe_2(BDT)_3$-2 exhibits spin-crossover behavior and low conductivities at $6.1 \cdot 10^{-8}$ $S \cdot cm^{-1}$, and $Fe_2(BDT)_3$-3 is reported as a high spin iron(II) material with an incredibly high conductivity of 1.8

S·cm^{-1} as stated previously (Figure 5).[48,66,67] While these polymorphs have been synthesized and noted for their different properties, they have only been synthesized in the context of obtaining large single-crystal samples to measure those properties. Reported in recent years, the size of MOF particles obtained from syntheses can heavily influence properties like optical gap, conductivity and spin-crossover temperature.[49,68] While these size-dependent property relationships have been explored in the quantum dot and metal nanoparticle fields, the same explanations do not always analogously correspond to nanoMOFs. Modulated synthesis of MOF growth has demonstrated efficacy in size control of the resulting particle.[69,70] This modulated synthesis utilizes an additional compound in the synthesis that can complex with the metal center but cannot continue particle growth with an additional site of functionalization. Modulators have also demonstrated influence of resulting phase and/or morphology of particles, typically with variations in pKa or steric bulk.[71–78]

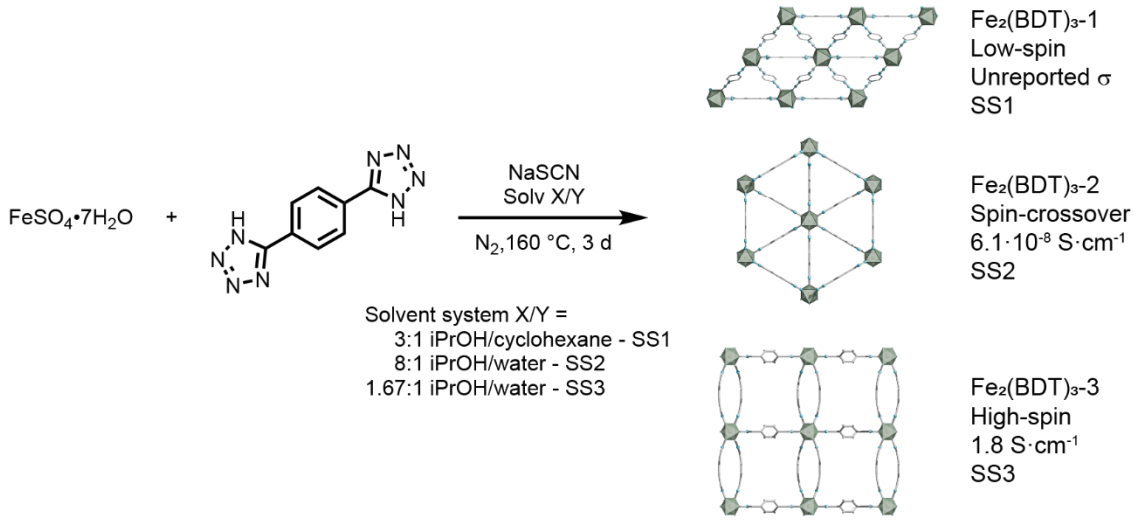

Figure 5. Synthesis of $Fe_2(BDT)_3$ as reported in literature. The structure of $Fe_2(BDT)_3$-X isomers are displayed on the right, with properties such as iron spin state, conductivity and solvent system reported to produce the corresponding phase.

Controlling the phase of $Fe_2(BDT)_3$ thus far has consisted of use of varied solvents, with no focus on the resulting size of the particle except to get large single crystals. We hypothesized that

use of modulator in the synthesis could effectively control for phase and size of the resulting $Fe_2(BDT)_3$ particles. We report the investigation of the formation of $Fe_2(BDT)_3$-X phases with variations of synthetic conditions and the addition of varied modulators.

Phase and nanoparticle size control of $Fe_2(BDT)_3$

Synthesis of $Fe_2(BDT)_3$ was carried out utilizing synthetic methods presented in literature. The resulting phase of the materials was analyzed with powder x-ray diffraction (PXRD) and compared against simulated data obtained from crystallographic information files available on the CCDC. Typically, the different phases of this material are accessed during solvothermal synthesis with variations in the solvent system. The solvent systems originally reported are mixtures of isopropanol and either cyclohexane or water (3:1 iPrOH/cyclohexane, 8:1 iPrOH/water, 1.67:1 iPrOH/water for phase 1, 2 and 3 respectively, referred to as SS1, SS2 and SS3.) When carrying out this synthesis based on the original reported conditions, we noticed a discrepancy between the solvent system used and the expected product. Even with conditions that would predict isomers 1, 2 and 3, the reactions resulted in solely isomer 1. The reported synthesis utilizes sodium thiocyanate as a reagent that does not remain in the final structure. The role of the sodium thiocyanate is not discussed much, but solubilization of iron sulfate in these solvent systems is aided by the presence of the sodium salt. Varying the concentration of NaSCN in the reaction surprisingly does not result in much change in the phase of the material produced, other than the introduction of phase 3 with higher equivalents of NaSCN and SS2. There is no observed $Fe_2(BDT)_3$ when no sodium thiocyanate is used, so it is key to the formation of the material in standard conditions (Table *2*).

Modulated syntheses were carried out using standard conditions with added 1-methyl imidazole (1-mIm) as a modulator, utilized previously to control the particle size of MOFs with

similar iron-nitrogen bonding environments (Figure *6*).[49] The amount of modulator added to the synthesis was ranged from 0 to 25.8 as a huge excess. Oxygen was minimized by sparging of solvents with nitrogen gas before the synthesis, with care taken to continue to exclude ambient air during setup. Once again, expected phases were not obtained in the control reaction with 0 equivalents of modulator, except for phase 1 (Table *2*). As the amount of modulator increased, we observed that phase 2 was the predominant resulting material in the system. When large amounts of 1-mIm was introduced to SS1 or any amount in SS2 or SS3, the resulting structure corresponded to $Fe_2(BDT)_3$-2. This prompted further investigation into the role of the 1-methyl imidazole and the formation of the material.

Table 2. Resulting phases of Fe_2BDT_3-X from varied equivalents of sodium thiocyanate or 1-methyl imidazole. Phase is denoted as 1, 2 or 3, with X representing no product. The solvent system used is indicated as SS1, SS2 or SS3, corresponding to 3:1 iPrOH/cyclohexane, 8:1 iPrOH/water and 1.67:1 iPrOH/water respectively.

Solvent system	NaSCN equivalents			
	0	0.5	2	5
SS1: iPrOH/cyclohexane (3:1)	X	1	1	1
SS2: iPrOH/water (8:1)	X	1	1	1,3
SS3: iPrOH/water (1.67:1)	X	1	1	1

	1-methyl imidazole equivalents					
	0	0.26	1.3	2.6	12.9	25.8
SS1	1	1	1	1,2,3	2	X
SS2	3	2	2	2	2	2
SS3	X	2	2	2	2	2

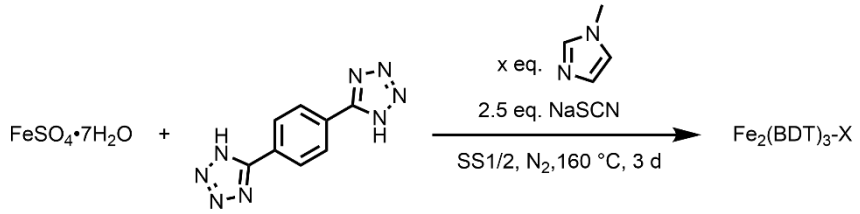

Figure 6. Reaction scheme of the modulated synthesis of $Fe_2(BDT)_3$. Equivalents of 1-mIm, x = 0, 0.26, 1.3, 2.6, 12.9 and 25.8.

A series of reactions with systematically varied modulator equivalents and reaction time

was carried out to demonstrate the time-dependent nature of the unmodulated and modulated reaction. In the first set of reactions, a set of six identical reactions were carried out in culture tubes at literature conditions with SS1. Each reaction in the set was utilized as a unique timepoint – 0.17, 0.5, 2, 4, 6, 24 and 48 hours. Three additional sets of six reactions were carried out with added 1-mIm as a modulator at 0.25, 2.5 and 10 equivalents. At the appropriate timepoint for each reaction, the culture tubes were taken off the heat, immediately centrifuged, washed to isolate the MOF product and analyzed with PXRD. The diffraction patterns were compared against the simulated patterns corresponding to all the known phases of $Fe_2(BDT)_3$. The diffraction data revealed formation of $Fe_2(BDT)_3$-1 in the unmodulated reaction around 4 hours, while the modulated reactions demonstrated formation of $Fe_2(BDT)_3$-1 with 0.25 equivalents of 1-mIm at 2 hours and formation of $Fe_2(BDT)_3$-2 with 2.5 and 10 equivalents of 1-mIm at 0.17 hours. This increased rate of formation of the material demonstrated the influence of the modulator for crystallization. Noting the speed and preference for the formation of phase 2 when a modulator was introduced, a similar set of reactions was carried out with SS2. Mimicking the series of reactions from before up to 24 hours, four different sets of reactions were carried out with modulator equivalents of 0, 0.25, 2.5 and 10. Each reaction set demonstrated product formation as early as ten minutes with a notable difference in phase purity. The reaction set with no modulator showed formation of both $Fe_2(BDT)_3$-2 and -3, with mixed phase formation at all time points. Each subsequent increase in equivalents of modulator show increased phase purity, with 10 equivalents resulting in incredibly consistent and pure diffraction patterns across all timepoints (Figure *7*). The resulting size of the particles (by Scherrer analysis) does not change with increased equivalents of modulator, suggesting that the modulator's role in the reaction is contributing to rapid crystal formation, and additional factors need to be considered to control the resulting particle size.

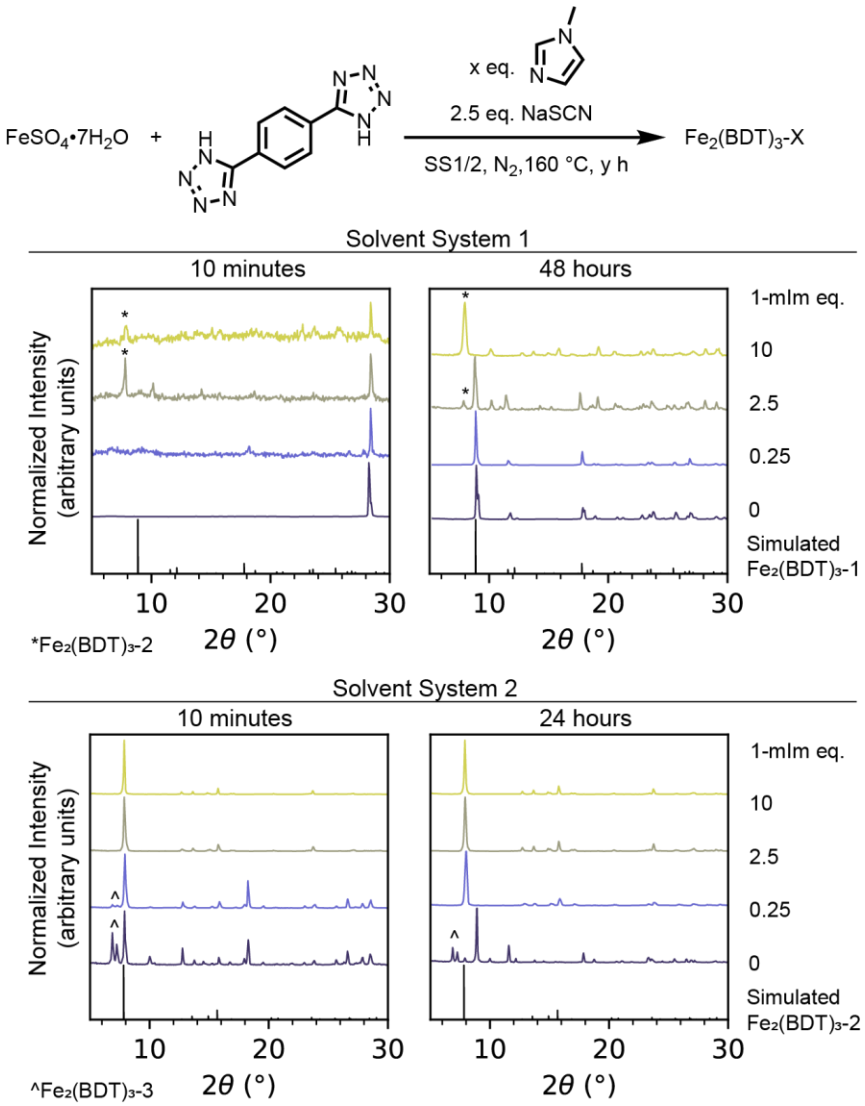

Figure 7. chemdraw reaction over a stacked pxrd of all the first and last reactions in each series. SS1 and SS2.

The observation of rapid material formation and the idea of precursor availability prompted an investigation of various iron salts and additional modulators to control the size and phase of the resulting material. Utilizing anions with varied ligand binding strength, syntheses were carried out using $FeBF_4 \cdot 6H_2O$, $FeCl_2 \cdot 4H_2O$ and the literature standard $FeSO_4 \cdot 7H_2O$. All solvent systems were combined with each iron precursor. Only the chloride and sulfate precursors showed any formation of $Fe_2(BDT)_3$ within the series of reactions, with little consistency between solvent system

used/expected product and the resulting phase. A series of added tetrabutyl ammonium salts with varied anions were evaluated with the standard $FeSO_4 \cdot 7H_2O$ system and $FeCl_2 \cdot 4H_2O$ to include external salts other than sodium thiocyanate as possible solubilizing agents or modulators. Due to the lack of formation of any product with the $FeBF_4 \cdot 6H_2O$ salts, it was excluded from these syntheses. The reactions were carried out at otherwise standard conditions with all solvent systems. Only $FeCl_2 \cdot 4H_2O$-based reactions with ammonium halide salts added displayed any indication of possible crystalline material, but no adequate confirmation could be obtained with the available diffraction patterns (Table *3*).

Table 3. Utilized iron precursor salts and added ionic salts as modulators/solubilizing agents. Resulting phase is reported as 1, 2 or 3, corresponding to $Fe_2(BDT)_3$-X.

Conditions	Produced $Fe_2(BDT)_3$-X phase		
	$FeSO_4 \cdot 7H_2O$	$Fe(BF_4)_2 \cdot 6H_2O$	$FeCl_2 \cdot 4H_2O$
SS1	1	X	1
SS2	1,3	X	X
SS3	3	X	X

	Solvent system 3 – standard conditions			
	*$TBABF_4$	$TBAPF_6$	TBABr	TBACl
$FeCl_2 \cdot 4H_2O$ + salt	X	X	2	2
$FeSO_4 \cdot 7H_2O$ + salt	X	X	X	X

*TBA = tetrabutyl ammonium

In order to investigate both low temperature conditions and modulators of differing identities, reactions using 1-mIm, octylamine and ethylenediaminetetraacetic acid (EDTA) were carried out. Octylamine was selected for its similarity to capping ligands used in quantum dot and metal nanoparticle syntheses, while EDTA was selected for its ion sequestering/chelating abilities. Noticing the results from the previous syntheses, $FeCl_2 \cdot 4H_2O$ was utilized in reactions paired with the three modulators of choice, solvent systems 2 and 3, and varied temperatures of 25, 40, 60, and 120 °C. Notably, no crystalline material was observed at 40 °C and lower temperatures. No

product formation was observed when EDTA was used as a modulator. Emergence of product with diffraction patterns matching the simulated $Fe_2(BDT)_3$-3 was most prominent in reactions utilizing $FeCl_2 \cdot 4H_2O$, 60 or 120 °C, octylamine and SS2 or SS3 (Figure *8*). Reactions containing 1-mIm produced $Fe_2(BDT)_3$-2, matching what we predicted from our observations during the time-monitored modulated syntheses.

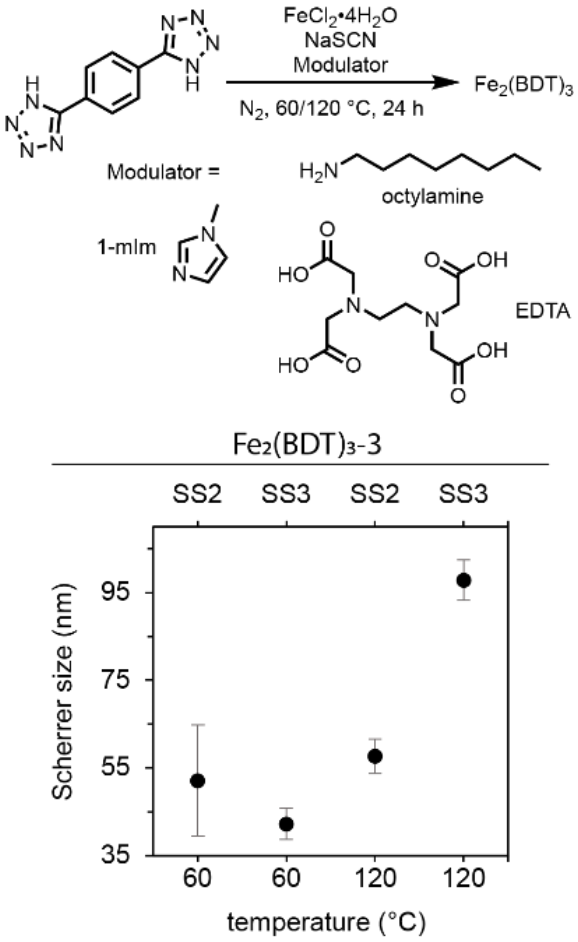

Figure 8. reaction scheme with $FeCl_24H_2O$, structure of modulators, varied temp and mod. graph of varied sizes from scherrer size with octylamine.

With a consideration for solvent properties, a series of reactions were carried out using methanol instead of isopropanol and hexane instead of cyclohexane. Given the polarities, protic (or aprotic) nature and functional groups similar to the analogous solvents, a similar outcome was

hypothesized. Using varied ratios of MeOH/hexane, a series of reactions were carried out at typical conditions. Using any combination of MeOH and hexane, resulted in successful formation of $Fe_2(BDT)_3$-1. Interestingly, the absence of either hexane or methanol produced no $Fe_2(BDT)_3$ (SI figure). With the observation that both solvents were necessary in the formation of the materials, an additional series of potential modulators was introduced to reactions with a 50:50 mixture of MeOH/hexane, referred to as SS4. Inconsistent with previous results, even when 1-mIm was present in the reaction, the resulting phase was $Fe_2(BDT)_3$-1. Notably, two other modulated reactions successfully produced $Fe_2(BDT)_3$-1. Only minor differences were observed in peak shape in the diffraction patterns, and calculated Scherrer sizes were between 55 and 108 nm with large error due to data quality (Figure *9*a). Minimal conclusions can be drawn reliably with these values, except that SS4 can be utilized in lieu of SS1 to obtain $Fe_2(BDT)_3$-1, and that there may be additional control of size possible with modulator but further data needs to be collected in this regard.

A final examination of solvent system and attempted size control was carried out with octylamine as a modulator, noted from our previous syntheses as effective in the formation of $Fe_2(BDT)_3$-3 at smaller sizes. The solvent systems present in the reactions were a 1:1 combination of methanol and either hexane, tetrahydrofuran (THF), dimethyl sulfoxide (DMSO), acetonitrile (MeCN) or dimethyl formamide (DMF). In an effort to control water and oxygen content, these reactions were set up in a nitrogen-filled glovebox with air- and water-free solvents and utilized anhydrous iron chloride as the metal precursor. Of these reaction conditions, only the MeOH/MeCN solvent mixture, SS5, produced a crystalline material that matched the simulated diffraction pattern of $Fe_2(BDT)_3$-2. Scherrer analysis of the peaks estimates the size as 11 nm, with high standard deviation due to peak fitting (Figure *9*b). While this did not correspond to our

targeted nano-$Fe_2(BDT)_3$-3, it represents the smallest estimate of synthesized $Fe_2(BDT)_3$-2.

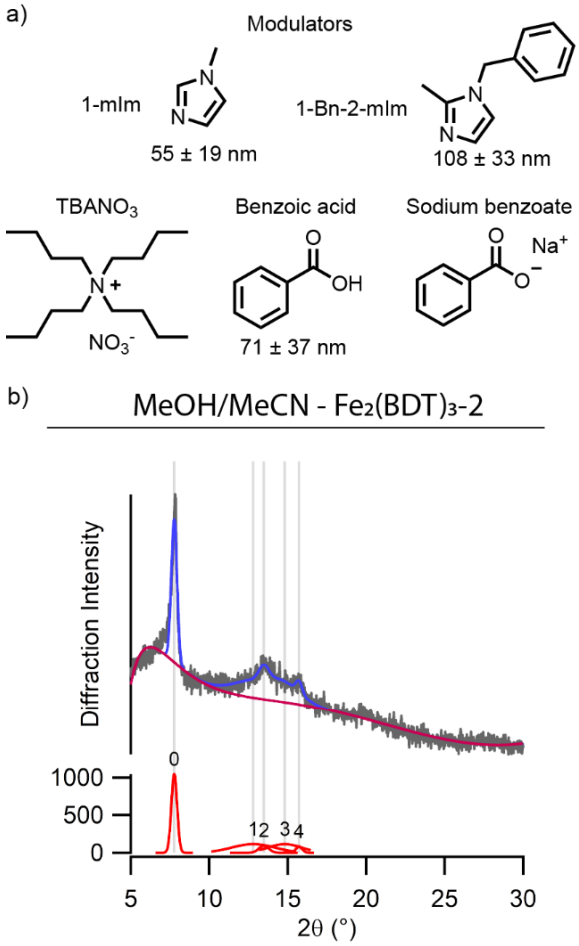

Figure 9. a) Chemdraw representation of modulators and Scherrer size for successful syntheses. b) PXRD pattern of Fe2(BDT)3-2 synthesized with MeOH/MeCN at 80 °C. Fitting of peaks for Scherrer analysis is pictured.

Additional synthetic conditions were screened in addition to the ones presented here (see _ for additional details). Notably, a large shift was observed in peak position in $Fe_2(BDT)_3$-2 diffraction patterns after washing the product with DMF, water and methanol. It is possible that solvent exchange is responsible for this difference.

Synthetic considerations and modulator identity

The idea of metal salt availability in its solvated form in the reaction mixture is not a novel concept. With the total lack of product formation in reactions with no sodium thiocyanate, it

follows that the solubilization of the iron precursor is an important part of the formation of $Fe_2(BDT)_3$. Typically, at room temperature when all the reaction components are mixed, the mixture is quite cloudy, and it is apparent that not all components of the reaction are well dissolved. Almost total dissolution of the starting materials is observed upon heating, when the solution becomes clear. When 1-mIm is added to the reaction mixture, the solution becomes clear and product formation is observed later upon heating. Notably, when oxidized Fe^{3+} ions are present in the reaction mixture, the solution also changes from a deep red to a light orange, suggesting that the thiocyanate anions, which classically form a blood-red solution when complexed with Fe^{3+}, are rapidly replaced by the added modulator.[79] Given the color change and incredibly fast formation of the $Fe_2(BDT)_3$ when 1-mIm is included in the reaction, we can infer that the 1-mIm not only has a role as a modulator, but a solubilizing agent and likely contributes to fast nucleation. When considering the rapid and reliable formation of $Fe_2(BDT)_3$-2 when 1-mIm is present, we suggest that the coordination of the 1-mIm with the Fe^{2+} ions in solution forms a system with a low barrier to formation of phase 2. A notable difference between phases 2 and 3 is the presence of a bent aromatic organic linker in $Fe_2(BDT)_3$-3, which would logically require unique conditions to crystallize due to a less stable out-of-plane aromatic environment. The high water content in the previously reported SS3 relative to the other solvent systems would imply a highly polar environment would lead to these strained systems. The tendency towards phase 2 with added modulator suggests that there is an interplay between the solubility of the species in the reaction, the stabilizing effect of the solvent and the kinetics of crystallization.

A similar solubilizing effect is observed with the addition of octylamine to the reaction with all starting materials dissolved before applied heat, but with the resulting product preferring the high symmetry $Fe_2(BDT)_3$-3 phase. It is possible that the Fe^{2+}, solubilized by octylamine, is

much more sterically hindered with the long alkyl chain of the modulator, allowing for bridging of bent BDT linkers rather than a rapid crystal growth with the planar linkers observed in $Fe_2(BDT)_3$-2. Curiously, the emergence of phase 3 with the addition of octylamine would seemingly contradict the increased water content in SS3. Octylamine's aliphatic nature, lower polarity and increased basicity compared to water puts the properties at odds when considering what leads to the formation of $Fe_2(BDT)_3$-3. It may be more apt to consider the role of the octylamine as a surfactant, with the water still primarily responsible for the resulting phase and the octylamine undergoing conversion into octylammonium cations that act to limit particle growth in a mechanism more conventional to typical nanoparticle growth. This type of modulation would infer that other surfactants would limit growth of $Fe_2(BDT)_3$-3 in a similar way.

With the formation of nano-$Fe_2(BDT)_3$-2 from a combination of methanol, acetonitrile, octylamine and $FeCl_2 \cdot 4H_2O$ as a precursor at 120 °C, we posit that a surfactant like modulator, a solvent system with a polar protic solvent and a weakly donating solvent, limited water content and a strongly binding counter anion are the optimal conditions to form nano-sized phase 2. Similar conditions but with increased water content are optimal conditions to form nano-$Fe_2(BDT)_3$-3.

Materials and methods

Synthetic manipulation was either carried out in a nitrogen-filled glovebox or in a nitrogen-filled glove-dome. Solvents were obtained from a solvent-purification system when possible, with HPLC-grade solvents. Water and isopropanol solutions were sparged with nitrogen gas before use and kept under inert atmosphere.

Reactions were carried out in 6 mL culture tubes with Teflon-lined caps or 20 mL scintillation vials equipped with septum caps. Reactions carried out in culture tubes were charged with solid reagents and solvents when applicable in a nitrogen-filled glovebox before the tubes

were sealed and brought out of the box. Sparged mixtures of SS1, SS2 or SS3 were added to the tubes in a nitrogen-filled glove dome. Liquid modulators were added before the tubes were again sealed and taken out. The reactions were sonicated for approximately 30 seconds before being heated in a custom-milled aluminum vial block on hot plates.

Reactions carried out in septum-capped scintillation vials were charged with solid reagents under ambient conditions before being sealed and flushed with nitrogen. Sparged solvent solutions were cannula transferred into the vials from a graduated cylinder to meter out solvent quantities. Liquid modulators were added with glass microsyringes. The reactions were sonicated for approximately 30 seconds before being heated with custom milled aluminum vial blocks or sand baths on hot plates. Reactions were removed from the heat and allowed to cool to room temperature before being washed in air with DMF (2 x 10 mL), water (2 x 10 mL), and methanol or isopropanol (2 x 10 mL), before being dried under vacuum.

Aliquots (approx. 0.1 mL) taken from septum capped reaction vials were subject to the same washing conditions (with 1.5 mL solvent) before powder x-ray diffraction data was obtained.

Conclusions

Through modulated synthesis of $Fe_2(BDT)_3$ with new reaction conditions, we present evidence of low temperature phase selective formation of a 3D-conductive MOF. We demonstrate rapid and phase pure selectivity of $Fe_2(BDT)_3$-2 with 1-methyl imidazole. Utilization of surfactant like modulator with variation of water content provides a synthetic route to nano-$Fe_2(BDT)_3$. The findings of this study suggest parameters leading to desired phase formation. While there still remains to be found specifics of the mechanism of particle formation and optimization of reaction conditions, this work stands as a general direction in the synthesis of $Fe_2(BDT)_3$.

CHAPTER III

SIZE-DEPENDENT REDOX POTENTIAL OF MIL-125

Introduction

Electronic tunability of semiconducting materials is vital to development of transistors and properly suited materials for electronic devices. Nanoparticles have been important contributors to tunability and processability of semiconductors.[80] Metal-oxo materials have been ubiquitous in the semiconductor field due to the synthetic availability of nanoparticle formation and dopant introduction.[81–84] With well-stabilized excited states and tunable band gaps, titanium oxide has been highlighted as a particularly well-suited system for this purpose. Metal-oxo cluster-based metal-organic frameworks (MOFs) have seen similar investigation, with additional emergent properties due to porosity and discreet building units.[85–87] MIL-125 is one of many titanium-oxo cluster MOFs at the center of numerous investigations. With an uncomplicated synthesis to obtain large quantities of the material and many computational studies to elucidate the electronics of the structure, MIL-125 sits at an advantaged position to corroborate and elucidate chemical principles (Figure *10*a).[88] Photodoping is a process to introduce additional charge carriers that has been applied to MIL-125, and other oxo-cluster MOFs, that takes advantage of the accessible band-gap and photochemistry analogous to dense titanium oxide systems.[83,87,89,90,54] When electrons are excited from the valence band into the conduction band of the material, the holes left behind are quenched by a reductant, usually a small simple alcohol like methanol or ethanol, which traps the excited electrons in the valence band (Figure 10b). For a material like MIL-125, which has eight Ti^{4+} centers, one would imagine that all titanium atoms could undergo this process, but experimentally when proton-coupled electron transfer (PCET) methods are employed, only two of the eight titanium atoms undergo this electronic doping (Figure 10c). Some have postulated that the observed limit represents an overlap of redox potential with the hydrogen evolution reaction

(HER) and any additional electrons contribute to H_2 production.[91,92]

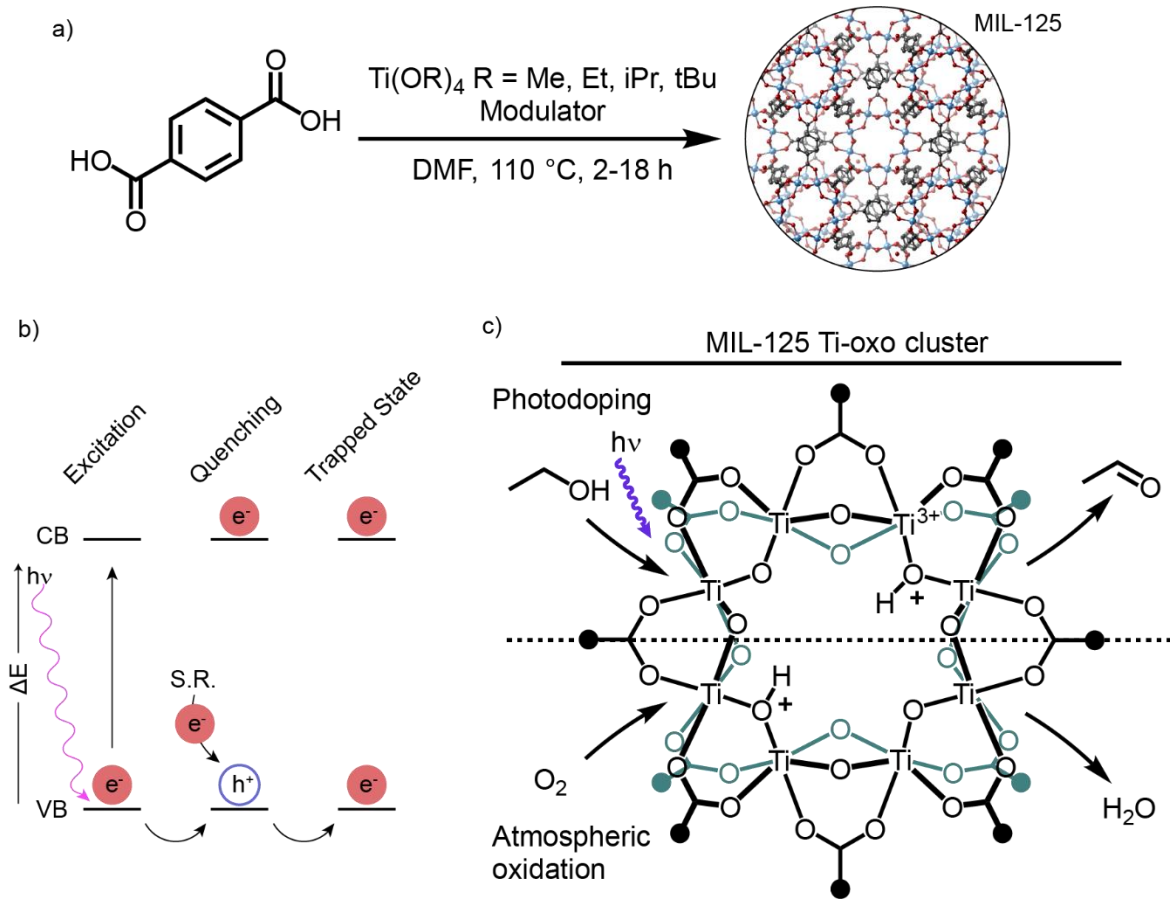

Figure 10. a) Synthesis of MIL-125 with various Ti^{4+} precursors. b) a schematic of the photodoping process. VB = valence band and CB = conduction band. c) Chemdraw schematic of the MIL-125 Ti_8 cluster. The top half represents the photodoping reaction, consuming a sacrificial alcohol and producing an aldehyde as a Ti^{3+} center is formed. Pictured on the bottom is oxidation of the reduced MIL-125 from atmospheric oxygen, producing water.

Computational evidence, combined with experimental analysis of the redox potential of the doped system, suggests that mid-gap states are introduced, lying just below HER potentials, that stabilize the conduction band electrons.[87] Recent studies have demonstrated that the size of the MOF particle also has an influence on the potential of the doped systems, and that pH dependence in aqueous media has large influence over the resulting energetics of the electronic environment.[54,93] While the potential of the system in relation to an open circuit voltage and buffer stabilized environment was elucidated, there still remains questions of the photodoped system's

ability to act as a solid reductant. Continuing work done previously, we proposed the use of colorimetric photoredox indicators to probe the size-dependence of the doped MIL-125 in non-aqueous environments. By observing colorimetric indicators outside of the typical absorbance range of the titanium-oxo clusters, we can probe the reduced MOF reliably as it reaches thermodynamic equilibrium in the non-aqueous system. We hypothesize that as the nanoparticle size decreases, the resulting redox potential will shift towards more reducing potentials. Concurrent analysis with nuclear magnetic resonance (NMR) spectroscopy allows for analysis of possible hydrogen production through the HER reaction. Based on previous literature results, we predicted there would be no observable hydrogen produced from reduction of MIL-125. We hypothesize that a limiting factor of titanium reduction is the reverse reaction with the produced aldehyde (Figure *11*a). Before the formation of hydrogen gas, we propose that reducible unsaturated organics produced from initial titanium reduction will recombine with proton counterions (Figure *11*b).

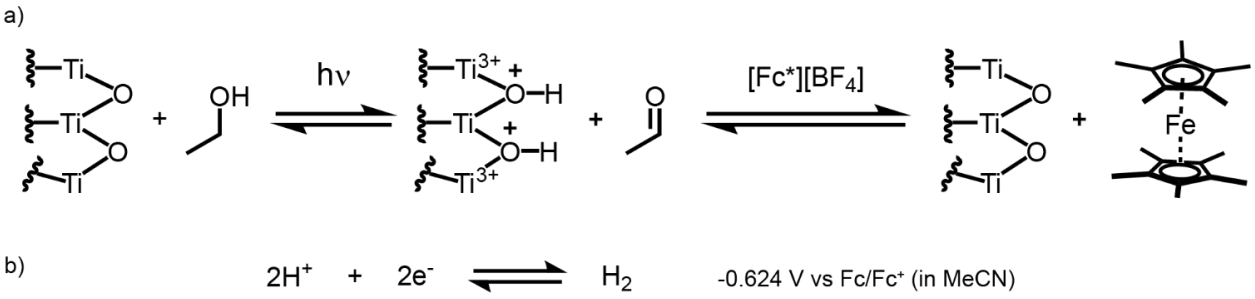

Figure 11. a) proposed reaction equilibria with included optical redox indicator, $[Fc^*][BF_4]$ which is reduced to neutral Fc^*. b) Hydrogen evolution reaction represented as a combination of protons and electrons to form gaseous hydrogen. This occurs at -0.624 V vs Fc/Fc^+ in MeCN.

Size-dependent redox potential of MIL-125 nanoparticles

When MIL-125 of three distinct sizes underwent the photodoping process in the presence of our optical indicator of choice, the measured redox potential varied based on particle size. We observe a shift in redox potential of 21 and 12 mV respectively to more reducing potential as the particle size shifts from large, >500 nm, to 32 and 18 nm respectively (Figure 12). The MIL-125

used was synthesized in multiple sizes using previously established literature methods.[88] Solvent exchange with methanol was employed several times to remove DMF from the synthesis. The particles were subjected to subsequent drying with vacuum and heat before varied sizes of MIL-125 were subjected to air-free photodoping conditions in acetonitrile. Dried ethanol was used as a sacrificial reductant to remain consistent with previous work. Air-free quartz cuvettes were utilized for UV light exposure and subsequently for UV-Vis spectroscopy. Decamethyl ferrocenium tetrafluoroborate ([Fc*][BF_4]) was utilized as an indicator of redox potential due its previous use and distinct UV-Vis signature. When a solution of MIL-125 is reduced in the presence of the Fc^{*+}, the reduced Ti^{3+} center is able to undergo an oxidative electron transfer to form neutral decamethyl ferrocene (Fc*). The decrease in the absorption feature present at 778 nm can be used to extract the new concentration of the indicator. The fermi level can be calculated with the use of the Nernst equation and $E^{0'}$ of Fc^{*}/Fc^{*+} vs Fc/Fc^{+} in MeCN (Figure *12*).[81,94,95] Air- and water-free solutions of [Fc^{*}][BF_4] and MIL-125 in MeCN were measured by UV-Vis spectroscopy in a sealed cuvette. The mixtures were exposed to UV light for 18 hours before the MIL-125 was removed with centrifugation to mitigate scattering effects and another UV-Vis was collected. The concentration of the [Fc^{*}][BF_4] in the pre- and post-dope solutions was calculated using Beer's Law and the extinction coefficient taken from literature.[96]

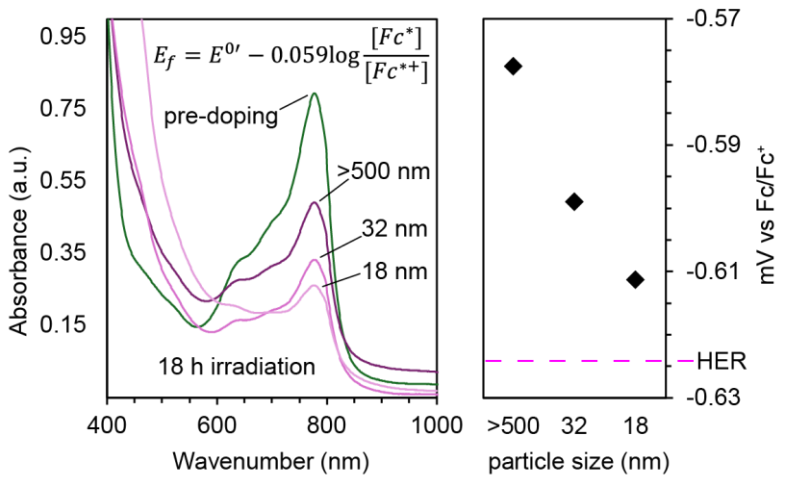

Figure 12. UV-Vis spectra of MIL-125 in MeCN before and after photodoping for 18 h. The extent of signal quenching at 778 nm is dependent on the size of the MIL-125 nanoparticles. On the right, the redox potential versus particle size is plotted relative to the Fc/Fc^+ redox couple.

When considering the equilibrium of the Fc^{*+}/Fc^*, we also considered that the role of the indicator could become that of the reductant. In an analogous fashion to the previous reactions, MIL-125 was suspended in a solution of Fc^*. Without the addition of primary alcohols or other reductants besides Fc^*, the reaction mixture was to UV irradiation. The emergence of a peak at 778 nm and an estimation of -531 mV vs Fc^+/Fc puts the system at a much milder redox potential when Fc^* is used as the reductant.

NMR analysis of the reaction in a quartz tubes sealed with a teflon tap reveals no evidence of hydrogen evolution and suggests transfer-hydrogenation taking place (Figure 13a). When the photodoping process was carried out in deuterated acetonitrile, with ethanol used as a sacrificial reductant, no peak corresponding to dissolved hydrogen gas was observed through NMR. In addition to the typical components of the reaction, acetone was added to the mixture so that a unique substrate would be available to observe a reduced product should it form. In the corresponding NMR, a peak that matches with literature standard values for the C2 proton of isopropanol was observed (Figure 13b).[97,98] The NMR spectrum of the reaction mixture was taken

before photodoping as well to ensure there was not a previous contamination of isopropanol that would produce a false positive. When large MIL-125 was used, the observed signal is quite weak and somewhat broad, even after 36 hours of irradiation. When 32 nm MIL-125 was used, the C2 proton resolves slightly more and a splitting resembling something closer to that of the classic C2 septet is observed. Paramagnetic effects of the reduced material most likely contribute to signal broadening. The peak corresponding to the OH of the ethanol becomes quite broad and diffuse after the photodoping process, with integration values deviating from what would be predicted for each proton signal (1H, s, -O*H*; 2H, q, -C*H*$_2$CH$_3$; 3H, t, -CH$_2$C*H*$_3$). This broadening and deviation can be attributed to hydrogen bonding interactions, changes in polarity of the environment or possibly pore confinement broadening the resulting signal. Without the addition of an external standard, no quantification can be made of reductant content.

When the identity of the sacrificial reductant was modified, no distinct variation in the presence of produced isopropanol was observed. A small quantity of isopropanol is produced, regardless of the reductant identity, but there exists some limit to the transfer. N-Butanol and 2-octanol were chosen as unique sacrificial reductants and reacted with MIL-125 in the presence of deuterated acetone. Deuterated acetone was utilized as a way to ensure a unique NMR signal resulted from the reduction of the unsaturated organics, rather than an environmental contaminant such as the very small chance of isopropanol cross contamination from the atmosphere of the glovebox (Figure 14a).

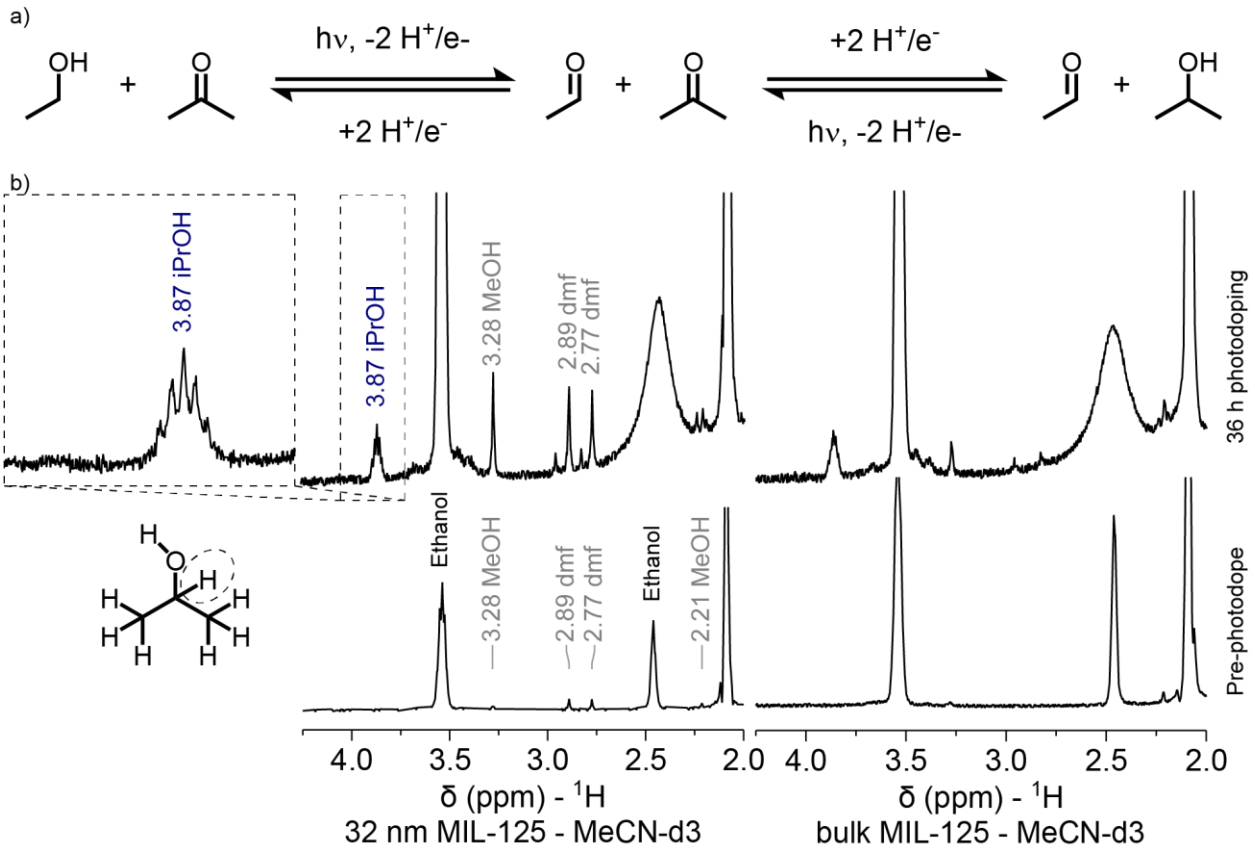

Figure 13. a) reaction equilibrium proposed to form isopropanol from the addition of acetone into the photodoping process. b) NMR spectra of pre- and post-photodoping reactions in MeCN-d3 of both 32 nm and bulk MIL-125. Expanded view of the isopropanol $(CH_3)_2CHOH$ proton signal is shown in the box on the left.

Each reaction showed the emergence of a singlet at 3.83 ppm, corresponding to deuterated isopropanol with a proton at the C2 position (Figure 14b). Even with a large excess (10:1) of deuterated acetone to alcohol reductant, much of the reductant remained and very little isopropanol emerged comparatively.

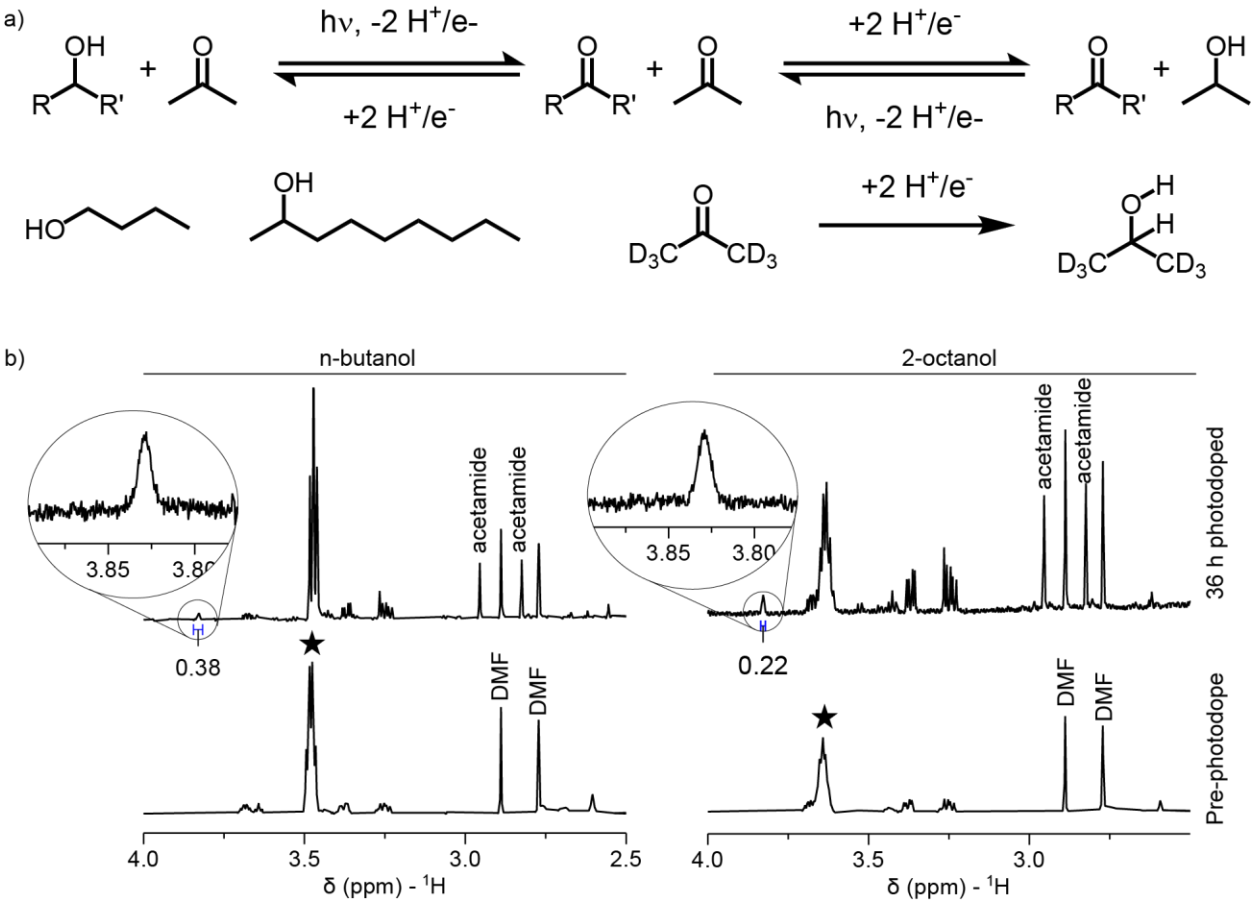

Figure 14. a) reaction equilibrium including varied reductants and use of deuterated acetone to produce a proton signal that is not split from the neighboring -CD_3. N-butanol and 2-octanol pictured. b) NMR spectra of pre- and post-photodoping reactions in MeCN-d3 with 32 nm MIL-125 using n-butanol and 2-octanol. C2 protonated isopropanol-d6 signal is expanded in circles. Leftover DMF and newly formed acetamide are labelled. Peaks labelled with a star correspond to proton signals from original alcohol structure.

When additional small unsaturated organic molecules were subjected to MIL-125 photodoping conditions using ethanol as a reductant, we observe the disappearance or decrease of key peaks in the NMR spectra that correspond to the starting aldehyde or ketone. The resulting spectra show many by-products however, suggesting that MIL-125 may not be selective as a transfer hydrogenation catalyst. Gas chromatography/mass spectroscopy traces taken from the resulting NMR mixtures suggests a mixture of rearrangement products. Further discussion can be found in appendix B.

Side-reactivity in MIL-125 photodoping

The redox properties of MIL-125 nanoparticles in non-aqueous media have been demonstrated to have a size-dependence, with smaller particles (18 nm) displaying more reducing redox potentials at equilibrium than larger particles (>500 nm). Our findings match well with other studies that look at size-dependent properties of MIL-125 in aqueous media or probe the band gap directly through UV-Vis. This method to estimate the redox potential of the fermi level in the photodoped system represents a practical and straightforward method to extract electrochemical properties of the varied systems of interest without having to utilize typical electrochemical methodology. The fact that our findings match well with other studies in varied media and systems adds to the validity of the methods presented. Given that our findings show that MIL-125 becomes more reducing as the particle size decreases, it is not so surprising that we observe a decrease in redox potential when using Fc^* as a reductant. The inability of the Fc^* to donate many electrons for the reduction process fits well with the idea that it is a weaker reductant relative to nanosized MIL-125.

The inability of Fc^{*+} to intercalate into the pores of the MOF calls into question the nature of electron transfer in the system and if the available surface of the nanoparticles is what dictates the redox potential. Although intercalation is limited due to sterics, ion transport through inclusion of protic solvents such as ethanol has displayed an increase in conductivity in MIL-125 by several orders of magnitude.[85] We suggest that due to adequate conductivity through proton-coupled electron transport, titanium clusters within the "bulk" of the crystal can be reduced in the same way as the surface sites. The extent of reduction can be compared as a function of thermodynamic equilibrium rather than simply a factor of surface area. The inability for $[Fc^{*+}][BF_4]$ to intercalate into the pores of the material means that the absorbance values obtained after centrifugation of the

post-photodoped solution should not be affected by removal of analyte trapped in the MOF.

Although some literature suggests that unaltered MIL-125 is able to photocatalytically produce minute amounts of hydrogen gas, we observed no hydrogen evolution in our NMR experiments.[91,92] Given previous findings that the redox potential sits at a less reducing potential relative to HER, it follows that we observe no hydrogen here. While the use of teflon-sealed quartz NMR tubes should be adequate for retention of produced hydrogen gas, it is possible that low solubility of hydrogen in acetonitrile would make any hydrogen produced very difficult to detect with this method.[99] Degassed reactions in flame-sealed vessels could be utilized, but we suggest that the observed results would likely not vary. With the model of a back reaction that reduces unsaturated hydrocarbons produced in the original photodoping, the lack of observable H_2 gas points to alternate mechanisms that limit titanium doping with alcohol-based reductants. The presence of acetone reduced to isopropanol in our study strongly supports our hypothesis that the potential of the system to reduce small unsaturated organics strongly limits the total amount of reducible titanium sites in the MOF. It is rather interesting, however, that this back-transfer process seems limited in extent. We would expect that when the system reaches a redox potential that can begin to reduce aldehydes or ketones, a much higher population of acetone present versus the aldehyde formed from the initial photoredox process would favor the formation of isopropanol. The small amount of $(CD_3)_2CHOH$ formed does not reflect rapid interconversion we would expect under irradiation. Even when the identity of the reductant is modified, only a small but detectable amount of isopropanol is produced.

An intriguing aspect of the NMR study is the observation of dimethyl acetamide in the spectra after photodoping. While acetamide is a common impurity in commercially available acetonitrile, the methylation of the amide to form dimethyl acetamide seems rather unlikely in this

case.[100] More likely, is the hydrolysis of DMF left in the pores from synthesis due to protic conditions and some rather interesting rearrangements with the free dimethyl amine. The emergence of dimethyl acetamide highlights the importance of adequate solvent exchange in appropriate solvents to remove DMF before photodoping occurs. Even though the MIL-125 used in these experiments was washed several times with fresh acetonitrile, the presence of DMF before irradiation can be seen in the NMR. With a high boiling point and low volatility, DMF is quite effectively trapped inside porous MOFs. We caution that prior to use as a photoreducible material, MIL-125 should undergo several extensive solvent exchanges to ensure complete removal of high-boiling solvents leftover from synthesis such as water or DMF.

Materials and methods

MIL-125 was synthesized using previously developed literature methods.[88] Decamethyl ferrocenium tetrafluoroborate was synthesized previously developed literature methods.[87] All solvents used for photodoping and NMR studies were stored in a nitrogen-filled glovebox. Acetonitrile used for photodoping was HPLC grade and obtained from a solvent purification system. Deuterated acetonitrile used for NMR studies was degassed using freeze-pump-thaw methods. Alcohol reductants were dried over 3 Å molecular sieves and distilled before degassing using freeze-pump-thaw methods.

Photodoping experiments were prepared in inert atmosphere and carried out in a custom air-free quartz cuvette with a teflon tap. The cuvette was equipped with a micro-stir bar and placed in front of a mercury arc lamp. Centrifugation of the photodoped reaction mixture was carried out in a nitrogen-filled glovebox before the solution was returned to the air-free cuvette and an additional spectrum was obtained.

NMR experiments were carried out by direct addition of MIL-125 to a quartz NMR tube

equipped with a teflon stopper in a nitrogen-filled glovebox. Deuterated acetonitrile, a reductant and an unsaturated hydrocarbon were added directly with the use of mechanical micropipettes. The tubes were sealed, and an NMR spectrum was obtained before the tube was placed in front of the Hg arc lamp for 36 hours with occasional shaking to mix the reagents. An additional NMR spectrum was obtained after allowing the majority of suspended particles to settle.

Conclusions

Decamethyl ferrocenium tetrafluoroborate was used successfully as an optical indicator, monitored by UV-Vis spectroscopy, to demonstrate the size-dependence redox potential of MIL-125 nanoparticles. As the size of MIL-125 nanoparticles reaches 18 nm, the redox potential sits just 13 mV positive of the hydrogen evolution reaction. NMR analysis of the reactions suggests that conversion of the spent reductant back to its protonated form is partly responsible for the limitations present in photodoping using PCET methodology. This study effectively monitors the change in fermi-level of photodoped MIL-125 nanoparticles without the use of buffer solutions, aqueous media or potentiometric measurements in organic solvents.

CHAPTER IV

MODELING COVALENCY IN 2-DIMENSIONAL CONDUCTIVE MOFS

Introduction

Metal-Organic Frameworks (MOFs) have emerged as highly tunable and modular platforms that allow for variations in regular, repeating structures that provide insight into structure-property relationships. The breadth of organic linkers and metal building units of MOFs result in materials that are adaptable to specific needs.[101,102] While the modularity and tunability of MOFs allow for a wide breadth of structural motifs, the most common organic linkers utilized for these frameworks features carboxylate groups that bind to metal centers, forming metal-oxygen bonds (Figure 15a).[103] Metal-carboxylate motifs in materials that are quite insulating and are more suited for applications not focused on conductivity. In carboxylate systems where electron transport mechanisms are introduced, conductivity is highly tied to externally introduced guests or proton donors and are limited in their conductivity.[104,105]

Conductive MOFs emerged as a subclass of extended materials that are of high interest for charge transport and electrocatalysis.[106–108] Within this small subset, 2-dimensional MOFs have demonstrated high conductivity and charge mobility in stable frameworks, with Cu_3(BHT) serving as a benchmark, displaying measured conductivity of 2500 $S \cdot cm^{-1}$ (Figure 15b).[109,110] The conductivity of Cu_3(BHT), sulfur-based, marks a stark contrast to $Cu_3(HOB)_2$ featuring copper-oxygen bonds, reported with a conductivity of $7.3 \cdot 10^{-8}$ $S \cdot cm^{-1}$.[111] When isostructural 2D conductive frameworks are compared, changing the heteroatom of 2D conductive MOF systems from oxygen to sulfur, nitrogen and even selenium has a substantial effect on the conductivity of isostructural frameworks.[111–124] The difference in electronic structure of inorganic complexes with an isoelectronic change from oxygen to sulfur were remarked upon by Cotton et al. some time ago, noting that electronic communication across the complexes increased with covalency afforded by

sulfur.[125] Along with the change in heteroatom, identity of the metal has varied isostructural 2D MOF properties from highly conductive (copper-sulfur 2D sheets), to a material that has lower conductivity, but highly sought after electrocatalytic properties (cobalt-sulfur 2D sheets).[126–129] Increasing covalency of metal-ligand bonding is one of several key components for increased conductivity and charge delocalization in materials. Dithiocarboxylate analogues of the typical MOF linkers 1,4-benzene dicarboxylic acid and 1,3,5-benzene tricarboxylic acid have been reported for the purpose of extended framework synthesis, with a follow-up study reporting conductivity of $5 \cdot 10^{-5}$ $S \cdot cm^{-1}$ in a Fe^{2+3+} mixed valent MOF.[130,131] The use of sulfur to increase covalency over -CO_2 functional groups does mark an undeniable increase in conductivity and new opportunities to continue to enhance conductivity in MOFs.

The introduction of charge carriers and modulation of oxidation state in 2D sheets impacts the resulting conductivity.[118,132–140] Park et al. reported the formation of stable, delocalized radicals on the ligands of palladium complexes based on N-heterocyclic carbene (NHC) dithiocarboxylate moieties, and shortly after, Luff et al. reported a similar stable, delocalized radical ligands of nickel complexes based on benzimidazolium-dithiocarboxylate ($BICS_2$) molecules (Figure 15c). 1D coordination polymers of non-radical imidazolium dithiocarboxylate with copper have been reported as a photocatalyst, but no conductivity was measured.[141] The delocalized nature of the radical ligand featuring metal-sulfur bonds positions NHC-dithiocarboxylate complexes as promising building units for new 2D conductive MOF frameworks (Figure 15d).[142–146]

*To measure, or estimate, covalency of heteroatoms in inorganic systems, density functional theory (DFT) and x-ray absorption techniques provide metrics useful for comparison.[147–153] For the general materials chemist, computational modeling provides a low-barrier methods to gain synthetic insight without need for access to x-ray techniques. With respect

to 2D conductive MOFs, computational analysis of extended structures or small representative clusters has predicted high thermal stability, accessible band gaps, heteroatom-dependent properties and need for crystalline ordering in bulk materials.[56,154,155] The atomic contributions of heteroatoms and bond covalency to materials properties has not been explored through computational modeling of molecular inorganic complex analogues as a way to investigate the covalency and electronic properties of 2D conductive MOF sheets.

The extent of covalency can be modeled as spin density delocalized away from atomic density through a molecular model.[156–158] * To determine optimal parameters of atom electronics and bonding environments, covalency of metals and heteroatoms were estimated through delocalization indices (DI) obtained through AIM analysis, with analysis of spin density utilizing Lowdin spin population (LSP).[153,159,160] Mayer bond orders (MBO) were used to corroborate DI and LSP calculations.[60] Nucleus-independent chemical shift (NICS) scans in both the z-axis and xy-plane to analyze aromaticity in the conjugated rings of the ligands.[161–163] *Models featuring metal-sulfur bonding are hypothesized to result in increased delocalization index and Löwdin spin density compared to oxygen analogues.* This suite of computational parameters are positioned as metrics to compare molecular analogue properties of the most widely used carboxylate-based ligands, catecholate-based analogues of ligands used in highly conductive 2D sheets and NHC-dithiocarboxylate radical ligands implicated for use as ligands in conductive MOFs (Figure 15e). Extracting parameters from molecular analogues of extended materials does neglect effects of multitopic linkers, larger conjugated/aromatic ring structures in annulated systems and stacking effects for through-space conductivity mechanisms, however, the resulting analysis does inform on the nature of covalency and spin at the key linkages of the experimentally realized structures the models are compared to. The results of this analysis are most appropriately applied to in-plane

charge transport and supply a general predictor of advantageous bonding environments.

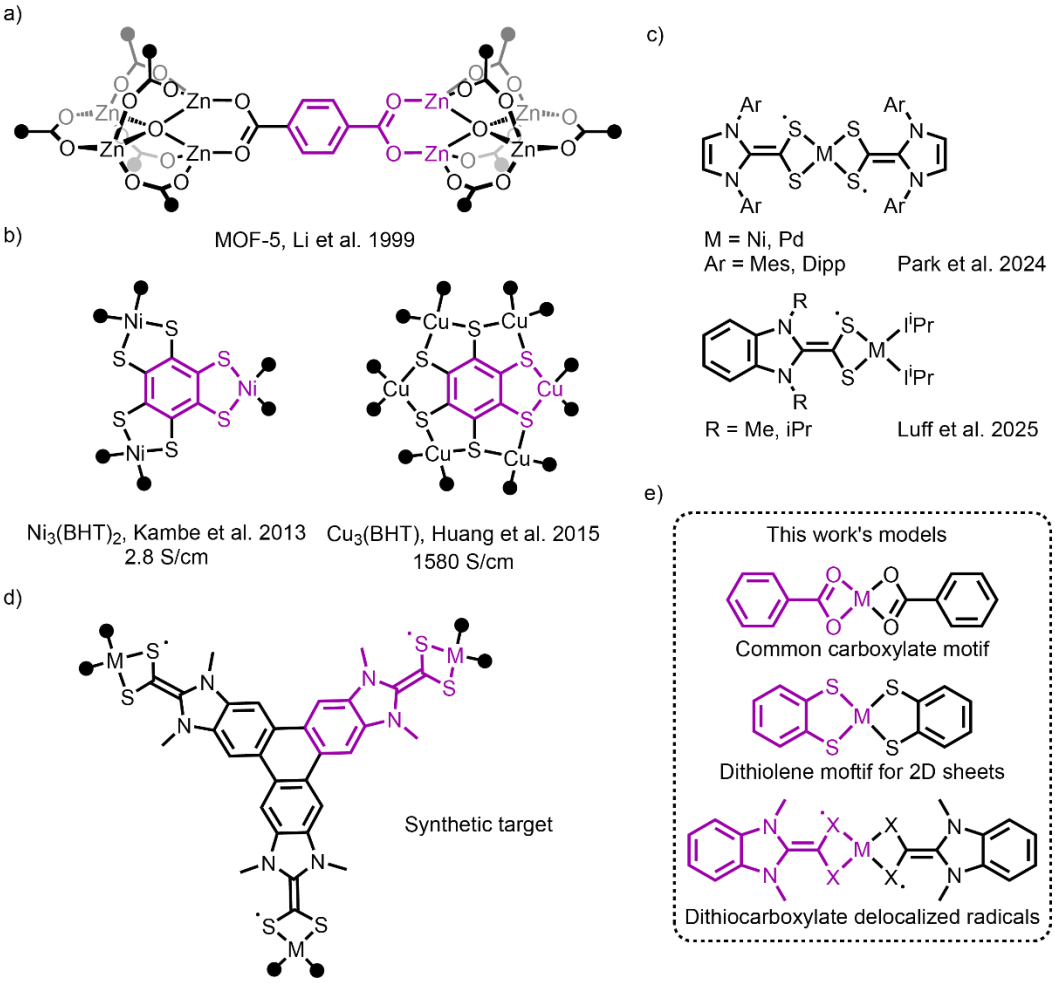

Figure 15. chemdraw schemes of model compounds a) Carboxylate linker motif found in MOF-5 b) 2D sulfur-based conductive MOFs utilizing the dithiolene motif c) radical ligand complexes of palladium and nickel utilizing NHC-dithiocarboxylates d) A proposed triphenylene-based synthetic target e) carboxylate, dithiolene and NHC-dithiocarboxylate molecular analogues

Modeling covalency and bonding in molecular analogues of 2D MOF sheets.

To compare analogous oxygen- and sulfur-based complexes, extract covalency and spin density, and demonstrate potential for a ligand motif in conductive frameworks, thirteen inorganic complexes were modeled. Metals for square planar complexes were chosen from highly studied systems of Cu^{2+}, Ni^{2+} and Co^{2+}, with Co^{3+}, Sc^{3+}, Cr^{3+} and chromium included for comparison with

$BICS_2$ of oxidation state, hard d^0 metals and a system with intrinsic high spin respectively (Figure 16). Neutral and reduced models of di(thi)olene models were included due to reported differences in conductivities of extended materials at varied oxidation state. Carboxylate and dithiocarboxylate systems were calculated to model a simple substitution of the heteroatom and establish a comparison with the different architectures of the $BICX_2$ and di(thi)olene models. DFT with the widely used B3LYP hybrid GGA (20% HF exchange) was employed for geometry optimization and property calculations. The calculated structures successfully converged and were compared by evaluation of AIM analysis, Löwdin spin population, Mayer bond analysis, HOMO/LUMO gaps and single point energies, electrostatic potential maps and spin density maps.

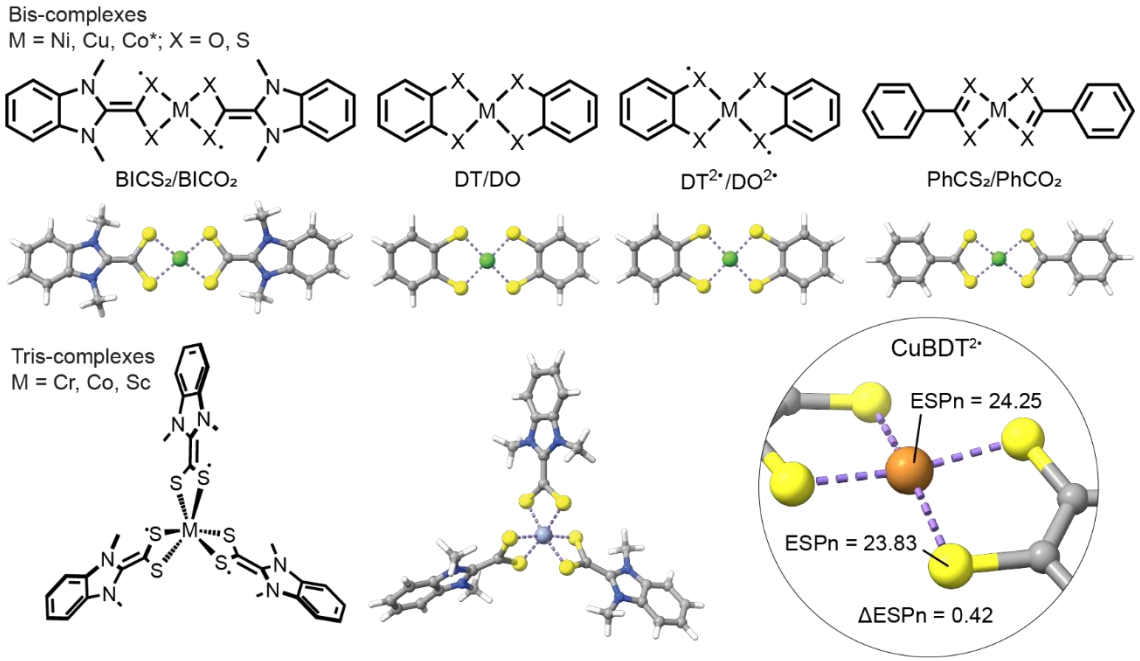

Figure 16. Chemdraw representations of modeled complexes and their optimized structures. From left to right: the synthetic target where X = S, N,N'-dimethyl benzimidazolium dithiocarboxylate (or it's carboxylate analogue where X = O) labelled as $BICS_2/BICO_2$; the molecular analogue of M(BHT) materials – di(thi)olenes, also known as catecholates labelled as DT/DO; the reduced diradical forms of di(thi)olenes, labelled as $DT^{2\bullet}/DO^{2\bullet}$; the (dithio)carboxylate models $PhCS_2/PhCO_2$. Below are both a chemdraw representation of a tris-coordinated $BICS_2$ complex and the modeled example. Pictured in the bottom right are electrostatic potentials of the nuclei in reduced copper bisdithiolene obtained from Atoms-in-Molecules analysis. *bis-cobalt complexes were not modeled with oxygen-based ligands or $PhCS_2$

$BICS_2$ as a ligand is zwitterionic and does not feature a delocalized radical. Comparison of the aromaticity of the ring system before and after the ligand was complexed was carried out to measure the extent of electronic influence of the delocalized radical. The free, N-methyl substituted ligand was synthesized and a crystal structure was obtained to use as a model for NICS calculations.

AIM Results

We report extracted DI of sulfur-based and oxygen-based analogous for comparison of covalency between the modeled complexes. Using AIMALL software, data was extracted from the wavefunction files obtained from Orca calculated using DFT (B3LYP functional and def2-TZVP/def2-TZVPPD basis sets). We report the delocalization indices of selected first row transition metals and either sulfur or oxygen bonded to them to form inorganic complexes. To compare models within a series featuring the same heteroatom and metal with a parameter that would describe the difference in electronic environment of each model, the reported delocalization indices are ordered by the difference in electrostatic potential of the metal to the heteroatom. Difference in electrostatic potential between the metal-heteroatom pair should be close to zero if the bonding environment is covalent in nature. Polarization and diffuse functions were included in the metal and heteroatom basis sets in order to most accurately account for polarity and delocalization of electron spin.[164] The electrostatic potential values of the nucleus (ESPn) are those as calculated by AIM analysis. The most negative ΔESPn (heteroatom has larger ESP) is positioned at the leftmost side of the x-axis, while the most positive (heteroatom has smaller ESP) is positioned to the right. With this arrangement, all oxygen-based molecules fall on the left of the plotted data (-4.7 to -4.1 ΔESPn), resulting from electrostatic potentials with a significant difference relative to the metal center. For the sulfur-based complexes, the difference in

electrostatic potential is closer to zero, but there is still some observed differences within the sulfur series complexed to the same metal (0.2 to 0.9 ΔESPn). This trend places the reduced nickel dithiolene complex ($NiBDT^{2\bullet}$) on the far right, whereas the copper series results in the non-reduced dithiolene model on the right end (Figure 17a/b, x-axis). Also observed is a much greater difference in the reduced versus non-reduced dithiolene ΔESPn values for copper, where in the nickel series, the analogous complexes are quite similar in comparison. *.

The reported data describes an estimate of differences in covalency across the modeled complexes. Starting with nickel and copper-based models, the DI of the heteroatom and metal center are compared. The delocalization index of sulfur is about 0.2 units higher than oxygen in the nickel-based examples at the smallest difference and about 0.35 units in the copper complexes. In general, this would point to a more covalent environment of sulfur as compared to oxygen. Using delocalization index to also compare the environment of the metal center, this same trend is observed as well, with larger metal delocalization indices in sulfur-based complexes as compared to the oxygen-based ones, with a much more apparent difference in the copper values. If the heteroatom of interest is in a more covalent bonding environment, this would make sense to be reflected in the analysis of the metal as well.

The delocalization index provided by AIM of the components in these systems shows an increased covalency of the heteroatoms and metals when switching from oxygen to sulfur. While there does appear to be a general observable trend of increasing DI as the ΔESPn becomes more positive, there are notable deviations to highlight. While we hypothesized that the $MeBICS_2$ complex would be comparable or possibly more covalent than systems like the dithiolenes, if delocalization index is taken as an estimate of covalency, the sulfur of the $MeBICS_2$ is the least covalent of the four compared examples in both the nickel and copper series, albeit by a small

amount. While the $BICS_2$ models provide a much higher delocalization index than any of the oxygen-based systems, this alone would point to a more ionic sulfur compared to the dithiolenes and dithiocarboxylates. Interestingly, in all of the metal-bisdithiolene systems, the reduced dithiolene model also displays a smaller delocalization index (Figure 17c). Beyond a look at just the delocalization index of the heteroatoms, what stands out is the difference in DI between the metal and the sulfur. Even between models in a series with the same heteroatom and metal, the difference in delocalization index varies in magnitude and with which species is assigned the larger DI. Notably in the sulfur-based examples, the difference in delocalization index is smallest in the reduced copper dithiolene, and smaller in the non-reduced nickel dithiolene as compared to the reduced analogue.

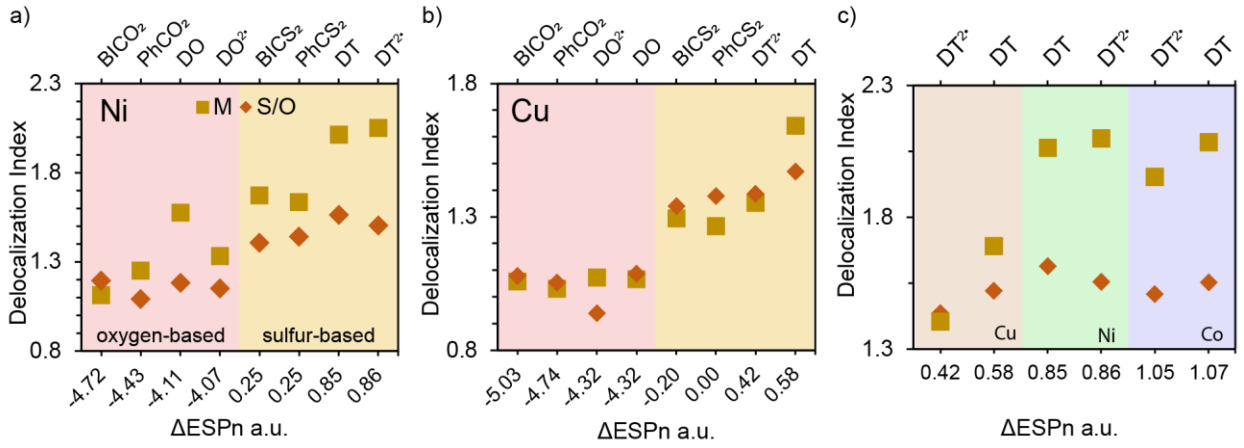

Figure 17. Calculated delocalization indices of the different modeled complexes. ΔESPn values in atomic units. a) Delocalization indices of modeled Ni complexes b) Delocalization indices of modeled Cu complexes. c) Delocalization indices of complexes of $BICS_2$, dithiolene and the reduced dithiolene of copper, nickel and cobalt.

Interestingly, when we go beyond the core of metals and heteroatoms to the dithiocarboxylate carbon, they have delocalization indices similar to that of the dithiolenes C-S carbon (the aromatic carbon directly bonded to the thiols) (Table 7 in Appendix C). This contrasts with the oxygen analogue, having carboxylate carbon DI that is 0.44 units lower than the

dithiocarboxylate carbon. This carboxylate carbon DI is also lower than the analogous diolene complex carbons directly attached to the oxygens (Table 7 in Appendix C). It makes intuitive sense that a carbon of a -CS_2 group would have a higher propensity to share electrons compared to a -CO_2, but the data is gratifying, nonetheless.

Even farther from the core, the delocalization indices of the NHC C2 carbon and nitrogen become quite similar between the oxygen and sulfur comparisons with both metals. If the pi system of the benzimidazole rings is not conjugated with the (dithio)carboxylate moiety, then a similar electronic environment would be expected between the different systems, regardless of the metal center or heteroatom of the carboxylate. Although the metal identity does not appear to affect the delocalization of atoms farther from the core, the metal's identity does affect the core quite a bit.

Considering this difference in results depending on the metal center and thinking of trends in the extended systems, we expanded our set of models. Wanting a prediction of the effects of varied transition metals and coordination environments for our target system, we included cobalt, chromium and scandium in conjunction with our ligand of interest in order to predict what properties may arise from different synthetic targets. Cobalt complexes of the $BICS_2$ model and ditholene systems were included in our calculations, as well as tris-coordinated Co^{3+}, Cr^{3+} and Sc^{3+} complexes. To model the tris-complexes, an additional $MeBICS_2$ ligand was added to the metal center and the geometry was optimized from a roughly octahedral environment. Each of these models successfully converged and the delocalization indices were extracted from AIM analysis. Cobalt is known form 2D sheets analogously to $Ni_3(BHT)_2$, so this was a logical target, as well as a metal with an empty d orbital like Sc^{3+} and Cr^{3+}. Since cobalt can adopt a 3+ state and an octahedral environment, this was included in the modeling. The results of the varied metal series

with $BICS_2$ are discussed below as future synthetic targets.

Continuing our investigation of the resulting delocalization index of the metal and heteroatoms with known systems in mind, we compared bis-coordinated copper, nickel and cobalt with dithiolene and reduced dithiolene. The delocalization index of sulfur across the metals is on average largest in the nickel models, with comparable values arising from cobalt. This would put the covalency of sulfur slightly higher in nickel and cobalt samples as compared to copper. The metal DIs reflect a similar pattern, with large indices for Ni^{2+} and Co^{2+} with much smaller values for Cu^{2+}.

Based on our hypothesis that increased covalency in metal-ligand bonding is a factor in increased conductivity, this data was surprising. Given reported literature conductivity trends of $Cu_3(BHT) > Ni_3(BHT)_2 > Co_3(BHT)_2$, we would predict that delocalization indices would be highest in copper-based models and lowest in cobalt-based models. We do note as well, that there is a prominent difference in the ΔESPn of the copper models versus the nickel and cobalt. While additional trends stand out in the results, such as the difference in delocalization indices between the metal and sulfur of the same model, we endeavored to find additional data to improve how the molecular models could inform on the properties of the extended material. It is clear that although the delocalization index, and therefore covalency, of the heteroatom and metal center increases as the identity changes from oxygen to sulfur, there are additional factors that may correlated with expected extended properties. Given the expected diradical nature of the target ligand and some of the reduced models, we also expect a distribution of electron spin throughout the systems in informative ways. We turned to spin population in valence orbitals.

Löwdin Spin population

The spin population of the valence orbitals of the constituent atoms in the modeled systems

was analyzed with Löwdin spin population analysis. The reported values were extracted from output files from Orca calculations. The tabulated results are averaged values within atom types (heteroatom of interest, carbon of the (dithio)carboxylate etc.) For complexes with benzimidazole rings, NHC C2 carbons and nitrogen atoms are also included in the analysis to aid in understanding of where spin is distributed across the molecule. The spin distribution across the ligands is consistent with literature analysis of the radical species as delocalized across the NHC and dithiocarboxylate. Carbon atoms in benzene rings of the di(thi)olene and phenyl models are distinguished between the typical carbons in the ring (C_{aro}) and those that are bonded directly to either the heteroatom of interest or carboxylate group ($C_{aro\text{-}X}$). The tabulated results describe both the spin population and spin state contained in the orbitals of interest (Table 10 in Appendix C).

The overall spin density is higher in the d orbitals of Cu^{2+} and Co^{2+} due to the additional unpaired electron native to the oxidized metals. All $PhCX_2$ models display very little to no spin density in both the carbon p orbitals of the ring and the (dithio)carboxylate carbon. The p orbitals of the $C_{aro\text{-}x}$ carbons in the neutral and reduced dithiolate nickel complexes contain very little spin density, while the copper di(thio)lene models assign some amount of spin density to this position.

In the case of the $BICS_2$ versus the $BICO_2$ complexes, a similar pattern is present in the spin densities of the, C_{CX2}(p), C_{NHC}(p) and N(p) of the sulfur-based system whereas in the oxygen analogue, higher spin density lies in the Ni(d) and C_{NHC}(p) with less in the O(p) and C_{CX2}(p). In the neutral and diradical di(thi)olenes the metal center shares the spin density with the p orbitals of the heteroatoms, but very little density is found in the $C_{aro.X}$(p) orbitals.

We expect that in neutral nickel systems, there should be relatively little spin in the nickel d orbitals and heteroatom p orbitals. In classically ionic systems with no delocalized spin like the carboxylate models, we observe little to no spin density assigned to the heteroatom p orbitals and

most remaining density to the metal d orbitals, with slightly more distribution observed in the copper system (Figure *18*a,b). The $CuPhCS_2$ model does display a slightly higher propensity to spin distribution to the sulfur atoms, but there still remains a large discrepancy. Contrasting this, the model of the reduced copper dithiolenes distributes this spin readily between the sulfur p orbitals and the copper d orbitals rather than the localization of the spin density at the core. The reduced nickel dithiolene system assigns a higher spin density at the metal center with about half of that per sulfur atom surrounding it. The modeled $BICS_2$ system assigns a slightly increased spin density at the copper center and decreased spin density in the sulfur p orbitals relative to the reduced dithiolene model. The spin in the $BICS_2$ model not found in the heteroatom p orbitals is distributed across the dithiocarboxylate carbon, the NHC C2 carbon and the nitrogens. The oxygen-based analogues present a similar picture of spin density in the ligand ring systems, although the carboxylate carbon is assigned much less spin.

Also noted in the data is the sign of the spin populations. In the case of the copper, only one of the oxygen containing models provides a different sign between the metal and the heteroatom, while in the nickel systems the spin alternates between the metal and heteroatom for most of the oxygen-based models. The oxygen-based systems generally display some concentration of spin onto either the oxygen or the metal center. While Löwdin spin population does not inform oxidation state, we can interpret these atomic centers with higher density assigned as having a higher likelihood of spin density. Models that produce spin density values that are more consistent between atomic species are more likely to have similar distribution of charge between them. For the neutral copper dithiolene system, some spin is distributed to the sulfurs, with a small amount of density at the metal center. When the copper dithiolene system is reduced, both the metal center and the surrounding sulfur take on more spin density, to a much more comparable extent.

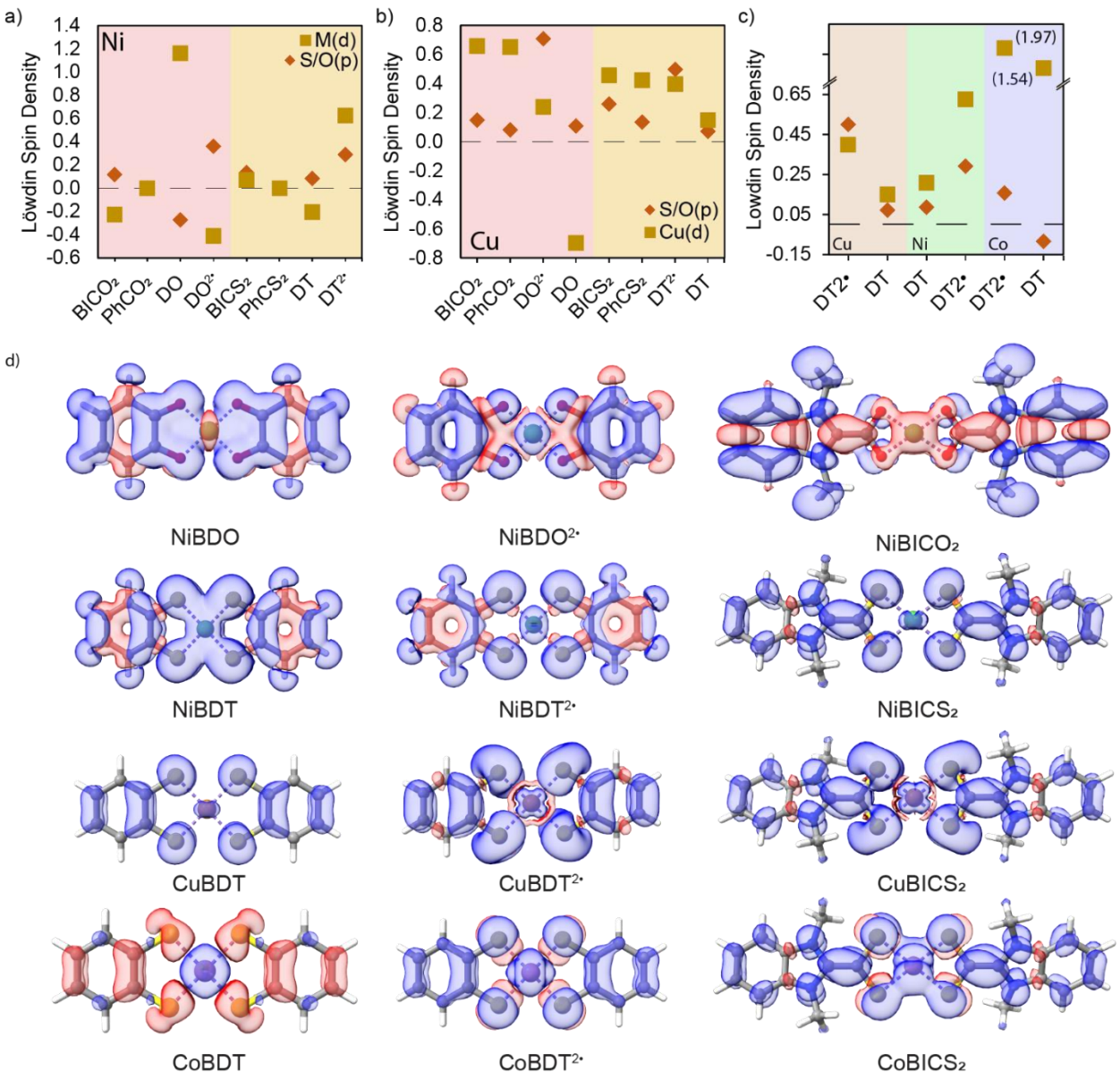

Figure 18. Löwdin spin population of the metal d orbitals and p orbitals of the sulfur or oxygen heteroatoms. a) spin population of modeled nickel complexes. b) spin density of modeled copper complexes. c) spin density of copper, nickel and cobalt modeled with $BICS_2$, dithiolene or reduced dithiolene. d) spin density maps of nickel, copper and cobalt models.

When comparing our series of isostructural models, especially when looking at the ditholene-based complexes, the reduced copper model is the only model that predicts a rather highly likelihood of spin density on the sulfurs and of roughly similar extent as the metal center

(Figure *18*c). The neutral copper dithiolene does not display this same ability to distribute the spin evenly, with a slightly higher assigned density at the metal center. Reflected as well in the case of the nickel and cobalt dithiolenes, there is the prediction of a higher spin density on the metal center with less distribution to the surrounding heteroatoms (Figure *18*d).

Mayer Bond Orders

Calculated Mayer Bond orders above 0.1 are reported. Some sulfur atoms in trans configurations relative to the metal center display bond character that is above the aforementioned threshold and are reported here. Cis sulfur atoms with bonding characteristic reside on the same ligand. No X-X_{cis} bonding interactions were calculated from heteroatoms in a cis configuration from one ligand to another. Only one oxygen-based model display any O-O_{trans} bonding interactions at this threshold and none show any O-O_{cis} bonding at this threshold. It is possible that there is some electronic communication between heteroatoms that do not produce any calculated bond order, but it is not observed with this analysis.

Given the initial calculation configuration of 2+ oxidation state in the bis-complexes and their 4-coordinate nature, we presume that not each M-X bond can have a full single bond characteristic. In the most delocalized and covalent systems where electrons are shared evenly between the metal center and the heteroatoms, it would follow that a bond order of about 0.5 between the metal center and the heteroatom would represent this situation well. Upon initial consideration, the $NiPhCO_2$ model assigns an M-X bonding order of 0.43, less than our idealized 0.5 value and indicating a more ionic environment. Expanding to the nickel diolene models, we find that the bond order reported is closer to 0.5, with the neutral form slightly over (Figure *19*a).

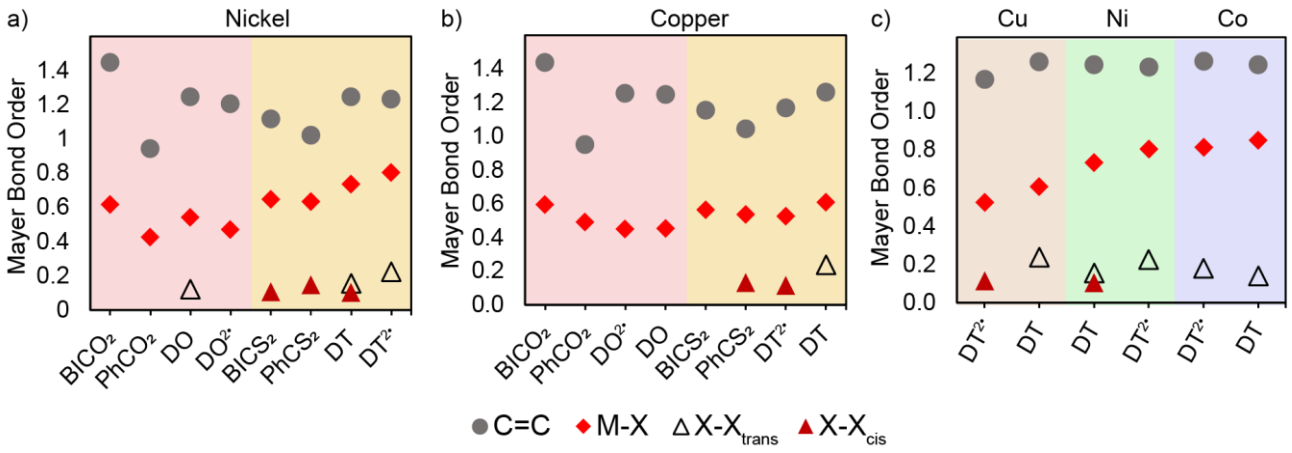

Figure 19. Mayer bond orders of each model, including some long range bonding interactions. a) bond order of modeled nickel complexes. b) bond order of modeled copper complexes. c) spin density of copper, nickel and cobalt modeled with dithiolene or reduced dithiolene. Legend: gray circles represent carbon-carbon bond order between the CX_2 carbon and it's nearest carbon neighbor, or the double bond between carbons of di(thi)olene motifs directly bonded to heteroatoms. Red diamonds represent metal to heteroatom bond order. Hollow triangles represent heteroatom to heteroatom bonding interactions across the metal center in a trans configuration. Solid triangles represent bond orders of heteroatoms in a cis configuration relative to the metal center on the same ligand.

The analysis of proximity to a bonding order of one-half is somewhat simplistic in this regard, and further consideration is required. Given the predicted Löwdin spin density at the nickel center greater than 1 and with the opposite sign with respect to oxygen, we would expect a slightly higher bonding order but would still characterize this as a rather ionic interaction. When we consider how this reported bonding changes when the sulfur system is analyzed, a slight increase in the bond order is observed. Alone this would seem to be indicative of a more reduced nickel center even when we expect this to behave as a Ni^{2+}. What is noted along with this increased bonding order is the emergence of a $S\text{-}S_{cis}$ bonding characteristic as well. The ability for some bonding characteristic between the two cis sulfurs is both indicative of a more delocalized electron environment and a sharing of electron density, which would point to increased covalency. Present in only the neutral nickel dithiolene is the combination of this $S\text{-}S_{cis}$ interaction as well as a long range $S\text{-}S_{trans}$ bond order. The $X\text{-}X_{trans}$ bonding order is observed in the nickel diolene and reduced

nickel dithiolene, but the cis-heteroatom interaction in not observed. When considering the copper system, all the M-X bond orders are much closer to our expected one-half with most of the oxygen-based systems slightly below (Figure *19*b). Contrasting the nickel somewhat, the reduced copper dithiolene is very near our idealized value and also displays some bonding character between the cis sulfurs with no significant S-S_{trans} bond order reported. Alongside the observed S-S_{cis} bonding, it appears that the copper sulfur bonding environment is able to distribute itself amongst the heteroatoms quite evenly. When considering the effect of the metal center on the calculated bonding, the bond orders returned from the isostructural models shows a steady increase from copper to nickel to cobalt. When viewed with delocalization index and Löwdin spin density in mind, the distribution of additional spin density around the metal center donated from covalent sulfur interactions is consistent with this picture.

Moving farther out from the core, the extent of bonding changes in notable ways when considering carbon-carbon bonds. In the carboxylate-based models, the bond between the aromatic carbon of the phenyl ring and the carbon of the -CX_2 are most reflective of a single bond, with a slight increase for sulfur examples. Quite a large difference between oxygen and sulfur models is observed in the $BICX_2$ systems. The bond order of the C_{aro}-C_{CX2} is much more reflective of double bond character in the oxygen models, but the sulfur analogues describe a bond order that is more reflective of the C=C bonds in the di(thi)olene models. While we typically simplify this bonding environment as double bonds in a ring, the delocalization around the phenyl ring means this becomes less of a formal double bond. Given the similarity between the $BICS_2$ C_{aro}-C_{CS2} bond and the C_{C-X}-C_{C-X} bonds of the di(thi)olenes, it matches quite well with the described delocalized radical from previous literature. This double bond character seems to be limited, however, by the benzimidazoles tendency to be somewhat rotated relative to the square planar metal centers.

Notably as well, the bonding characteristic of the reduced copper dithiolene aromatic carbons is the lowest of all the di(thi)olate systems (Figure *19*c). In fact, when comparing across the di(thi)olene systems, the calculated aromatic C=C bond order is consistent except for the $CuBDT^{2\bullet}$ model. The change in bonding order found in the aromatic ring prompted an investigation into the aromaticity of the ligands in varied environments.

Spin density maps were plotting keeping the isosurface value consistent across models. This resulted in the (dithio)carboxylate models showing no visible spin density at those values, so they are not included in the resulting figure. All other models display observable regions of α and β spin density across the pictured structure.

These maps describe how heteroatom and ligand structure affect the spin density distribution across the modeled systems. Observed in the oxygen examples is a distinct separation of phase. In the nickel diolene model, the metal center and the heteroatoms adjacent to it display high likelihood of spin, but in alternate phases. In the reduced diolene, the phase of spin surrounding the metal and heteroatoms is of the same phase, but spin density of the opposite phase is observed in the volume between. Interestingly, the dithiolene shows spin density delocalized across the metal center and sulfurs with no change of phase, whereas when the system is reduced, these node-like areas emerge. The spin density within the aromatic ring displays a further disrupted pattern in the reduced system as well. When looking at our targeted system, what stands out is the observance of a consistent phase across the sulfur-based system, whereas the oxygen-based ligand shows distinct

Nucleus-independent chemical shift

Utilizing the "sigma-only-method" (SOM) to account for non-π electron effects, zNICS scans were carried out on the nickel-based model compounds and the synthetically obtained free

ligand. Chemical shifts were calculated from 2 to 6 Å in the z direction from the center of each ring, which was placed in the xy-plane. Data for each model was fit to an exponential curve and the integral from 0 to 10 was taken as the total. (10 Å was taken to be a sufficiently far distance from the ring to be free from magnetic effects of the ring.) Only the $NiBICS_2$-im data was unable to be fit to a curve, so the area under the calculated data points was used as a placeholder for a rough comparison. The resulting values were compared as a percentage relative to benzene calculated with the same theory and basis set. The resulting plot therefore shows a simple comparison relative to benzene taken as a standard and does not inform on any sort of absolute linkage to aromaticity.

xyNICS(SOM) data was obtained from construction of a grid of dummy atoms 2 Å above the ring system in the same xy-plane. In the same fashion of the zNICS scans, the "sigma-only-method" was employed to remove effects induced by the sigma bonds of the system. The chemical shifts were plotted as colormaps in the xy-plane, with the color corresponding to obtained shifts. These results describe points/area of high magnetic influence due to ring current in the π system.

The plots are shown below alongside discussion (Figure *20*). Analysis of NICS scans in the z-axis certain results in useful data, but for molecules that extend beyond that of just a small aromatic system, a more global analysis is fitting to observe changes in electron localization. Utilization of xyNICS(SOM) methodology can visualize how ring current is disrupted, shifted across the multi-ring system or effectively disrupted by other electronic factors. As we would expect, modeling the benzene in this way and obtaining the 2D maps shows a strong effect from delocalized ring current centered over the ring.

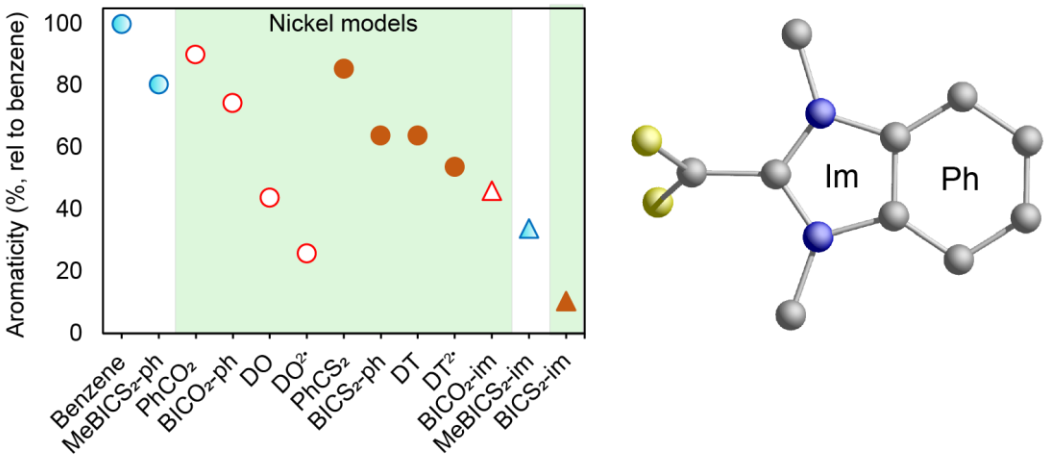

Figure 20. zNICS(SOM) aromaticity values relative to benzene modeled and calculated with the same theory and basis set as were used to optimize and calculate energies. The phenyl ring and imidazole ring of the $BICS_2$/$BICO_2$ models were evaluated separately, denoted as $BICO_2$-ph/im or $BICS_2$-ph/im. Values are in percentage of ratio of integrated value from 0 to 10 from exponential curves fit to data, *with the exception of Ni$BICS_2$-im which could not be fit, so the area of the data from 2 to 6 was used in lieu of an integrated value. In the structure of Me$BICS_2$ obtained from SCXRD, the ring labelled "Im" denotes to the imidazolium ring of the molecule and "Ph" denotes the phenyl ring where the zNICS scans were taken. Yellow spheres represent sulfur atoms, blue spheres represent nitrogen and grey represent carbon. Hydrogen atoms are not shown.

When this is extended out to the imidazole ring of the free Me$BICS_2$ ligand, we observe there is a strong magnetic effect centered in the phenyl ring that becomes weaker towards and into the imidazolium portion of the molecule. This matches well with the obtained zNICS(SOM) scans that reports about 80% aromaticity in the phenyl ring versus about 34% in the imidazolium ring (relative to benzene.) This is consistent with literature that shows a decrease in ring current of the phenyl ring of multicyclic systems functionalized with similar motifs.[165] We expect the electron withdrawing nature of the extended ring to change how the phenyl ring is able to delocalize its π electrons.

When the series is extended to our modeled complexes, the effect of the metal and heteroatom becomes apparent. The aromaticity of the series of nickel complexes was compared in the xy plane 2 Å above the plane of the aromatic ligands (Figure 21). Firstly, when comparing our

free ligand to the $NiBICS_2$ complex, we see a high decrease in the aromaticity of the imidazolium ring alongside a decrease in the phenyl aromaticity. This effect is also highlighted by the opposite magnetic effects seen around the nitrogens and closer to the metal center. Given our analysis of spin density, it follows well that delocalized spin density out to the imidazolium nitrogens, NHC C2 carbon and CS_2 carbon would have a notable effect on this region. When the oxygen analogue, the $NiBICO_2$ model, is examined, we observe a higher extent of aromaticity in the imidazolium ring, with slightly less in the phenyl ring. This is interesting when compared to the zNICS data, which reports a higher aromaticity in the phenyl ring as compared to the sulfur-based example. This highlights the interesting difference in simply probing above the rings in the z-axis versus a more global view of the molecule. It should be noted as well that the oxygen analogue is far more planar relative to the square planar nickel center compared to the $NiBICS_2$ which adopts a rotated geometry in the optimized structure. This breaking of planarity would also follow well with slightly more ring current localized in the sulfur analogue.

The most immediate data apparent in the di(thi)olene models is that the oxygen heavily disrupts the ring current of the phenyl ring, migrating a great deal of magnetic effects out towards the heteroatoms and nickel. Some ring current is maintained in the reduced $NiBDO^{2\bullet}$ model, but it is heavily dampened by the electronic effects of the oxygen and metal center. The dithiolenes display a stark contrast, with much more ring current maintained (although still greatly decreased relative to benzene) and what appears to be a strong reversed magnetic influence originating at the sulfurs and metal center. The decrease in aromaticity of the reduced dithiolene model also points to our earlier discussion of the additional radicals introduced to $Ni_3(BHT)_2$ disrupting the aromatic system in order to carry charge across the extended framework. This would be a destabilizing effect and decrease the ability for charge transport.

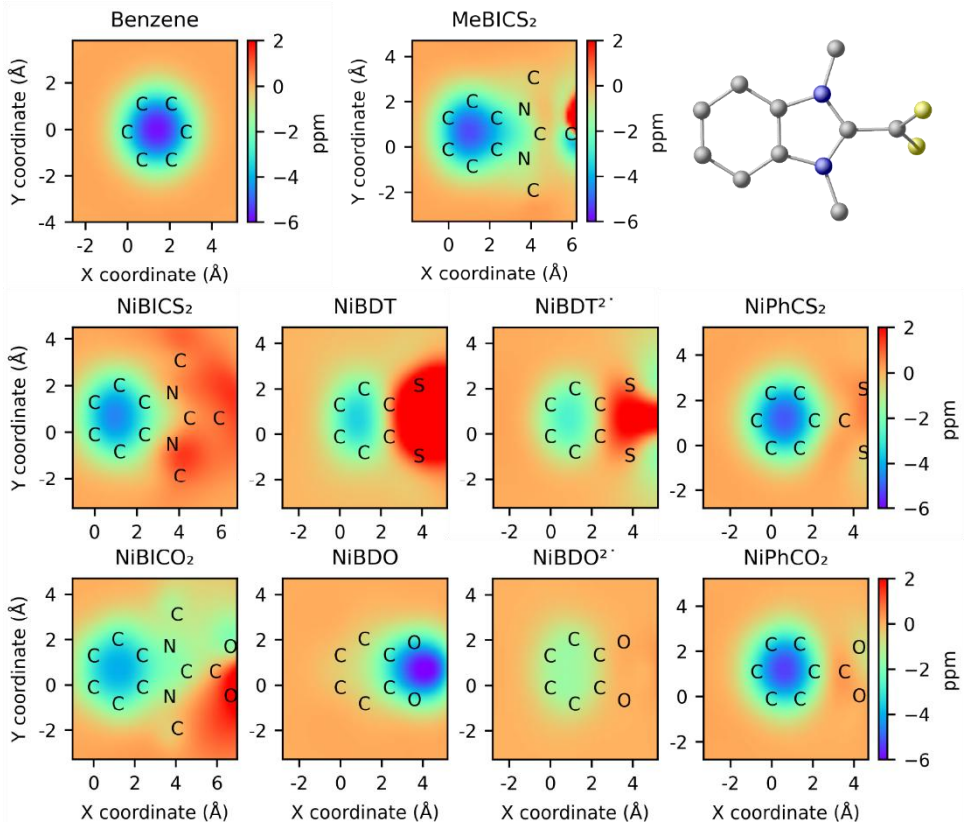

Figure 21. xy-NICS(SOM) scans taken at 2 Å above the plane of the ring. Chemical shifts calculated at the same level of theory as all other calculations. Yellow spheres represent sulfur atoms, blue spheres represent nitrogen and grey represent carbon. Hydrogen atoms are not shown.

Further reflected in the xyNICS data is the non-conjugated nature of the aromatic ring with the (dithio)carboxylate groups. Given a bond order of about 1 in both examples it makes sense that the carbon-carbon bond between the phenyl ring and the CX_2 is not involved in any sort of charge delocalization. Given carboxylate-based frameworks to exhibit incredibly low or even insulating conductivities, it would not be unreasonable to draw parallels between pockets of localized aromatic electron density and difficulty moving charge through an extended material. One could also draw a parallel to our earlier point on large differences in delocalization index leading to points that act as potential energy wells, making it difficult for charge to continuously flow.

Prediction of conductive properties with NHC-CS_2 ligand

While there are limitations with DFT, especially when utilizing functionals like B3LYP that are computationally "cheaper", we find merit in its use here to provide computational results in reasonable timeframes which elucidate trends but are not trying to predict exact values. Due to its wide employment in the computational field and consistent use across the models, we believe this analysis is of value for insight into the design of materials. Of course, there will always be some variations that are not accounted for in molecular systems when compared to extended materials. Materials properties arise, however, from a combination of the molecular components, and we posit that the extracted value from the calculated results benefits from corroboration with experimentally known data. Within the designed system, consistent use of functional and basis sets across the modeled compounds results in a series that is comparable. Even with error inherent to different types of calculations, with all systems modeled and computed with the same foundation and without over-interpretation of the calculated results, the trends observed should be able to reasonably inform on synthetic design of materials.

Initially, we had set out to utilize computational methods to test our hypothesis that an increase in heteroatom covalency would correlate with materials that are more conductive. Comparing various modeled systems with a simple exchange of an oxygen atom to a sulfur, observed is an increase in our chosen metric, delocalization index, that would support this hypothesis on initial interpretation. When considering reported literature with hexa-functionalized benzene and triphenylene materials, this increase in calculated covalency does trend nicely, exemplified with Cu_3(BHT) conductivity far exceeding the oxygen-based analogues. Considering different aspects such as electronegativity or "softness" as described in HSAB, it follows with chemical intuition that the decrease in more ionic or "harder" interactions will result in systems

that are more conductive due to less localized potential wells for charge to dwell in. Frameworks that have localized pockets of positive or negative charge due to ionic bonding motifs increase the barrier for charge mobility. Importantly however, if we consider our findings across copper, nickel and cobalt, there emerges a trend that would point to higher delocalization indices in systems that are less conductive. The calculated DIs are lower in the copper than in nickel or planar cobalt complexes, but when in extended frameworks, the Cu_3(BHT) forms a densely packed sheet that is currently the most conductive coordination polymer/MOF measured. There is some variation to the optimal metal-heteroatom combination across analogous hexa-functionalized benzene or triphenylene sheet materials, with an emphasis that packing structures, mechanisms of transport, oxidation states and size of conjugated linker matter heavily. Thinking primarily of how metal-ligand bonding might affect in-plane charge transport, a consideration of the difference between delocalization index of metal and heteroatom is again returned to. Evaluating resulting delocalization index, we return to our observations of a relatively small difference in copper and sulfur DI from our reduced model system that is known to be the building unit of Cu_3(BHT), the most conductive extended framework. Based on the idea of covalent interactions producing a more equally shared density of electrons, it follows quite logically that atoms with very similar delocalization indices will not localize electrons in a disparate manner and will not act as a potential well for mobile charges to experience difficulty navigating. It would stand to reason that the most covalent interaction would feature a similar extent of delocalization, or electron sharing, between each atom in the bond. When comparing to the known extended systems these analogues were modeled for, a trend becomes apparent when it comes to the difference in DI. It has been demonstrated that in $Ni_3(BHT)_2$ materials, the reduced system actually has a lower conductivity relative to the neutral form. This matches well with a larger gap in delocalization indices. This idea

is highlighted by the small difference of DI in the copper models where a much closer match in the reduced dithiolene versus the neutral form featuring a larger gap in the indices.

Even when comparing systems like the $Cu_3(HOTP)_2$ and $Ni_9(HOTP)_4$, with a ΔDI of 0.02 and 0.18 for their models CuBDO and $NiBDO^{2\bullet}$ respectively, the comparison with literature holds. While they are not as conductive as the small benzene hexathiol analogues, $Cu_3(HOTP)_2$ has been measured with conductivities of up to 1.5 $S \cdot cm^{-1}$ whereas $Ni_9(HOTP)_4$ is two orders of magnitude lower, at 0.01 $S \cdot cm^{-1}$. We posit that this combination of increased DI from oxygen to sulfur and small ΔDI for copper-based models points to the ideal properties extracted from predictors of covalency. Keeping this in mind and looking to theorize on our future synthetic goals, we considered the BICS2 ligand with the metal series referenced before: Cu^{2+}, Ni^{2+}, Co^{2+}, Co^{3+}, Cr^{3+} and Sc^{3+}.

When comparing the same $BICS_2$ ligand across different metals (and different coordination environments) the delocalization index highlights the Co^{3+} system as an incredibly delocalized metal center (Figure *22*). Both the sulfur and metal have the largest delocalization indices in their respective series. Of note however is the broad gap between the indices of the Co^{3+} and the sulfur. Based in our previous observation, we would predict that utilization of Co^{3+} with $BICS_2$ as a ligand would produce a system that is far less conductive than if paired with Cu^{2+} with a ΔDI of -0.03. Once again, referencing observed trends in conductivity, the cobalt complex having a large gap in delocalization index makes sense, with both the bis- and tris- coordinated system. Because the design of a system resulting in a similar covalency of metal and heteroatom presents as the most promising synthetic target, it is possible that an extended system based on nickel or cobalt and the imidazolium dithiocarboxylate motif would display increased conductivity relative to their dithiolene analogues. This does seem to indicate that a pairing of Sc^{3+} and the $BICS_2$ ligand could

be a logical target, however the overall magnitudes of the indices are smaller. We also know that scandium is considered a harder acid than copper, so this decrease in magnitude makes sense. Still, for a 3-dimensional system, this could pose as an interesting model. This of course does not preclude the use of systems with wide heteroatom-metal DI gaps for useful applications. $Co_3(BHT)_2$ and $Co_3(THT)_2$ have seen utilization in electrocatalysis. In fact, further study of DI in electrocatalytically active systems could elucidate how metal-heteroatom ΔDI could relate to activity.

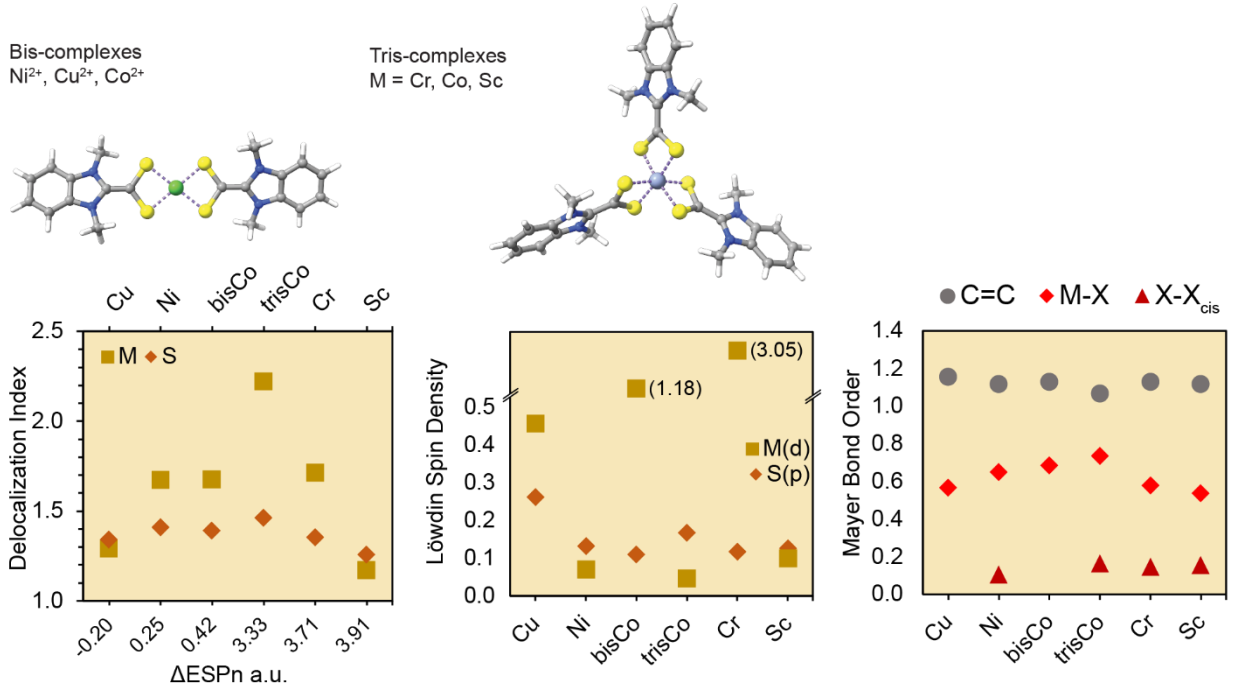

Figure 22. Calculated data of bis- and tris-complexed models of $BICS_2$ for prediction of properties. Delocalization index, Lowdin spin population and Mayer bond order are plotted with Cu^{2+}, Ni^{2+}, Co^{2+}, Co^{3+}, Cr^{3+} and Sc^{3+}.

Once again, adding to our comparison of covalency and returning to spin density, it would be reasonable to suspect that if there exists a large discrepancy between the heteroatom and metal spin density, it could act as a potential well that makes electron transport more difficult than in examples where the spin is quite evenly distributed. Observed in the reduced copper bisdithiolene

model, both the sulfur and the copper center are assigned spin densities that suggest there is only a slight preference for spin to reside in the sulfur p orbitals. From the perspective of covalency, this would indicate that the spin density is shared equally and that localization on either of the heteroatoms is not particularly favorable. In the nickel dithiolene model, we do observe that there is more spin focused at the metal center that is flipped relative to the assigned sulfur spin density. It is possible that this out of phase system is somewhat limiting for the neutral nickel dithiolene system and would support the idea that electrons pass from sulfur to sulfur in $Ni_3(BHT)_2$, but we hesitate to over analyze this idea.

Going beyond the core of the models again, low spin density in the ring system of the dithiolene aromatic carbons makes sense from a perspective of aromaticity and trends with the fact that the extended system, $Cu_3(THT)_2$, is less conductive than the incredibly dense $Cu_3(BHT)$. Placing additional spin density in the ring of the pi system of the ring would induce electronic environments that deviate from what is classically understood to be aromatic. When the 2D sheet of $Cu_3(BHT)$ is undergoing some electron transport process, given the connectivity and distribution of spin, there is no need to disturb the aromatic system of the benzene rings. This does suggest that the $BICS_2$ system may have increased barriers to charge transport when extended out into a di- or tritopic linker if chare is moving through the aromatic core. The spin density of all the modeled $BICS_2$ systems suggest there is about the same extent of spin density distributed to the imidazolium-dithiocarboxylate portion of the molecule, and that the heteroatom-metal center will have some discrepancy in the spin density that trends with the difference in delocalization index. Although the ΔDI of the $CuBICS_2$ model is promisingly small, the overall slightly lower DI of the system is consistent with slightly more localized spin and slight decreases in covalency. Considering other models of the metal series, we observe minimal assignment of spin density into

the cobalt d orbitals beyond what would be expected from a Co^{2+} and a Co^{3+} (1 and 0 unpaired electrons respectively.) In fact, the tris-coordinated Co^{3+} model does not appear to have much likelihood of taking on any additional spin density in the d orbital. If one assumes a typical octahedral orbital splitting, then addition of unpaired spin would populate the antibonding e_g orbitals for a rather energetically costly exchange. In the case of chromium, the large d-orbital spin population make sense given the 3 unpaired electrons native to its octahedral configuration in a 3+ state, but interestingly it is still able to distribute the remaining radical species in a manner quite similar to the other modeled complexes with lower inherent spin. The chromium complex is able to distribute some of the spin density to the surrounding sulfurs, but less so than the copper model, and takes on almost no extra spin density. Once again, analyzed through the lens of a typical octahedral splitting, taking on additional spin in the t_{2g} orbitals would incur a spin pairing cost and populating the e_g orbitals would require overcoming the octahedral splitting energy. The scandium complex displays a very similar distribution to the other models that we don't expect to have unpaired electrons in the d orbital.

The Mayer bond orders of the copper-nickel-cobalt comparison with reduced and neutral dithiolenes suggest that beyond maximizing or minimizing any one specific value, consideration must be taken with respect to multiple parts of the system. Given the emergence of S-S_{cis} bonding indicated only in the reduced copper dithiolene and neutral nickel dithiolene models, it stands to reason that this type of bonding interaction is important for the design of the extended materials. When analyzing our series of models with varied metals and oxidation states, what stands out is a similar deviation from a bonding order of 0.5 as we change from copper to nickel and beyond. Curiously, again scandium gets quite close to our predicted ideal bond order. We might expect that a smaller cation, typically considered a harder acid, would participate in ionic bonding and that it

may be in a similar situation as some of the copper-oxygen containing models with a small. The difference in electrostatic potential between the elements also seems to be of significance in this case. With a difference of 3.91 a.u., this would point to two distinct electronic environments of the metal-ligand pair. This would pose as quite an interesting synthetic target to compare to our predictions.

These factors considered, we postulate that the ideal candidate for design of a new material would be a system that includes; a high degree of covalency between the heteroatom and metal, measured with delocalization index; a small difference in the delocalization of the heteroatom and metal center; a small difference in electrostatic potential of heteroatom and metal; a similar spin distribution in the atomic valence orbitals; a bond order that would distribute a bond order of 0.5 to each metal-heteroatom ligand with some bonding characteristics between the cis heteroatoms; a retention of some aromaticity of the ligand without introducing a high energy barrier to conjugation with the ring system. When we model our radical ligand of interest, $BICS_2$, with various metals, we find that a square planar configuration with copper comes close to our postulated ideal system. It is possible that the aromaticity of the ring system is higher than optimal relative to the rest of the ligand, but the distribution of the radical across the imidazolium ring and dithiocarboxylate provides interesting opportunities for encouraged electron mobilization. Testing this hypothesis with an extended material made of copper and scandium would aid in verification of our proposed metrics of interest.

Experimental and Methods

Computation: Complexes were modeled using Avogadro 1.2.0 and optimized using Orca 6.0.1/6.1.0.[166–177] DFT was employed with the widely used B3LYP hybrid GGA (20% HF exchange) for geometry optimization and property calculations. The complexes were geometry

optimized iteratively using Orca's internal "loose", "normal" then "tight" optimization and SCF convergence criteria. Final geometry optimization was completed at Orca's native "Tight" convergence thresholds and SCF convergence at Orca's "VeryTight" threshold. Each complex was calculated using unrestricted Kohn-Sham orbitals. Löwdin spin populations and Mayer bond order values were extracted directly from the Orca output files. Multiwfn was used to extract Mulliken populations, Hirschfield atomic orbital contributions to MOs and orbital delocalization indices.[178] Multiwfn was used to calculate AIM (3, -3) and (3, -1) critical points and the various parameters at those points. AIMALL software was also used to calculate (3, -3) and (3, -1) critical points which supplied the delocalization indices of atoms.[179] ChimeraX was used to visualize electrostatic potential maps and spin density maps generated from Orca's plotting tool.[180–182] Z-axis NICS scans were carried out by creating a series of dummy atoms starting at 2 Å from the center of each ring to 6 Å along the z-axis at a spacing of 0.1 Å. XY-NICS scans were carried out by creating a 2D grid of dummy atoms at a spacing of 0.2 Å from +4 to -4 Å in the x and y direction relative to the center of the aromatic ring. Chemical shifts were calculated using the same parameters as was used for the final model optimizations.

Conclusion

The covalency of metal-ligand bonds of 13 models were evaluated with DFT. Delocalization index (DI) was used as an estimate of covalency, showing an increase in covalency when ionic oxygen-based ligands were modeled with sulfur instead. When the models were compared to reported conductivity values of extended 2D MOF structures, systems with calculated DI values of the heteroatom and metal that were similar in magnitude correlated with highly conductive 2D sheets. Löwdin spin population revealed that the models corresponding to highly conductive 2D MOFs predict a similarity in spin density between the heteroatom and metal. Mayer

bond order analysis assigns bond orders closer to 0.5 in models that correspond to reported conductive frameworks. Models of benzimidazolium dithiocarboxylate were evaluated with the same parameters as the molecular analogues, predicting that $BICS_2$-based linkers would form highly conductive extended frameworks with intrinsic delocalized electrons as charge carriers.

CHAPTER V

CONCLUDING REMARKS

The work presented in this thesis represents a new synthetic perspective for the formation of highly conductive porous MOF $Fe_2(BDT)_3$. The importance of phase purity in the resulting product directly corresponds to the ability to utilize the material in applications beyond single crystal fundamental studies. The use of 1-methyl imidazole as a modulator demonstrates the rapid, low-temperature phase-selective formation of one of three known phases, highlighting the modulator's role as a nucleation-promoting reagent. Choice of solvent mixture, metal precursor salt and inclusion of octylamine as a modulator enabled the formation of nano-sized particles of either the spin-crossover active phase or highly conductive phase. The discovery of new size- and phase-selective conditions will be instrumental in order for incredibly conductive porous $Fe_2(BDT)_3$ MOFs to see practical application outside of an isolated, single crystal study.

Use of photodoped metal oxides in porous frameworks as dynamic reducing agents requires precise control on redox potential. A demonstration on the size-dependent redox potential of MIL-125 nanoparticles sits well within the context of literature. This work continues the use of decamethyl ferrocenium tetrafluoroborate as a probe for monitoring of in-situ equilibrium potentials of photoreduced MIL-125. As the nanoparticle size of the titanium-oxo-based MOF decreased from bulk to 32 nm to 18 nm, more reducing redox potentials were observed but did not reach the threshold of the hydrogen evolution reaction. A lack of gaseous hydrogen production corroborated the proposal of a transfer hydrogenation equilibrium, which was validated with NMR studies. An analysis of the in-situ redox potential in a non-aqueous environment modeled a practical use of photodoped titanium-oxo MOFs as organometallic reductants.

The theoretical investigation of a series of models, acting as molecular analogues to extended conductive frameworks, demonstrated a set of optimal parameters for the design of

conductive materials. Using the theoretical modeling framework of Atoms-in-Molecules, an estimate of covalency was extracted from calculated delocalization indices. This work establishes a molecular viewpoint from which to design ligands for conductive materials. Proposed is a ligand based on N-heterocyclic carbene dithiocarboxylate zwitterions which become reduced in the presence of zero-valent metal species to form stable, delocalized radicals.

APPENDIX A

SUPPLEMENTARY INFORMATION FOR CHAPTER 2

Materials

All commercial chemicals were used as received and handled in inert conditions unless stated otherwise. All solvents were collected from a solvent purification system and stored over 4Å molecular sieves, and all liquid reagents were freeze-pump-thawed four cycles prior to use. N,N-dimethylformamide (DMF, ACS grade, Fisher Scientific), acetonitrile (MeCN, HPLC grade, Fisher Scientific), isopropanol (99.5%, Fisher Chemical) iron (II) sulfate heptahydrate (99%, Millipore-Sigma), iron (II) chloride tetrahydrate (98% Alfa Aesar), iron (II) tetrafluoroborate hexahydrate (98%, Alfa Aesar), sodium azide (99%, Bio Basic) sodium thiocyanate (98% Sigma-Aldrich), 1-methylimidazole (99%, Sigma-Aldrich), 1,2,3-triazole (≥98%, TCI).

Powder x-ray diffraction patterns were obtained with a Bruker D2 Phaser benchtop diffractometer with a Cu Kα radiation source.

Scanning electron microscopy was obtained with a ThermoFisher Scientific Apreo 2 SEM.

Synthetic Methods

Synthesis of 1,4 benzene di-tetrazole (H_2BDT): A mixture of terephthalonitrile (1.64 mg, 12.8 mmol), sodium azide (5 g, 76.5 mmol) and triethylamine hydrochloride (10.,6 g, 76.5 mmol) in dry toluene (~75 mL) was heated under reflux for two days. The reaction mixture was mixed with NaOH solution (1 M, 20 mL), stirred for 30 mins and filtered, the aqueous part was acidified (pH = 1) with concentrated HCl and filtered to give the crude powder of 1.

The crude powder was suspended in 50 mL 1 M NaOH solution, stirred at ambient temperature for 30 mins and filtered. The filtrate was adjusted to pH5 by addition of 1 M HCl solution and filtered to give pale grayish powder, which was washed with DI water several times.

^{1}H-NMR (400 MHz, DMSO-d_6): d (ppm) = 8.03 (s, 4H, Ar-H)

General unmodulated synthesis

In a nitrogen atmosphere, to culture tubes with teflon-lined caps, $FeSO_4 \cdot 7H_2O$, H_2BDT and NaSCN were added. The tubes were capped and moved from the glovebox. The tubes and sparged solvents were moved to a benchtop glovebox with a nitrogen atmosphere. The solvents (5 mL total) were added to the respective tubes (see main text for solvent systems). The tubes were capped and taken out of the benchtop glovebox. The tubes were heated in a vial block at 160 °C for 3 days. At the end of the 3 days, the tubes were allowed to cool to room temperature before the reaction mixtures were transferred to centrifuge tubes in ambient conditions. The reactions were centrifuged and washed with DMF (2x, 10 mL), water (2x, 10 mL) and isopropanol (2x, 10 mL) before being dried in ambient conditions. Resulting powders were analyzed with PXRD for structure confirmation.

General modulated syntheses

Glovebox setup: In a nitrogen atmosphere, to culture tubes with teflon-lined caps, Fe(II) salts, H_2BDT, NaSCN and any applicable solid modulators were added. The tubes were capped and moved from the glovebox. The tubes and sparged solvents were moved to a benchtop glovebox with a nitrogen atmosphere. The solvents and liquid modulators were added to the respective tubes. The tubes were capped and taken out of the benchtop glovebox. The tubes were heated in a vial block at a preset temperature for varied times. At the end of the reaction time, the tubes were allowed to cool to room temperature before the reaction mixtures were transferred to centrifuge tubes in ambient conditions. The reactions were centrifuged and washed with DMF (2x, 10 mL), water (2x, 10 mL) and isopropanol (2x, 10 mL) before being dried in ambient conditions. Resulting powders were analyzed with PXRD for structure confirmation.

Benchtop setup: In ambient conditions, to 20 mL scintillation vials with septum caps, Fe(II) salts, H_2BDT, NaSCN and any applicable solid modulators were added and the vials were capped. In a 50 mL graduated cylinder, the desired solvent system was prepared and the graduated cylinder was capped with a rubber septum. The solvent system was sparged for ~10 minutes before it was cannula transferred to each septum capped vial. Liquid modulators were added via a glass microsyringe where applicable. The reaction mixtures were sparged before being placed in a vial block at a preset temperature for varied times. At the end of the reaction time, the tubes were allowed to cool to room temperature before the reaction mixtures were transferred to centrifuge tubes in ambient conditions. The reactions were centrifuged and washed with DMF (2x, 10 mL), water (2x, 10 mL) and isopropanol (2x, 10 mL) before being dried in ambient conditions. Resulting powders were analyzed with PXRD for structure confirmation.

Culture tubes and custom machined vial blocks for MOF synthesis

Aluminum vial blocks were custom machined from spare aluminum.

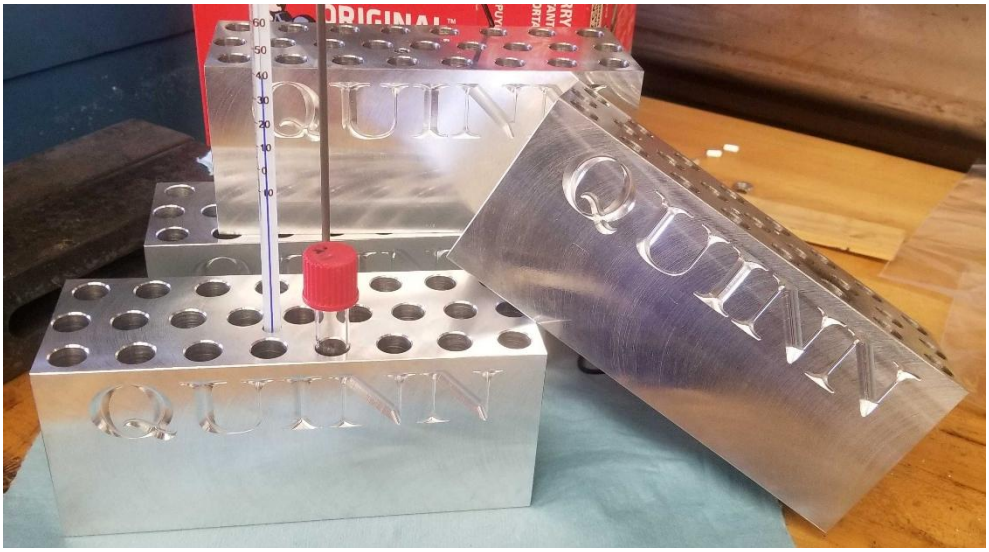

Scherrer analysis

PXRD patterns were analyzed and fit using Igor Pro 6 software using the Multipeak fitting

2 package. Crystallite sizes were averaged over at least 2 peaks and standard deviate is utilized as error. A Scherrer constant of 1 was used. Peaks were fit to gaussians.

PXRD patterns of reactions with varied synthetic parameters

PXRD patterns of syntheses with varied NaSCN equivalents with typical conditions.

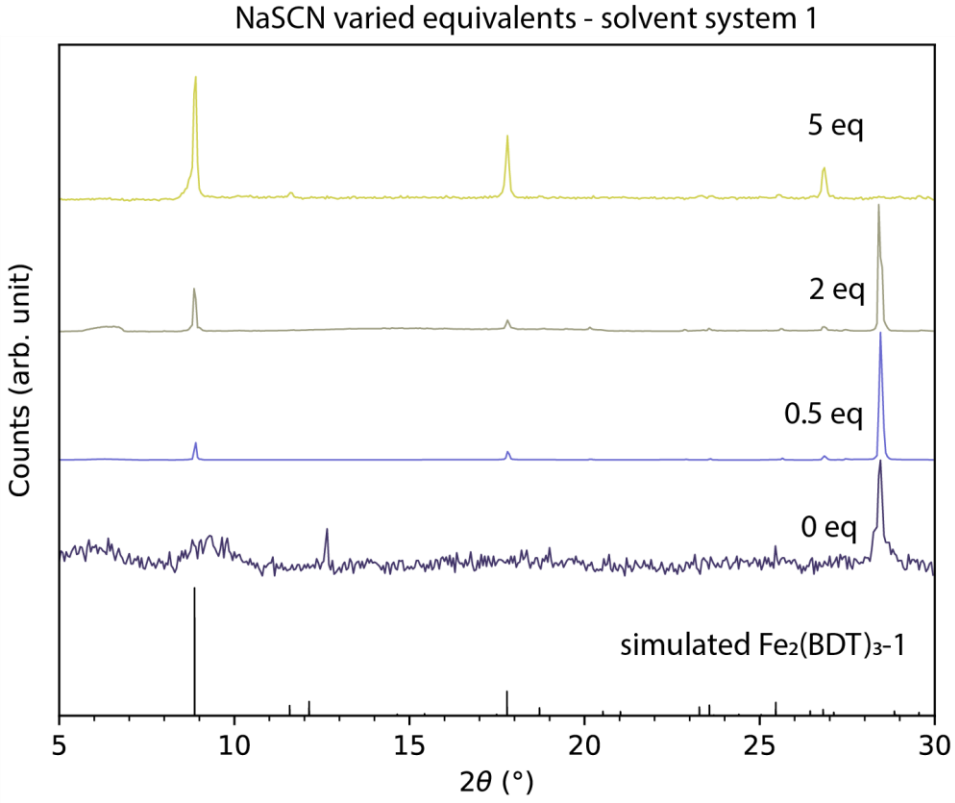

Figure 23. PXRD patterns of $Fe_2(BDT)_3$ syntheses in solvent system 1. Varied sodium thiocyanate equivalents with all other parameters kept standard

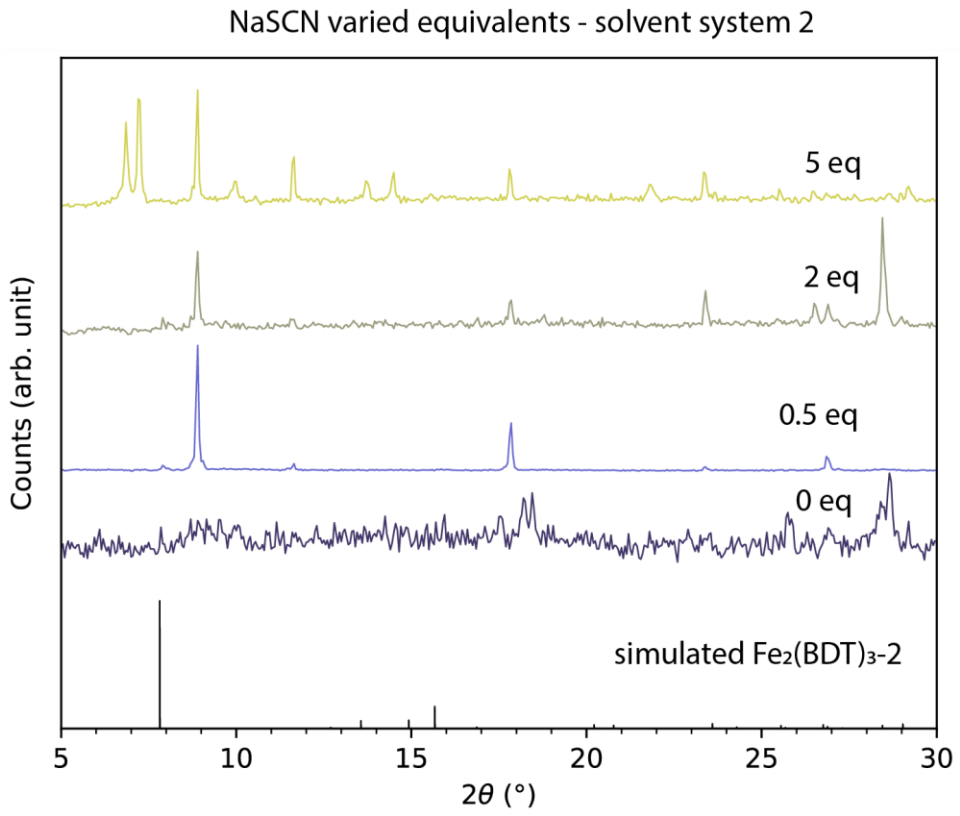

Figure 24. PXRD patterns of $Fe_2(BDT)_3$ syntheses in solvent system 2. Varied sodium thiocyanate equivalents with all other parameters kept standard

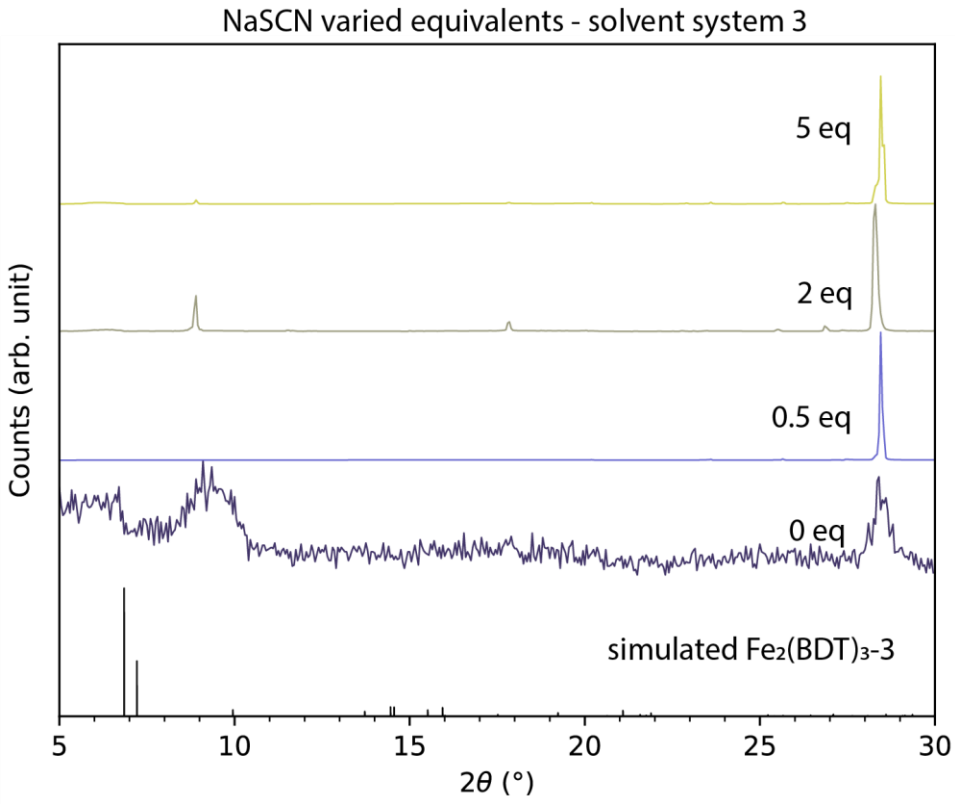

Figure 25. PXRD patterns of $Fe_2(BDT)_3$ syntheses in solvent system 3. Varied sodium thiocyanate equivalents with all other parameters kept standard

PXRD patterns of syntheses with varied 1-mIm equivalents with typical conditions.

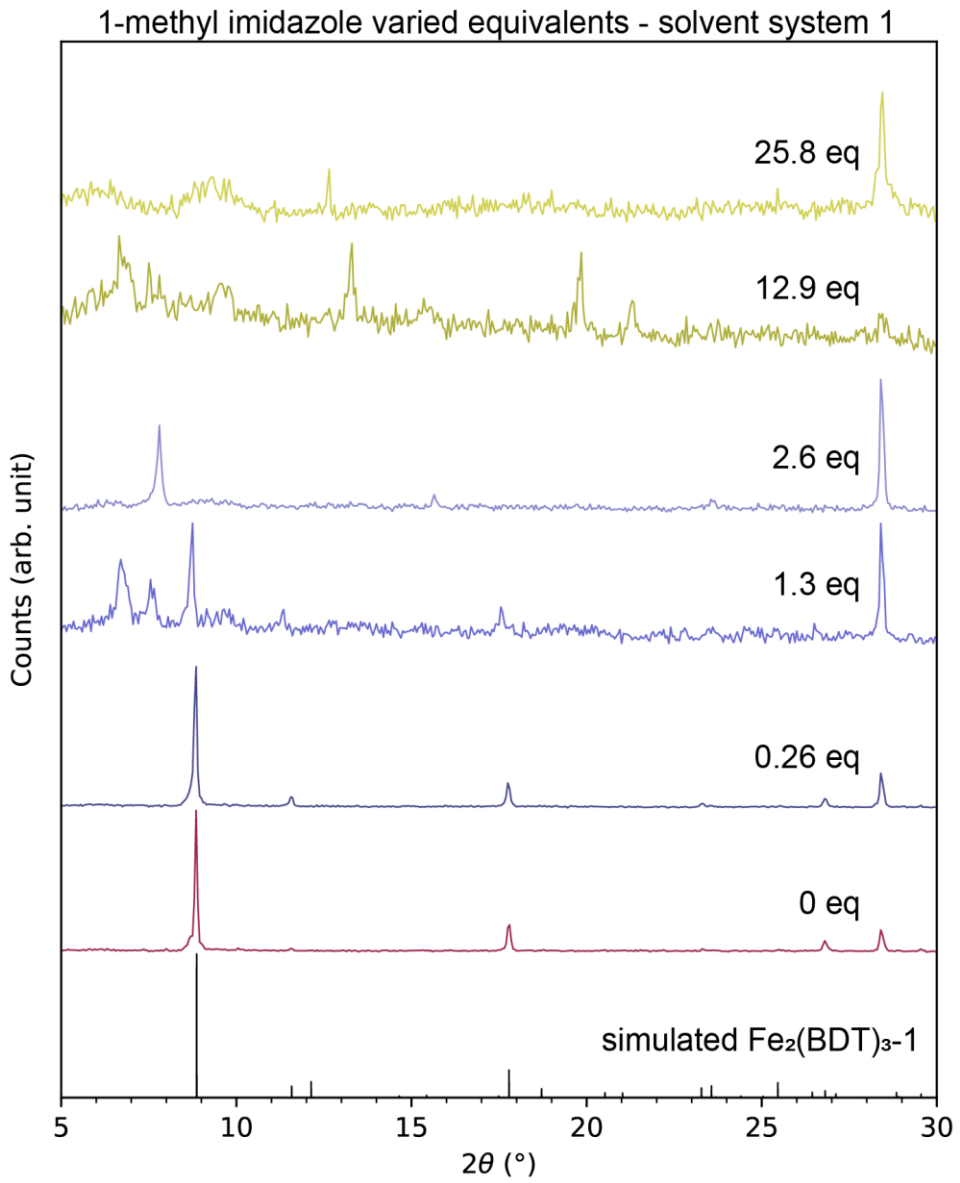

Figure 26. PXRD patterns of $Fe_2(BDT)_3$ syntheses in solvent system 1. Varied equivalents of 1-methyl imidazole added as a modulator with all other parameters kept standard

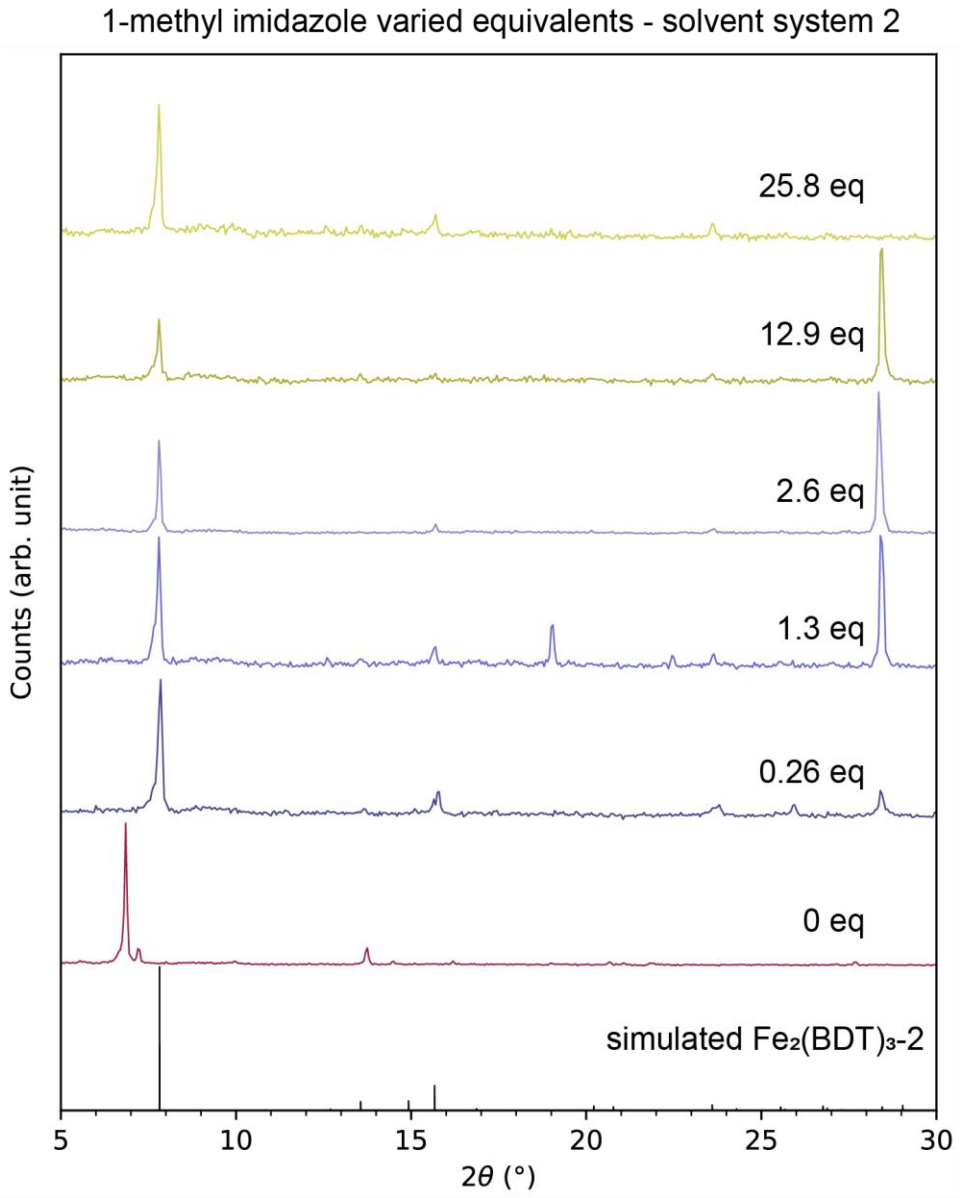

Figure 27. PXRD patterns of $Fe_2(BDT)_3$ syntheses in solvent system 2. Varied equivalents of 1-methyl imidazole added as a modulator with all other parameters kept standard

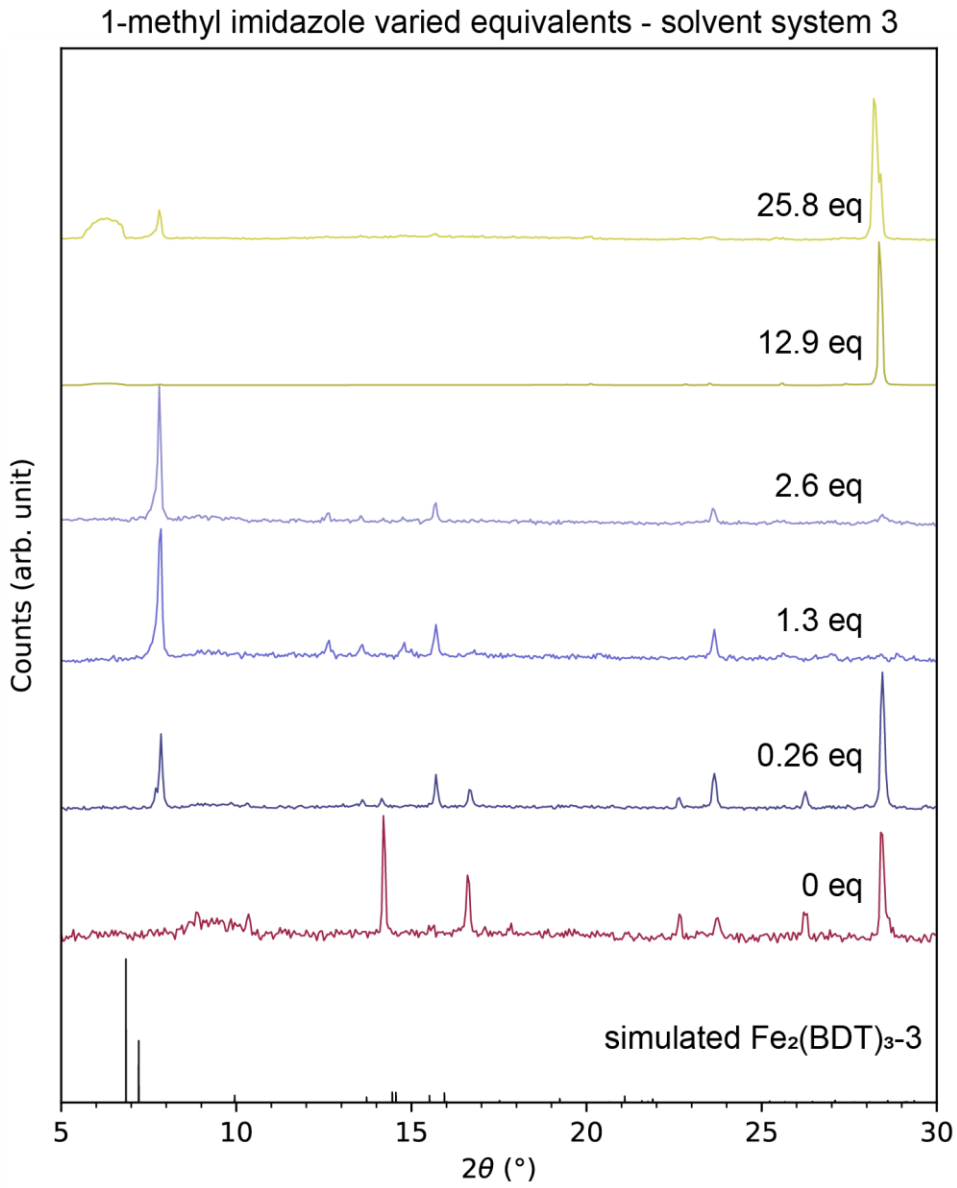

Figure 28. PXRD patterns of $Fe_2(BDT)_3$ syntheses in solvent system 3. Varied equivalents of 1-methyl imidazole added as a modulator with all other parameters kept standard

Time-dependent diffraction patterns in SS1

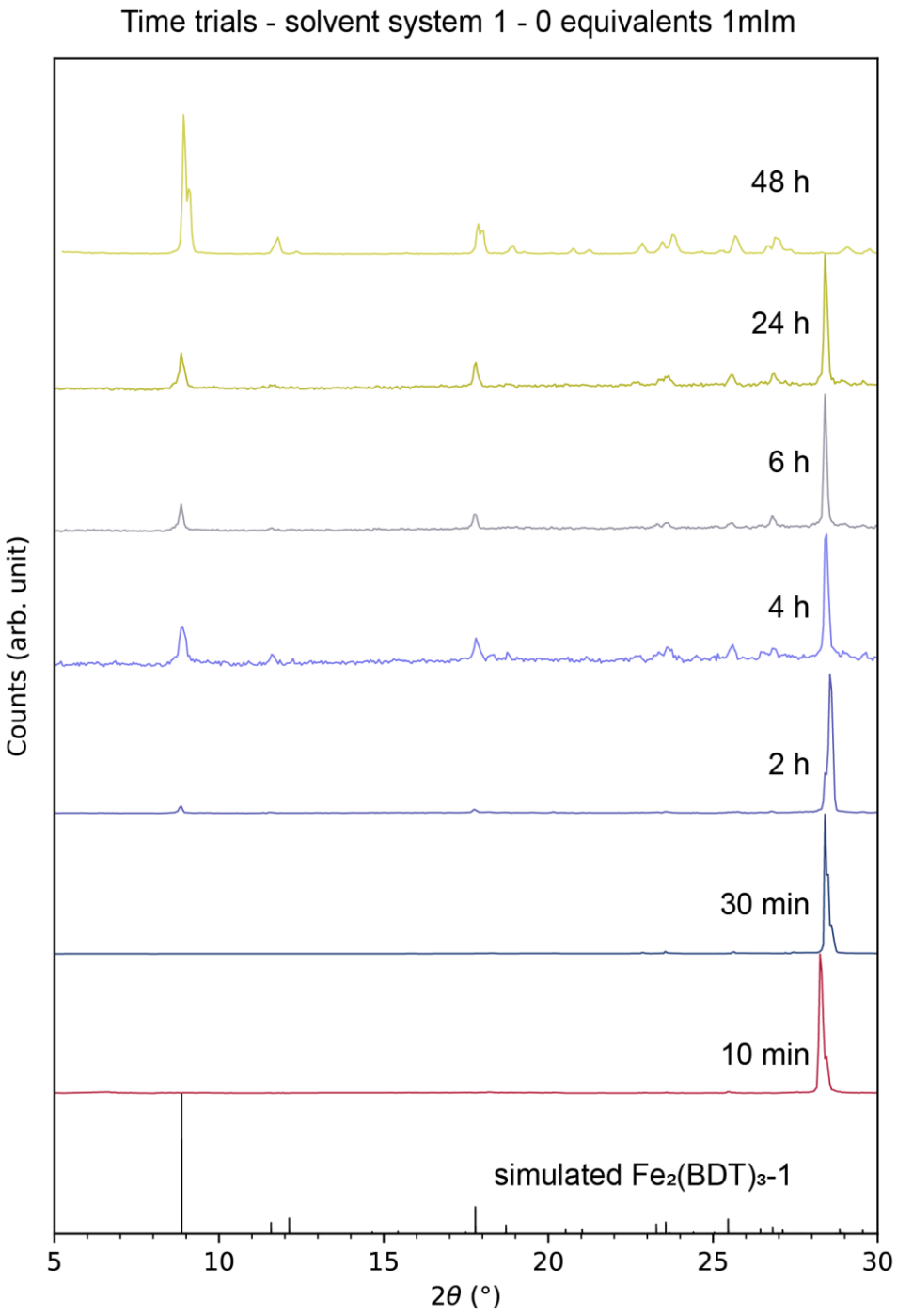

Figure 29. PXRD patterns of $Fe_2(BDT)_3$ syntheses in solvent system 1. 0 equivalents of 1-methyl imidazole added as a modulator at varied reaction times.

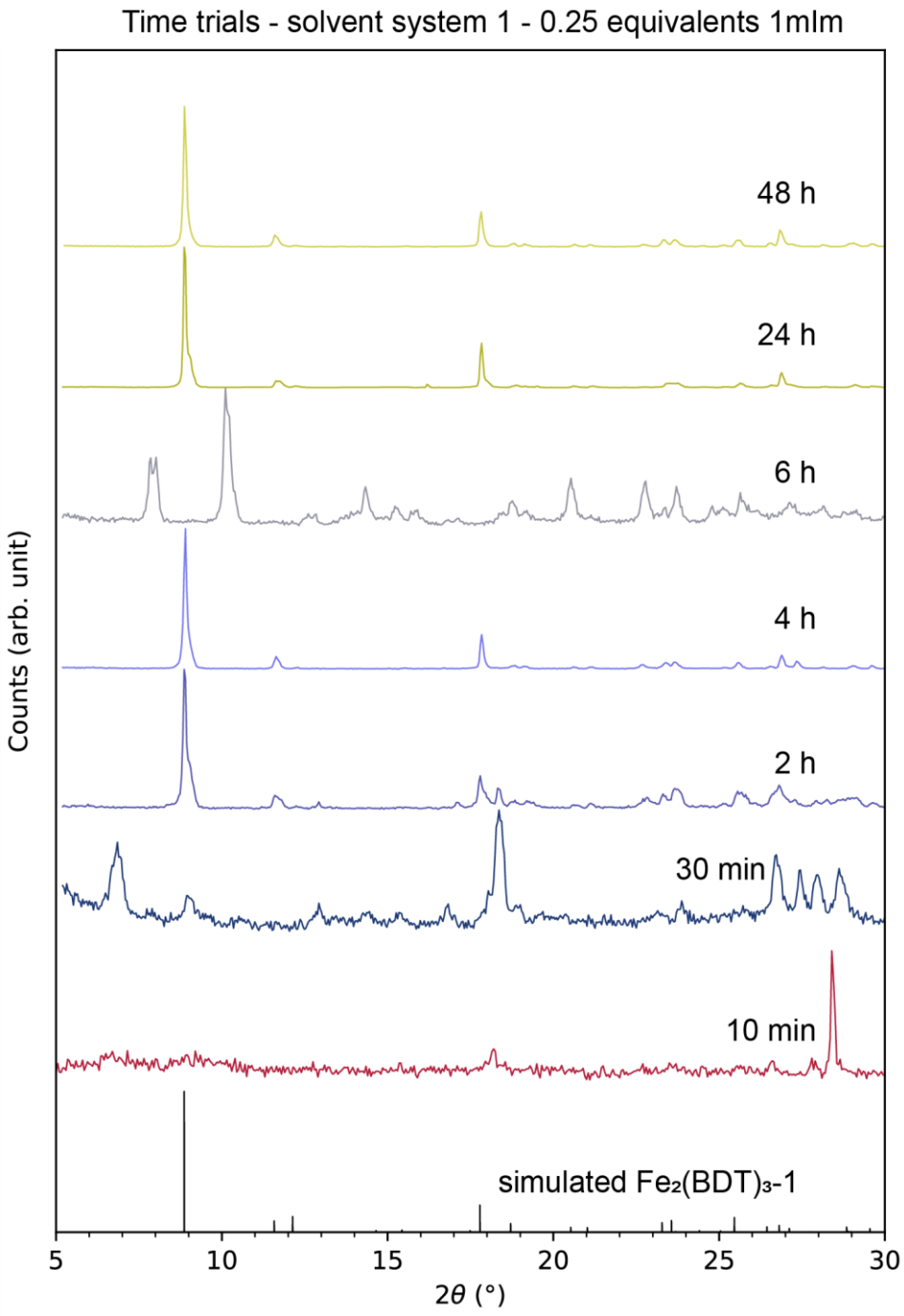

Figure 30. PXRD patterns of $Fe_2(BDT)_3$ syntheses in solvent system 1. 0.25 equivalents of 1-methyl imidazole added as a modulator at varied reaction times.

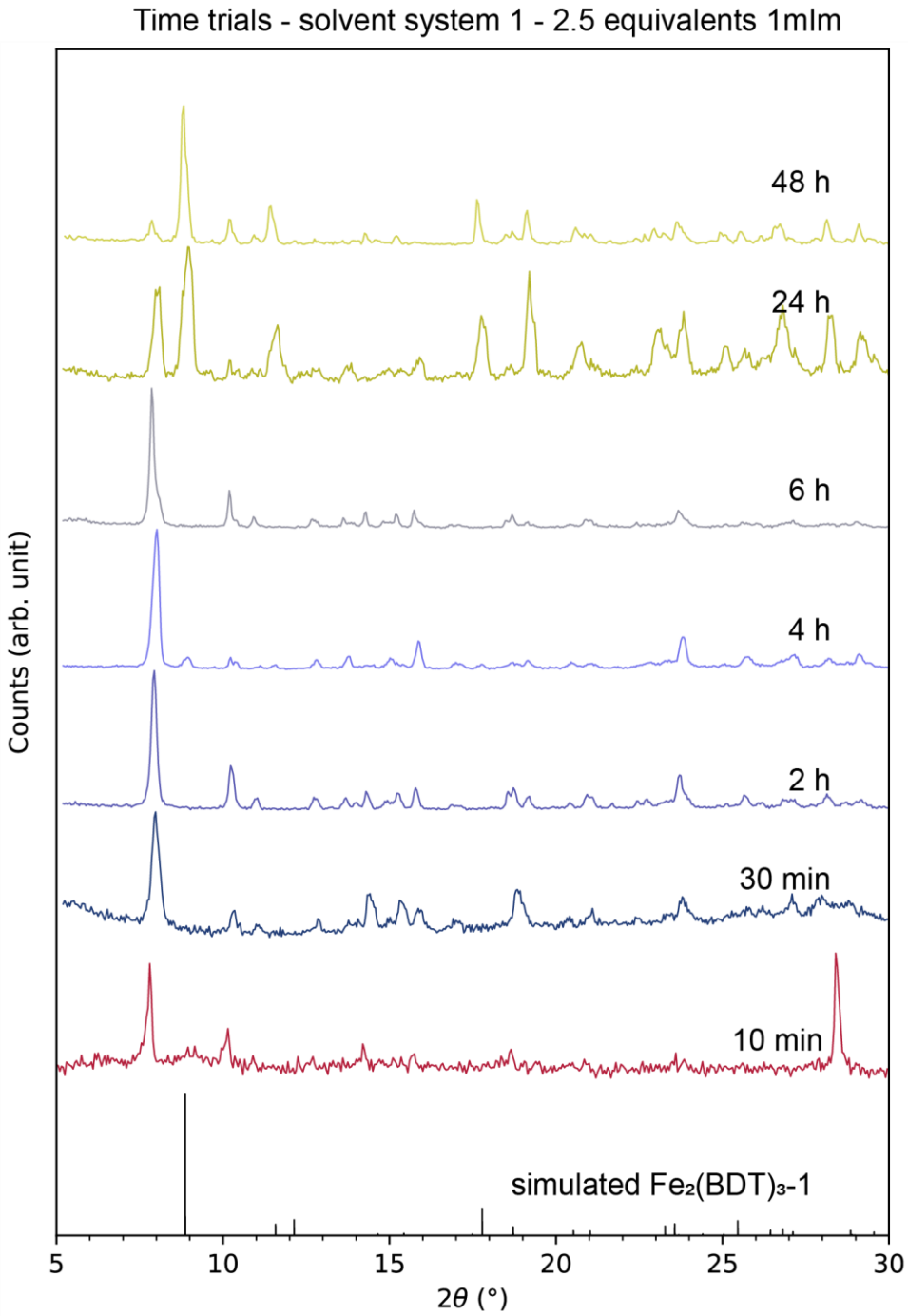

Figure 31. PXRD patterns of $Fe_2(BDT)_3$ syntheses in solvent system 1. 2.5 equivalents of 1-methyl imidazole added as a modulator at varied reaction times.

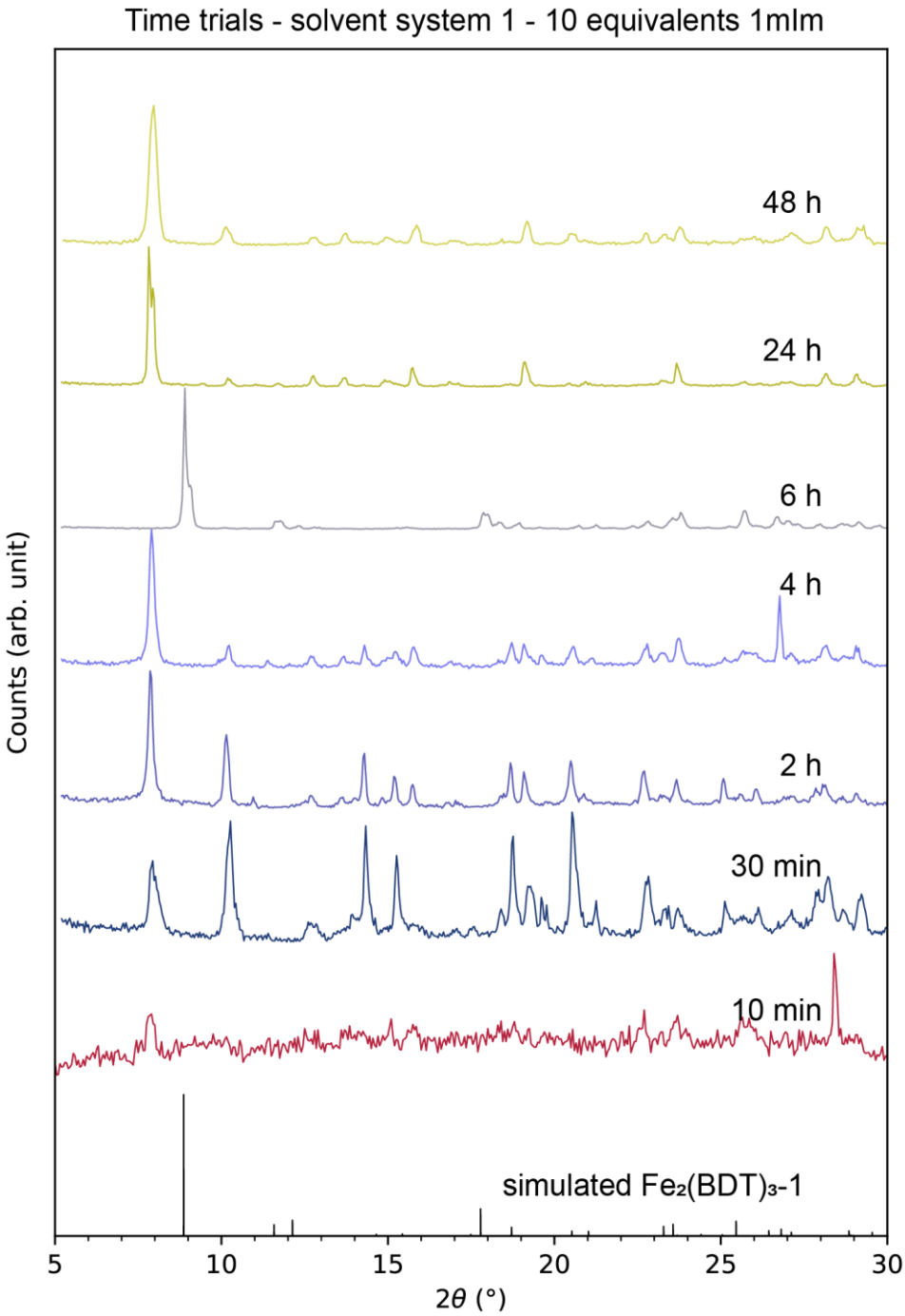

Figure 32. PXRD patterns of $Fe_2(BDT)_3$ syntheses in solvent system 1. 10 equivalents of 1-methyl imidazole added as a modulator at varied reaction times.

Time-dependent diffraction patterns in SS2

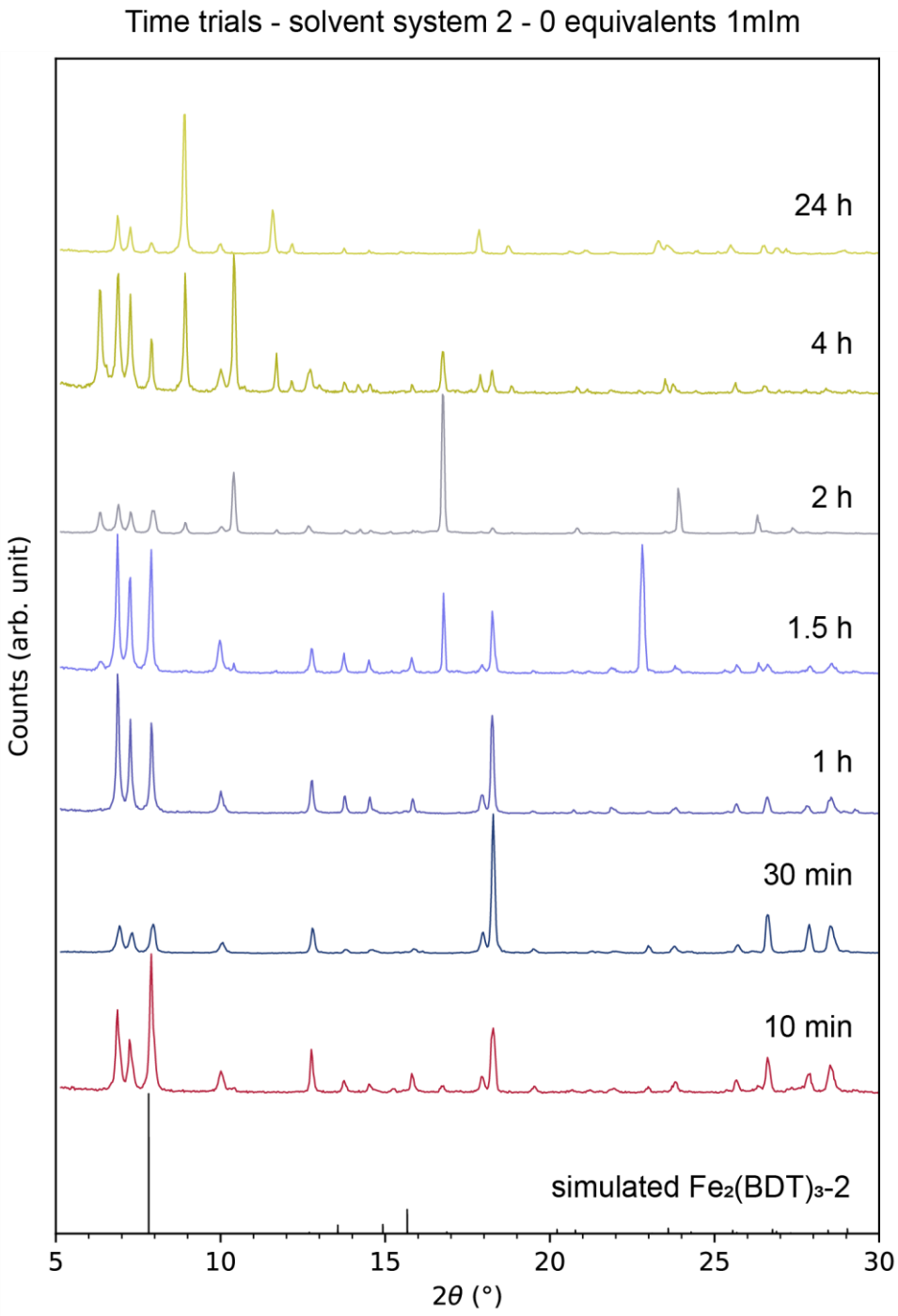

Figure 33. PXRD patterns of $Fe_2(BDT)_3$ syntheses in solvent system 2. 0 equivalents of 1-methyl imidazole added as a modulator at varied reaction times.

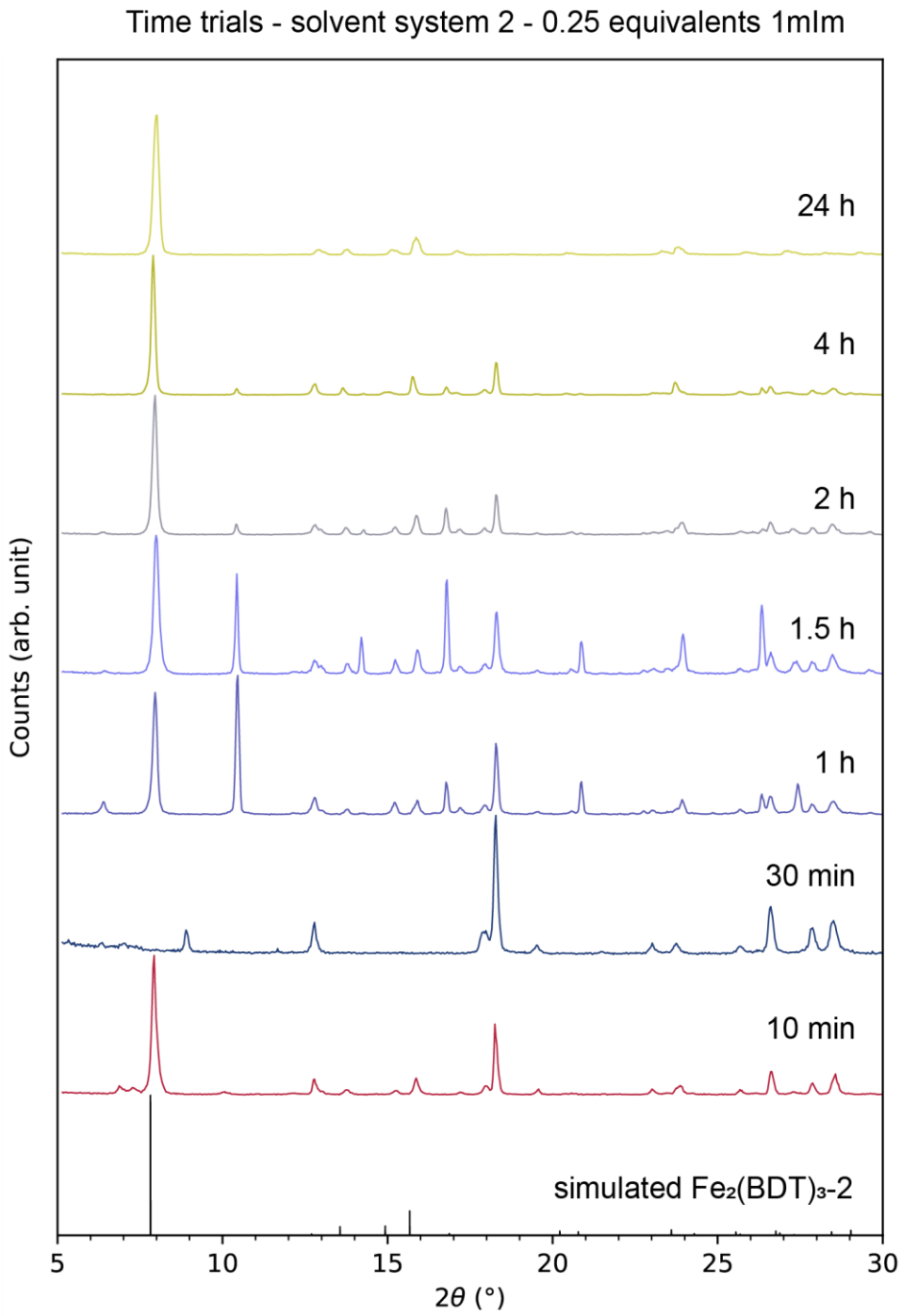

Figure 34. PXRD patterns of $Fe_2(BDT)_3$ syntheses in solvent system 2. 0.25 equivalents of 1-methyl imidazole added as a modulator at varied reaction times.

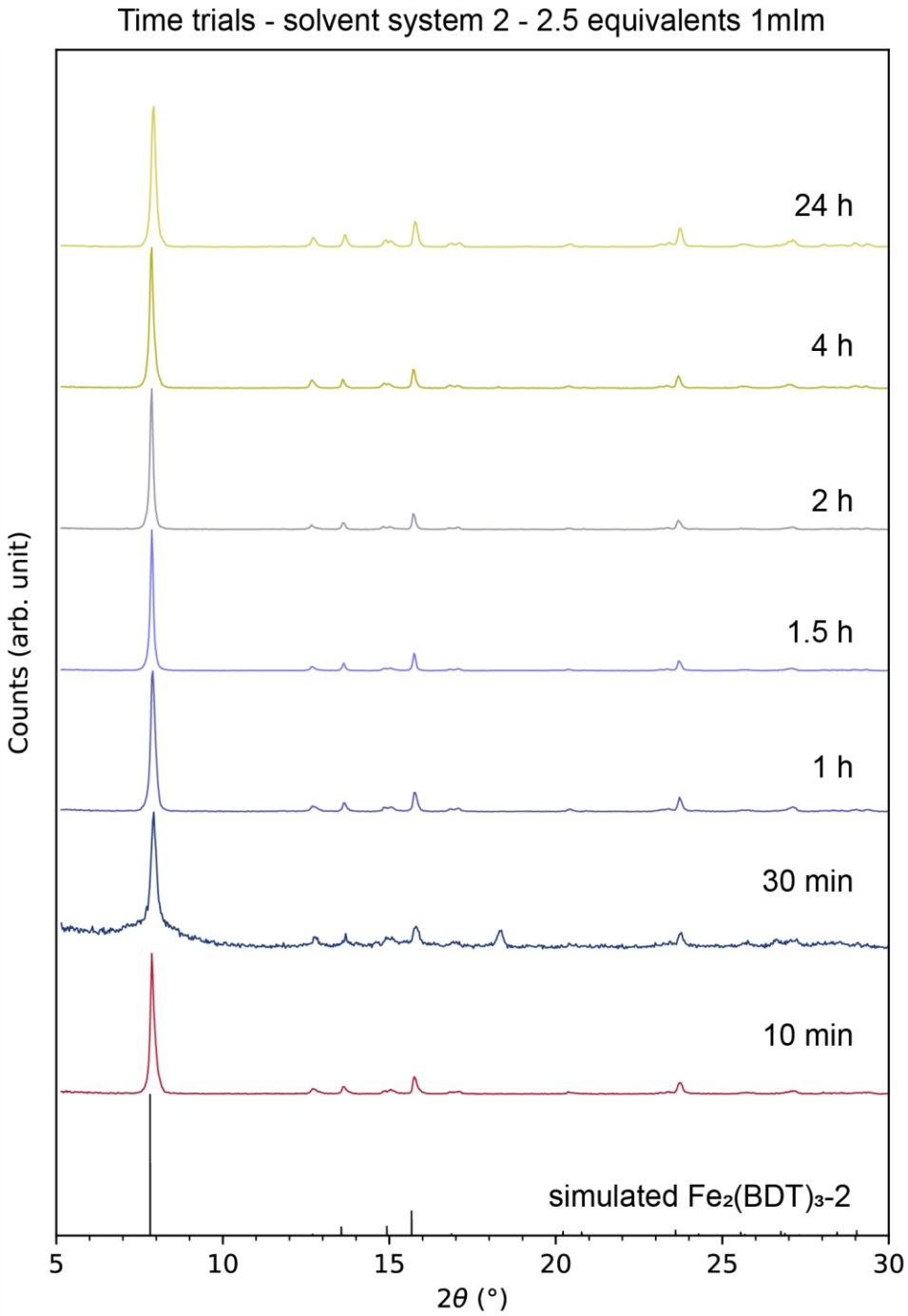

Figure 35. PXRD patterns of $Fe_2(BDT)_3$ syntheses in solvent system 2. 2.5 equivalents of 1-methyl imidazole added as a modulator at varied reaction times.

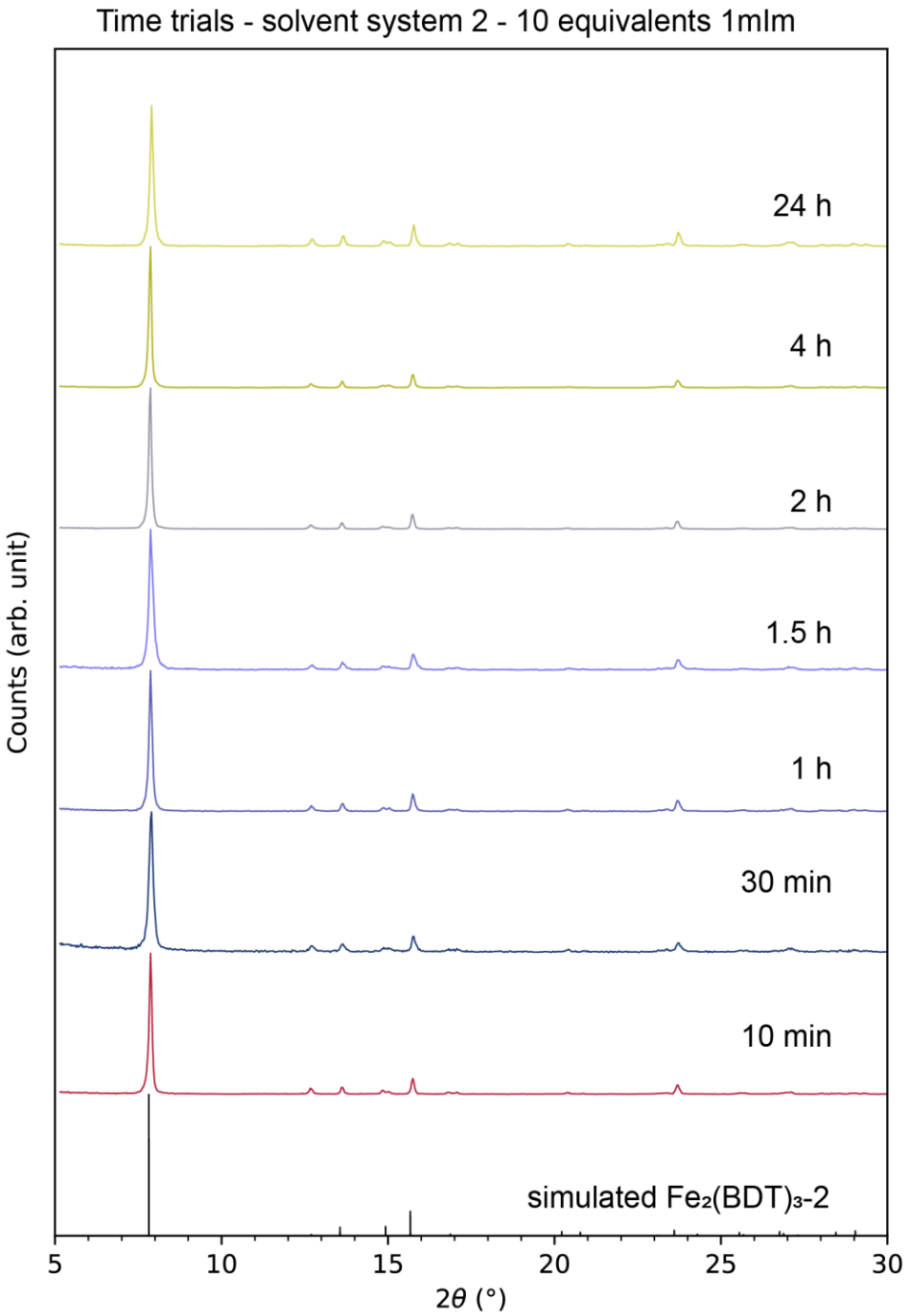

Figure 36. PXRD patterns of $Fe_2(BDT)_3$ syntheses in solvent system 2. 10 equivalents of 1-methyl imidazole added as a modulator at varied reaction times.

PXRD patterns of syntheses with varied iron precursor salts

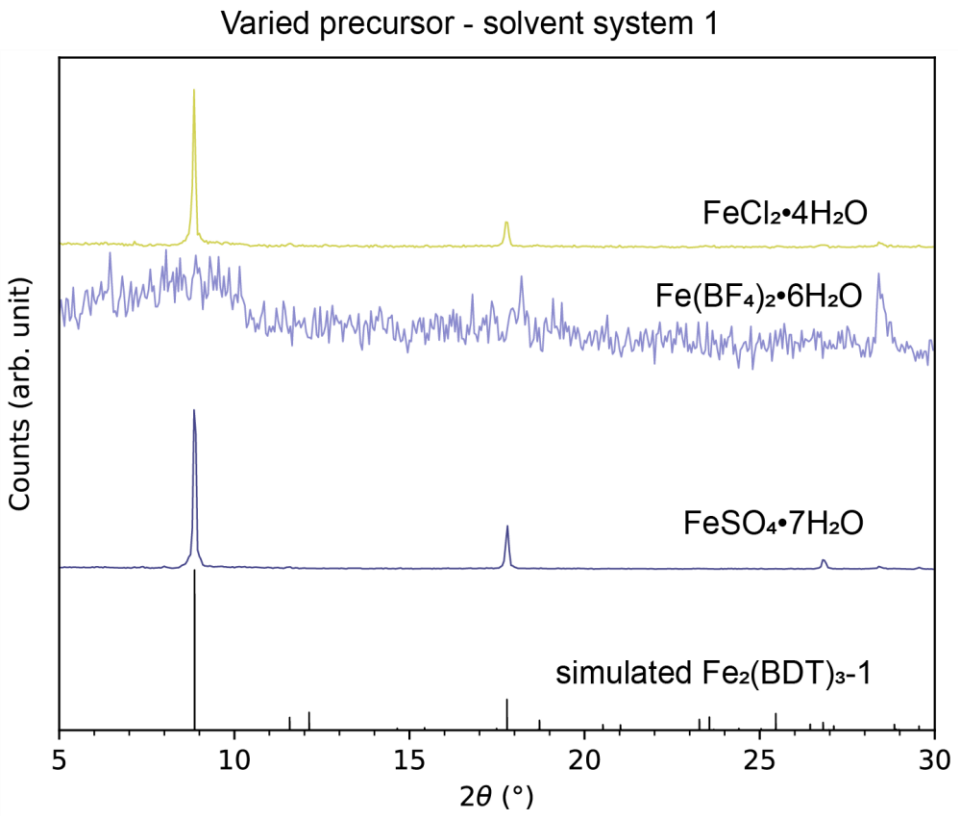

Figure 37. PXRD patterns of $Fe_2(BDT)_3$ syntheses in solvent system 1. Iron precursors used: $FeSO_4 \cdot 7H_2O$, $Fe(BF_4)_2 \cdot 6H_2O$, $FeCl_2 \cdot 4H_2O$

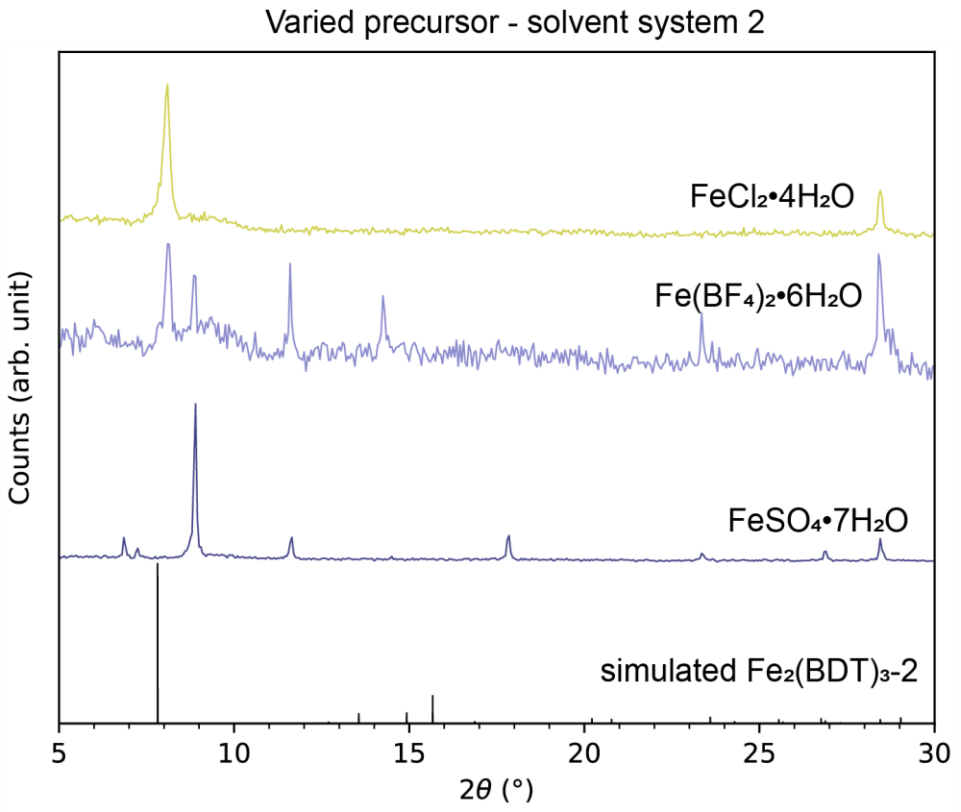

Figure 38. PXRD patterns of $Fe_2(BDT)_3$ syntheses in solvent system 2. Iron precursors used: $FeSO_4 \cdot 7H_2O$, $Fe(BF_4)_2 \cdot 6H_2O$, $FeCl_2 \cdot 4H_2O$

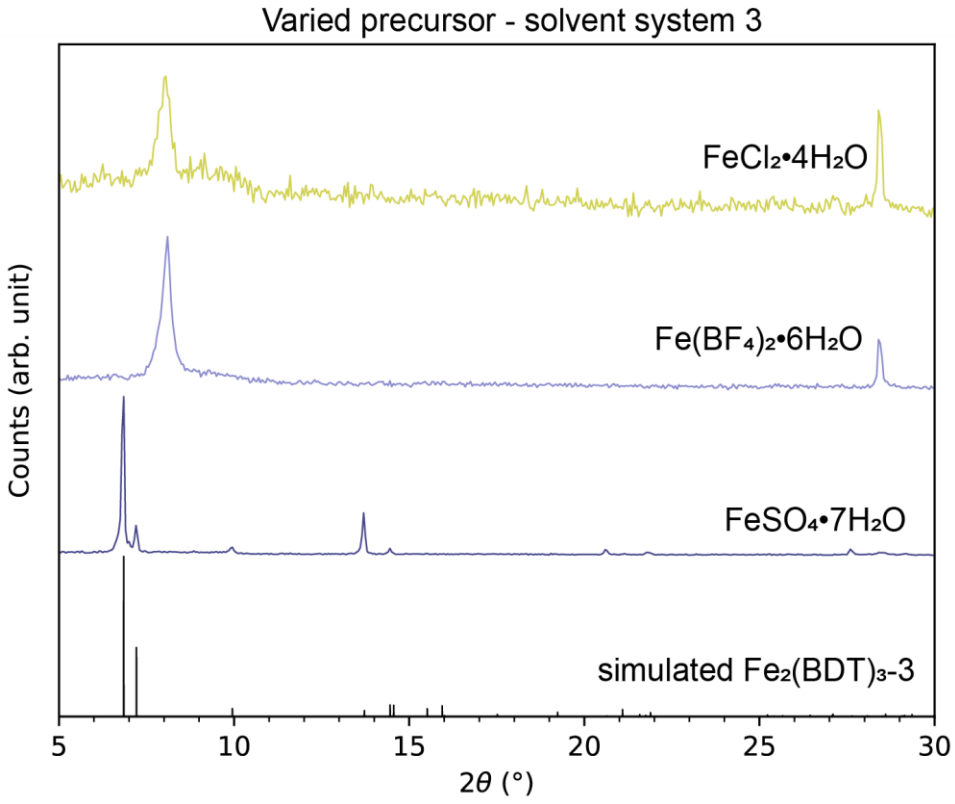

Figure 39. PXRD patterns of $Fe_2(BDT)_3$ syntheses in solvent system 1. Iron precursors used: $FeSO_4 \cdot 7H_2O$, $Fe(BF_4)_2 \cdot 6H_2O$, $FeCl_2 \cdot 4H_2O$

PXRD patterns of syntheses with varied modulator/solubilizing agent salts

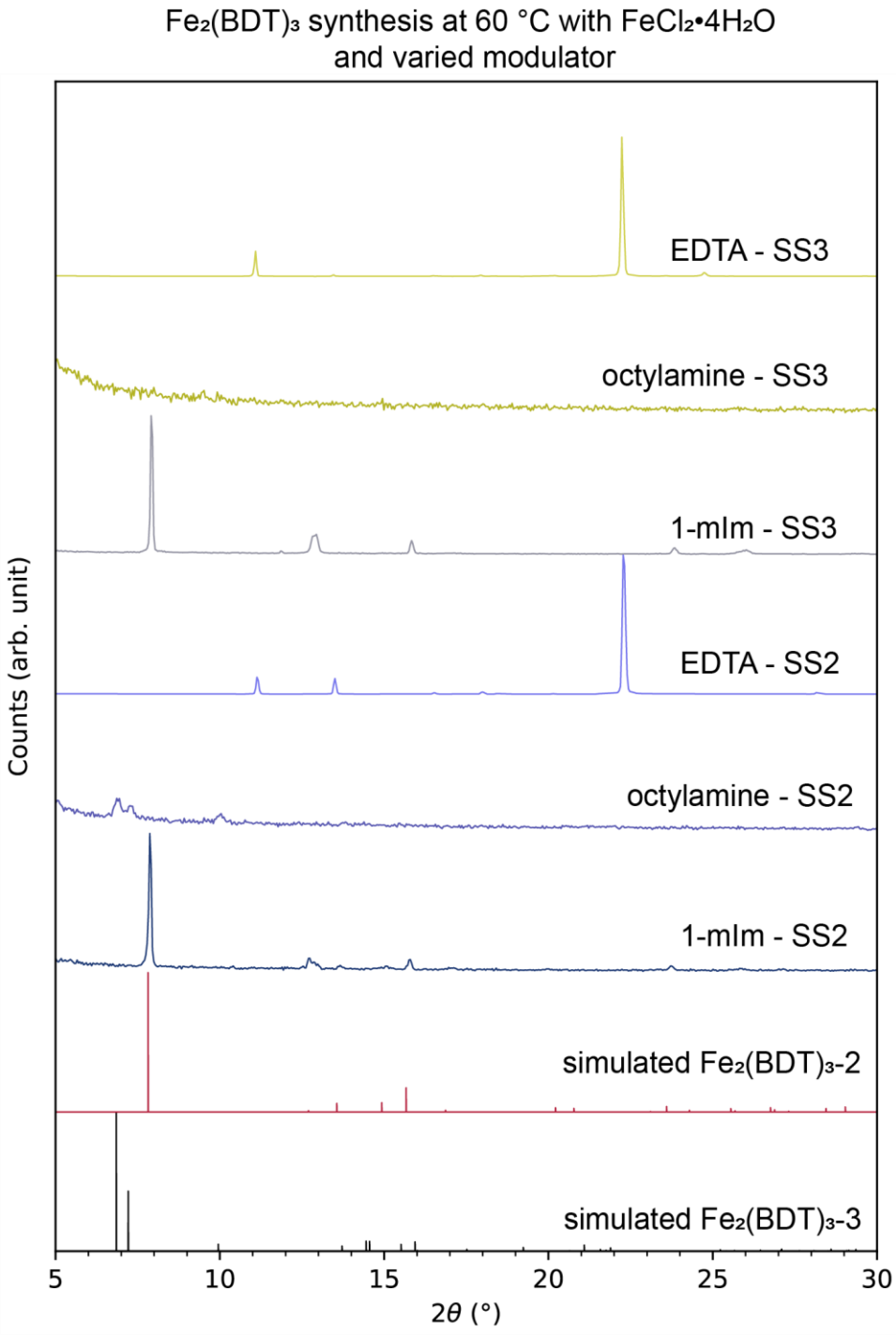

Figure 40. PXRD patterns of $Fe_2(BDT)_3$ syntheses in varied solvent systems with modulators 1-methyl imidazole, octylamine or EDTA. Reactions run at 60 ℃ with $FeCl_2 \cdot 4H_2O$ precursor

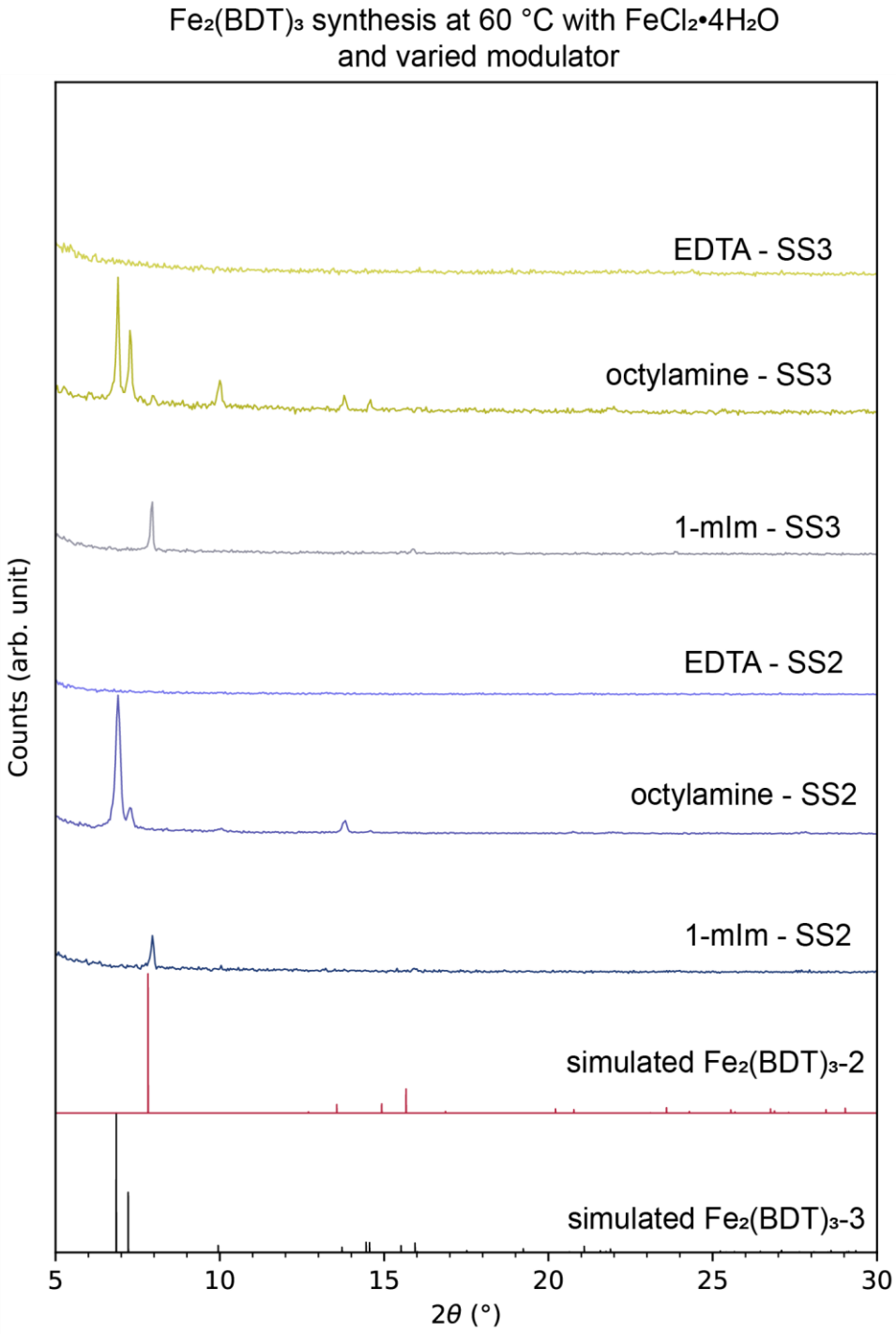

Figure 41. PXRD patterns of $Fe_2(BDT)_3$ syntheses in varied solvent systems with modulators 1-methyl imidazole, octylamine or EDTA. Reactions run at 120 °C with FeCl2·4H2O precursor

PXRD patterns of Methanol/Hexane Solvent mixtures

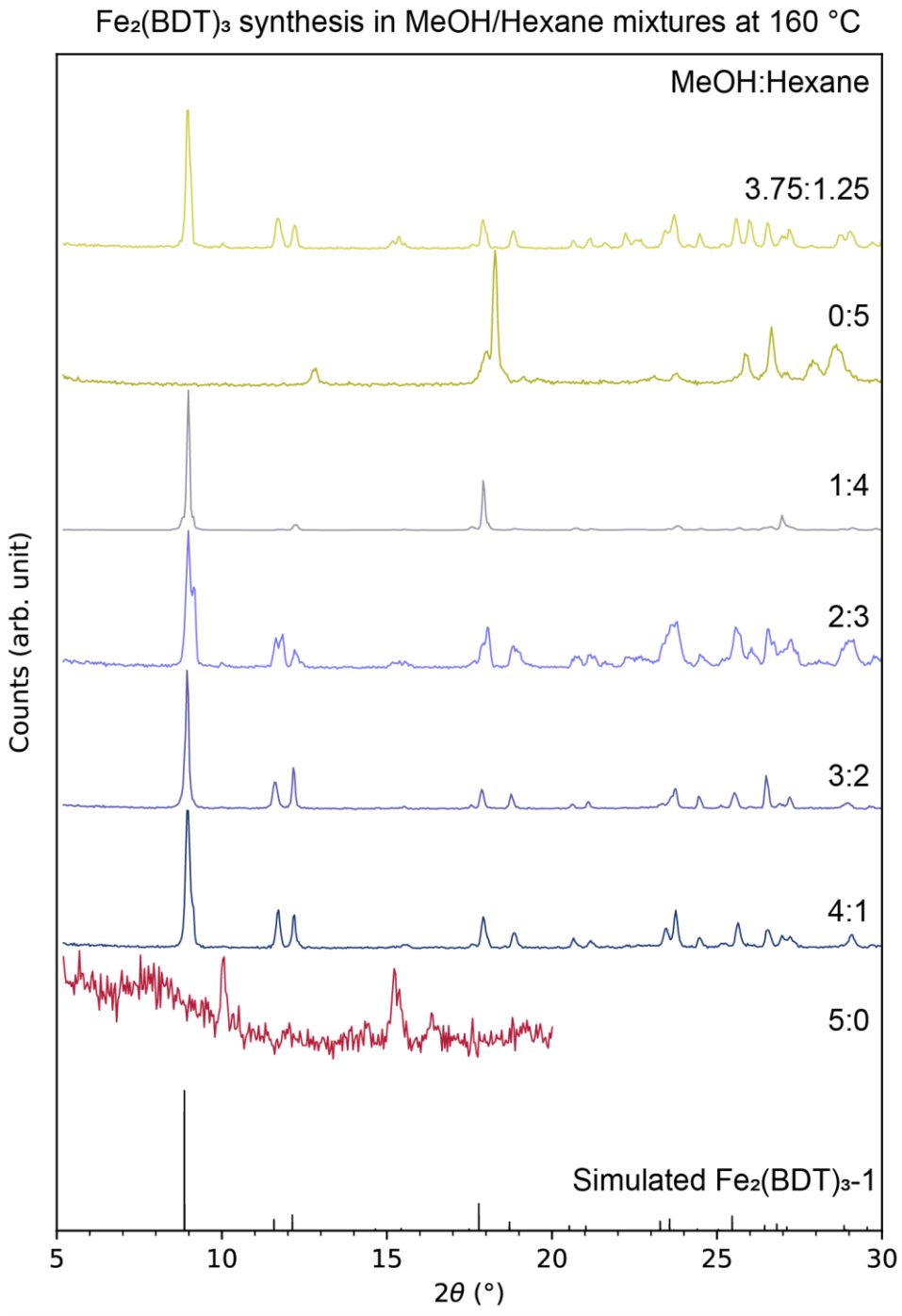

Figure 42. PXRD patterns of $Fe_2(BDT)_3$ syntheses in varied mixtures of methanol and hexane. Reactions run at 160 °C with $FeSO_4 \cdot 7H_2O$ precursor

SEM Images

SEM images of $Fe_2(BDT)_3$ particles with varied equivalents of 1-mIm

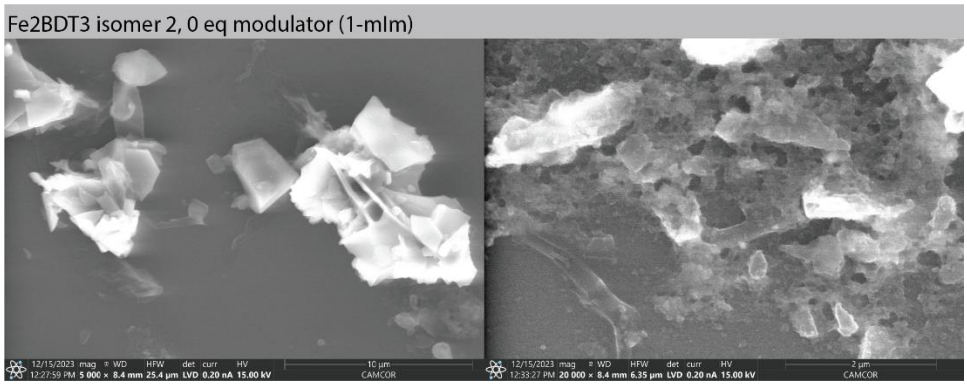

Figure 43. SEM images of $Fe_2(BDT)_3$ with 0 eq 1-mIm modulator

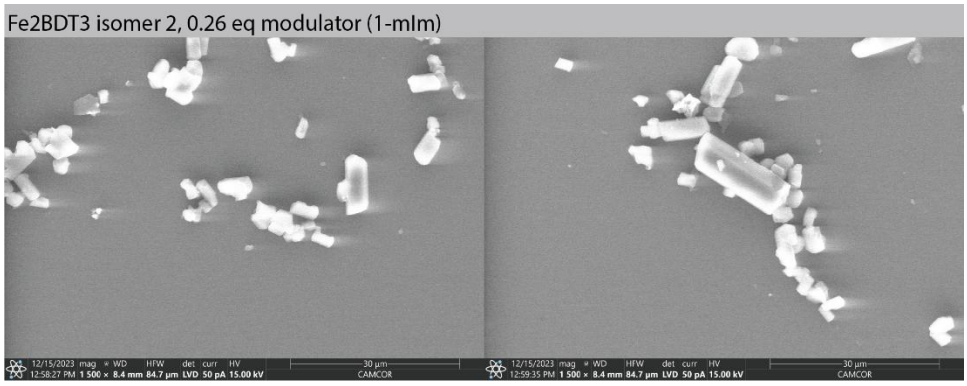

Figure 44. SEM images of $Fe_2(BDT)_3$ with 0.26 eq 1-mIm modulator

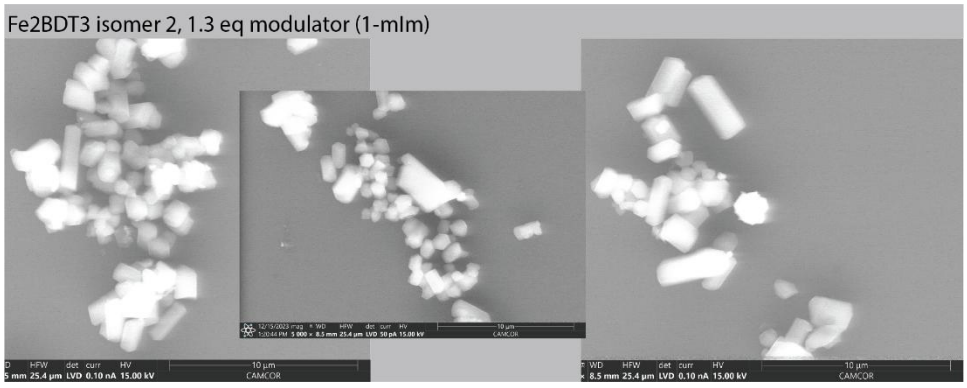

Figure 45. SEM images of $Fe_2(BDT)_3$ with 1.3 eq 1-mIm modulator

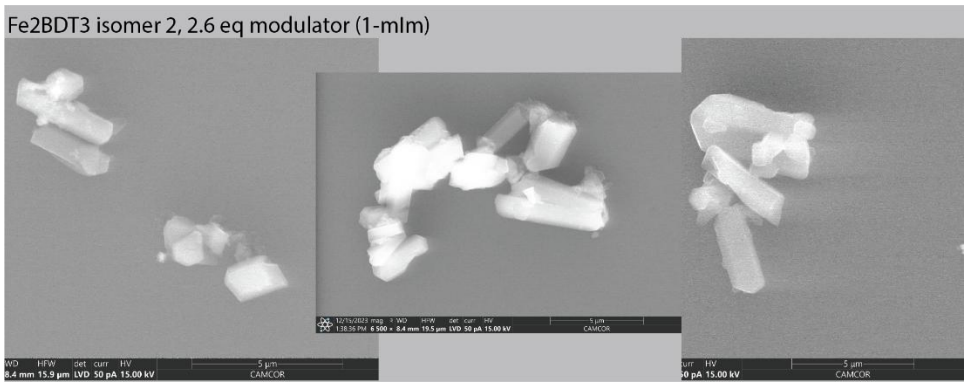

Figure 46. SEM images of $Fe_2(BDT)_3$ with 2.6 eq 1-mIm modulator

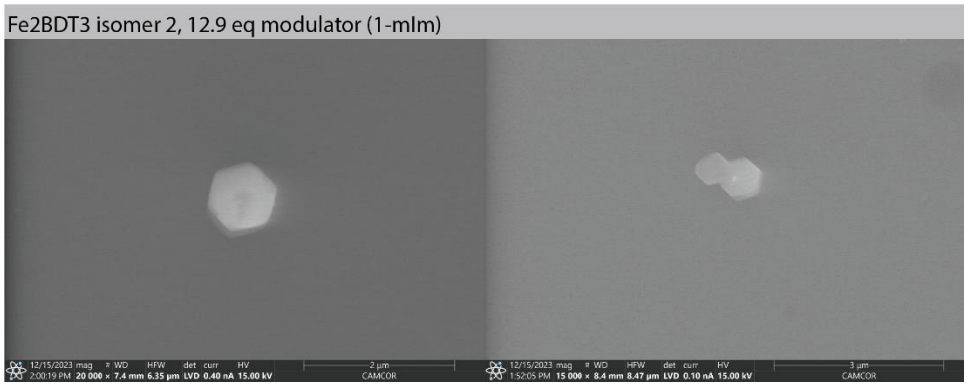

Figure 47. SEM images of $Fe_2(BDT)_3$ with 12.9 eq 1-mIm modulator

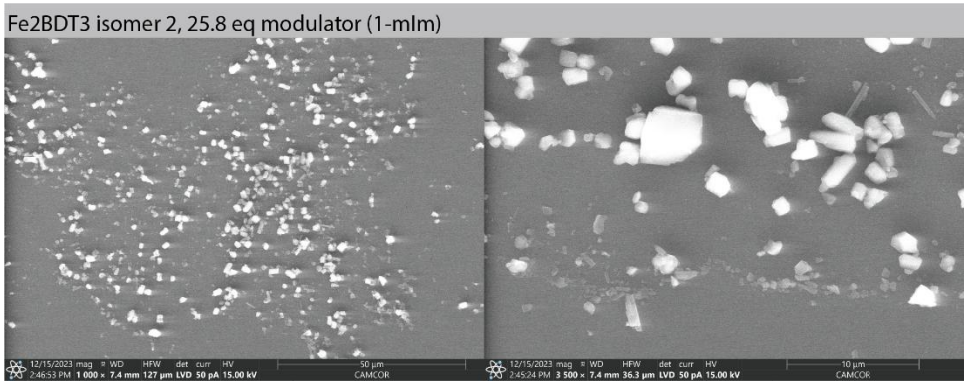

Figure 48. SEM images of $Fe_2(BDT)_3$ with 25.8 eq 1-mIm modulator

SEM images of $Fe_2(BDT)_3$-3 synthesized with octylamine

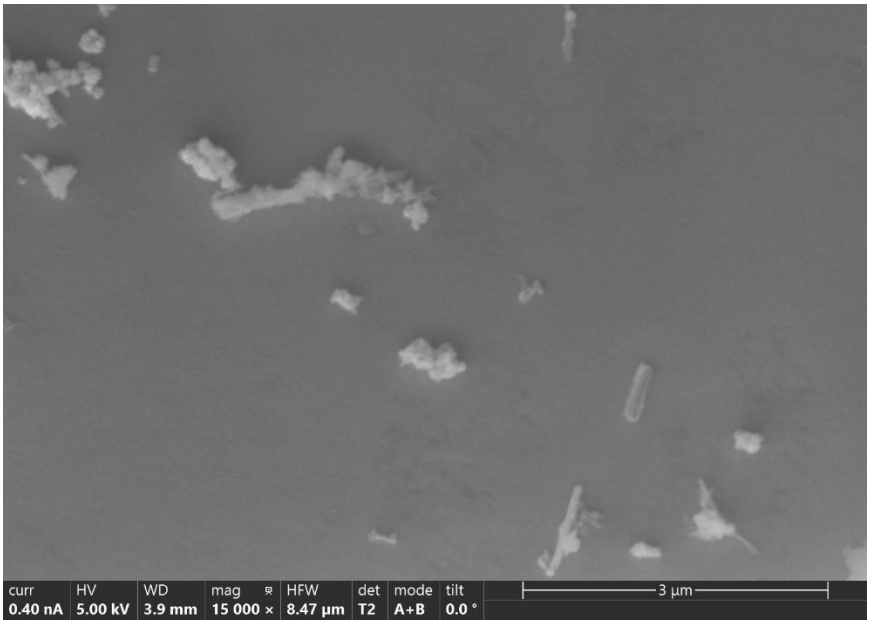

Figure 49. SEM images of $Fe_2(BDT)_3$ synthesized at 60 °C with octylamine as a modulator

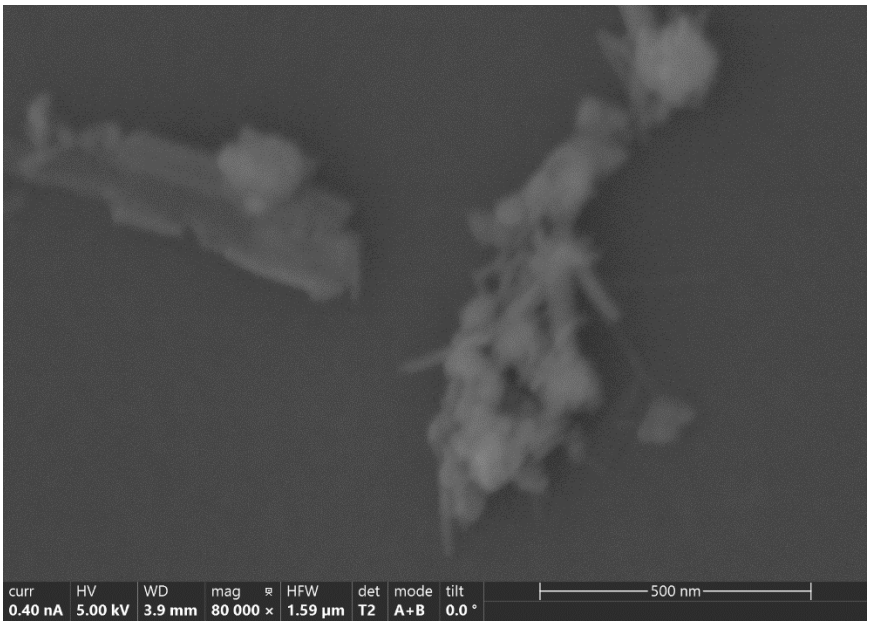

Figure 50. SEM images of $Fe_2(BDT)_3$ synthesized at 60 °C with octylamine as a modulator (2)

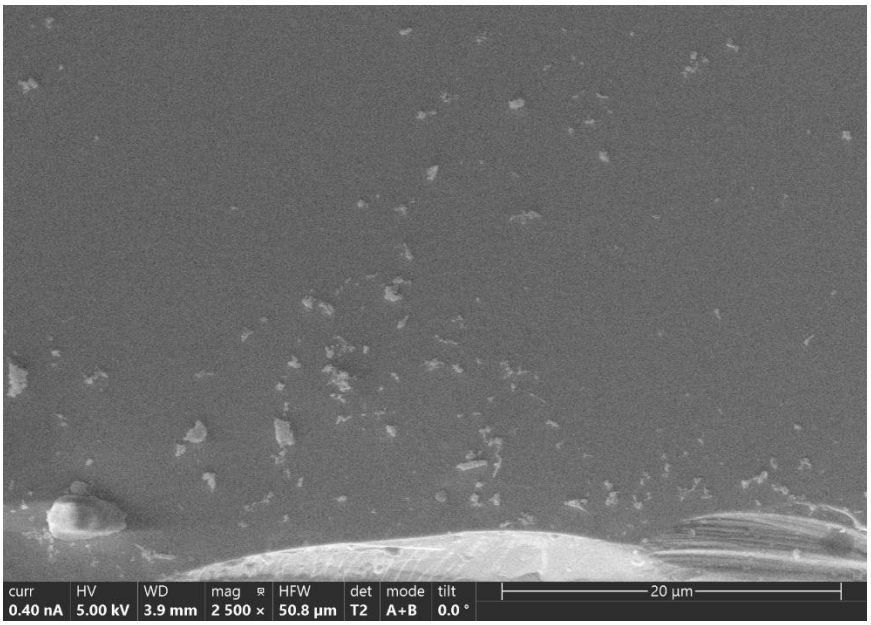

Figure 51. SEM images of $Fe_2(BDT)_3$ synthesized at 60 °C with octylamine as a modulator (3)

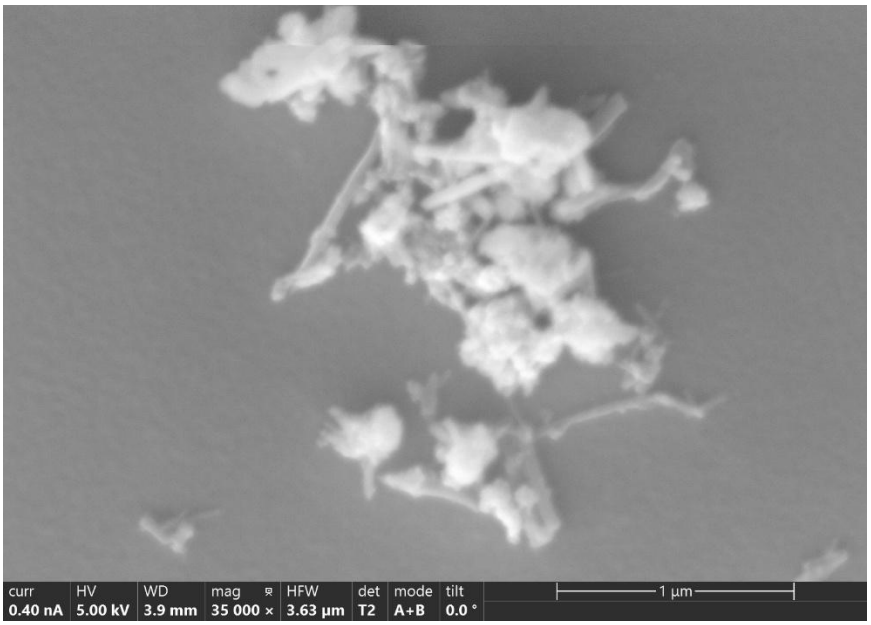

Figure 52. SEM images of $Fe_2(BDT)_3$ synthesized at 60 °C with octylamine as a modulator (4)

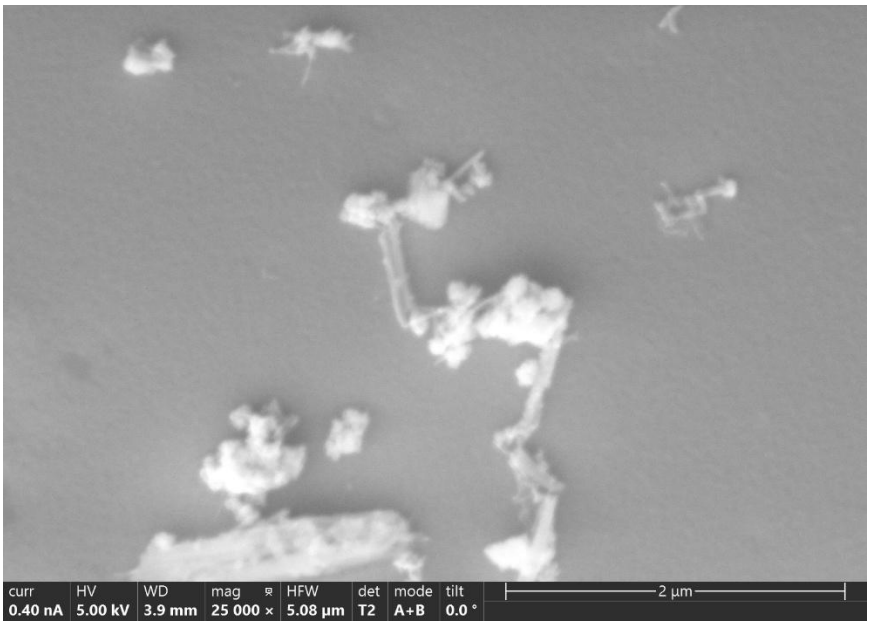

Figure 53. SEM images of $Fe_2(BDT)_3$ synthesized at 60 °C with octylamine as a modulator (5)

APPENDIX B

SUPPLEMENTARY INFORMATION FOR CHAPTER 3

Methods

Materials. All commercial chemicals were used as received unless stated otherwise. Titanium(IV) methoxide (95%, Sigma-Aldrich), 1,4-benzenedicarboxylic acid (terephthalic acid, Sigma-Aldrich), methanol (ACS grade, Fisher Scientific), N,N-dimethylformamide (DMF, ACS grade, Fisher Scientific), benzoic acid (JT Baker).

Characterization. Sample purity was verified by powder X-Ray diffraction (PXRD) with a Bruker D2 Phaser benchtop diffractometer and infrared spectroscopy (IR) using a Bruker Alpha II compact IR with an ATR attachment in a N2 glovebox. UV-vis-NIR spectra were collected on an Agilent Cary 5000 UV-Vis-NIR spectrophotometer in the range of 200-2000 nm and all samples were collected with a baseline solvent mixture matching the sample medium. Gaussian fittings were performed in Igor Pro Version 6.37 using the Multipeak Fitting 2 package.

Synthesis

In a nitrogen filled glovebox, $Ti(OMe)_4$ was added to 4 test tubes sealed with a septum. To oven-dried 50 mL schlenk flasks was added terepthalic acid and the corresponding amount of benzoic acid as a modulator. 15 mL DMF and 5 mL MeOH was added to each schlenk flask as well as a stir bar. The flasks were sealed all reaction mixtures and solids were moved out of the box. In a fume hood, the schlenk flasks were placed under nitrogen flow from a schlenk line and 37.5 μL sparged ultrapure water was added to each. The flasks were equipped with oven-dried condensers. The mixture was stirred at 110 °C for 30 min and the solids appeared to be fully dissolved before $Ti(OMe)_4$ was added to each under nitrogen flow. The reactions were refluxed for 2 hours before 20 mL cold DMF was added to quench the reactions. The reactions were centrifuged and the collected solids were washed 2x with cold DMF (about 30 mL) and 2x with

cold MeOH (about 20 mL).

Powder x-ray diffraction patterns of MIL-125 materials

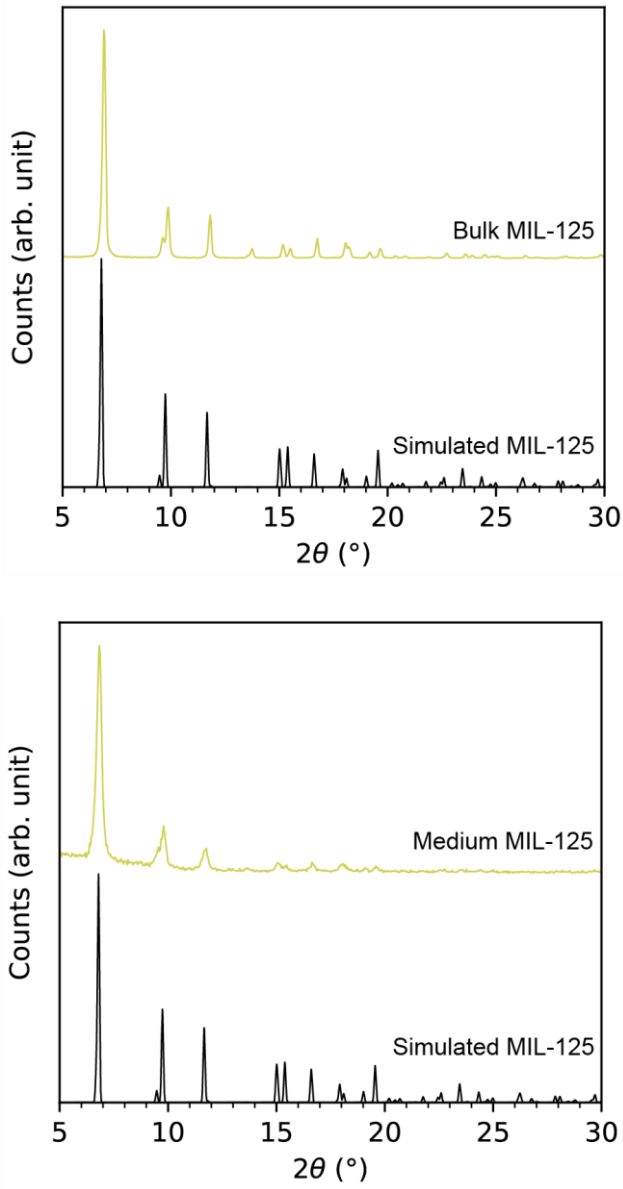

Figure 54. Powder x-ray diffraction patterns of MIL-125

SEM images of MIL-125 particles

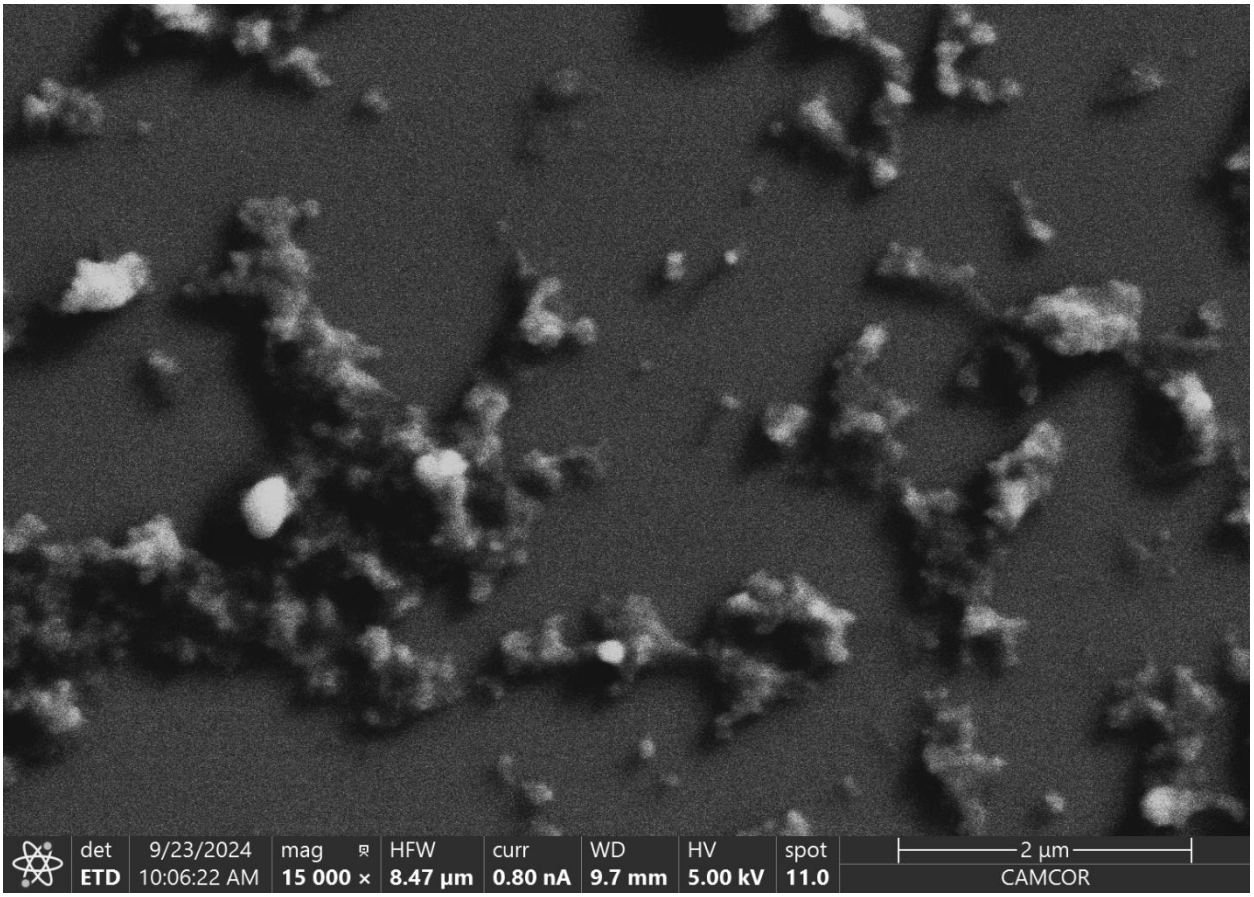

Figure 55. SEM image of medium MIL-125 nanoparticles

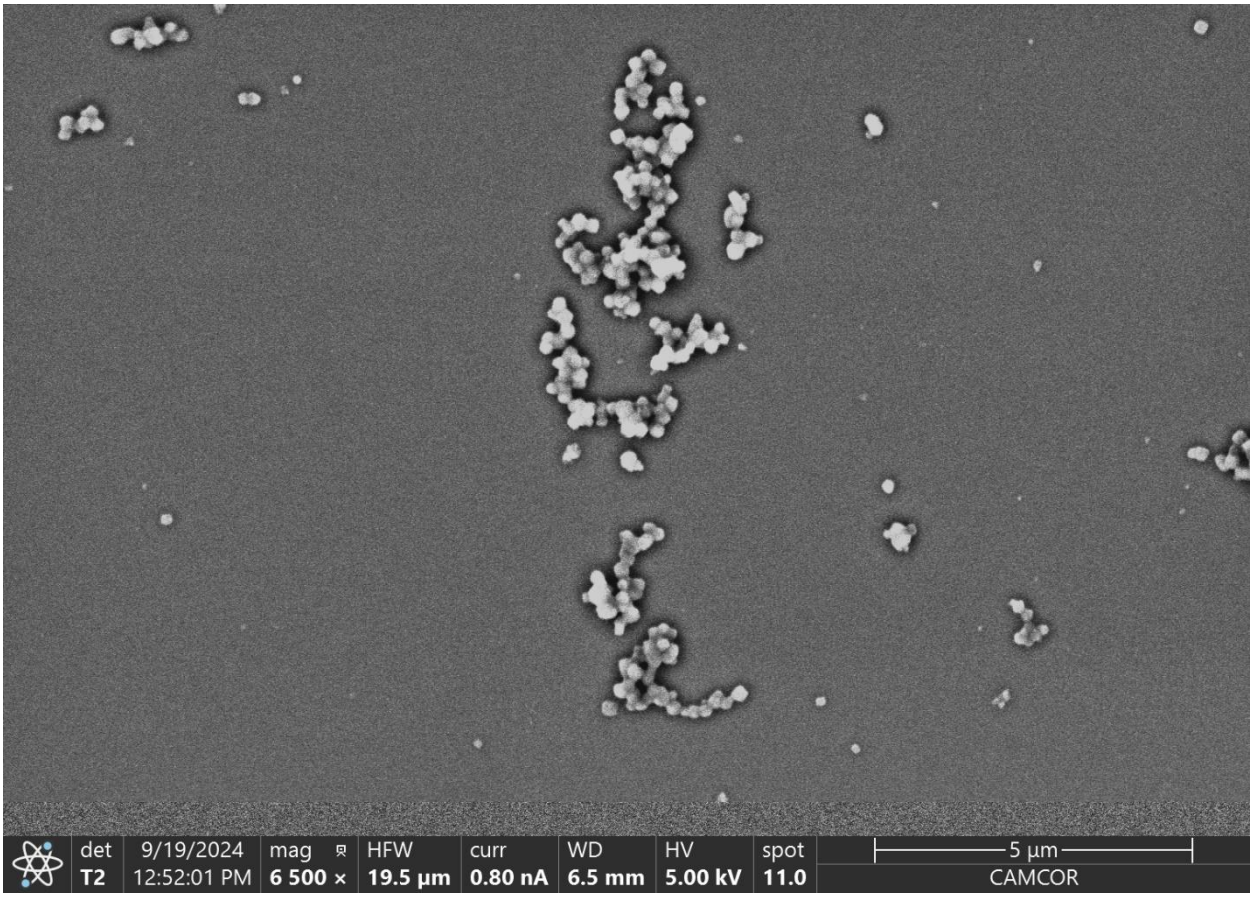

Figure 56. SEM image of large MIL-125 nanoparticles

Spectra of photodoping experiments in NMR tubes

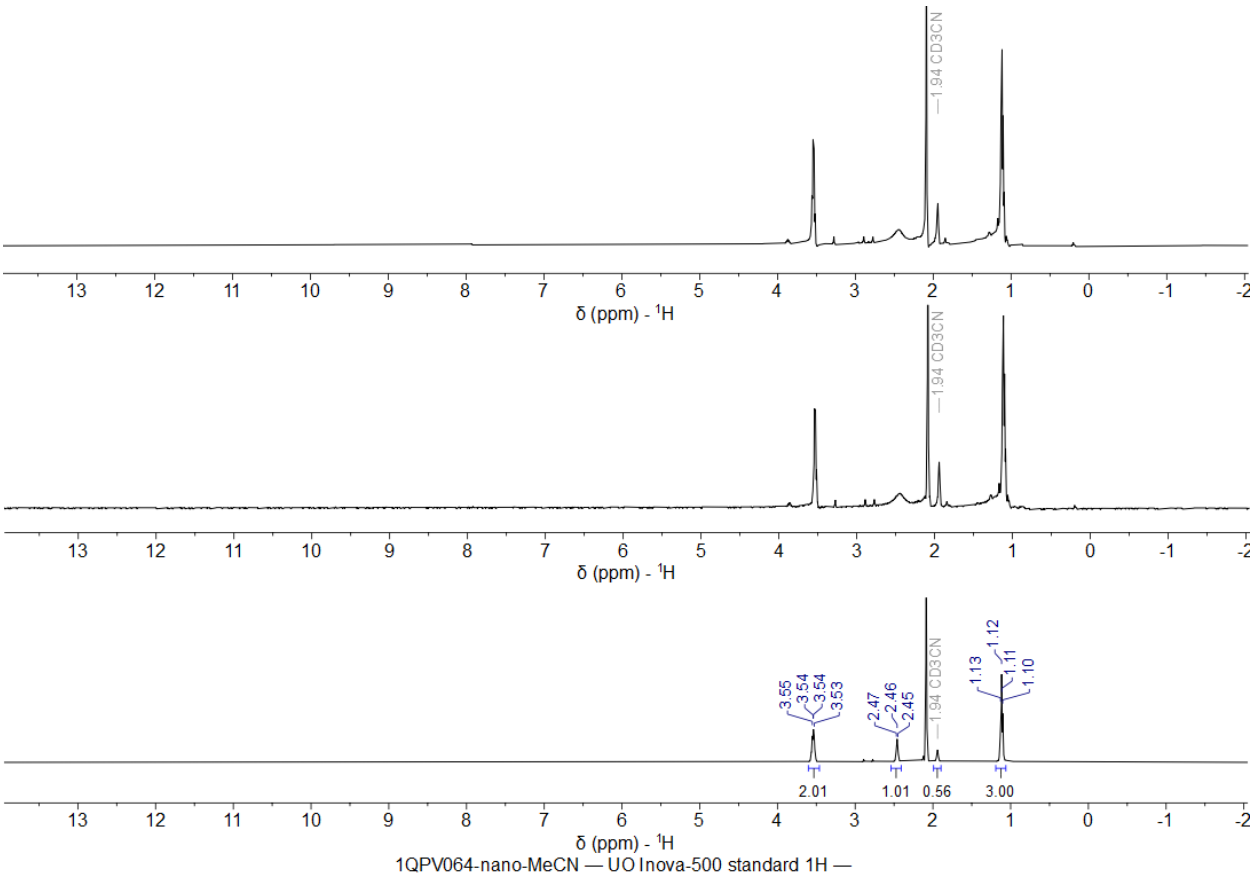

Figure 57. Stacked NMR spectra of Pre- and Post-photodoping experiments of 32 nm MIL-125with ethanol and acetone. Bottom to top: pre-photodopoing, 20 hours, 36 hours of photodoping.

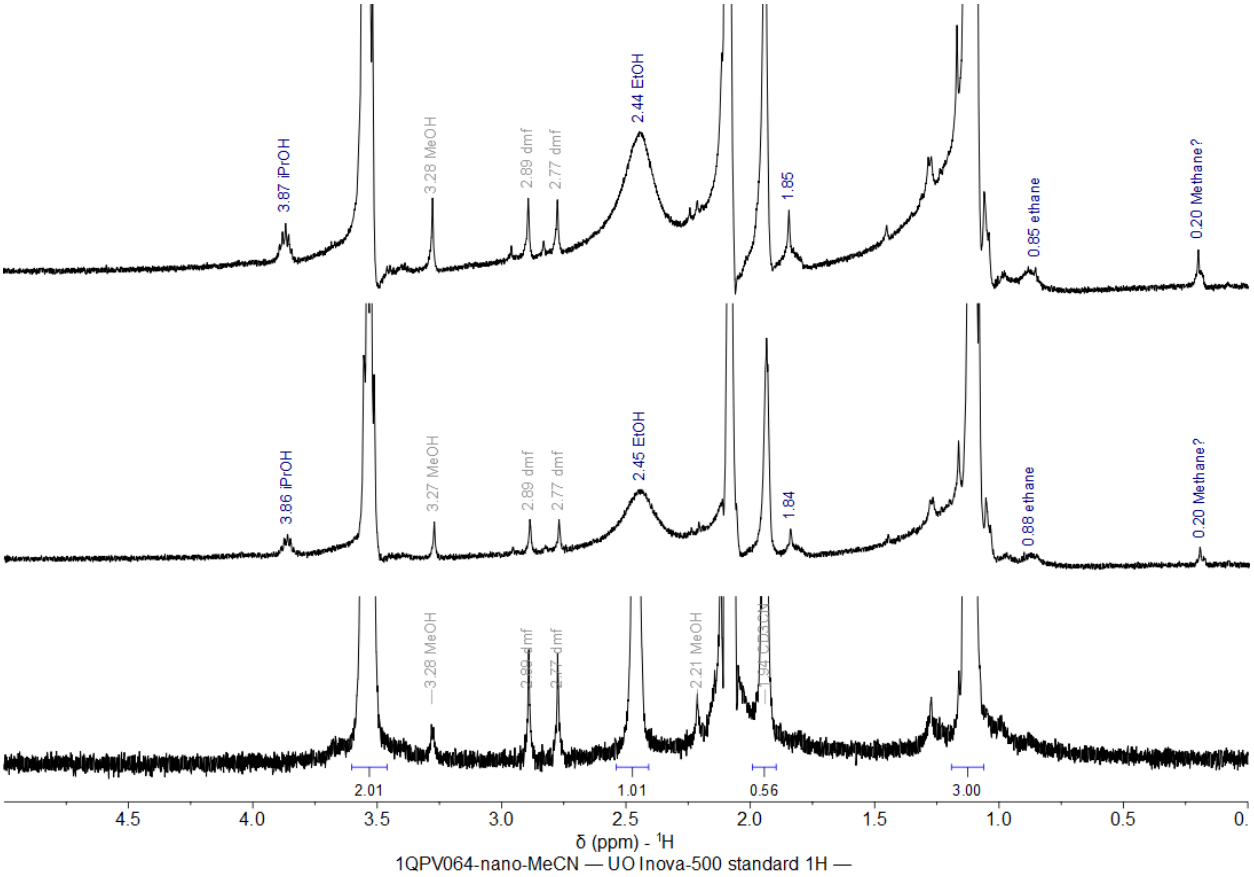

Figure 58. Stacked NMR spectra of Pre- and Post-photodoping experiments of 32 nm MIL-125 with ethanol and acetone. Scaled from 5 to 0 ppm. Bottom to top: pre-photodopoing, 20 hours, 36 hours of photodoping.

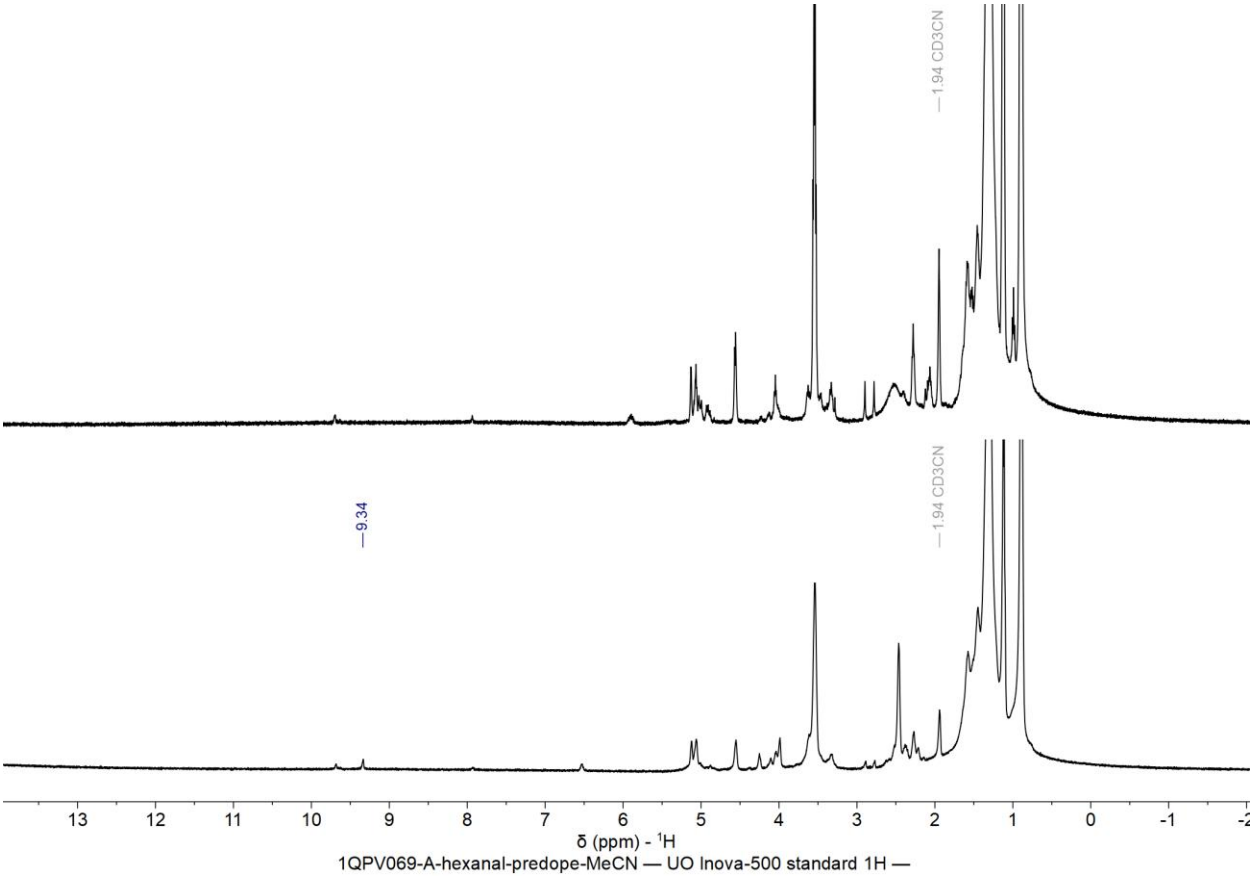

Figure 59. NMR of pre- and post-photodoping (96 h) of 32 nm MIL-125 with hexanal with ethanol. NMR in MeCN-d3

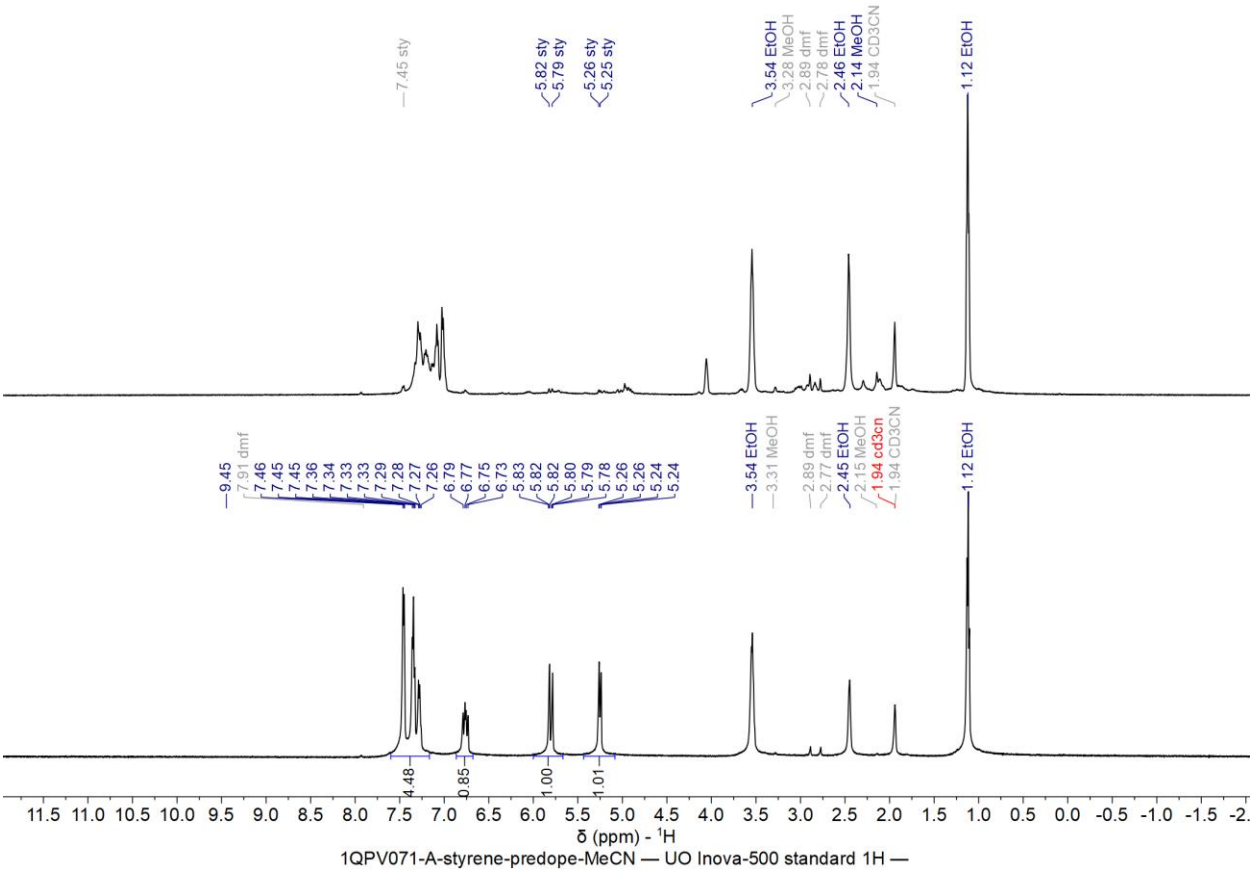

Figure 60. NMR of pre- and post-photodoping (96 h) of 32 nm MIL-125 with styrene with ethanol. NMR in MeCN-d3

Photos of photodoped materials

Picture of 18 nm MIL-125 particles after photodoping before centrifugation

Figure 61. Photo of 18 nm MIL-125 in acetonitrile with decamethyl ferrocenium tetrafluoroborate in solution after being photodoped.

Picture of 32 nm MIL-125 particles in NMR tube after settling

Figure 62. Photo of 32 nm MIL-125 particles in a quartz teflon-capped NMR tube after being photodoped and allowed to settle.

GCMS traces of various unsaturated organics

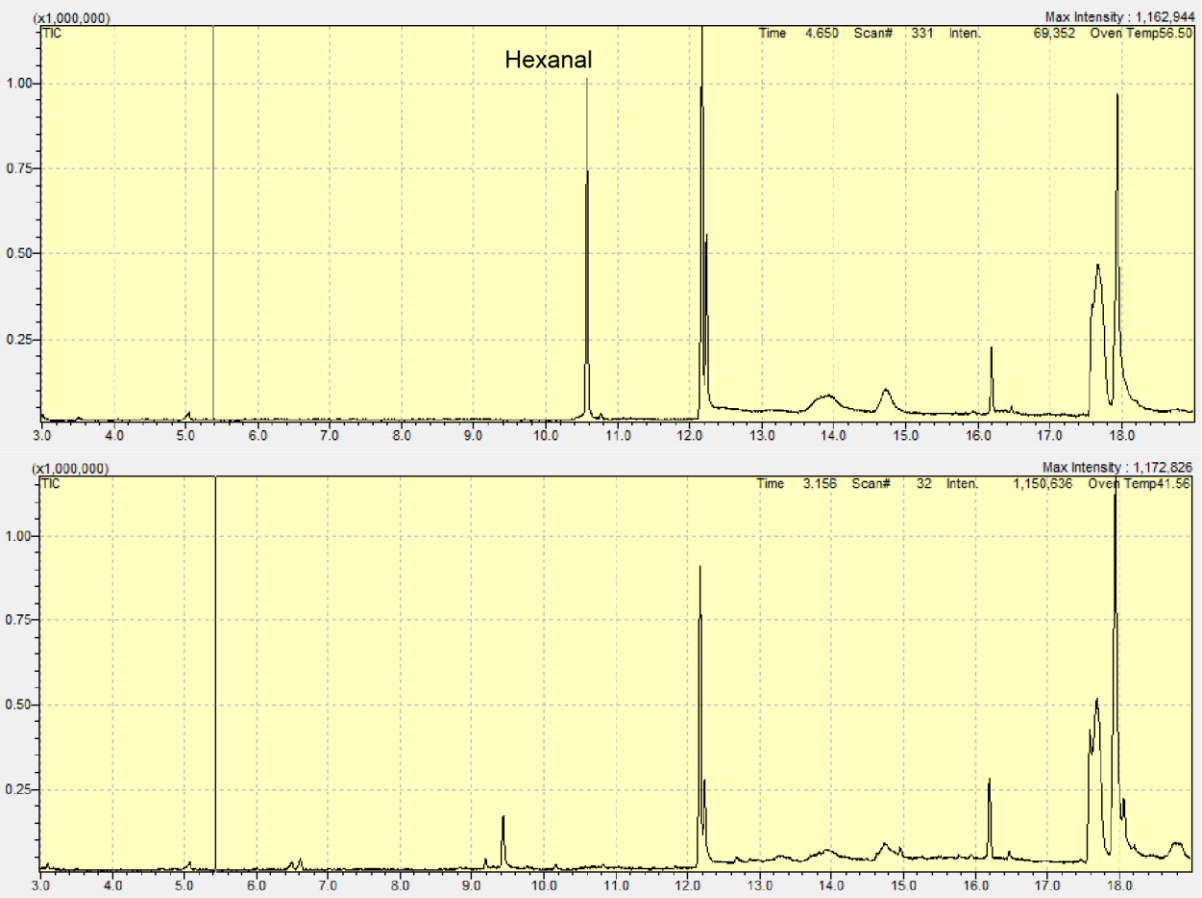

Figure 63. GCMS trace of pure hexanal (top) and the post reaction mixture (bottom) after 32 nm MIL-125 photodoping reaction

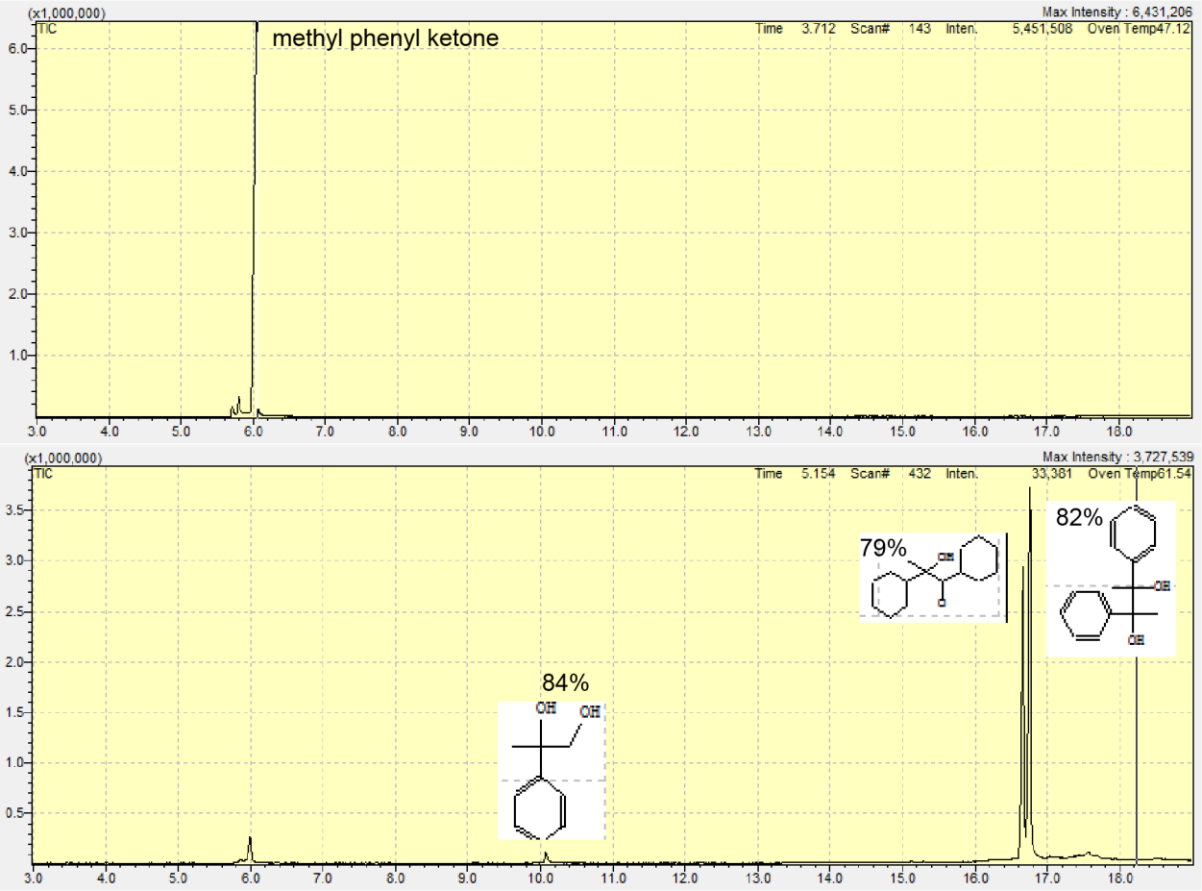

Figure 64. GCMS trace of pure methyl phenyl ketone (top) and the post reaction mixture (bottom) after 32 nm MIL-125 photodoping reaction. Database-matched structure and similarity in percent are overlaid at peak positions.

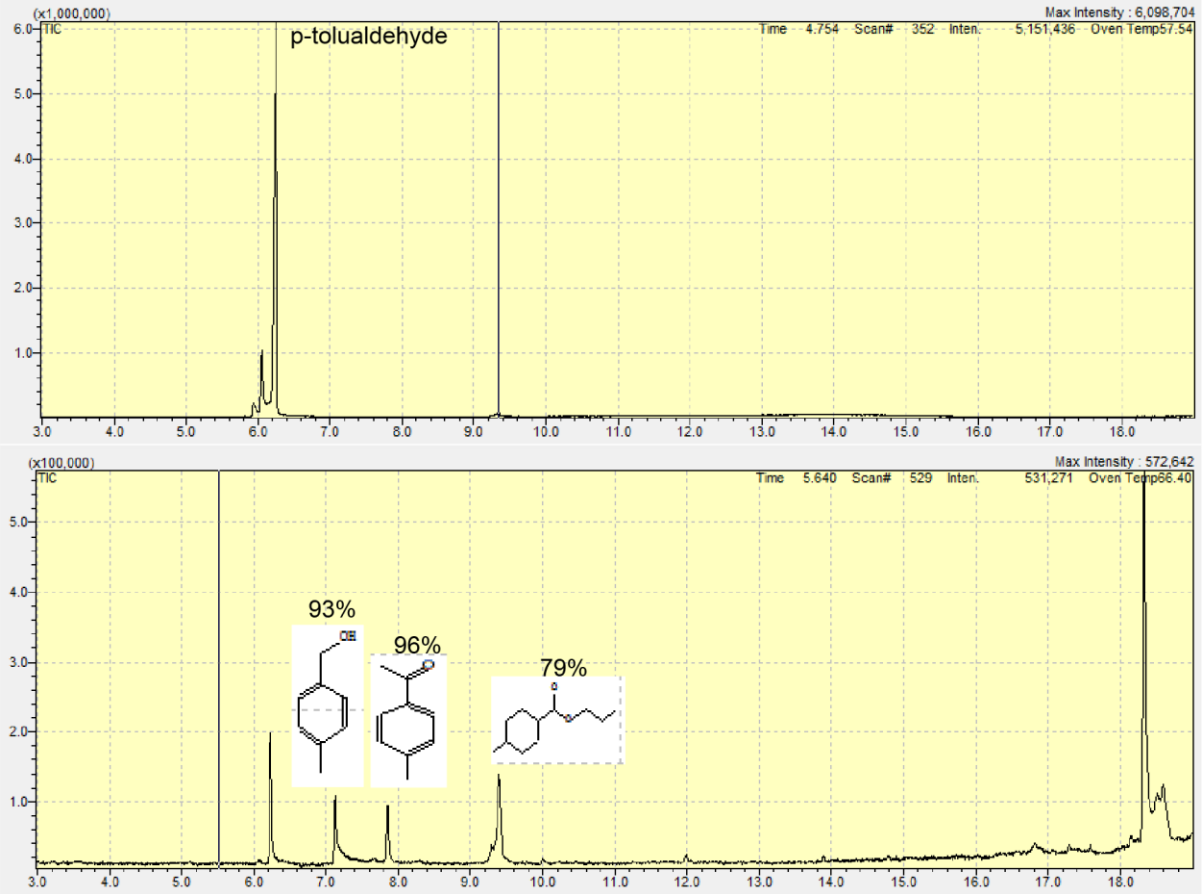

Figure 65. GCMS trace of pure hexanal (top) and the post reaction mixture (bottom) after 32 nm MIL-125 photodoping reaction. Database-matched structure and similarity in percent are overlaid at peak positions.

Discussion on GCMS data

Although the GCMS data collected does not present a clean transfer hydrogenation, it is evident that the starting material introduced into the reaction mixture is being consumed. Given the acidic nature of the reaction mixture, it is unsurprising that unsaturated ketones or aldehydes are subject to reaction, hence there being limited conclusions that can be drawn from this data. There is some evidence, however, given similarity matched structures that there is some hydrogenation of unsaturated starting materials. The disappearance of the hexanal aldehyde proton in the NMR is matched with the disappearance of the starting material in the GCMS trace.

APPENDIX C

SUPPLEMENTARY INFORMATION FOR CHAPTER 4

General:

Materials: All commercial chemicals were used as received unless stated otherwise. Benzimidazole (99%, Alfa Aesar), Methyl iodide (99%, stabilized with copper, Thermo Scientific), Potassium Carbonate (99%, Fisher Chemical), Sodium tert-butoxide(97%, Alfa Aesar)

Carbon disulfide (99.9+%, Alfa Aesar) was dried over commercially available dessicant (Drierite) in a Schlenk flask under nitrogen for several days. With standard Schlenk technique, the carbon disulfide was distilled in inert atmosphere and degassed with freeze-pump-thaw cycles 3 times. The carbon disulfide was stored in a nitrogen-filled glovebox in a Schlenk flask equipped with a teflon tap.

Synthetic manipulations were carried out under inert atmosphere unless otherwise specified.

Computational:

Avogadro 1.100.0 was utilized for modeling and MO visualization. Orca 6.0.1 and 6.1.0 were used for calculation of geometries, orbitals, energies and atomic parameters. DFT theory with the B3LYP functional was used for all structure analysis with Def2-TZVP basis sets employed for all atoms except the heteroatoms at the core and the metal atoms, which utilized Def2-TZVPPD (example script below.) Orca's internal wavefunction file (.wfn) generator (orca_2aim) was used to produce .wfn files from completed calculations to be used in atoms-in-molecules (AIM) analysis. AIMALL software was used with produced .wfn files to calculate (3, -3) and (3, -1) critical points, which were then used to evaluate delocalization index. Multiwfn was also used to calculate (3, -3) and (3, -1) critical points from .wfn files and reported AIM electron density, spin density and electron localization function (ELF) values were extracted. ChimeraX was used for electron and

spin density visualization. Electrostatic potential maps were visualized with ChimeraX by mapping generated ESP values on electron density maps. The appropriate isosurface plotting values and electrostatic potential ranges were chosen to stay consistent between all models to construct reasonable and interpretable comparisons. Orca 6.1.0 was used to calculate chemical shift values for nucleus-independent chemical shift (NICS) analysis with tzhe B3LYP functional and Def2-TZVP basis set for all atoms except the metal centers and sulfur or oxygen which used Def2-TZVP. The modeled system was arranged to place the ring system in the x-y plane so that the dummy atom could be iterated across varied heights of the z-axis in a grid with spacing of 0.2 Å between points.

Experimental:

Synthesis of N,N'-dimethyl benzimidazolium iodide: Based off of literature procedures.[183–185] In a nitrogen-filled glovebox*, to a 6 mL Teflon capped culture tube was added benzimidazole (300 mg, 2.540 mmol, 1 eq.) and K_2CO_3 (386 mg, 2.793 mmol, 1.1 eq.) and a stir bar. MeCN (3 mL) was added and the mixture was stirred for 2 h. Methyl iodide (1.14 mL, 15.23 mmol, 6 eq.) was added. The Tube was sealed with a Teflon-lined cap and removed from the glovebox. The reaction was heated at 105 C for 3 days. The reaction was allowed to cool to room temperature before being uncapped in ambient conditions and concentrated under vacuum. The crude product was taken up in methanol and filtered through celite to remove salts. The filtered solution was concentrated under vacuum to afford a brown solid. The solid was suspended in ethyl acetate and heated gently forming an off-white suspension in an orange/brown solution. The suspension was filtered and the solid was washed several times with ethyl acetate to afford a white powder**.

1H NMR (500 MHz, DMSO-*d*6) δ 9.63 (s, 1H) 8.02 (dd, *J* = 6.2, 3.1 Hz, 2H), 7.71 (dd, *J* =

6.3, 3.1 Hz, 2H) 4.08 (s, 6H).

*Synthesis prepared under inert conditions in attempt to minimize what was hypothesized to be the oxidized form of the product, imidazolidinone.

**If needed, a heated recrystallization in ethanol afforded a purer product at the expense of yield.

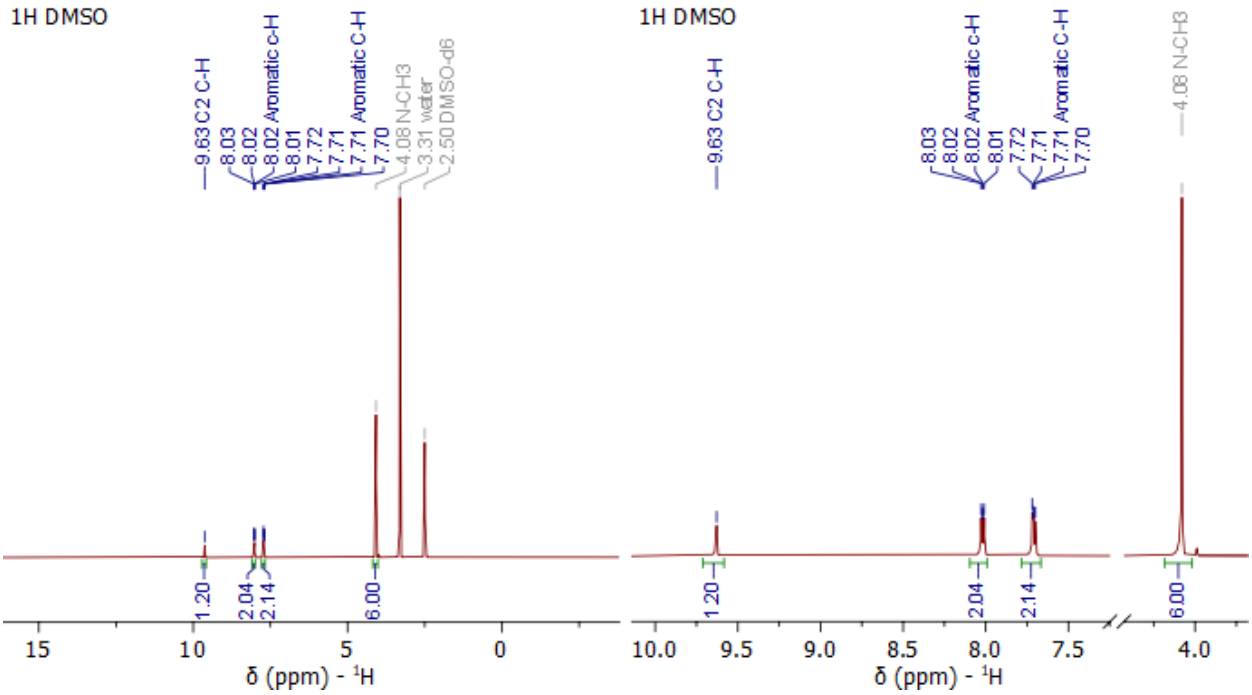

Figure 66. ^{1}H NMR spectrum of N,N'-dimethyl benzimidazole. Left, full spectrum from -2.5 to 15.5 ppm. Right, enlarged spectrum.

Synthesis of dimethyl benzimidazole dithiocarboxylate: Modified from literature procedures. In a nitrogen-filled glovebox, N,N'-dimethyl benzimidazolium iodide (200 mg, 0.732 mmol, 1 eq) and sodium tert-butoxide (140.65 mg, 1.4635 mmol, 2 eq.) were added to a 6 mL culture tube with a teflon-lined cap. THF (3 mL) was added with a stir bar and the mixture was stirred at room temperature overnight. Carbon disulfide (176 uL, 2.927 mmol, 4 eq.) was added via a micropipet. The mixture turned a dark red color. The mixture was stirred for 2 hours before being concentrated under vacuum. The precipitate was washed with a small amount of fresh THF and

diethyl ether. A pink solid was collected. ^{1}H NMR (500 MHz, DMSO) δ 7.92 (m, 2H) 7.64 (dd, J = 3.13, 6.18, 2H) 3.87 (s, 6H).

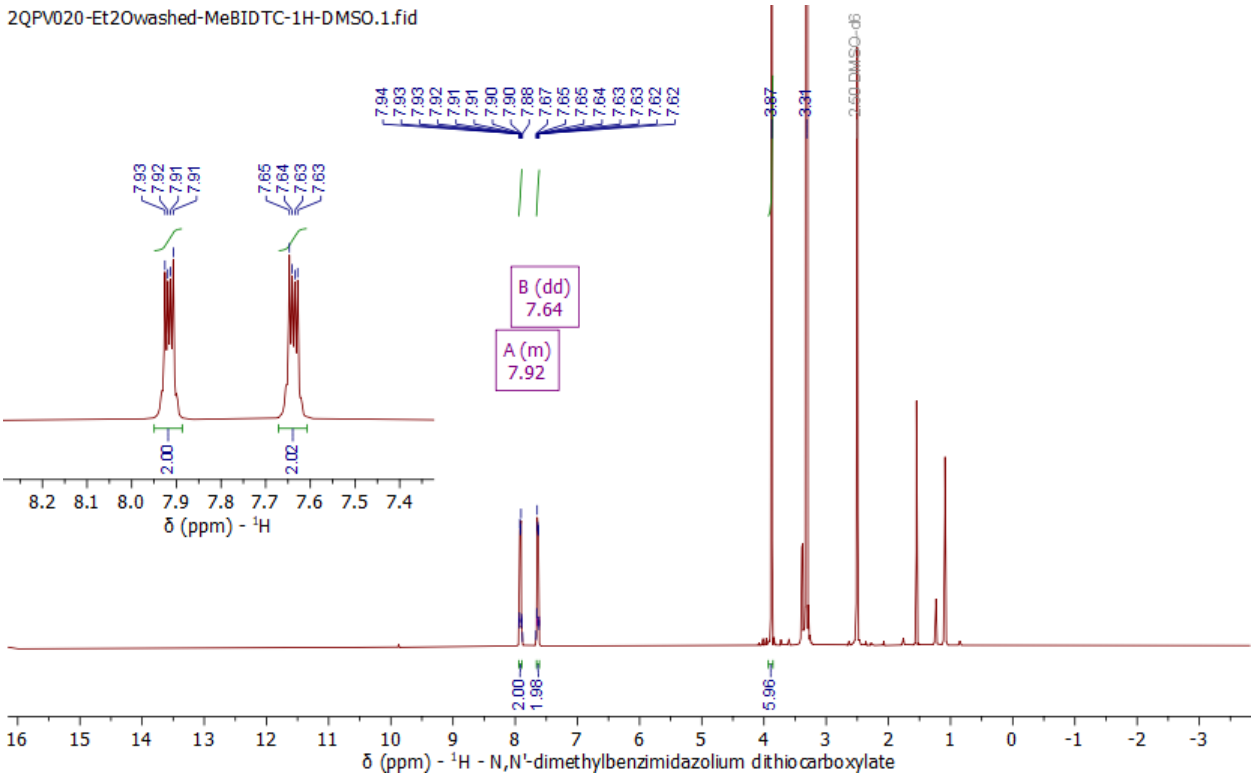

Figure 67. ^{1}H NMR Spectrum of N,N'-dimethyl benzimidazolium dithiocarboxylate in DMSO.

Calculated Energies

Table 4. Unpaired electron count and single point energy of modeled complexes

	Unpaired e^-	kj/mol
	Ni	
$BICO_2$	2	-1757536
$PhCO_2$	0	-1473245
DO	0	-1425119
$DO^{2\bullet}$	2	-1425149
BICS2	2	-2568971
PhDTC	0	-2284368
DT	0	-2235782
$DT^{2\bullet}$	2	-2235773
	Cu	
$BICO_2$	2	-1841320
$PhCO_2$	0	-1556741
$DO^{2\bullet}$	2	-1508126
DO	0	-1508124
$BICS_2$	2	-2651897
$PhCS_2$	0	-2367300
$DT^{2\bullet}$	2	-2318715
DT	0	-2318726
	Co	
$BICS_2$	3	-2490174
DT	1	-2157015
$DT^{2\bullet}$	3	-2157006
	$TrisBICS_2$	
Co^{3+}	3	-3301403
Cr^{3+}	6	-3089133
Sc^{3+}	3	-2911117

Calculated HOMO/LUMOs

Table 5. Calculated α and β HOMO and LUMO of Models. Calculated α and β HOMO/LUMO gap

.	HOMO		LUMO		H/L gap	
.	α	β	α	β	α	β
.	**Nickel**					
$BICO_2$	0.036	-4.771	-6.973	-6.958	6.937	2.186
$PhCO_2$	-6.974	-6.974	-2.393	-2.393	4.582	4.582
DO	-5.738	-6.138	-3.017	-2.516	2.721	3.622
$DO^{2\bullet}$	-5.536	-6.681	-0.715	-3.960	4.821	2.721
$BICS_2$	-3.788	-4.813	-1.248	-2.730	2.541	2.083
$PhCS_2$	-5.898	-5.898	-3.020	-3.020	2.878	2.878
DT	-6.894	-6.237	-4.173	-4.391	2.721	1.846
$DT^{2\bullet}$	-6.136	-6.156	-1.737	-3.435	4.400	2.721
.	**Copper**					
$BICO_2$	-3.916	-5.290	-0.804	-2.622	3.112	2.668
$PhCO_2$	-5.777	-6.010	-3.967	-4.551	1.811	1.459
$DO^{2\bullet}$	-5.476	-6.450	-2.971	-3.200	2.505	3.249
DO	-5.706	-6.143	-1.115	-4.617	4.591	1.526
$BICS_2$	-3.658	-6.370	-0.265	-2.628	3.393	3.742
$PhCS_2$	-5.684	-6.779	-3.127	-3.971	2.557	2.808
$DT^{2\bullet}$	-7.301	-7.367	-1.829	-3.451	5.471	3.916
DT	-5.737	-6.744	-0.584	-3.965	5.153	2.779
.	**Other Metals**					
Cr	-3.665	-5.115	-1.013	-2.340	2.651	2.775
Sc	-3.659	-5.231	-0.744	-2.362	2.916	2.869
trisCo	-3.590	-4.972	-1.119	-2.223	2.471	2.749
$CoBICS_2$	-3.811	-4.916	-1.315	-2.756	2.496	2.160
CoBDT	-6.060	-6.383	-4.530	-3.457	1.530	2.927
$CoBDT^{2\bullet}$	-5.767	-6.029	-3.427	-4.361	2.340	1.667

Graphs of plotted HOMO-LUMO gaps

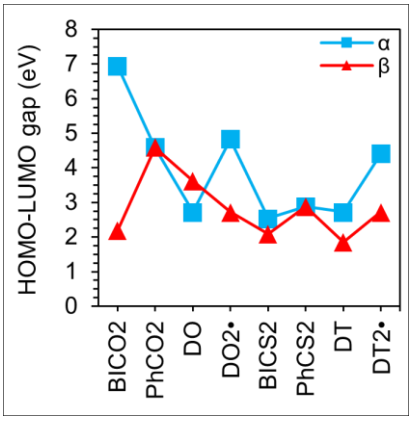

Figure 68. HOMO-LUMO gaps of Nickel Complexes

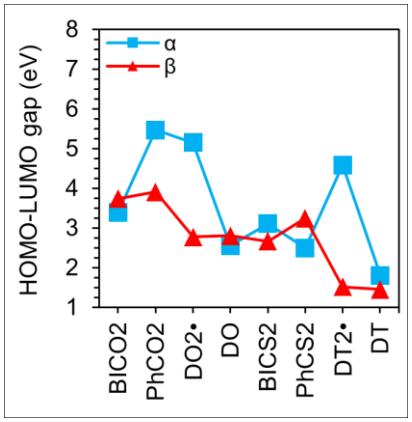

Figure 69. HOMO-LUMO gaps of Copper Complexes

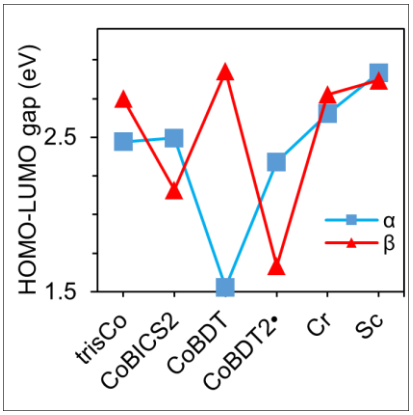

Figure 70. HOMO-LUMO gaps of tris complexes

Select MO visualizations

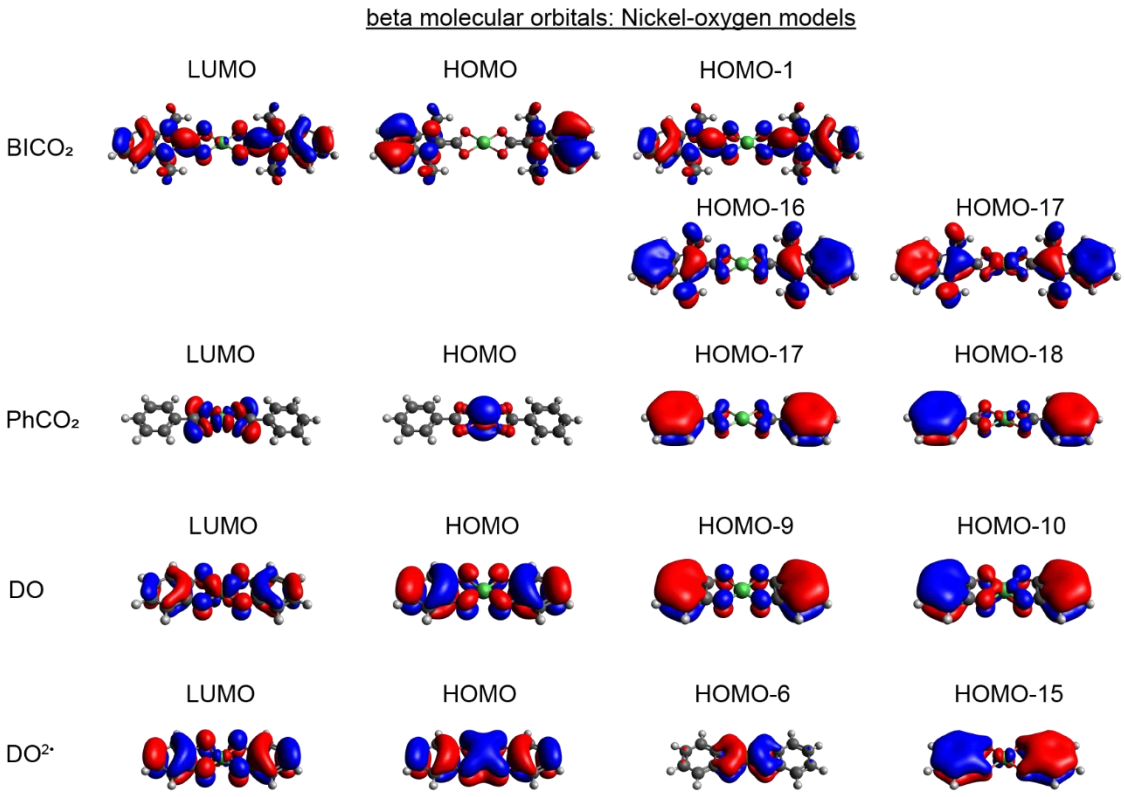

Figure 71. Molecular orbitals of nickel-oxygen models

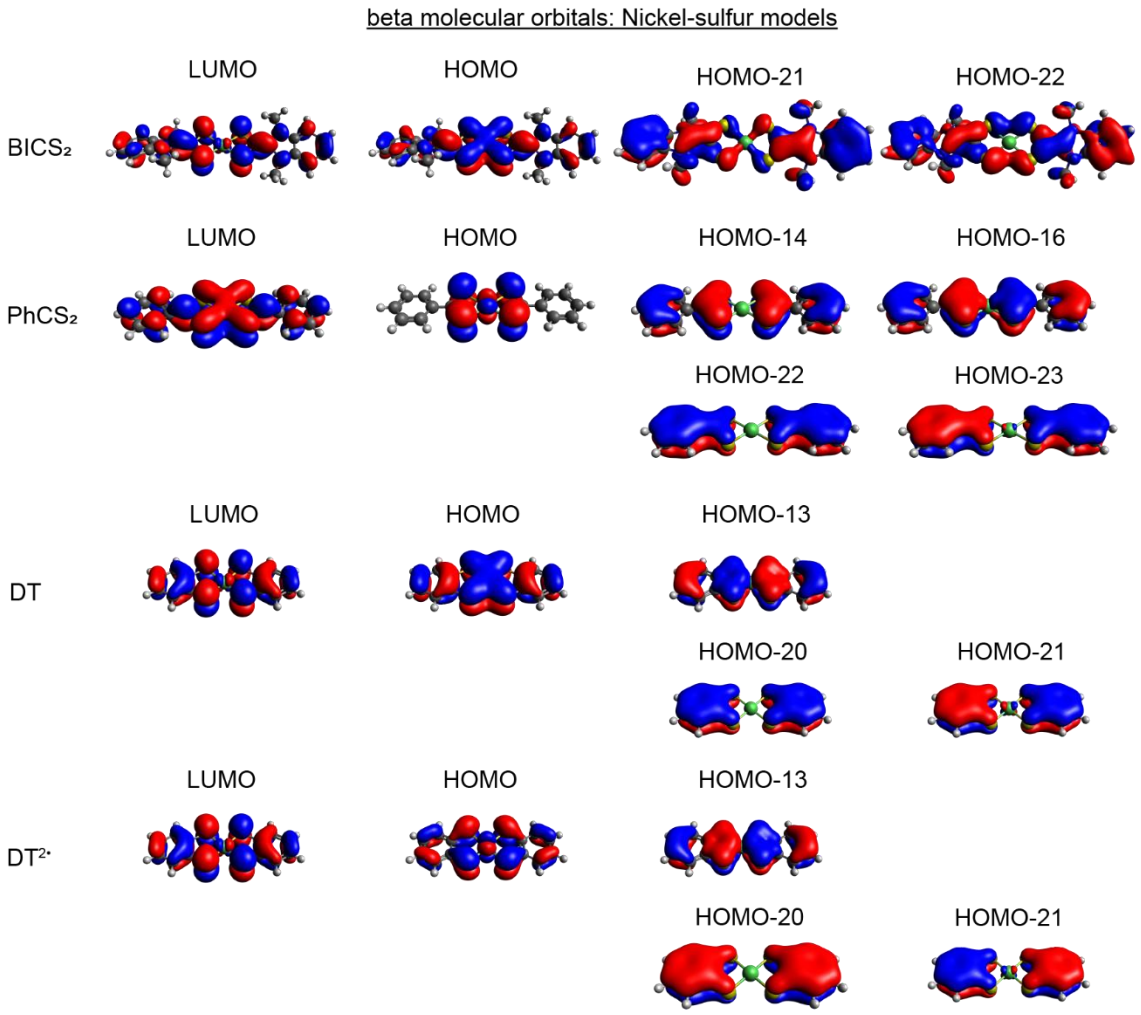

Figure 72. Molecular orbitals of nickel-sulfur models

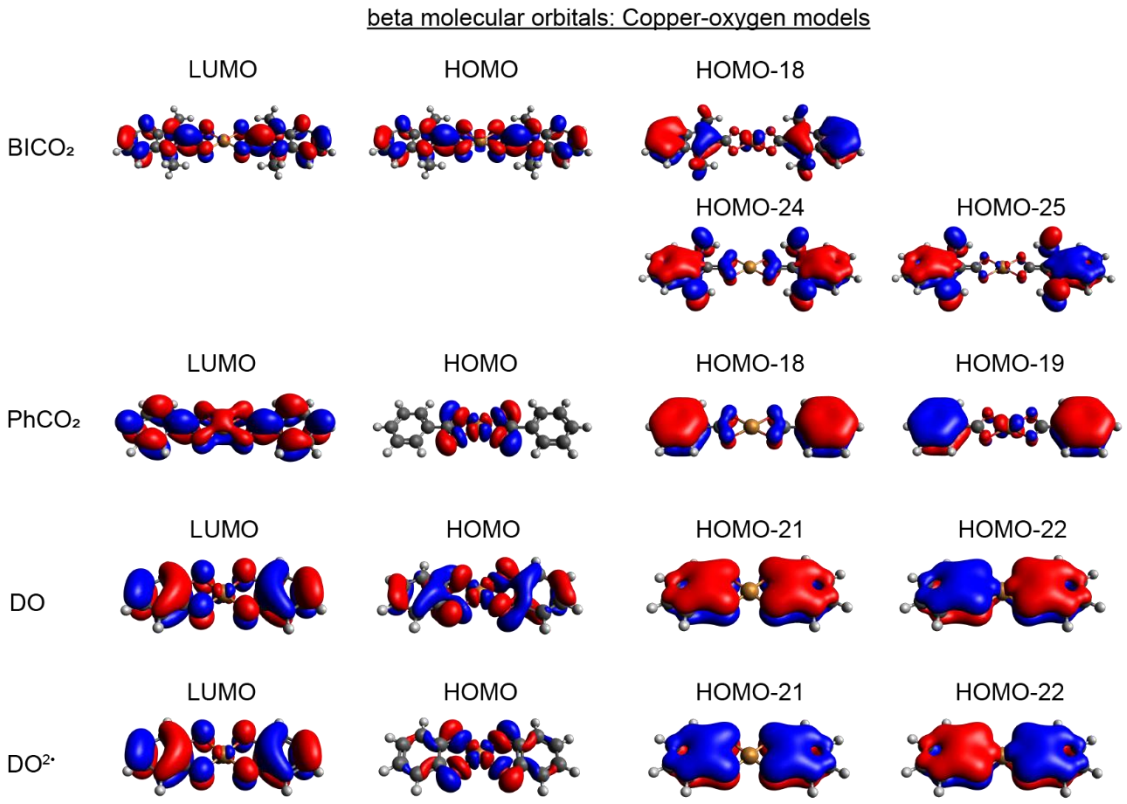

Figure 73. Molecular orbitals of copper-oxygen models

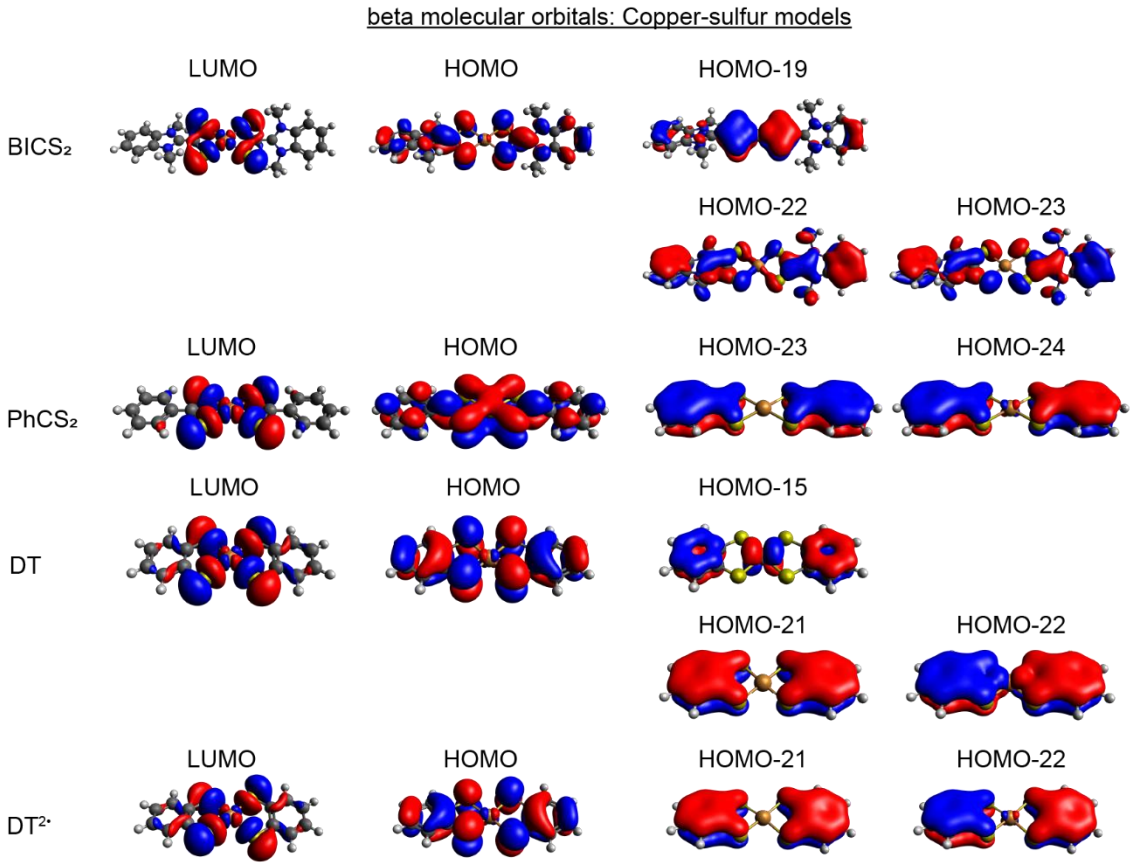

Figure 74. Molecular orbitals of copper-sulfur models

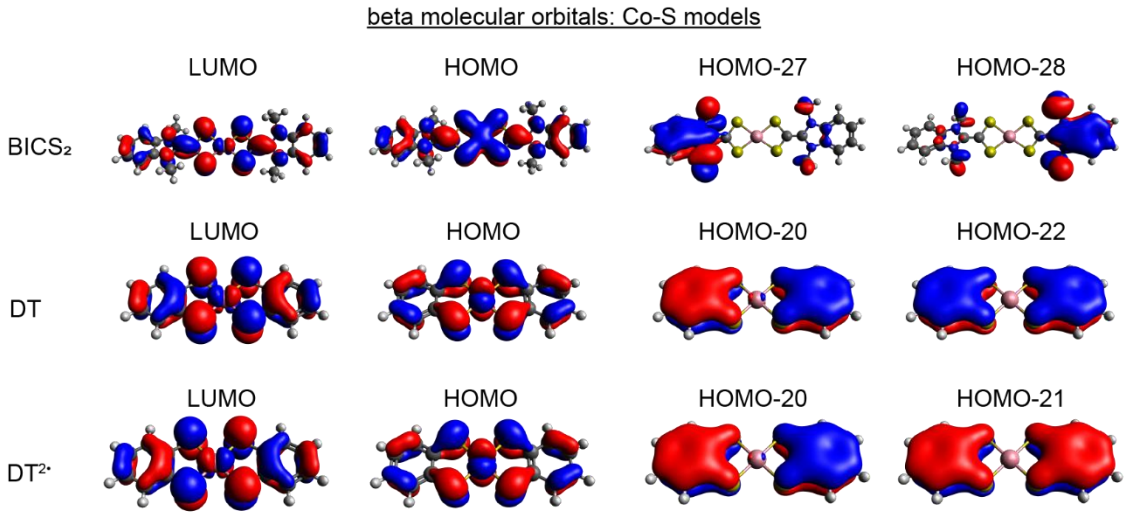

Figure 75. Molecular orbitals of bis-cobalt-sulfur models

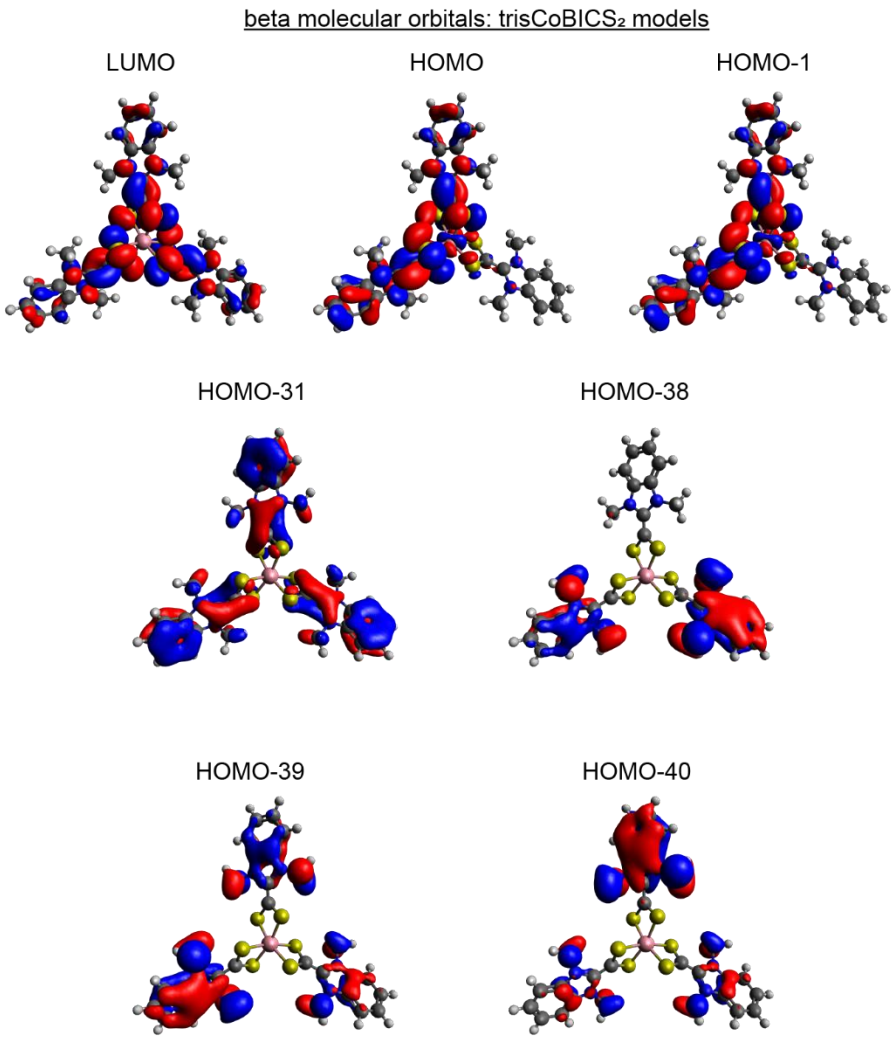

Figure 76. Molecular orbitals of tris-cobalt-BICS$_2$ models

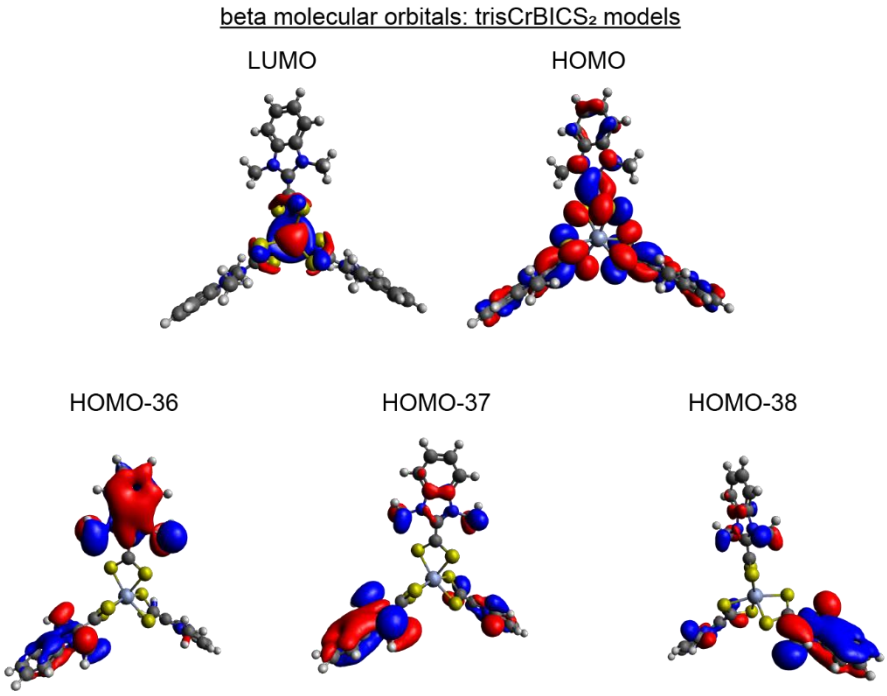

Figure 77. Molecular orbitals of tris-chromium-BICS2 models

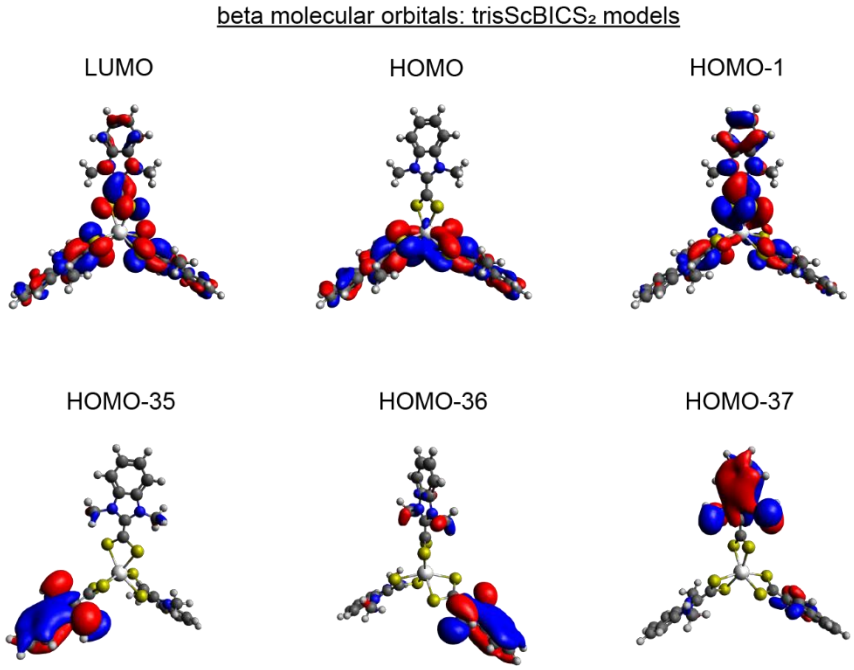

Figure 78. Molecular orbitals of tris-scandium-BICS2 models

AIM electrostatic potentials

Table 6. AIM-derived electrostatic potentials

.	ESP	ESPe	ESPn	ESP	ESPe	ESPn	ΔESPn	X/M (%)
.	Ni			S/O			Δ	%
$BICO_2$	-128.56	-154.84	26.28	-22.33	-53.33	31.00	-4.72	117.96
$PhCO_2$	-128.62	-148.82	20.20	-22.35	-46.98	24.64	-4.43	121.95
DO	-128.65	-149.29	20.64	-22.25	-47.00	24.75	-4.11	119.89
$DO^{2\bullet}$	-128.71	-148.96	20.25	-22.29	-46.60	24.31	-4.07	120.09
$BICS_2$	-128.69	-159.80	31.11	-59.28	-90.15	30.87	0.25	99.21
$PhCS_2$	-128.55	-152.84	24.29	-59.22	-83.26	24.04	0.25	98.97
DT	-128.59	-154.32	25.73	-59.23	-84.11	24.88	0.85	96.69
$DT^{2\bullet}$	-128.57	-154.14	25.57	-59.22	-83.94	24.71	0.86	96.65
.	Cu			S/O			Δ	%
$BICO_2$	-135.27	-161.12	25.85	-22.38	-53.27	30.89	-5.03	119.47
$PhCO_2$	-135.24	-154.84	19.59	-22.35	-46.69	24.33	-4.74	124.19
$DO^{2\bullet}$	-135.24	-155.03	19.79	-22.35	-46.46	24.11	-4.32	121.84
DO	-135.24	-155.03	19.78	-22.35	-46.45	24.10	-4.32	121.83
$BICS_2$	-135.32	-165.44	30.12	-59.28	-89.60	30.32	-0.20	100.68
$PhCS_2$	-135.29	-159.54	24.26	-59.24	-83.49	24.25	0.00	99.98
$DT^{2\bullet}$	-135.28	-159.53	24.25	-59.24	-83.06	23.83	0.42	98.26
DT	-135.23	-160.55	25.32	-59.22	-83.95	24.73	0.58	97.69
.	Co			S			Δ	%
$BICS_2$	-122.13	-152.96	30.83	-59.28	-89.69	30.42	0.42	98.65368
DT	-122.04	-147.53	25.49	-59.22	-83.65	24.42	1.07	95.79812
$DT^{2\bullet}$	-122.01	-147.27	25.25	-59.22	-83.43	24.21	1.05	95.85286
.	M			S ($BICS_2$)			Δ	%
trisCo	-122.11	-167.88	45.76	-59.28	-101.72	42.44	3.33	92.7282
trisCr	-103.31	-147.44	44.13	-59.29	-99.70	40.41	3.71	91.58276
trisSc	-85.75	-127.94	42.19	-59.30	-97.58	38.28	3.91	90.72889

AIM delocalization index

Table 7. AIM Delocalization Index (total) of all complexes

.	Delocalization Index - Total (avg)					
.	M	S/O	C_{DTC}	C_{NHC}	C_{C-X}	N
.	Nickel					
$BICO_2$	1.11	1.20	1.72	1.87		1.94
$PhCO_2$	1.25	1.09	1.63		2.10	
DO	1.58	1.18			1.94	
$DO^{2\bullet}$	1.33	1.15			1.92	
$BICS_2$	1.67	1.41	2.15	1.91		1.88
$PhCS_2$	1.64	1.44	2.18		2.11	
DT	2.01	1.56			2.14	
$DT^{2\bullet}$	2.05	1.51			2.14	
.	Copper					
$BICO_2$	1.06	1.08	1.71	1.88		1.88
$PhCO_2$	1.03	1.05	1.63		2.10	
$DO^{2\bullet}$	1.07	0.94			1.89	
DO	1.07	1.09			1.89	
$BICS_2$	1.29	1.34	2.15	1.91		1.88
$PhCS_2$	1.26	1.38	2.18		2.11	
$DT^{2\bullet}$	1.35	1.39			2.14	
DT	1.64	1.47			2.14	
.	Cobalt					
$CoBICS_2$	1.68	1.39	2.15	1.91		1.88
CoBDT	2.04	1.50			2.14	
$CoBDT^{2\bullet}$	1.90	1.46			2.14	
.	Tris complexes					
trisCo	2.22	1.46	2.16	1.91		1.88
Cr	1.72	1.36	2.16	1.91		1.88
Sc	1.17	1.26	2.16	1.91		1.89

Table 8. AIM Delocalization index (alpha) of all complexes

.	Delocalization Index - alpha (avg)				
.	M	S/O	$C_{DTC/X-C}$	C_{NHC}	N
.	Nickel				
$BICO_2$	0.48	0.63	0.84	0.90	0.96
$PhCO_2$	0.63	0.55	0.82	1.05	
DO	0.78	0.67		0.98	
$DO^{2\bullet}$	0.56	0.48		0.96	
$BICS_2$	0.83	0.66	1.09	0.97	0.92
$PhCS_2$	0.82	0.72	1.09	1.05	
DT	1.05	0.78		1.07	
$DT^{2\bullet}$	0.88	0.69		1.07	
.	Copper				
$BICO_2$	0.43	0.50	0.89	0.95	0.92
$PhCO_2$	0.41	0.50	0.82		
$DO^{2\bullet}$	0.44	0.51	0.97		
DO	0.63	0.52	0.97		
$BICS_2$	0.55	0.60	1.09	0.97	0.92
$PhCS_2$	0.52	0.66	1.09		
$DT^{2\bullet}$	0.58	0.60	1.08		
DT	0.81	0.69	1.08		
.	Cobalt				
$CoBICS_2$	0.83	0.66	1.08	0.97	0.92
CoBDT	0.90	0.78	1.07		
$CoBDT^{2\bullet}$	0.84	0.68	1.07		
.	Tris complexes				
trisCo	1.08	0.68	1.09	0.97	0.92
Cr	1.00	0.67	1.09	0.97	0.93
Sc	0.61	0.59	1.09	0.97	0.93

Table 9. Aim Delocalization Index (beta) of all complexes

.	Delocalization Index - beta (avg)				
.	M	S/O	$C_{DTC/X-C}$	C_{NHC}	N
.	Nickel				
$BICO_2$	0.63	0.57	0.88	0.97	0.98
$PhCO_2$	0.63	0.55	0.82	1.05	
DO	0.79	0.51		0.96	
$DO^{2\bullet}$	0.77	0.67		0.96	
$BICS_2$	0.84	0.74	1.07	0.94	0.96
$PhCS_2$	0.82	0.72	1.09	1.05	
DT	0.96	0.79		1.07	
$DT^{2\bullet}$	1.17	0.81		1.07	
.	Copper				
$BICO_2$	0.62	0.58	0.83	0.93	0.96
$PhCO_2$	0.62	0.55	0.82		
$DO^{2\bullet}$	0.63	0.73	0.92		
DO	0.44	0.56	0.92		
$BICS_2$	0.75	0.74	1.06	0.94	0.96
$PhCS_2$	0.74	0.72	1.09	1.05	
$DT^{2\bullet}$	0.78	0.79	1.06		
DT	0.80	1.00	1.07		
.	Cobalt				
$CoBICS_2$	0.85	0.73	1.07	0.94	0.96
CoBDT	1.13	0.72	1.07		
$CoBDT^{2\bullet}$	1.07	0.77	1.07		
.	Tris complexes				
trisCo	1.14	0.78	1.07	0.94	0.96
Cr	0.71	0.69	1.07	0.94	0.96
Sc	0.56	0.66	1.07	0.94	0.96

Lowdin Spin Population

Table 10. Lowdin Spin Population of all complexes

.	S/O(p)	M(d)	C_{DTC}(p)	C_{NHC}(p)	C_{aro}(C-X,p)	C_{aro}(p)	N(p)
.	**Nickel**						
$BICO_2$	0.12	-0.23	-0.05	-0.30			0.05
$PhCO_2$	0.00	0.00	0.00		0.00		
DO	-0.27	1.16			0.05	-0.05	
$DO^{2\bullet}$	0.36	-0.41			0.03	0.07	
$BICS_2$	0.13	0.07	0.16	0.09			0.08
$PhCS_2$	0.00	0.00	0.00		0.00		
DT	0.09	-0.21			-0.01	-0.02	
$DT^{2\bullet}$	0.29	0.62			0.00	0.00	
.	**Copper**						
$BICO_2$	0.150	0.660	0.103	0.176			0.103
$PhCO_2$	0.081	0.651	-0.005		0.001	0.000	
$DO^{2\bullet}$	0.711	0.238			0.110	0.051	
DO	0.108	-0.696			0.113	0.050	
$BICS_2$	0.261	0.457	0.177	0.086			0.077
$PhCS_2$	0.135	0.423	-0.003		0.001	0.001	
$DT^{2\bullet}$	0.499	0.397			0.081	0.026	
DT	0.070	0.149			0.037	0.012	
.	**Cobalt**						
$CoBICS_2$	0.11	1.18	0.16	0.08			0.07
CoBDT	-0.09	1.54					
$CoBDT^{2\bullet}$	0.16	1.97					
.	**tris Complexes**						
trisCo	0.17	0.05	0.12	0.11			0.07
trisCr	0.12	3.05	0.17	0.10			0.07
trisSc	0.13	0.10	0.19	0.09			0.07

Mayer Bond orders

Table 11. Mayer Bond Orders of all complexes

.	**Mayer bond orders**				
.	M-X	$X\text{-}X_{cis}$	$X\text{-}X_{trans}$	C=C	$M\text{-}C_{CX2}$
.	**Nickel**				
$BICO_2$	0.62	-	-	1.45	-
$PhCO_2$	0.43	-	-	0.94	-
DO	0.54	-	0.12	1.25	-
$DO^{2\bullet}$	0.47	-	-	1.21	-
$BICS_2$	0.65	0.11	-	1.12	-
$PhCS_2$	0.63	0.15	-	1.02	-
DT	0.74	0.11	0.16	1.25	-
$DT^{2\bullet}$	0.80	-	0.23	1.24	-
.	**Copper**				
$BICO_2$	0.60	-	-	1.44	-0.37
$PhCO_2$	0.49	-	-	0.95	-0.28
$DO^{2\bullet}$	0.45	-	-	1.25	-
DO	0.46	-	-	1.25	-
$BICS_2$	0.57	-	-	1.15	-0.13
$PhCS_2$	0.54	0.13	-	1.04	-
$DT^{2\bullet}$	0.53	0.11	-	1.17	-
DT	0.61		0.24	1.26	-
.	**Other metals**				
Cr	0.58	0.15	-	1.13	-
Sc	0.54	0.16	-	1.12	-
trisCo	0.74	0.17	-	1.07	-
$CoBICS_2$	0.69	-	-	1.13	-
CoBDT	0.85	-	0.14	1.25	-
$CoBDT^{2\bullet}$	0.81	-	0.18	1.26	-

Bond lengths

Table 12. Select bond lengths/atomic distances in all complexes

.	Bond Lengths			
.	M-X	$X\text{-}X_{cis}$	$X\text{-}X_{trans}$	C=C
.	**Nickel**			
$BICO_2$	1.929	2.182	3.858	1.412
$PhCO_2$	1.907	2.514	3.815	1.471
DO	1.84	2.53	3.68	1.44
$DO^{2\bullet}$	1.89	2.58	3.79	1.46
$BICS_2$	2.24	2.83	4.48	1.40
$PhCS_2$	2.25	2.81	4.49	1.46
DT	2.16	3.11	4.32	1.42
$DT^{2\bullet}$	2.18	3.14	4.35	1.41
.	**Copper**			
$BICO_2$	1.98	2.19	3.96	1.41
$PhCO_2$	1.99	2.71	3.99	1.48
$DO^{2\bullet}$	1.96	2.63	3.92	1.47
DO	1.96	2.63	3.91	1.47
$BICS_2$	2.36	2.90	4.72	1.41
$PhCS_2$	2.37	2.87	4.74	1.47
$DT^{2\bullet}$	2.34	3.27	4.65	1.44
DT	2.21	3.17	4.42	1.41
.	**Other metals**			
Cr	2.44	2.93	4.84	1.41
Sc	2.61	2.98	5.11	1.41
trisCo	2.30	2.83	4.57	1.40
$CoBICS_2$	2.27	2.84	4.54	1.40
CoBDT	2.19	3.13	4.37	1.41
$CoBDT^{2\bullet}$	2.21	3.16	4.42	1.41

Mulliken Atomic Orbital analysis

Table 13. Mulliken Atomic Orbital Analysis - NiBICO2

AO analysis				
Mulliken	alpha	beta	spin pop.	ato. chg.
Ni	14.83041	13.70717	1.12325	-0.53758
S/O	4.21573	4.28918	-0.07345	-0.50492
S/O	4.21573	4.28918	-0.07345	-0.50492
S/O	4.21573	4.28918	-0.07345	-0.50492
S/O	4.21573	4.28918	-0.07345	-0.50492
C (DTC)	2.78006	2.67645	0.10361	0.5435
C (DTC)	2.78006	2.67645	0.10361	0.5435
C (NHC)	2.61276	3.17548	-0.56271	0.21176
C (NHC)	2.61276	3.17548	-0.56271	0.21176
N	3.521	3.4539	0.0671	0.0251
N	3.521	3.4539	0.0671	0.0251
N	3.521	3.4539	0.0671	0.0251
N	3.521	3.4539	0.0671	0.0251

Table 14. Mulliken Atomic Orbital Analysis - $NiPhCO_2$

AO analysis				
Mulliken	alpha	beta	spin pop.	ato. chg.
Ni	15.09689	14.19874	0.89816	-1.29563
S/O	4.45424	4.37765	0.07659	-0.83189
S/O	4.45424	4.37765	0.07659	-0.83189
S/O	4.45424	4.37765	0.07659	-0.83189
S/O	4.45424	4.37765	0.07659	-0.83189
C (DTC)	2.01379	1.97237	0.04142	2.01384
C (DTC)	2.01379	1.97237	0.04142	2.01384
C (ring,-DTC)	3.73206	3.61145	0.12061	-1.3435
C (ring,-DTC)	3.73206	3.61145	0.12061	-1.3435
C (ring)	3.0136	2.90372	0.10989	0.08268
C (ring)	3.1133	3.07938	0.03392	-0.19268
C (ring)	3.04458	2.97734	0.06724	-0.02192
C (ring)	3.04458	2.97734	0.06724	-0.02192
C (ring)	3.1133	3.07938	0.03392	-0.19268
C (ring)	3.0136	2.90372	0.10989	0.08268
C (ring)	3.1133	3.07938	0.03392	-0.19268
C (ring)	3.1133	3.07938	0.03392	-0.19268
C (ring)	3.04458	2.97734	0.06724	-0.02192
C (ring)	3.04458	2.97734	0.06724	-0.02192

Table 15. Mulliken Atomic Orbital Analysis - NiBDO

AO analysis				
Mulliken	alpha	beta	spin pop.	ato. chg.
Ni	14.37293	12.98707	1.38586	0.64
S/O	4.0874	4.37092	-0.28352	-0.45832
S/O	4.08734	4.37092	-0.28359	-0.45826
S/O	4.08739	4.37092	-0.28353	-0.45831
S/O	4.08737	4.37092	-0.28355	-0.45829
C (C-S)	2.91906	2.79235	0.1267	0.28859
C (C-S)	2.91877	2.79235	0.12642	0.28888
C (C-S)	2.91896	2.79235	0.12661	0.28869
C (C-S)	2.9191	2.79235	0.12675	0.28855
C (ring)	2.97685	3.15253	-0.17568	-0.12938
C (ring)	3.0212	3.08936	-0.06816	-0.11055
C (ring)	3.02108	3.08936	-0.06828	-0.11043
C (ring)	2.97664	3.15253	-0.17589	-0.12917
C (ring)	2.97655	3.15253	-0.17598	-0.12908
C (ring)	3.02131	3.08936	-0.06805	-0.11066
C (ring)	2.97661	3.15253	-0.17592	-0.12914
C (ring)	3.0211	3.08936	-0.06825	-0.11046

Table 16. Mulliken Atomic Orbital Analysis - $NiBDO^{2\bullet}$

AO analysis				
Mulliken	alpha	beta	spin pop.	ato. chg.
Ni	13.49004	14.18796	-0.69792	0.32199
S/O	4.4215	4.02603	0.39547	-0.44753
S/O	4.4215	4.02603	0.39547	-0.44753
S/O	4.4215	4.02605	0.39545	-0.44755
S/O	4.4215	4.02607	0.39543	-0.44757
C (C-S)	2.8469	2.79878	0.04812	0.35432
C (C-S)	2.8469	2.79905	0.04785	0.35405
C (C-S)	2.8469	2.79914	0.04776	0.35396
C (C-S)	2.8469	2.79909	0.04781	0.35401
C (ring)	3.13566	3.06029	0.07537	-0.19595
C (ring)	3.12691	2.94421	0.1827	-0.07112
C (ring)	3.12691	2.94395	0.18296	-0.07086
C (ring)	3.13566	3.06052	0.07514	-0.19618
C (ring)	3.13566	3.06009	0.07557	-0.19575
C (ring)	3.12691	2.94409	0.18282	-0.071
C (ring)	3.13566	3.06007	0.07559	-0.19574
C (ring)	3.12691	2.94424	0.18267	-0.07114

Table 17. Mulliken Atomic Orbital Analysis - $NiBICS_2$

AO analysis				
Mulliken	alpha	beta	spin pop.	ato. chg.
Ni	13.9259	13.84641	0.07949	0.2277
S/O	8.28008	8.11085	0.16923	-0.39093
S/O	8.28071	8.11232	0.16839	-0.39302
S/O	8.28187	8.11362	0.16825	-0.39549
S/O	8.28036	8.11111	0.16925	-0.39148
C (DTC)	3.0359	2.84472	0.19117	0.11938
C (DTC)	3.03559	2.84427	0.19132	0.12014
C (NHC)	2.94074	2.80476	0.13598	0.2545
C (NHC)	2.94102	2.80506	0.13596	0.25391
N	3.5714	3.47351	0.0979	-0.04491
N	3.57177	3.47394	0.09783	-0.04571
N	3.57126	3.47352	0.09773	-0.04478
N	3.5715	3.47358	0.09793	-0.04508

Table 18. Mulliken Atomic Orbital Analysis - $NiPhCS_2$

AO analysis				
Mulliken	alpha	beta	spin pop.	ato. chg.
Ni	13.87022	13.87022	0	0.25957
S/O	8.15172	8.15172	0	-0.30343
S/O	8.15172	8.15172	0	-0.30343
S/O	8.15172	8.15172	0	-0.30343
S/O	8.15172	8.15172	0	-0.30343
C (DTC)	2.78793	2.78793	0	0.42413
C (DTC)	2.78793	2.78793	0	0.42413
C (ring,-DTC)	2.9834	2.9834	0	0.03321
C (ring,-DTC)	2.9834	2.9834	0	0.03321
C (ring)	3.04561	3.04561	0	-0.09123
C (ring)	3.05364	3.05364	0	-0.10727
C (ring)	3.07988	3.07988	0	-0.15977
C (ring)	3.07988	3.07988	0	-0.15977
C (ring)	3.05364	3.05364	0	-0.10727
C (ring)	3.04561	3.04561	0	-0.09123
C (ring)	3.05364	3.05364	0	-0.10727
C (ring)	3.05364	3.05364	0	-0.10727
C (ring)	3.07988	3.07988	0	-0.15977
C (ring)	3.07988	3.07988	0	-0.15977

Table 19. Mulliken Atomic Orbital Analysis - NiBDT

AO analysis				
Mulliken	alpha	beta	spin pop.	ato. chg.
Ni	13.75332	14.0438	-0.29048	0.20288
S/O	8.15119	8.03505	0.11614	-0.18623
S/O	8.1511	8.03505	0.11606	-0.18615
S/O	8.15117	8.03505	0.11612	-0.18622
S/O	8.15114	8.03505	0.11609	-0.18618
C (C-S)	2.87888	2.9219	-0.04302	0.19921
C (C-S)	2.87878	2.9219	-0.04312	0.19932
C (C-S)	2.87888	2.9219	-0.04302	0.19921
C (C-S)	2.87867	2.9219	-0.04323	0.19942
C (ring)	3.08914	3.11808	-0.02894	-0.20722
C (ring)	2.98048	3.07701	-0.09653	-0.0575
C (ring)	2.98071	3.07701	-0.0963	-0.05773
C (ring)	3.08896	3.11808	-0.02912	-0.20704
C (ring)	3.08905	3.11808	-0.02903	-0.20713
C (ring)	2.98062	3.07701	-0.09639	-0.05764
C (ring)	3.08926	3.11808	-0.02882	-0.20734
C (ring)	2.98049	3.07701	-0.09653	-0.0575

Table 20. Mulliken Atomic Orbital Analysis - $NiBDT^{2\bullet}$

AO analysis				
Mulliken	alpha	beta	spin pop.	ato. chg.
Ni	14.16868	13.66781	0.50087	0.1635
S/O	8.29787	7.90357	0.3943	-0.20144
S/O	8.29785	7.90357	0.39429	-0.20142
S/O	8.29796	7.90357	0.3944	-0.20153
S/O	8.29779	7.90357	0.39422	-0.20136
C (C-S)	2.94156	2.92973	0.01183	0.12871
C (C-S)	2.94133	2.92973	0.0116	0.12893
C (C-S)	2.94188	2.92973	0.01215	0.12839
C (C-S)	2.94135	2.92973	0.01162	0.12891
C (ring)	3.04791	3.09803	-0.05012	-0.14594
C (ring)	2.99184	3.05767	-0.06583	-0.04951
C (ring)	2.99242	3.05767	-0.06525	-0.05009
C (ring)	3.04744	3.09803	-0.05059	-0.14547
C (ring)	3.04687	3.09803	-0.05116	-0.1449
C (ring)	2.99289	3.05767	-0.06478	-0.05056
C (ring)	3.04781	3.09803	-0.05022	-0.14584
C (ring)	2.99175	3.05767	-0.06592	-0.04942

Table 21. Mulliken Atomic Orbital Analysis - $CuBICO_2$

AO analysis				
Mulliken	alpha	beta	spin pop.	ato. chg.
Cu	14.58021	13.95378	0.62643	0.46601
S/O	4.4391	4.25679	0.18231	-0.69589
S/O	4.43842	4.25598	0.18243	-0.6944
S/O	4.43842	4.25598	0.18243	-0.6944
S/O	4.4391	4.25679	0.18231	-0.69589
C (DTC)	2.61035	2.47898	0.13137	0.91067
C (DTC)	2.61035	2.47898	0.13137	0.91067
C (NHC)	3.14365	2.85755	0.2861	-0.0012
C (NHC)	3.14365	2.85755	0.2861	-0.0012
N	3.58321	3.45726	0.12595	-0.04047
N	3.58268	3.45671	0.12597	-0.03939
N	3.58268	3.45671	0.12597	-0.03939
N	3.58321	3.45726	0.12595	-0.04047

Table 22. Mulliken Atomic Orbital Analysis - $CuPhCO_2$

AO analysis				
Mulliken	alpha	beta	spin pop.	ato. chg.
Cu	14.49984	13.89311	0.60673	0.60705
S/O	4.34703	4.24496	0.10207	-0.59199
S/O	4.34703	4.24496	0.10207	-0.59199
S/O	4.34703	4.24496	0.10207	-0.59199
S/O	4.34703	4.24496	0.10207	-0.5919
C (DTC)	2.57088	2.58136	-0.01048	0.84776
C (DTC)	2.57088	2.58136	-0.01048	0.84776
C (ring,-DTC)	2.99372	2.99501	-0.00129	0.01126
C (ring,-DTC)	2.99372	2.99501	-0.00129	0.01126
C (ring)	3.04172	3.04277	-0.00105	-0.0845
C (ring)	3.05639	3.05582	0.00057	-0.11221
C (ring)	3.08478	3.08292	0.00186	-0.1677
C (ring)	3.08478	3.08292	0.00186	-0.1677
C (ring)	3.05639	3.05582	0.00057	-0.11221
C (ring)	3.04172	3.04277	-0.00105	-0.0845
C (ring)	3.05639	3.05582	0.00057	-0.11221
C (ring)	3.05639	3.05582	0.00057	-0.11221
C (ring)	3.08478	3.08292	0.00186	-0.1677
C (ring)	3.08478	3.08292	0.00186	-0.1677

Table 23. Mulliken Atomic Orbital Analysis - CuBDO

AO analysis				
Mulliken	alpha	beta	spin pop.	ato. chg.
Cu	13.89882	14.54884	-0.65002	0.55234
S/O	4.31816	4.1936	0.12456	-0.51176
S/O	4.31816	4.1936	0.12456	-0.51176
S/O	4.31816	4.1936	0.12456	-0.51176
S/O	4.31816	4.1936	0.12456	-0.51176
C (C-S)	2.87729	2.69314	0.18416	0.42957
C (C-S)	2.87729	2.69314	0.18416	0.42957
C (C-S)	2.87729	2.69314	0.18416	0.42957
C (C-S)	2.87729	2.69314	0.18416	0.42957
C (ring)	3.10157	3.12943	-0.02786	-0.231
C (ring)	3.10854	2.96781	0.14073	-0.07634
C (ring)	3.10854	2.96781	0.14073	-0.07634
C (ring)	3.10157	3.12943	-0.02786	-0.231
C (ring)	3.10157	3.12943	-0.02786	-0.231
C (ring)	3.10854	2.96781	0.14073	-0.07634
C (ring)	3.10157	3.12943	-0.02786	-0.231
C (ring)	3.10854	2.96781	0.14073	-0.07634

Table 24. Mulliken Atomic Orbital Analysis - $CuBDO^{2-}$

AO analysis				
Mulliken	alpha	beta	spin pop.	ato. chg.
Cu	14.54981	13.89869	0.65112	0.5515
S/O	4.40062	4.10739	0.29323	-0.50801
S/O	4.40062	4.10739	0.29323	-0.50801
S/O	4.40062	4.10739	0.29323	-0.50801
S/O	4.40062	4.10739	0.29323	-0.50801
C (C-S)	2.87762	2.69311	0.18451	0.42927
C (C-S)	2.87762	2.69311	0.18451	0.42927
C (C-S)	2.87762	2.69311	0.18451	0.42927
C (C-S)	2.87762	2.69311	0.18451	0.42927
C (ring)	3.10675	3.12694	-0.02018	-0.23369
C (ring)	3.10726	2.96935	0.13791	-0.0766
C (ring)	3.10726	2.96935	0.13791	-0.0766
C (ring)	3.10675	3.12694	-0.02018	-0.23369
C (ring)	3.10675	3.12694	-0.02018	-0.23369
C (ring)	3.10726	2.96935	0.13791	-0.0766
C (ring)	3.10675	3.12694	-0.02018	-0.23369
C (ring)	3.10726	2.96935	0.13791	-0.0766

Table 25. Mulliken Atomic Orbital Analysis - $CuBICS_2$

AO analysis				
Mulliken	alpha	beta	spin pop.	ato. chg.
Cu	14.69738	14.30923	0.38815	-0.00661
S	8.34827	8.0072	0.34107	-0.35547
S	8.34788	8.0061	0.34178	-0.35398
S	8.34947	8.00816	0.34131	-0.35763
S	8.34795	8.00643	0.34152	-0.35438
C(DTC)	3.02199	2.83017	0.19182	0.14784
C(DTC)	3.0217	2.82963	0.19207	0.14867
C(NHC)	2.93901	2.80269	0.13633	0.2583
C(NHC)	2.93896	2.80274	0.13622	0.25831
N	3.5703	3.47313	0.09717	-0.04343
N	3.57039	3.47305	0.09734	-0.04344
N	3.57032	3.47321	0.09711	-0.04353
N	3.57026	3.47296	0.09729	-0.04322

Table 26. Mulliken Atomic Orbital Analysis - $CuPhCS_2$

AO analysis				
Mulliken	alpha	beta	spin pop.	ato. chg.
Cu	17.28321	14.58187	2.70134	-2.86508
S/O	7.42808	8.42347	-0.99539	0.14845
S/O	7.42808	8.42347	-0.99539	0.14845
S/O	7.42808	8.42347	-0.99539	0.14845
S/O	7.42808	8.42347	-0.99539	0.14845
C (DTC)	3.9204	3.2309	0.6895	-1.1513
C (DTC)	3.9204	3.2309	0.6895	-1.1513
C (ring,-DTC)	2.42169	2.09273	0.32897	1.48558
C (ring,-DTC)	2.42169	2.09273	0.32897	1.48558
C (ring)	1.88262	3.9035	-2.02088	0.21389
C (ring)	3.7256	2.48077	1.24483	-0.20638
C (ring)	2.41233	2.87827	-0.46594	0.7094
C (ring)	2.41233	2.87827	-0.46594	0.7094
C (ring)	3.7256	2.48077	1.24483	-0.20638
C (ring)	1.88262	3.9035	-2.02088	0.21389
C (ring)	3.7256	2.48077	1.24483	-0.20638
C (ring)	3.7256	2.48077	1.24483	-0.20638
C (ring)	2.41233	2.87827	-0.46594	0.7094
C (ring)	2.41233	2.87827	-0.46594	0.7094

Table 27. Mulliken Atomic Orbital Analysis - CuBDT

AO analysis				
Mulliken	alpha	beta	spin pop.	ato. chg.
Cu	14.64457	14.65876	-0.01419	-0.30333
S/O	8.12008	7.93527	0.18481	-0.05535
S/O	8.12008	7.93527	0.18481	-0.05535
S/O	8.12008	7.93527	0.18481	-0.05535
S/O	8.12008	7.93527	0.18481	-0.05535
C (C-S)	2.93514	2.89217	0.04297	0.17268
C (C-S)	2.93514	2.89217	0.04297	0.17268
C (C-S)	2.93514	2.89217	0.04297	0.17268
C (C-S)	2.93514	2.89217	0.04297	0.17268
C (ring)	3.0897	3.09921	-0.0095	-0.18891
C (ring)	3.06752	3.03006	0.03746	-0.09757
C (ring)	3.06752	3.03006	0.03746	-0.09757
C (ring)	3.0897	3.09921	-0.0095	-0.18891
C (ring)	3.0897	3.09921	-0.0095	-0.18891
C (ring)	3.06752	3.03006	0.03746	-0.09757
C (ring)	3.0897	3.09921	-0.0095	-0.18891
C (ring)	3.06752	3.03006	0.03746	-0.09757

Table 28. Mulliken Atomic Orbital Analysis - $CuBDT^{2\cdot}$

AO analysis				
Mulliken	alpha	beta	spin pop.	ato. chg.
Cu	14.71904	14.34664	0.37239	-0.06568
S/O	8.33748	7.82197	0.5155	-0.15945
S/O	8.33748	7.82197	0.5155	-0.15945
S/O	8.33748	7.82197	0.5155	-0.15945
S/O	8.33748	7.82197	0.5155	-0.15945
C (C-S)	2.94355	2.86077	0.08277	0.19568
C (C-S)	2.94355	2.86077	0.08277	0.19568
C (C-S)	2.94355	2.86077	0.08277	0.19568
C (C-S)	2.94355	2.86077	0.08277	0.19568
C (ring)	3.08751	3.10051	-0.013	-0.18802
C (ring)	3.08009	3.0047	0.07539	-0.08479
C (ring)	3.08009	3.0047	0.07539	-0.08479
C (ring)	3.08751	3.10051	-0.013	-0.18802
C (ring)	3.08751	3.10051	-0.013	-0.18802
C (ring)	3.0801	3.0047	0.0754	-0.08479
C (ring)	3.08751	3.10051	-0.013	-0.18802
C (ring)	3.0801	3.0047	0.0754	-0.08479

Table 29. Mulliken Atomic Orbital Analysis - $CoBICS_2$

AO analysis				
Mulliken	alpha	beta	spin pop.	ato. chg.
Co	14.02301	12.72308	1.29993	0.25391
S/O	8.26382	8.13904	0.12478	-0.40286
S/O	8.26318	8.13825	0.12493	-0.40143
S/O	8.2609	8.13693	0.12398	-0.39783
S/O	8.2603	8.13649	0.12381	-0.39679
C (DTC)	3.03295	2.84982	0.18313	0.11723
C (DTC)	3.03092	2.84303	0.18788	0.12605
C (NHC)	2.93539	2.80341	0.13197	0.2612
C (NHC)	2.93585	2.80678	0.12906	0.25737
N	3.56956	3.47421	0.09536	-0.04377
N	3.57014	3.47479	0.09534	-0.04493
N	3.56979	3.47527	0.09452	-0.04506
N	3.56958	3.47498	0.0946	-0.04456

Table 30. Mulliken Atomic Orbital Analysis - CoBDT

AO analysis				
Mulliken	alpha	beta	spin pop.	ato. chg.
Co	14.24848	12.56479	1.68369	0.18673
S/O	8.02855	8.15235	-0.1238	-0.18091
S/O	8.02855	8.15235	-0.1238	-0.18091
S/O	8.02855	8.15235	-0.1238	-0.18091
S/O	8.02855	8.15235	-0.1238	-0.18091
C (C-S)	2.89646	2.93463	-0.03817	0.16891
C (C-S)	2.89646	2.93463	-0.03817	0.16891
C (C-S)	2.89646	2.93463	-0.03817	0.16891
C (C-S)	2.89646	2.93463	-0.03817	0.16891
C (ring)	3.10394	3.08881	0.01513	-0.19275
C (ring)	3.03289	3.05787	-0.02498	-0.09076
C (ring)	3.03289	3.05787	-0.02498	-0.09076
C (ring)	3.10394	3.08881	0.01513	-0.19275
C (ring)	3.10394	3.08881	0.01513	-0.19275
C (ring)	3.03289	3.05787	-0.02498	-0.09076
C (ring)	3.10394	3.08881	0.01513	-0.19275
C (ring)	3.03289	3.05787	-0.02498	-0.09076

Table 31. Mulliken Atomic Orbital Analysis - $CoBDT^{2\bullet}$

AO analysis				
Mulliken	alpha	beta	spin pop.	ato. chg.
Co	14.42275	12.35909	2.06366	0.21817
S/O	8.17309	8.00869	0.1644	-0.18178
S/O	8.17309	8.00869	0.1644	-0.18178
S/O	8.17309	8.00869	0.1644	-0.18178
S/O	8.17309	8.00869	0.1644	-0.18178
C (C-S)	2.93195	2.90088	0.03107	0.16717
C (C-S)	2.93195	2.90088	0.03107	0.16717
C (C-S)	2.93195	2.90088	0.03107	0.16717
C (C-S)	2.93195	2.90088	0.03107	0.16717
C (ring)	3.09767	3.09292	0.00476	-0.19059
C (ring)	3.06634	3.02969	0.03665	-0.09603
C (ring)	3.06634	3.02969	0.03665	-0.09603
C (ring)	3.09767	3.09292	0.00476	-0.19059
C (ring)	3.09767	3.09292	0.00476	-0.19059
C (ring)	3.06634	3.02969	0.03665	-0.09603
C (ring)	3.09767	3.09292	0.00476	-0.19059
C (ring)	3.06634	3.02969	0.03665	-0.09603

Table 32. Mulliken Atomic Orbital Analysis - Tris-CoBICS$_2$

AO analysis				
Mulliken	alpha	beta	spin pop.	ato. chg.
Co	13.08047	13.00205	0.07842	0.91748
S/O	8.29754	8.10523	0.19231	-0.40278
S/O	8.29669	8.10391	0.19278	-0.4006
S/O	8.2974	8.10464	0.19276	-0.40203
S/O	8.29773	8.10553	0.1922	-0.40326
S/O	8.29637	8.1037	0.19267	-0.40007
S/O	8.29824	8.10623	0.19201	-0.40447
C (DTC)	3.08211	2.94715	0.13497	-0.02926
C (DTC)	3.08324	2.94782	0.13541	-0.03106
C (DTC)	3.08233	2.94711	0.13522	-0.02944
C (NHC)	2.94735	2.77613	0.17121	0.27652
C (NHC)	2.94674	2.77561	0.17113	0.27765
C (NHC)	2.94669	2.77541	0.17128	0.2779
N	3.56876	3.47731	0.09145	-0.04606
N	3.56874	3.47709	0.09165	-0.04583
N	3.56873	3.47733	0.0914	-0.04606
N	3.56838	3.47687	0.09151	-0.04525
N	3.56884	3.47734	0.09151	-0.04618
N	8.29824	8.10623	0.19201	-0.40447

Table 33. Mulliken Atomic Orbital Analysis - Tris-$CrBICS_2$

AO analysis				
Mulliken	alpha	beta	spin pop.	ato. chg.
Cr	13.4101	10.00177	3.40833	0.58813
S/O	8.26923	8.16092	0.10832	-0.43015
S/O	8.26945	8.16147	0.10798	-0.43092
S/O	8.28255	8.1717	0.11085	-0.45425
S/O	8.27507	8.16501	0.11006	-0.44008
S/O	8.27375	8.16358	0.11017	-0.43733
S/O	8.28192	8.17064	0.11127	-0.45256
C (DTC)	3.04865	2.83693	0.21172	0.11441
C (DTC)	3.03584	2.83058	0.20526	0.13359
C (DTC)	3.03578	2.83022	0.20556	0.134
C (NHC)	2.9295	2.77482	0.15468	0.29567
C (NHC)	2.94058	2.78423	0.15635	0.27519
C (NHC)	2.94089	2.78452	0.15637	0.27459
N	3.5671	3.47579	0.09131	-0.04289
N	3.56697	3.47546	0.09151	-0.04243
N	3.56668	3.47493	0.09175	-0.04162
N	3.56701	3.47514	0.09187	-0.04215
N	3.56664	3.47492	0.09172	-0.04156
N	3.56698	3.475	0.09197	-0.04198

Table 34. Mulliken Atomic Orbital Analysis - Tris-ScBICS$_2$

AO analysis				
Mulliken	alpha	beta	spin pop.	ato. chg.
Sc	10.51562	10.36696	0.14866	0.11742
S/O	8.27315	8.1063	0.16686	-0.37945
S/O	8.27285	8.10537	0.16748	-0.37821
S/O	8.27145	8.11082	0.16063	-0.38227
S/O	8.26519	8.10456	0.16063	-0.36975
S/O	8.26521	8.10518	0.16003	-0.3704
S/O	8.27131	8.10972	0.16159	-0.38103
C (DTC)	3.05263	2.82903	0.2236	0.11834
C (DTC)	3.04889	2.82871	0.22018	0.12241
C (DTC)	3.05043	2.82998	0.22045	0.1196
C (NHC)	2.91543	2.78264	0.13279	0.30192
C (NHC)	2.92234	2.7849	0.13744	0.29276
C (NHC)	2.92106	2.78358	0.13748	0.29536
N	3.56483	3.47654	0.08829	-0.04136
N	3.56471	3.47627	0.08844	-0.04098
N	3.56437	3.47617	0.0882	-0.04055
N	3.56433	3.47627	0.08806	-0.04059
N	3.5642	3.4763	0.0879	-0.04051
N	3.56421	3.4761	0.08811	-0.04031

Electrostatic Potential Maps

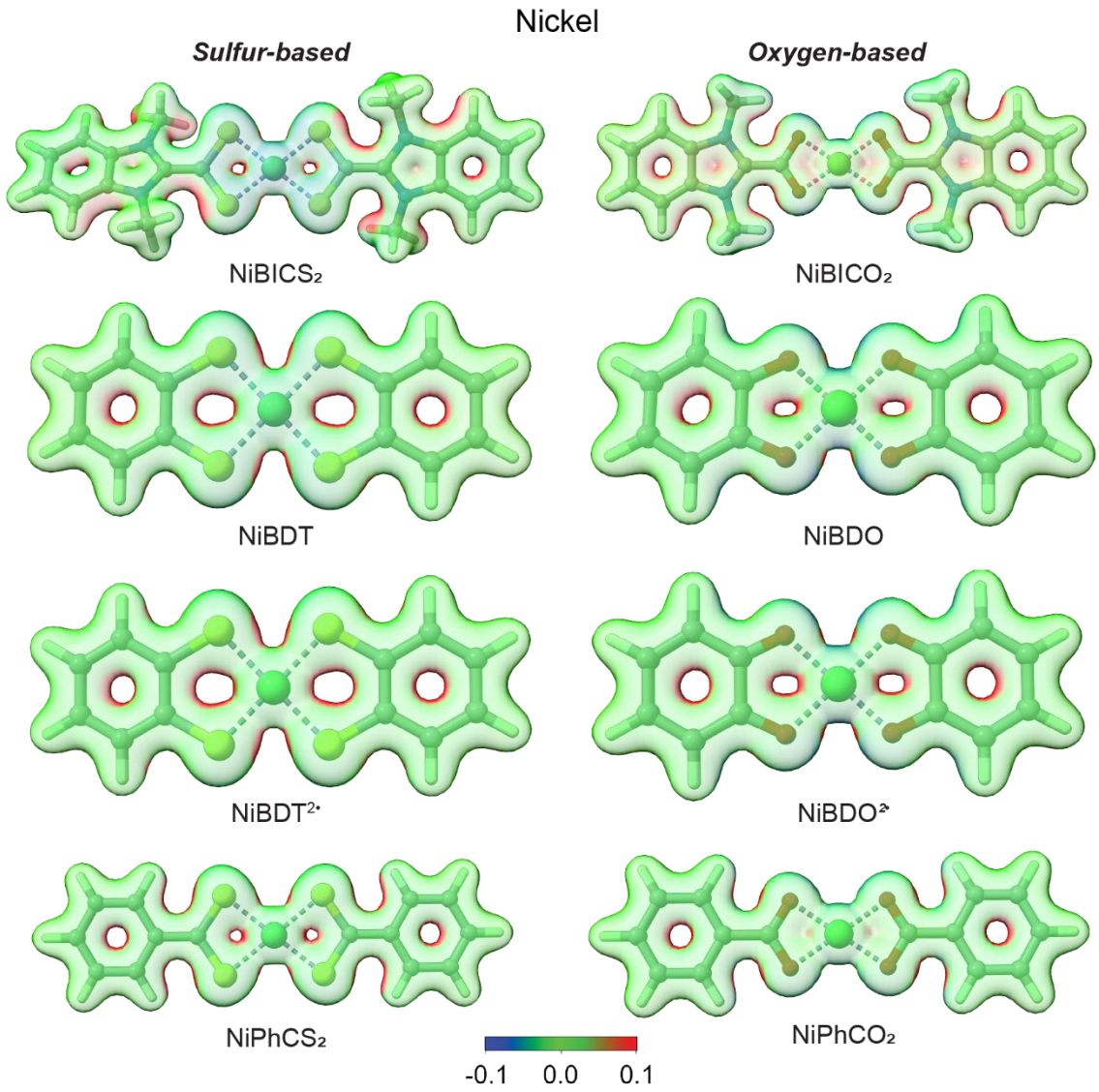

Figure 79. Electrostatic potential maps of nickel complexes, plotted at 0.05 isosurface level, colormap from -0.1 to 0.0 to 0.1 a.u. (Red-Green-Blue).

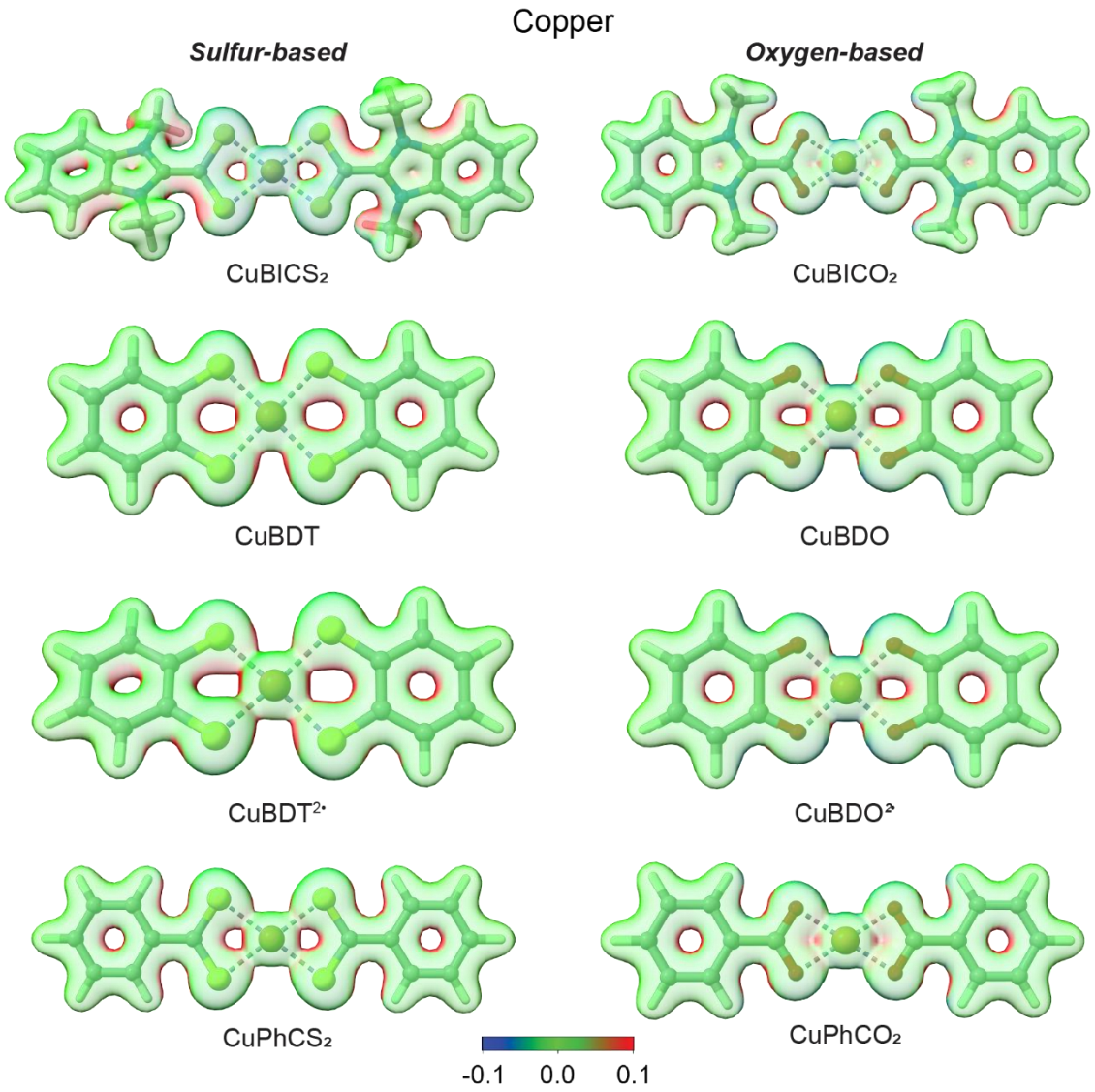

Figure 80. Electrostatic potential maps of copper complexes, plotted at 0.05 isosurface level, colormap from -0.1 to 0.0 to 0.1 a.u. (Red-Green-Blue).

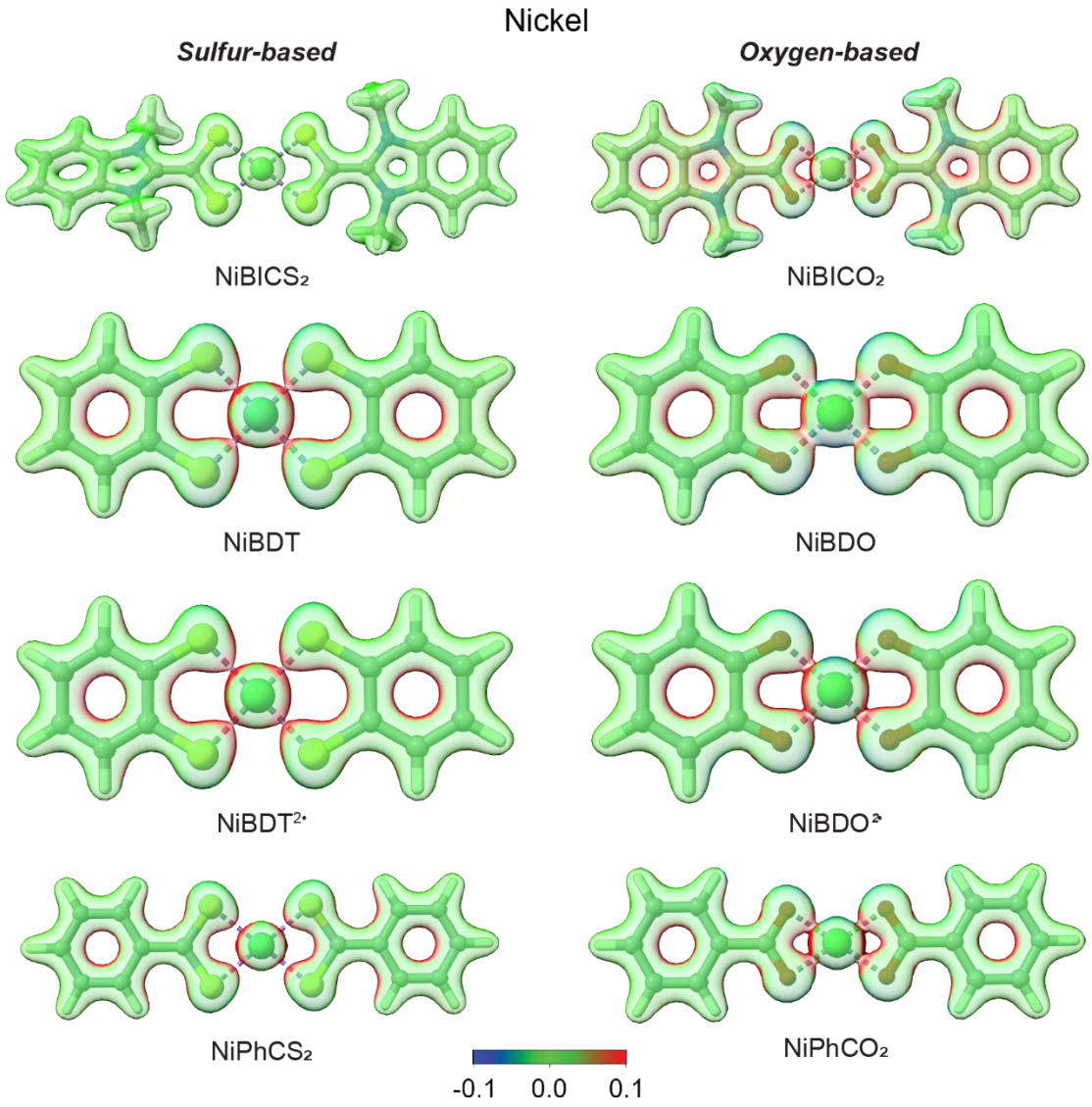

Figure 81. Electrostatic potential maps of nickel complexes, plotted at 0.1 isosurface level, colormap from -0.1 to 0.0 to 0.1 a.u. (Red-Green-Blue).

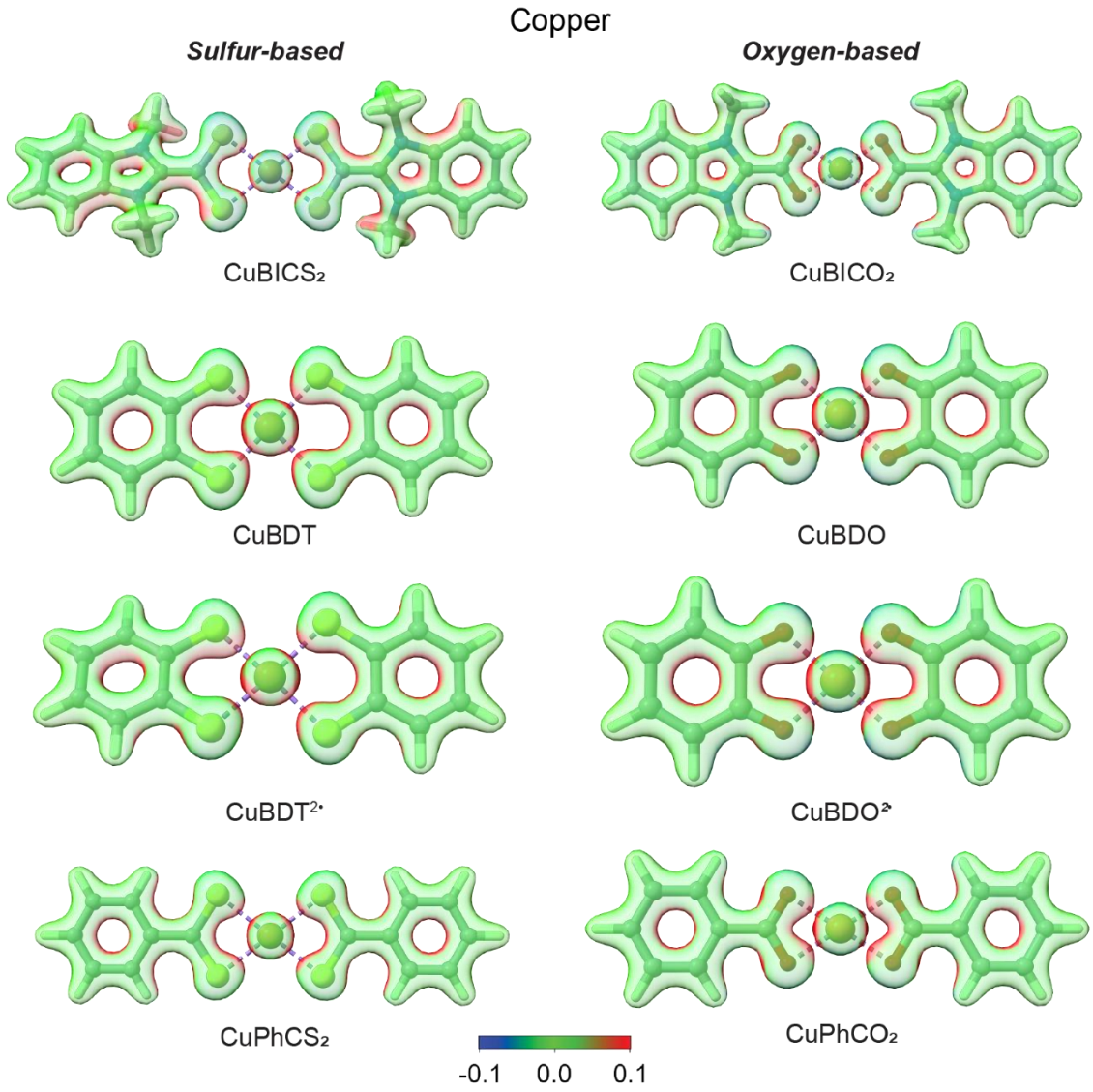

Figure 82. Electrostatic potential maps of copper complexes, plotted at 0.05 isosurface level, colormap from -0.1 to 0.0 to 0.1 a.u. (Red-Green-Blue).

Integrated zNICS values

Table 35. xNICS fit values and integrations. Calulated data fit to exponential functions

y = y0 +Ae^(-invTau*x)				
exp_fit	y0	A	invTau	int 0-10
Benzene	-0.25526	-43.028	1.02632	-44.4755
MeBICS2ph	-0.28138	-29.8732	0.908877	-35.6783
$NiPhCO_2$	-0.26377	-37.2832	0.998111	-39.9898
$NiBICO_2ph$	-0.18596	-28.3723	0.911279	-32.9908
NiBDO	0.035173	-28.2223	1.41872	-19.541
NiBDOr	-0.03693	-10.8165	0.968794	-11.5335
$NiPhCS_2$	-0.23671	-35.6544	0.999281	-38.0455
$NiBICS_2ph$	-0.17229	-20.527	0.770118	-28.3653
NiBDT	-0.31585	-24.2415	0.962817	-28.3346
NiBDTr	-0.07644	-26.985	1.1657	-23.9134
$NiBICO_2im$	-0.10575	-17.8291	0.916146	-20.5164
$MeBICS_2im$	-0.16069	-8.92589	0.662053	-15.071
$NiBICS_2im$	-	-	-	-4.626*

*no fit, area under data obtained, 2-6

zNICS curve fits

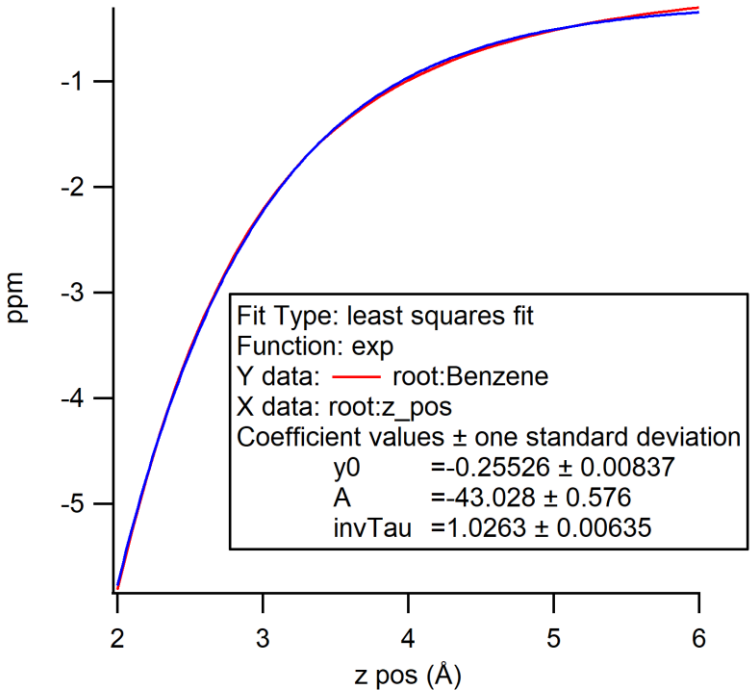

Figure 83. zNICS exponential fit: Benzene

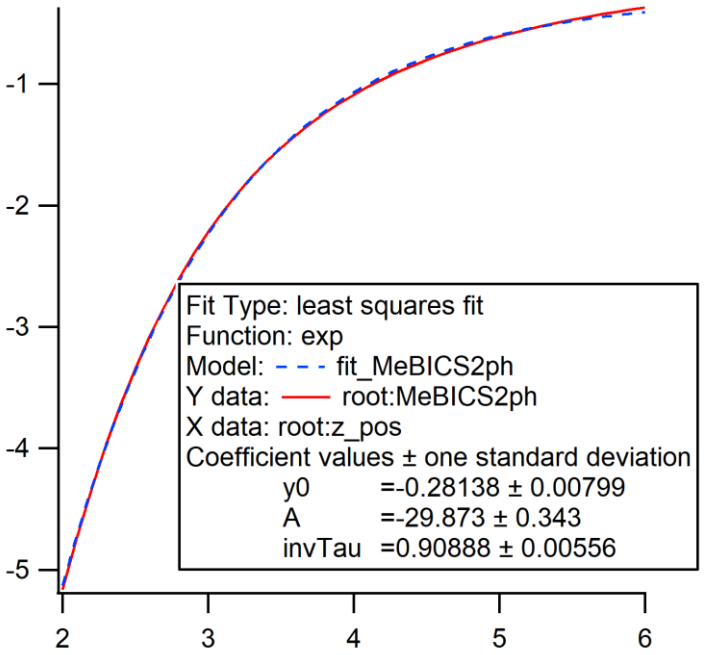

Figure 84. zNICS exponential fit: Benzimidazole dithiocarboxylate – phenyl ring

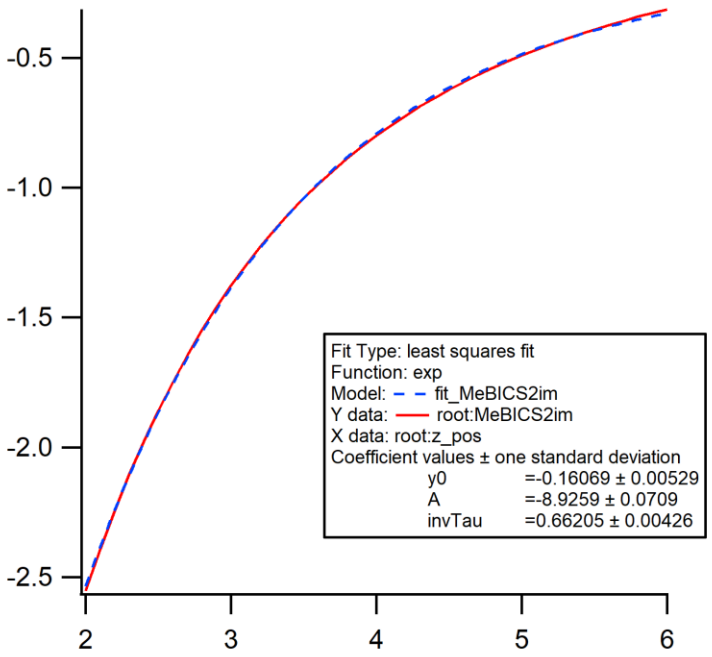

Figure 85. zNICS exponential fit: Benzimidazole dithiocarboxylate – imidazole ring

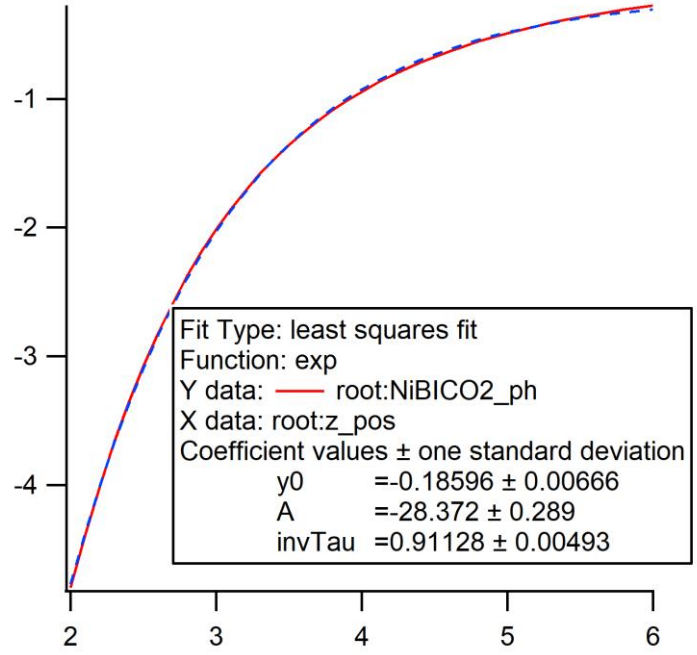

Figure 86. zNICS exponential fit: Nickel-Benzimidazole carboxylate – phenyl ring

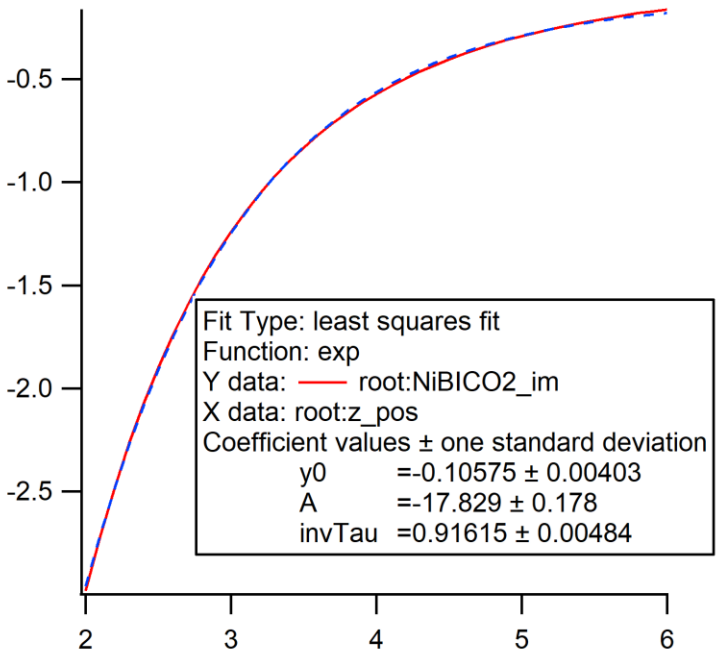

Figure 87. zNICS exponential fit: Nickel-Benzimidazole carboxylate – imidazole ring

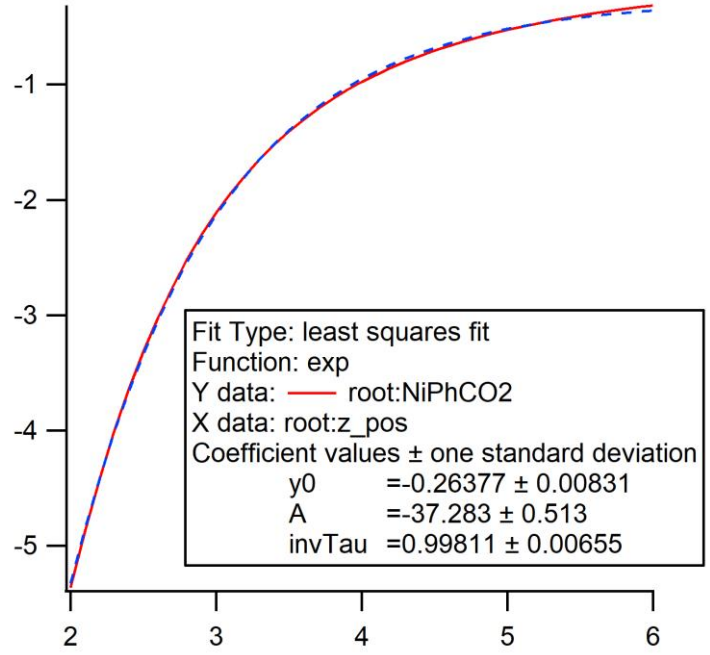

Figure 88. zNICS exponential fit: Nickel-Benzene carboxylate

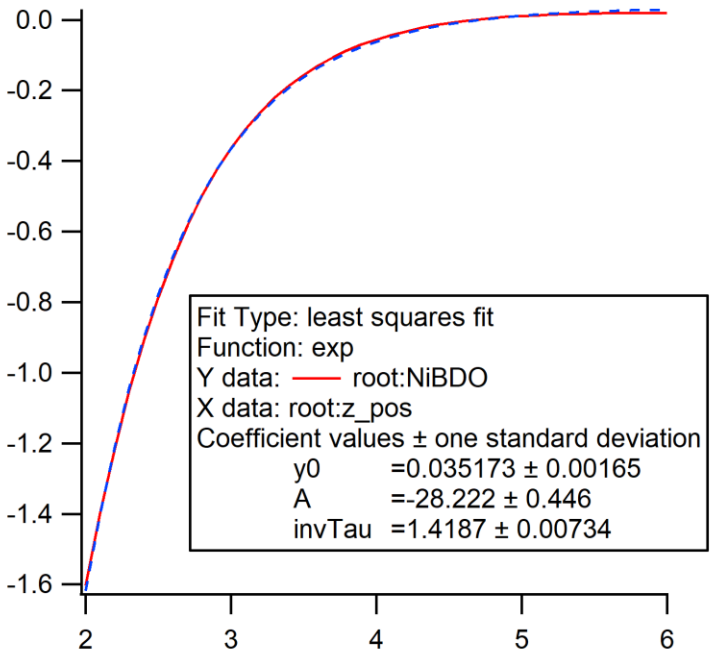

Figure 89. zNICS exponential fit: Nickel-bisdiolene

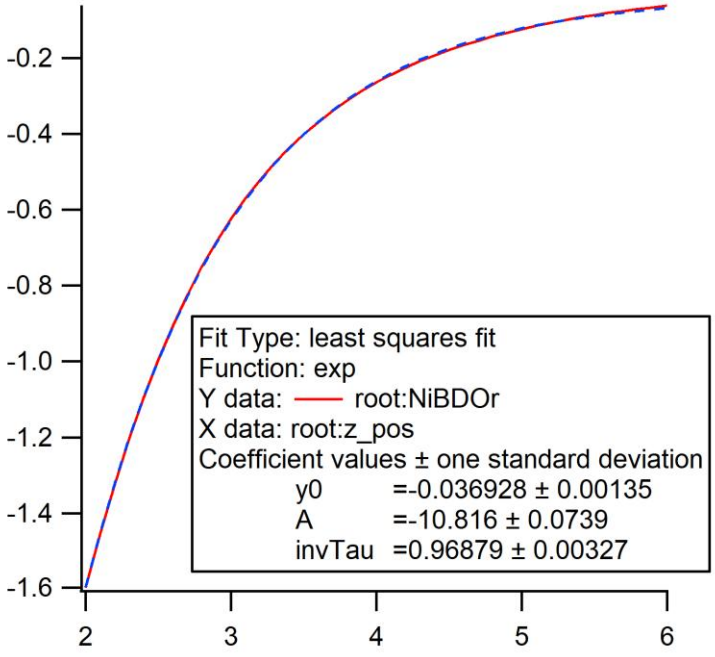

Figure 90. zNICS exponential fit: reduced Nickel-bisdiolene

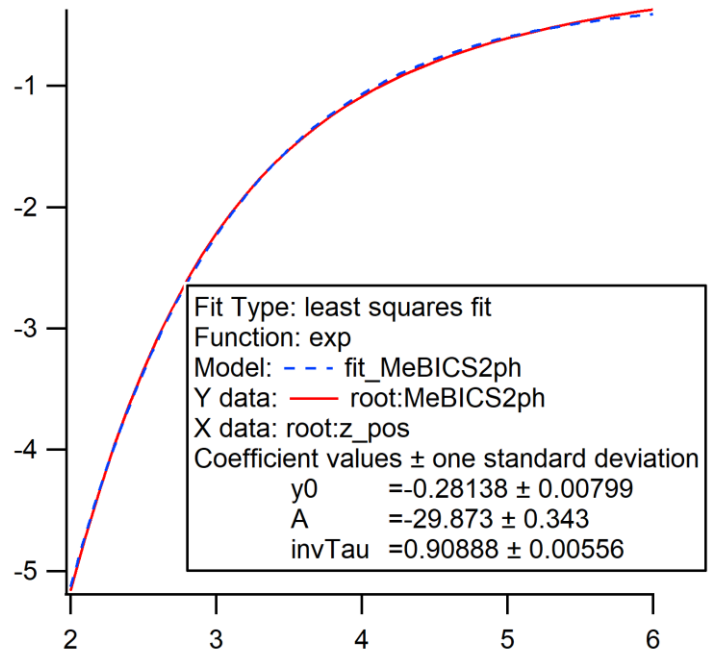

Figure 91. zNICS exponential fit: Nickel benzimidazole dithiocarboxylate – phenyl ring

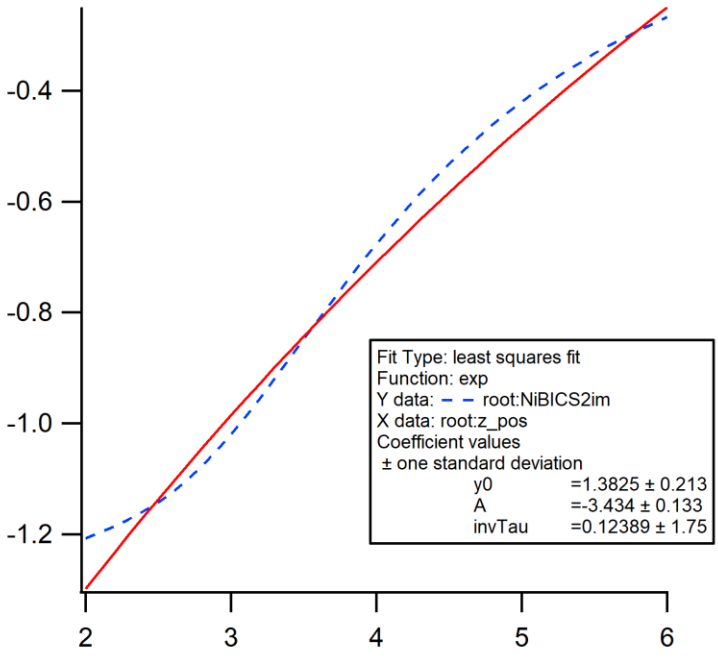

Figure 92. zNICS exponential fit: Nickel benzimidazole dithiocarboxylate – phenyl ring

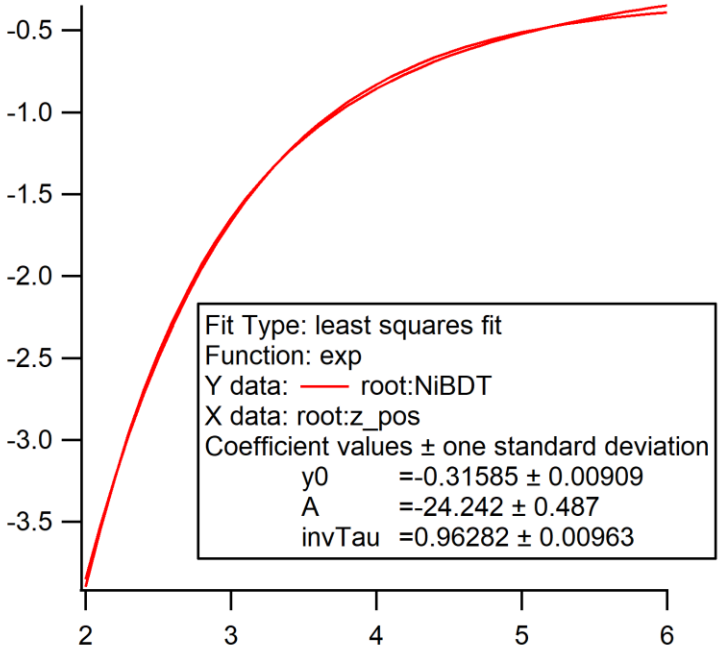

Figure 93. zNICS exponential fit: Nickel-bisdthiolene

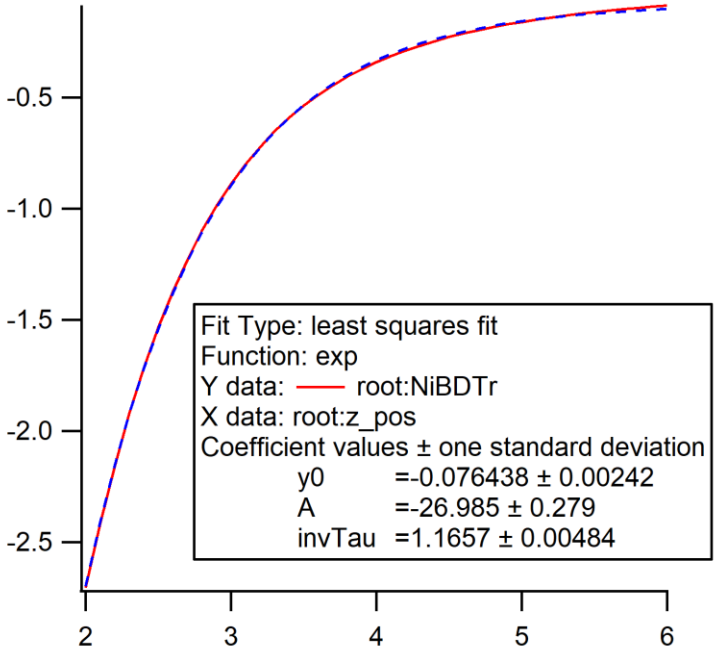

Figure 94. zNICS exponential fit: reduced Nickel-bisdiolene

Example Orca compound script

```
#to use this compound file as a general template, all you need to do is specify a few things. There are already some values there, so if you do not want to change some aspects then leave as is
#input theory in theo
#input basis set in basis
#input auxillary basis set in auxb
#input your filename in the compname variable with no file extension (no .inp)
#input the metal of interest in metal (as atomic symbol)
#input metal basis set in mbasis
#input heteroatom identity in hetatm
#input heteroatom basis set in hetbasis
#input charge in chg
#input unpaired electrons in upe, the multiplicity will be calculated for you
%Compound
Variable theo = "B3LYP";
Variable basis = "def2-TZVP";
Variable auxb = "def2/J";
Variable compname = "CuBICS2";
Variable metal = "Cu";
Variable mbasis = "def2-TZVP";
Variable hetatm = "S";
Variable hetbasis = "def2-TZVP";
Variable chg = 0;
Variable upe = 3;
Variable nproc = 16;
Variable smult;
smult = 2 * upe / 2 + 1;
New_Step
        !UKS &{theo} &{basis} &{auxb} USESYM VerySlowConv LOOSEOPT LOOSESCF
        %basis
```

```
        NewGTO &{metal} "&{mbasis}" end
        NewGTO &{hetatm} "&{hetbasis}" end
        end
    %scf
        AutoStart true
        end
    %pal
        nprocs &{nproc}
        end
    * xyzfile &{chg} &{smult} &{compname}.xyz *
STEP_END
New_Step
    !UKS &{theo} &{basis} &{auxb} USESYM OPT NORMALSCF
    %basis
        NewGTO &{metal} "&{mbasis}" end
        NewGTO &{hetatm} "&{hetbasis}" end
        end
    %pal
        nprocs &{nproc}
        end
    * xyzfile &{chg} &{smult} &{compname}_Compound_1.xyz *
STEP_END
New_Step
    !UKS &{theo} &{basis} &{auxb} USESYM TIGHTOPT TIGHTSCF
    %basis
        NewGTO &{metal} "&{mbasis}" end
        NewGTO &{hetatm} "&{hetbasis}" end
        end
    %pal
        nprocs &{nproc}
        end
```

```
        * xyzfile &{chg} &{smult} &{compname}_Compound_2.xyz *
STEP_END
New_Step
        !UKS &{theo} &{basis} &{auxb} USESYM ENERGY VERYTIGHTSCF
        !PrintBasis
        %basis
                NewGTO &{metal} "def2-TZVPPD" end
                NewGTO &{hetatm} "def2-TZVPPD" end
                end
        %pal
                nprocs &{nproc}
                end
        %Sym
                SymThresh 0.01
                end
        %output
        print[P_Density]1
        print[P_SpinDensity]1
        print[P_MOs]1
        print[P_OrbEn]1
        print[P_Loewdin]1
        XYZFile true
                end #output
        * xyzfile &{chg} &{smult} &{compname}_Compound_3.xyz *
STEP_END
End
```

Optimized structure geometries

Table 36. Optimized geometry coordinates of $NiBICO_2$

$NiBICO_2$	x	y	z
H	2.634898	0.759519	0.579895
C	1.702596	0.447996	0.107208
C	0.753800	1.421351	-0.242339
H	0.942491	2.476156	-0.045179
C	-0.429215	0.989961	-0.846187
C	-0.660252	-0.386454	-1.098061
C	0.286990	-1.350445	-0.746563
H	0.119110	-2.410451	-0.934049
C	1.473468	-0.910747	-0.139491
H	2.229275	-1.644262	0.143937
N	-1.537736	1.683973	-1.298785
N	-1.901702	-0.493038	-1.700352
C	-2.453564	0.778888	-1.828923
C	-1.713688	3.124685	-1.243608
C	-2.532734	-1.731238	-2.122377
C	-3.713036	1.093759	-2.392959
O	-4.517563	0.191586	-2.876276
O	-4.168150	2.310957	-2.473267
H	-0.842301	3.561893	-0.747349
H	-2.621030	3.383338	-0.685158
H	-1.808054	3.545377	-2.252640
H	-1.843616	-2.557181	-1.923059
H	-2.768082	-1.700981	-3.192791
H	-3.469716	-1.898188	-1.576313
H	-9.672802	5.766208	-4.698114
C	-8.982029	4.941165	-4.500749
H	-8.046516	5.109806	-5.048941
H	-8.744175	4.910700	-3.430934
H	-11.630982	5.618536	-5.697265
C	-11.798473	4.558130	-5.883152
H	-13.738399	4.850243	-6.779742
N	-9.612363	3.702213	-4.921702
C	-12.983419	4.117337	-6.492560
C	-10.852201	3.594701	-5.527301
O	-7.346423	0.899473	-4.143120
C	-9.060562	2.430547	-4.790441
C	-7.801646	2.116531	-4.224620

Table *36* Cont.	x	y	z
O	-6.997654	3.019172	-3.741222
C	-13.212009	2.758134	-6.737098
C	-11.082659	2.217857	-5.777410
N	-9.975357	1.524578	-5.320867
C	-12.264164	1.785460	-6.383402
H	-14.143104	2.445707	-7.211550
C	-9.798793	0.083899	-5.374197
H	-12.452414	0.730374	-6.579273
H	-8.894000	-0.175519	-5.936544
H	-9.699262	-0.334530	-4.364808
H	-10.672311	-0.354748	-5.865390
Ni	-5.757483	1.605502	-3.308243

Table 37. Optimized geometry coordinates of $NiPhCO_2$

$NiPhCO_2$	x	y	z
H	0.000000	0.000000	7.591385
C	0.000000	0.000000	6.508286
C	-1.207557	0.000000	5.815109
H	-2.144487	0.000000	6.357459
C	-1.210833	0.000000	4.427694
H	-2.139327	0.000000	3.872619
C	0.000000	0.000000	3.731149
C	0.000000	0.000000	2.260085
O	1.076774	0.000000	1.574470
O	-1.076774	0.000000	1.574470
C	1.210833	0.000000	4.427694
H	2.139327	0.000000	3.872619
C	1.207557	0.000000	5.815109
H	2.144487	0.000000	6.357459
O	-1.076774	0.000000	-1.574470
C	0.000000	0.000000	-6.508286
C	-1.207557	0.000000	-5.815109
C	1.207557	0.000000	-5.815109
C	-1.210833	0.000000	-4.427694
H	0.000000	0.000000	-7.591385
C	1.210833	0.000000	-4.427694
C	0.000000	0.000000	-3.731149
H	-2.144487	0.000000	-6.357459
C	0.000000	0.000000	-2.260085
H	2.144487	0.000000	-6.357459
H	-2.139327	0.000000	-3.872619
H	2.139327	0.000000	-3.872619
O	1.076774	0.000000	-1.574470
Ni	0.000000	0.000000	0.000000

Table 38. Optimized geometry coordinates of NiBDO

NiBDO	x	y	z
C	-0.721446	-2.511866	0.000000
C	0.721446	-2.511866	0.000000
C	1.429741	-3.731072	0.000000
H	2.511644	-3.717578	0.000000
C	0.710443	-4.902692	0.000000
H	1.232069	-5.851369	0.000000
C	-0.710443	-4.902692	0.000000
H	-1.232069	-5.851369	0.000000
C	-1.429741	-3.731072	0.000000
H	-2.511644	-3.717578	0.000000
O	-1.263484	-1.334616	0.000000
O	1.263484	-1.334616	0.000000
O	-1.263484	1.334616	0.000000
C	-0.721446	2.511866	0.000000
C	-1.429741	3.731072	0.000000
O	1.263484	1.334616	0.000000
C	0.721446	2.511866	0.000000
H	-2.511644	3.717578	0.000000
C	-0.710443	4.902692	0.000000
C	1.429741	3.731072	0.000000
C	0.710443	4.902692	0.000000
H	-1.232069	5.851369	0.000000
H	2.511644	3.717578	0.000000
H	1.232069	5.851369	0.000000
Ni	0.000000	0.000000	0.000000

Table 39. Optimized geometry coordinates of $NiBDO^{2\bullet}$

$NiBDO^{2\bullet}$	x	y	z
C	-0.728206	-2.544086	0.000000
C	0.728206	-2.544086	0.000000
C	1.428832	-3.773926	0.000000
H	2.510842	-3.760424	0.000000
C	0.712504	-4.943061	0.000000
H	1.233518	-5.892254	0.000000
C	-0.712504	-4.943061	0.000000
H	-1.233518	-5.892254	0.000000
C	-1.428832	-3.773926	0.000000
H	-2.510842	-3.760424	0.000000
O	-1.291232	-1.386736	0.000000
O	1.291232	-1.386736	0.000000
O	-1.291232	1.386736	0.000000
C	-0.728206	2.544086	0.000000
C	-1.428832	3.773926	0.000000
O	1.291232	1.386736	0.000000
C	0.728206	2.544086	0.000000
H	-2.510842	3.760424	0.000000
C	-0.712504	4.943061	0.000000
C	1.428832	3.773926	0.000000
C	0.712504	4.943061	0.000000
H	-1.233518	5.892254	0.000000
H	2.510842	3.760424	0.000000
H	1.233518	5.892254	0.000000
Ni	0.000000	0.000000	0.000000

Table 40. Optimized geometry coordinates of $NiBICS_2$

$NiBICS_2$	x	y	z
H	2.802899	0.542889	1.126678
C	1.963496	0.285139	0.494168
C	0.907067	1.186009	0.365239
H	0.923049	2.137143	0.879111
C	-0.150926	0.819118	-0.456328
C	-0.155293	-0.409502	-1.131840
C	0.897368	-1.306145	-1.002790
H	0.895712	-2.260768	-1.510430
C	1.959141	-0.937059	-0.177788
H	2.793874	-1.614990	-0.056445
N	-1.328882	1.467344	-0.777593
N	-1.324664	-0.468429	-1.866854
C	-2.065843	0.684952	-1.654650
C	-1.765273	2.679513	-0.101027
C	-1.579005	-1.506048	-2.854926
C	-3.311985	0.996926	-2.215637
S	-4.444110	-0.151704	-2.859494
S	-3.974642	2.593695	-2.380781
H	-1.321459	2.692994	0.893903
H	-2.846869	2.684896	-0.013984
H	-1.458382	3.572074	-0.647925
H	-0.619726	-1.890064	-3.199830
H	-2.124389	-1.089683	-3.695780
H	-2.166918	-2.321963	-2.432702
H	-9.381963	5.423615	-6.611967
C	-9.011859	4.919980	-5.719674
H	-7.983657	4.611797	-5.879234
H	-9.038062	5.609976	-4.875262
H	-11.681366	5.632771	-6.646848
C	-11.993626	4.608259	-6.499150
H	-13.953441	4.903874	-7.311250
N	-9.846611	3.752865	-5.477455
C	-13.272939	4.190845	-6.864471
C	-11.150523	3.664002	-5.927930
S	-7.515452	0.620760	-4.284686
C	-9.443070	2.523935	-4.976002
C	-8.194183	2.213602	-4.420017

Table *40* cont.	x	y	z
S	-7.075032	3.360651	-3.750856
C	-13.691028	2.875712	-6.662230
C	-11.570959	2.342027	-5.724434
N	-10.521135	1.664894	-5.132489
C	-12.845301	1.927078	-6.088566
H	-14.690043	2.582598	-6.957405
C	-10.663049	0.323249	-4.587192
H	-13.172826	0.906633	-5.945818
H	-10.374572	-0.434527	-5.317020
H	-10.032958	0.213200	-3.710760
H	-11.705440	0.177541	-4.305536
Ni	-5.752115	1.606316	-3.319351

Table 41. Optimized geometry coordinates of $NiPhCS_2$

$NiPhCS_2$	x	y	z
H	0.000000	8.054341	0.000000
C	0.000000	6.971408	0.000000
C	0.000000	6.274692	-1.205434
H	0.000000	6.813710	-2.144285
C	0.000000	4.889204	-1.207265
H	0.000000	4.347348	-2.143847
C	0.000000	4.174725	0.000000
C	0.000000	2.711442	0.000000
S	0.000000	1.754510	1.403015
S	0.000000	1.754510	-1.403015
C	0.000000	4.889204	1.207265
H	0.000000	4.347348	2.143847
C	0.000000	6.274692	1.205434
H	0.000000	6.813710	2.144285
S	0.000000	-1.754510	-1.403015
C	0.000000	-6.971408	0.000000
C	0.000000	-6.274692	-1.205434
C	0.000000	-6.274692	1.205434
C	0.000000	-4.889204	-1.207265
H	0.000000	-8.054341	0.000000
C	0.000000	-4.889204	1.207265
C	0.000000	-4.174725	0.000000
H	0.000000	-6.813710	-2.144285
C	0.000000	-2.711442	0.000000
H	0.000000	-6.813710	2.144285
H	0.000000	-4.347348	-2.143847
H	0.000000	-4.347348	2.143847
S	0.000000	-1.754510	1.403015
Ni	0.000000	0.000000	0.000000

Table 42. Optimized geometry coordinates of NiBDT

NiBDT	x	y	z
C	-0.710976	-2.994714	0.000000
C	0.710976	-2.994714	0.000000
C	1.403708	-4.226052	0.000000
H	2.486213	-4.219857	0.000000
C	0.705975	-5.408620	0.000000
H	1.241180	-6.349692	0.000000
C	-0.705975	-5.408620	0.000000
H	-1.241180	-6.349692	0.000000
C	-1.403708	-4.226052	0.000000
H	-2.486213	-4.219857	0.000000
S	-1.556276	-1.500670	0.000000
S	1.556276	-1.500670	0.000000
S	-1.556276	1.500670	0.000000
C	-0.710976	2.994714	0.000000
C	-1.403708	4.226052	0.000000
S	1.556276	1.500670	0.000000
C	0.710976	2.994714	0.000000
H	-2.486213	4.219857	0.000000
C	-0.705975	5.408620	0.000000
C	1.403708	4.226052	0.000000
C	0.705975	5.408620	0.000000
H	-1.241180	6.349692	0.000000
H	2.486213	4.219857	0.000000
H	1.241180	6.349692	0.000000
Ni	0.000000	0.000000	0.000000

Table 43. Optimized geometry coordinates of $NiBDT^{2\bullet}$

$NiBDT^{2\bullet}$	x	y	z
C	-0.703537	-3.024632	0.000000
C	0.703537	-3.024632	0.000000
C	1.396931	-4.241024	0.000000
H	2.479662	-4.235776	0.000000
C	0.698706	-5.437891	0.000000
H	1.240557	-6.374983	0.000000
C	-0.698706	-5.437891	0.000000
H	-1.240557	-6.374983	0.000000
C	-1.396931	-4.241024	0.000000
H	-2.479662	-4.235776	0.000000
S	-1.568463	-1.508248	0.000000
S	1.568463	-1.508248	0.000000
S	-1.568463	1.508248	0.000000
C	-0.703537	3.024632	0.000000
C	-1.396931	4.241024	0.000000
S	1.568463	1.508248	0.000000
C	0.703537	3.024632	0.000000
H	-2.479662	4.235776	0.000000
C	-0.698706	5.437891	0.000000
C	1.396931	4.241024	0.000000
C	0.698706	5.437891	0.000000
H	-1.240557	6.374983	0.000000
H	2.479662	4.235776	0.000000
H	1.240557	6.374983	0.000000
Ni	0.000000	0.000000	0.000000

Table 44. Optimized geometry coordinates of $CuBICO_2$

$CuBICO_2$	x	y	z
H	8.426437	-0.858003	3.879124
C	7.496453	-1.166582	3.419439
C	6.559387	-0.193764	3.058207
H	6.750784	0.856414	3.230977
C	5.379126	-0.629876	2.471396
C	5.136524	-1.996777	2.249894
C	6.067976	-2.961443	2.609279
H	5.885578	-4.013935	2.441042
C	7.256093	-2.520454	3.199930
H	8.002114	-3.248349	3.491553
N	4.281161	0.065436	2.012371
N	3.895612	-2.107282	1.660454
C	3.346519	-0.835490	1.504149
C	4.181714	1.512509	2.084979
C	3.315279	-3.385157	1.286837
C	2.089283	-0.521353	0.940319
O	1.278362	-1.433008	0.489123
O	1.656615	0.700738	0.833120
H	4.243243	1.836258	3.127223
H	3.235279	1.826620	1.660803
H	5.003938	1.968524	1.527474
H	3.965100	-3.890708	0.567831
H	2.340869	-3.218186	0.843173
H	3.213128	-4.018329	2.172010
H	-3.965100	3.890708	-0.567831
C	-3.315279	3.385157	-1.286837
H	-3.213128	4.018329	-2.172010
H	-2.340869	3.218186	-0.843173
H	-5.885578	4.013935	-2.441042
C	-6.067976	2.961443	-2.609279
H	-8.002114	3.248349	-3.491553
N	-3.895612	2.107282	-1.660454
C	-7.256093	2.520454	-3.199930
C	-5.136524	1.996777	-2.249894
O	-1.656615	-0.700738	-0.833120
C	-3.346519	0.835490	-1.504149
C	-2.089283	0.521353	-0.940319

Table *44* cont.	x	y	z
O	-1.278362	1.433008	-0.489123
C	-7.496453	1.166582	-3.419439
C	-5.379126	0.629876	-2.471396
N	-4.281161	-0.065436	-2.012371
C	-6.559387	0.193764	-3.058207
H	-8.426437	0.858003	-3.879124
C	-4.181714	-1.512509	-2.084979
H	-6.750784	-0.856414	-3.230977
H	-3.235279	-1.826620	-1.660803
H	-5.003938	-1.968524	-1.527474
H	-4.243243	-1.836258	-3.127223
Cu	0.000000	0.000000	0.000000

Table 45. Optimized geometry coordinates of $CuPhCO_2$

$CuPhCO_2$	x	y	z
H	0.000000	0.000000	7.674813
C	0.000000	0.000000	6.591676
C	-1.207141	0.000000	5.898054
H	-2.144365	0.000000	6.439982
C	-1.209933	0.000000	4.510436
H	-2.138282	0.000000	3.955413
C	0.000000	0.000000	3.812417
C	0.000000	0.000000	2.336157
O	1.086770	0.000000	1.670441
O	-1.086770	0.000000	1.670441
C	1.209933	0.000000	4.510436
H	2.138282	0.000000	3.955413
C	1.207141	0.000000	5.898054
H	2.144365	0.000000	6.439982
O	-1.086770	0.000000	-1.670441
C	0.000000	0.000000	-6.591676
C	-1.207141	0.000000	-5.898054
C	1.207141	0.000000	-5.898054
C	-1.209933	0.000000	-4.510436
H	0.000000	0.000000	-7.674813
C	1.209933	0.000000	-4.510436
C	0.000000	0.000000	-3.812417
H	-2.144365	0.000000	-6.439982
C	0.000000	0.000000	-2.336157
H	2.144365	0.000000	-6.439982
H	-2.138282	0.000000	-3.955413
H	2.138282	0.000000	-3.955413
O	1.086770	0.000000	-1.670441
Cu	0.000000	0.000000	0.000000

Table 46. Optimized geometry coordinates of CuBDO

CuBDO	x	y	z
C	-0.731984	-2.596099	-0.048176
C	0.731984	-2.596099	0.048176
C	1.424343	-3.832927	0.081901
H	2.504507	-3.820127	0.146609
C	0.711501	-5.002063	0.041074
H	1.232432	-5.950914	0.071112
C	-0.711501	-5.002063	-0.041074
H	-1.232432	-5.950914	-0.071112
C	-1.424343	-3.832927	-0.081901
H	-2.504507	-3.820127	-0.146609
O	-1.309765	-1.452751	-0.098119
O	1.309765	-1.452751	0.098119
O	-1.309765	1.452751	0.098119
C	-0.731984	2.596099	0.048176
C	-1.424343	3.832927	0.081901
O	1.309765	1.452751	-0.098119
C	0.731984	2.596099	-0.048176
H	-2.504507	3.820127	0.146609
C	-0.711501	5.002063	0.041074
C	1.424343	3.832927	-0.081901
C	0.711501	5.002063	-0.041074
H	-1.232432	5.950914	0.071112
H	2.504507	3.820127	-0.146609
H	1.232432	5.950914	-0.071112
Cu	0.000000	0.000000	0.000000

Table 47. Optimized geometry coordinates of $CuBDO^{2\bullet}$

$CuBDO^{2\bullet}$	x	y	z
C	-0.710412	-3.112613	-0.119911
C	0.710412	-3.112613	0.119911
C	1.378484	-4.358701	0.240789
H	2.444603	-4.352829	0.426321
C	0.696984	-5.540069	0.122547
H	1.225802	-6.480273	0.215137
C	-0.696984	-5.540069	-0.122547
H	-1.225802	-6.480273	-0.215137
C	-1.378484	-4.358701	-0.240789
H	-2.444603	-4.352829	-0.426321
S	-1.616142	-1.670729	-0.256097
S	1.616142	-1.670729	0.256097
S	-1.616142	1.670729	0.256097
C	-0.710412	3.112613	0.119911
C	-1.378484	4.358701	0.240789
S	1.616142	1.670729	-0.256097
C	0.710412	3.112613	-0.119911
H	-2.444603	4.352829	0.426321
C	-0.696984	5.540069	0.122547
C	1.378484	4.358701	-0.240789
C	0.696984	5.540069	-0.122547
H	-1.225802	6.480273	0.215137
H	2.444603	4.352829	-0.426321
H	1.225802	6.480273	-0.215137
Cu	0.000000	0.000000	0.000000

Table 48. Optimized geometry coordinates of $CuBICS_2$

$CuBICS_2$	x	y	z
H	2.817057	0.481634	1.241694
C	2.001039	0.245200	0.571382
C	0.911092	1.110957	0.494950
H	0.878212	2.015442	1.086398
C	-0.115065	0.773229	-0.378079
C	-0.056255	-0.393497	-1.152644
C	1.030389	-1.255108	-1.076699
H	1.077147	-2.162695	-1.662499
C	2.060174	-0.915179	-0.200773
H	2.920085	-1.566961	-0.118145
N	-1.312804	1.398906	-0.671584
N	-1.208993	-0.437041	-1.915084
C	-1.999569	0.663903	-1.625304
C	-1.823086	2.516366	0.109410
C	-1.390069	-1.385909	-3.003940
C	-3.251195	0.974827	-2.187756
S	-4.333382	-0.220665	-2.831890
S	-3.868302	2.593339	-2.308541
H	-1.390454	2.458331	1.107742
H	-2.904094	2.454226	0.179400
H	-1.562709	3.471738	-0.346855
H	-0.405431	-1.672213	-3.372491
H	-1.956399	-0.923767	-3.805757
H	-1.928254	-2.273871	-2.671140
H	-9.368158	5.260741	-6.906686
C	-8.999076	4.834264	-5.974366
H	-7.989418	4.464663	-6.119944
H	-8.975001	5.605202	-5.203778
H	-11.662761	5.583490	-6.891690
C	-12.011886	4.588969	-6.650877
H	-13.975856	4.894157	-7.448737
N	-9.877980	3.736340	-5.598663
C	-13.313895	4.194618	-6.955226
C	-11.194166	3.662979	-6.016128
S	-7.644185	0.605544	-4.324486
C	-9.511523	2.538980	-5.004413
C	-8.258868	2.224956	-4.445863
S	-7.172800	3.419516	-3.806582
C	-13.778436	2.919226	-6.633202

Table *48* cont.	x	y	z
C	-11.660471	2.381005	-5.693894
N	-10.623568	1.714044	-5.067612
C	-12.957972	1.988992	-5.996938
H	-14.794471	2.643221	-6.883388
C	-10.810837	0.439495	-4.389962
H	-13.321222	0.997938	-5.762742
H	-10.567278	-0.397590	-5.044902
H	-10.168764	0.388086	-3.516873
H	-11.852994	0.369210	-4.079576
Cu	-5.754509	1.598749	-3.318588

Table 49. Optimized geometry coordinates of $CuPhCS_2$

$CuPhCS_2$	x	y	z
H	0.000000	0.000000	8.147291
C	0.000000	0.000000	7.064278
C	-1.170719	0.283562	6.366801
H	-2.083780	0.504832	6.904778
C	-1.172074	0.283802	4.981131
H	-2.082747	0.504636	4.440838
C	0.000000	0.000000	4.263730
C	0.000000	0.000000	2.792945
S	1.397222	-0.328495	1.883142
S	-1.397222	0.328495	1.883142
C	1.172074	-0.283802	4.981131
H	2.082747	-0.504636	4.440838
C	1.170719	-0.283562	6.366801
H	2.083780	-0.504832	6.904778
S	-1.397222	0.328495	-1.883142
C	0.000000	0.000000	-7.064278
C	-1.170719	0.283562	-6.366801
C	1.170719	-0.283562	-6.366801
C	-1.172074	0.283802	-4.981131
H	0.000000	0.000000	-8.147291
C	1.172074	-0.283802	-4.981131
C	0.000000	0.000000	-4.263730
H	-2.083780	0.504832	-6.904778
C	0.000000	0.000000	-2.792945
H	2.083780	-0.504832	-6.904778
H	-2.082747	0.504636	-4.440838
H	2.082747	-0.504636	-4.440838
S	1.397222	-0.328495	-1.883142
Cu	0.000000	0.000000	0.000000

Table 50. Optimized geometry coordinates of CuBDT

CuBDT	x	y	z
C	-0.705092	-3.033405	0.000000
C	0.705092	-3.033405	0.000000
C	1.398437	-4.256321	0.000000
H	2.481203	-4.251485	0.000000
C	0.701934	-5.446593	0.000000
H	1.242028	-6.384723	0.000000
C	-0.701934	-5.446593	0.000000
H	-1.242028	-6.384723	0.000000
C	-1.398437	-4.256321	0.000000
H	-2.481203	-4.251485	0.000000
S	-1.587123	-1.535683	0.000000
S	1.587123	-1.535683	0.000000
S	-1.587123	1.535683	0.000000
C	-0.705092	3.033405	0.000000
C	-1.398437	4.256321	0.000000
S	1.587123	1.535683	0.000000
C	0.705092	3.033405	0.000000
H	-2.481203	4.251485	0.000000
C	-0.701934	5.446593	0.000000
C	1.398437	4.256321	0.000000
C	0.701934	5.446593	0.000000
H	-1.242028	6.384723	0.000000
H	2.481203	4.251485	0.000000
H	1.242028	6.384723	0.000000
Cu	0.000000	0.000000	0.000000

Table 51. Optimized geometry coordinates of $CuBDT^{2\bullet}$

$CuBDT^{2\bullet}$	x	y	z
C	-0.710412	-3.112613	-0.119911
C	0.710412	-3.112613	0.119911
C	1.378484	-4.358701	0.240789
H	2.444603	-4.352829	0.426321
C	0.696984	-5.540069	0.122547
H	1.225802	-6.480273	0.215137
C	-0.696984	-5.540069	-0.122547
H	-1.225802	-6.480273	-0.215137
C	-1.378484	-4.358701	-0.240789
H	-2.444603	-4.352829	-0.426321
S	-1.616142	-1.670729	-0.256097
S	1.616142	-1.670729	0.256097
S	-1.616142	1.670729	0.256097
C	-0.710412	3.112613	0.119911
C	-1.378484	4.358701	0.240789
S	1.616142	1.670729	-0.256097
C	0.710412	3.112613	-0.119911
H	-2.444603	4.352829	0.426321
C	-0.696984	5.540069	0.122547
C	1.378484	4.358701	-0.240789
C	0.696984	5.540069	-0.122547
H	-1.225802	6.480273	0.215137
H	2.444603	4.352829	-0.426321
H	1.225802	6.480273	-0.215137
Cu	0.000000	0.000000	0.000000

Table 52. Optimized geometry coordinates of bis-CoBICS$_2$

bisCoBICS$_2$	z	y	z
H	2.894420	0.592127	1.021902
C	2.027210	0.310697	0.438921
C	1.008018	1.241967	0.242797
H	1.080610	2.238618	0.655610
C	-0.087707	0.843353	-0.511730
C	-0.164625	-0.445948	-1.057224
C	0.850915	-1.372745	-0.861689
H	0.793127	-2.372787	-1.268654
C	1.950583	-0.971785	-0.103735
H	2.757900	-1.671980	0.066854
N	-1.244843	1.509531	-0.870421
N	-1.355077	-0.525075	-1.755675
C	-2.039927	0.677221	-1.646027
C	-1.612591	2.799046	-0.305492
C	-1.674149	-1.641000	-2.633417
C	-3.285967	0.988428	-2.206185
S	-4.485194	-0.171718	-2.698622
S	-3.876193	2.594821	-2.518601
H	-1.128097	2.896472	0.665514
H	-2.688967	2.852990	-0.178541
H	-1.300632	3.620437	-0.951638
H	-0.739210	-2.085660	-2.972956
H	-2.237839	-1.286339	-3.490074
H	-2.269693	-2.395415	-2.117893
H	-9.341373	5.273162	-6.872863
C	-8.959871	4.826668	-5.955410
H	-7.953659	4.457515	-6.125234
H	-8.921594	5.583230	-5.170747
H	-11.618506	5.565339	-6.893422
C	-11.969537	4.573676	-6.643754
H	-13.933537	4.877669	-7.442966
N	-9.836249	3.724777	-5.588273
C	-13.273228	4.180293	-6.944193
C	-11.153241	3.651193	-6.002424
S	-7.615833	0.612895	-4.149519
C	-9.471424	2.531379	-4.980930
C	-8.224107	2.219673	-4.423756
S	-7.039507	3.379791	-3.896419
C	-13.740356	2.909043	-6.611850

Table *52* cont.	x	y	z
C	-11.623269	2.373484	-5.667122
N	-10.588562	1.709586	-5.034435
C	-12.921451	1.982263	-5.967575
H	-14.756949	2.632841	-6.859575
C	-10.771197	0.431606	-4.363500
H	-13.287580	0.994205	-5.725359
H	-10.490400	-0.400880	-5.009818
H	-10.158314	0.392623	-3.468753
H	-11.820800	0.339320	-4.087166
Co	-5.754444	1.604085	-3.316459

Table 53. Optimized geometry coordinates of CoBDT

CoBDT	x	y	z
C	-0.707078	-3.028183	0.000000
C	0.707078	-3.028183	0.000000
C	1.400065	-4.252011	0.000000
H	2.482646	-4.245937	0.000000
C	0.702611	-5.441021	0.000000
H	1.240914	-6.380279	0.000000
C	-0.702611	-5.441021	0.000000
H	-1.240914	-6.380279	0.000000
C	-1.400065	-4.252011	0.000000
H	-2.482646	-4.245937	0.000000
S	-1.566677	-1.522764	0.000000
S	1.566677	-1.522764	0.000000
S	-1.566677	1.522764	0.000000
C	-0.707078	3.028183	0.000000
C	-1.400065	4.252011	0.000000
S	1.566677	1.522764	0.000000
C	0.707078	3.028183	0.000000
H	-2.482646	4.245937	0.000000
C	-0.702611	5.441021	0.000000
C	1.400065	4.252011	0.000000
C	0.702611	5.441021	0.000000
H	-1.240914	6.380279	0.000000
H	2.482646	4.245937	0.000000
H	1.240914	6.380279	0.000000
Co	0.000000	0.000000	0.000000

Table 54. Optimized geometry coordinates of $CoBDT^{2\bullet}$

$CoBDT^{2\bullet}$	x	y	z
C	-0.704839	-3.055046	0.000000
C	0.704839	-3.055046	0.000000
C	1.396682	-4.274318	0.000000
H	2.479366	-4.269167	0.000000
C	0.699775	-5.468925	0.000000
H	1.241203	-6.406317	0.000000
C	-0.699775	-5.468925	0.000000
H	-1.241203	-6.406317	0.000000
C	-1.396682	-4.274318	0.000000
H	-2.479366	-4.269167	0.000000
S	-1.581032	-1.544678	0.000000
S	1.581032	-1.544678	0.000000
S	-1.581032	1.544678	0.000000
C	-0.704839	3.055046	0.000000
C	-1.396682	4.274318	0.000000
S	1.581032	1.544678	0.000000
C	0.704839	3.055046	0.000000
H	-2.479366	4.269167	0.000000
C	-0.699775	5.468925	0.000000
C	1.396682	4.274318	0.000000
C	0.699775	5.468925	0.000000
H	-1.241203	6.406317	0.000000
H	2.479366	4.269167	0.000000
H	1.241203	6.406317	0.000000
Co	0.000000	0.000000	0.000000

Table 55. Optimized geometry coordinates of tris-CoBICS$_2$

trisCoBICS$_2$	x	y	z
H	-2.557175	0.538062	4.862977
C	-2.598639	0.404834	3.789771
C	-3.527500	1.136644	3.048326
H	-4.193197	1.838342	3.531610
C	-3.549981	0.939422	1.674243
C	-2.670135	0.040389	1.054401
C	-1.746879	-0.687818	1.792632
H	-1.075399	-1.393361	1.323215
C	-1.724860	-0.489130	3.173942
H	-1.016170	-1.042954	3.775830
N	-4.341856	1.487453	0.682489
N	-2.930112	0.082280	-0.302693
C	-3.967876	0.972092	-0.552734
C	-5.515031	2.294985	0.976093
C	-2.068683	-0.557921	-1.283812
C	-4.524269	1.288318	-1.799694
S	-4.429339	0.295961	-3.217924
S	-5.410633	2.734042	-2.160033
H	-5.878962	2.020160	1.965785
H	-6.288529	2.101992	0.239694
H	-5.281146	3.360441	0.958235
H	-1.070368	-0.645305	-0.855863
H	-2.024335	0.045309	-2.184890
H	-2.436657	-1.549555	-1.551270
H	-10.473371	4.454666	-7.366342
C	-9.761621	4.355720	-6.546913
H	-8.867896	3.852800	-6.901575
H	-9.479787	5.347428	-6.189743
H	-12.596495	5.019641	-6.616559
C	-12.787906	4.224997	-5.908764
H	-14.918729	4.446610	-5.968630
N	-10.383815	3.568595	-5.494334
C	-14.092353	3.899716	-5.533589
C	-11.754511	3.502187	-5.328179
S	-7.673885	0.932223	-3.964327
C	-9.767357	2.631246	-4.674119
C	-8.390864	2.397659	-4.550183
S	-7.144505	3.530840	-4.960516
C	-14.348020	2.888488	-4.609477

Table *55* cont.	x	y	z
C	-12.011753	2.484780	-4.397975
N	-10.790097	1.974036	-4.000860
C	-13.309533	2.161329	-4.025639
H	-15.370417	2.658726	-4.338961
C	-10.654574	1.048612	-2.887647
H	-13.516304	1.369115	-3.319409
H	-10.643460	0.012466	-3.229269
H	-9.728547	1.243346	-2.356221
H	-11.497886	1.198591	-2.213897
Co	-5.629957	1.929469	-4.303551
H	-4.834075	1.755891	-10.519435
H	-4.872120	0.315071	-9.475113
C	-4.746045	1.398652	-9.493602
H	-2.940510	1.342185	-11.778423
H	-5.527797	1.844486	-8.887140
C	-2.173914	1.800353	-11.168913
H	-0.772308	2.006787	-12.776954
S	-5.322717	1.037569	-6.400362
N	-3.442168	1.791384	-8.983877
C	-0.947423	2.172034	-11.721830
C	-2.360839	2.027292	-9.812077
C	-3.134081	2.187650	-7.687903
C	-3.965378	2.103827	-6.562475
C	0.053097	2.747419	-10.940940
C	-1.353741	2.605641	-9.026088
N	-1.836631	2.683633	-7.733149
H	0.993527	3.025691	-11.398536
C	-0.134121	2.975458	-9.576711
S	-3.793864	3.048993	-5.119326
C	-0.989304	3.028559	-6.602875
H	0.641752	3.434787	-8.979952
H	-1.309934	2.481763	-5.722113
H	-1.035248	4.095901	-6.381048
H	0.036349	2.753620	-6.848269

Table 56. Optimized geometry coordinates of $CrBICS_2$

$CrBICS_2$	x	y	z
H	-2.633493	0.456542	4.992695
C	-2.640924	0.350040	3.915728
C	-3.583995	1.055855	3.168636
H	-4.295050	1.712382	3.650852
C	-3.560714	0.894208	1.789606
C	-2.624753	0.051591	1.172154
C	-1.685394	-0.649714	1.916599
H	-0.969248	-1.310282	1.447705
C	-1.708489	-0.485272	3.301533
H	-0.989469	-1.019461	3.908911
N	-4.349950	1.431586	0.789115
N	-2.854339	0.113750	-0.190107
C	-3.921941	0.960819	-0.442273
C	-5.586822	2.148688	1.061575
C	-1.924416	-0.427937	-1.169742
C	-4.465660	1.280031	-1.701544
S	-4.419246	0.178558	-3.045505
S	-5.234366	2.804368	-2.028045
H	-5.954153	1.833634	2.037829
H	-6.325248	1.908673	0.303033
H	-5.430387	3.227606	1.059820
H	-0.934461	-0.463564	-0.715656
H	-1.897606	0.213174	-2.045077
H	-2.218006	-1.429282	-1.485901
H	-9.331248	5.943080	-5.113500
C	-9.691685	5.397864	-4.240660
H	-8.844611	5.188890	-3.595545
H	-10.416890	6.008181	-3.702709
H	-12.482276	6.062867	-4.771874
C	-12.707934	5.007407	-4.836540
H	-14.821558	5.290969	-5.043387
N	-10.339444	4.152116	-4.623034
C	-14.021018	4.564236	-4.995958
C	-11.708813	4.044488	-4.781882
S	-7.839726	1.071602	-3.845851
C	-9.769182	2.887928	-4.637257
C	-8.401697	2.578157	-4.509326
S	-7.143017	3.669792	-5.006858
C	-14.319087	3.206016	-5.098666

Table *56* cont.	x	y	z
C	-12.008966	2.678355	-4.881548
N	-10.812695	1.989394	-4.802175
C	-13.316162	2.238062	-5.042242
H	-15.347872	2.893687	-5.222429
C	-10.703663	0.573425	-5.121211
H	-13.556288	1.185925	-5.109270
H	-9.748804	0.375942	-5.596973
H	-10.774751	-0.043018	-4.224587
H	-11.511240	0.315692	-5.806238
Cr	-5.594059	1.928450	-4.278907
H	-4.307855	-0.699087	-8.986439
H	-2.578170	-1.123164	-8.949989
C	-3.348702	-0.488707	-8.512389
H	-1.922277	-0.383069	-11.056667
H	-3.437183	-0.704820	-7.452737
C	-1.625811	0.632407	-10.833046
H	-0.365692	0.831865	-12.554350
S	-5.343399	0.923226	-6.489407
N	-2.955756	0.899787	-8.700705
C	-0.755260	1.326112	-11.673877
C	-2.105459	1.301325	-9.714618
C	-3.135688	1.943012	-7.804804
C	-3.934254	1.930089	-6.645237
C	-0.382257	2.642067	-11.402887
C	-1.727809	2.623644	-9.440320
N	-2.374352	3.001360	-8.277677
H	0.294665	3.153651	-12.074702
C	-0.862458	3.314097	-10.278691
S	-3.590787	2.923051	-5.259000
C	-2.425156	4.383551	-7.824275
H	-0.558262	4.329932	-10.067355
H	-1.643263	4.591952	-7.093441
H	-3.386478	4.583883	-7.362761
H	-2.296367	5.031003	-8.691368

Table 57. Optimized geometry coordinates of $ScBICS_2$

$ScBICS_2$	x	y	z
H	-2.450880	0.489394	5.168161
C	-2.491019	0.352717	4.095364
C	-3.409200	1.090325	3.349532
H	-4.069353	1.800956	3.827347
C	-3.428358	0.887606	1.975718
C	-2.558768	-0.025545	1.363286
C	-1.643060	-0.758835	2.106704
H	-0.977475	-1.472828	1.641690
C	-1.623054	-0.553361	3.485344
H	-0.921554	-1.110594	4.092462
N	-4.209023	1.440747	0.976662
N	-2.818592	0.011382	0.005163
C	-3.839206	0.910867	-0.246761
C	-5.395438	2.236613	1.257647
C	-1.944344	-0.611728	-0.978245
C	-4.394683	1.226976	-1.506340
S	-4.473652	0.038820	-2.775167
S	-5.020286	2.816718	-1.836084
H	-5.764446	1.957212	2.244187
H	-6.159042	2.031786	0.514153
H	-5.172264	3.303066	1.235904
H	-0.946476	-0.685168	-0.546407
H	-1.906686	-0.001552	-1.874850
H	-2.300579	-1.604352	-1.253044
H	-9.456846	6.016009	-4.629001
C	-9.877501	5.343385	-3.881731
H	-9.080335	5.036594	-3.212398
H	-10.650334	5.861030	-3.313850
H	-12.642832	6.064990	-4.497865
C	-12.842836	5.031313	-4.743995
H	-14.941769	5.326303	-5.052297
N	-10.477877	4.171112	-4.501418
C	-14.132240	4.608144	-5.063497
C	-11.831326	4.080031	-4.771599
S	-8.027884	1.038998	-3.955477
C	-9.886366	2.931899	-4.674268
C	-8.520679	2.616297	-4.500262
S	-7.280157	3.790401	-4.831443
C	-14.396278	3.280317	-5.400045

Table *57* cont.	x	y	z
C	-12.097248	2.744880	-5.106384
N	-10.895082	2.062839	-5.051404
C	-13.381655	2.324535	-5.426362
H	-15.408081	2.983227	-5.643359
C	-10.730993	0.716808	-5.582166
H	-13.595877	1.294341	-5.675068
H	-9.747852	0.616488	-6.030455
H	-10.828273	-0.033825	-4.798152
H	-11.494992	0.556675	-6.342568
Sc	-5.584360	1.907618	-4.212414
H	-3.897877	-0.942644	-8.804884
H	-2.123939	-1.117312	-8.784980
C	-2.969260	-0.560330	-8.381371
H	-1.603455	-0.481123	-10.965781
H	-3.007700	-0.688696	-7.304562
C	-1.453775	0.582063	-10.837853
H	-0.259356	0.805451	-12.601706
S	-5.170751	0.766922	-6.521324
N	-2.779725	0.846965	-8.701648
C	-0.704247	1.315075	-11.756970
C	-2.009571	1.272733	-9.768849
C	-3.093716	1.927887	-7.896544
C	-3.868518	1.904266	-6.715755
C	-0.520907	2.690125	-11.609595
C	-1.822461	2.654023	-9.618768
N	-2.500940	3.036160	-8.475387
H	0.066217	3.230927	-12.340380
C	-1.077060	3.383745	-10.535636
S	-3.554046	3.016027	-5.415144
C	-2.747401	4.430871	-8.137091
H	-0.919325	4.447151	-10.420166
H	-2.004248	4.806456	-7.434075
H	-3.727915	4.530414	-7.682823
H	-2.711802	5.013859	-9.057038

Single-crystal x-ray diffraction

Table 58. Crystallographic details for $MeBICS_2$. SCXRD data were collected on a Bruker Apex2 diffractometer, using Cu Kα (λ = 1.54178 Å) radiation.

Identification code	**$MeBICS_2$**
Empirical formula	$C_{10}H_{10}N_2S_2$
Formula weight	222.32 g mol^{-1}
Temperature	173(2) K
Wavelength	1.54178 Å
Crystal system	monoclinic
Space group	*C*2/*c* (No. 15)
Unit cell dimensions	*a* = 10.1015(7) Å
	b = 17.0483(11) Å
	c = 6.6865(10) Å
	β = 99.848(3)°
Volume	1134.5(2) $Å^3$
Z	4
Density (calc.)	1.302 g cm^{-3}
Absorption coefficient	3.946 mm^{-1}
F(000)	464
Crystal size	0.01 × 0.01 × 0.13 mm^3
θ range for data collection	5.146 to 66.568°
Index ranges	$-11 \leq h \leq 11$
	$-20 \leq k \leq 20$
	$-6 \leq l \leq 7$
Reflections collected	5373
Independent reflections	1001
	[R(int) = 0.0695]
Absorption correction	Multi-scan
Min. and max. transmission	0.6026 and 0.7528
Data / restr. / param.	5373/0/ 66
Goodness-of-fit on F^2	1.063
Final R indices [$I > 2\sigma(I)$]	R1 = 0.0421,
	wR2 = 0.1193
Largest diff. peak and hole	0.222 and -0.277 e $Å^{-3}$

REFERENCES

(1) Nasalevich, M. A.; Veen, M. van der; Kapteijn, F.; Gascon, J. Metal–Organic Frameworks as Heterogeneous Photocatalysts: Advantages and Challenges. *CrystEngComm* **2014**, *16* (23), 4919–4926.

(2) Silva, C. G.; Corma, A.; García, H. Metal–Organic Frameworks as Semiconductors. *J. Mater. Chem.* **2010**, *20* (16), 3141–3156.

(3) Stavila, V.; Talin, A. A.; Allendorf, M. D. MOF-Based Electronic and Opto-Electronic Devices. *Chem. Soc. Rev.* **2014**, *43* (16), 5994–6010.

(4) Zhao, L.-L.; Wang, J.-Y.; Wu, Y.-M.; Wang, P.-F.; Liu, Z.-L.; Shu, J.; Yi, T.-F.; Zhang, Q. Unlocking the Multidimensional Application and Optimization Mechanism of MOFs Materials in Aqueous Zinc Ion Batteries. *J. Energy Chem.* **2025**, *111*, 249–273.

(5) Cui, H.; Liu, X.; Liu, C.; Zhu, H.; Liu, M.; Guo, R. Recent Progress on Cu-Based MOF Electrocatalysts for CO2 Reduction. *Fuel* **2026**, *403*, 136133.

(6) Mussa, N.-S.; Toshtay, K.; Dumeignil, F. Recent Developments in the Field of MOF-Based Catalytic Systems: A Review. *Appl. Catal. Gen.* **2025**, *708*, 120555.

(7) Zhu, L.; Yang, H.; Xu, T.; Shen, F.; Si, C. Precision-Engineered Construction of Proton-Conducting Metal–Organic Frameworks. *Nano-Micro Lett.* **2024**, *17* (1), 87.

(8) Mohtaram, M. S.; Abolghasemi, A.; Sayahi, S.; Rajabi, H.; Mohtaram, S.; Long, M.; Sabbaghi, S. MOF-Derived Nanomaterials: Transformative Innovations for Renewable Energy and Environmental Sustainability. *Coord. Chem. Rev.* **2026**, *546*, 217083.

(9) Nail, A.; Liu, H.; Meng, D.; Zhu, L.; Guo, X.; Li, C.; Ye, X.; Li, H. Metal-Organic Frameworks for Microneedles: Bridging the Gap between Nanomaterials and Transdermal Therapeutics. *J. Drug Deliv. Sci. Technol.* **2025**, *114*, 107444.

(10) So, S. H.; Lee, S. Y.; Kang, H.; Min, H.; Jung, H.; Lee, K. H.; Kim, D. W. Metal-Organic Frameworks for Gas Sensors: Comprehensive Review from Principal, Fabrication to Application. *Int. J. Extreme Manuf.* **2025**, *8* (1), 012001.

(11) Zhang, L.; Wang, Y.; Chen, Y.; Wu, Z.; Tan, J.; Li, J.; Chen, B.; Li, L. Metal-Organic Frameworks for Ethane-Selective Adsorption: A Comprehensive Review on Structural Design and Separation Applications. *Coord. Chem. Rev.* **2025**, *544*, 216974.

(12) Dai, Z.; Su, Y.; Liu, D.; Han, Q.; Greaves, T. L.; Lei, W.; Liu, Z.; Chen, Z. Metal-Organic Frameworks Based Solid-State Electrolytes for High-Performance Lithium Metal Batteries. *Chem. Eng. J.* **2025**, *524*, 169365.

(13) Zhang, Y.; Sun, S.; Wang, M.; Shen, Q.; Cong, S.; Zhao, Y.; Peng, J.; Pang, H. Metal-Organic Framework (MOF) Membranes for Mg2+/Li+ Separation. *Sep. Purif. Technol.* **2025**, *374*, 133737.

(14) Qin, Y.; Singh, N.; Singh, S.; Singh, V.; Mishra, V.; Li, S. Metal Organic Framework for Sustainable Removal of Heavy Metals Contamination from Wastewater: A Review. *Green Chem. Lett. Rev.* **2025**, *18* (1), 2545418.

(15) Prabhakar, N.; Pramoda, K.; Keri, R. S. Influence on Choice of Dopants for MOF-Based Supercapacitor Application: Synthesis, Properties and Electrochemistry. *J. Energy Storage* **2025**, *140*, 118986.

(16) Lou, C.; Li, X.; Keshta, B. E.; Wang, L.; Zhang, Y. Hofmann-Type Metal-Organic Frameworks: A Review on Gas Separation and Purification. *Sep. Purif. Technol.* **2025**, *374*, 133691.

(17) Fu, Y.; Qiu, W.; Zhou, S.-H.; Huang, H.; Luo, Y.; Lin, X.; Zhu, Q.-L. First-Principles Calculation Studies of Metal-Organic Frameworks and Their Derivatives for Electrochemical Energy Conversion and Storage. *Coord. Chem. Rev.* **2025**, *544*, 216982.

(18) Chang, X.-L.; Yan, T.; Pan, W.-G.; Wang, L.-W. Designing and Screening Metal-Organic Frameworks for Enhancing CO2 Capture and Separation Performance. *Coord. Chem. Rev.* **2025**, *543*, 216929. https://doi.org/10.1016/j.ccr.2025.216929.

(19) Jiang, Z.; Wang, S.; Lu, Y.; Meng, Z.; Pang, H. Conductive Metal–Organic Framework as an Emerging Platform with Electrochemical Energy Storage. *Coord. Chem. Rev.* **2025**, *544*, 216983.

(20) Taherinia, Z.; Ghorbani-Choghamarani, A. Catalysis and Photocatalysis by Metal–Organic Frameworks. *Top. Curr. Chem.* **2025**, *383* (4), 47.

(21) Arshad, M.; Khan, Z. U. H.; Talib, S.; Sabahat, S.; Shah, N. S.; Ajab, H.; Ahmad, F.; Khasim, S.; Diab, M. A.; El-Sabban, H. A. A Comprehensive Review: MOFs and Their Derivatives as High-Performance Supercapacitor Electrodes. *Chin. J. Struct. Chem.* **2025**, *44* (9), 100676.

(22) Walsh, A.; Butler, K. T.; Hendon, C. H. Chemical Principles for Electroactive Metal–Organic Frameworks. *MRS Bull.* **2016**, *41* (11), 870–876.

(23) Wu, C.; Geng, P.; Zhang, G.; Li, X.; Pang, H. Synthesis of Conductive MOFs and Their Electrochemical Application. *Small* **2024**, *20* (17), 2308264.

(24) Zhu, R.; Liu, L.; Zhang, G.; Zhang, Y.; Jiang, Y.; Pang, H. Advances in Electrochemistry of Intrinsic Conductive Metal-Organic Frameworks and Their Composites: Mechanisms, Synthesis and Applications. *Nano Energy* **2024**, *122*, 109333.

(25) Duan, P.; Dai, W.; Wang, Z.; Chen, M.; Niu, L.; Wu, T.; Zeng, L.; Feng, G. Conductive MOFs: Synthesis and Applications in Supercapacitors and Batteries. *Batter. Supercaps* **2024**, *7* (3), e202300536.

(26) Xie, L. S.; Skorupskii, G.; Dincă, M. Electrically Conductive Metal–Organic Frameworks. *Chem. Rev.* **2020**, *120* (16), 8536–8580.

(27) Saha, R.; Gupta, K.; Gómez García, C. J. Strategies to Improve Electrical Conductivity in Metal–Organic Frameworks: A Comparative Study. *Cryst. Growth Des.* **2024**, *24* (5), 2235–2265.

(28) Sun, L.; Park, S. S.; Sheberla, D.; Dincă, M. Measuring and Reporting Electrical Conductivity in Metal–Organic Frameworks: Cd2(TTFTB) as a Case Study. *J. Am. Chem. Soc.* **2016**, *138* (44), 14772–14782.

(29) Givaja, G.; Amo-Ochoa, P.; Gómez-García, C. J.; Zamora, F. Electrical Conductive Coordination Polymers. *Chem. Soc. Rev.* **2011**, *41* (1), 115–147.

(30) Murase, R.; Leong, C. F.; D'Alessandro, D. M. Mixed Valency as a Strategy for Achieving Charge Delocalization in Semiconducting and Conducting Framework Materials. *Inorg. Chem.* **2017**, *56* (23), 14373–14382.

(31) Kulesza, P. J.; Galus, Z. Mixed-Valence Electron Hopping, Redox Conduction and Migration Effects in Solid-State Electrochemistry of Transition Metal Hexacyanoferrates. *J. Electroanal. Chem.* **1992**, *323* (1), 261–274.

(32) Aubrey, M. L.; Kapelewski, M. T.; Melville, J. F.; Oktawiec, J.; Presti, D.; Gagliardi, L.; Long, J. R. Chemiresistive Detection of Gaseous Hydrocarbons and Interrogation of Charge Transport in Cu[Ni(2,3-Pyrazinedithiolate)2] by Gas Adsorption. *J. Am. Chem. Soc.* **2019**, *141* (12), 5005–5013.

(33) Pedersen, K. S.; Perlepe, P.; Aubrey, M. L.; Woodruff, D. N.; Reyes-Lillo, S. E.; Reinholdt, A.; Voigt, L.; Li, Z.; Borup, K.; Rouzières, M.; Samohvalov, D.; Wilhelm, F.; Rogalev, A.; Neaton, J. B.; Long, J. R.; Clérac, R. Formation of the Layered Conductive Magnet CrCl2(Pyrazine)2 through Redox-Active Coordination Chemistry. *Nat. Chem.* **2018**, *10* (10), 1056–1061.

(34) Hua, C.; Doheny, P. W.; Ding, B.; Chan, B.; Yu, M.; Kepert, C. J.; D'Alessandro, D. M. Through-Space Intervalence Charge Transfer as a Mechanism for Charge Delocalization in Metal–Organic Frameworks. *J. Am. Chem. Soc.* **2018**, *140* (21), 6622–6630.

(35) Park, S. S.; Hontz, E. R.; Sun, L.; Hendon, C. H.; Walsh, A.; Van Voorhis, T.; Dincă, M. Cation-Dependent Intrinsic Electrical Conductivity in Isostructural Tetrathiafulvalene-Based Microporous Metal–Organic Frameworks. *J. Am. Chem. Soc.* **2015**, *137* (5), 1774–1777.

(36) Heintz, R. A.; Zhao, H.; Ouyang, X.; Grandinetti, G.; Cowen, J.; Dunbar, K. R. New Insight into the Nature of Cu(TCNQ): Solution Routes to Two Distinct Polymorphs and Their Relationship to Crystalline Films That Display Bistable Switching Behavior. *Inorg. Chem.* **1999**, *38* (1), 144–156.

(37) Zhang, X.; Wang, Z.-X.; Xie, H.; Li, M.-X.; Woods, T. J.; Dunbar, K. R. A Cobalt(II) Spin-Crossover Compound with Partially Charged TCNQ Radicals and an Anomalous Conducting Behavior. *Chem. Sci.* **2016**, *7* (2), 1569–1574.

(38) Talin, A. A.; Centrone, A.; Ford, A. C.; Foster, M. E.; Stavila, V.; Haney, P.; Kinney, R. A.; Szalai, V.; El Gabaly, F.; Yoon, H. P.; Léonard, F.; Allendorf, M. D. Tunable Electrical Conductivity in Metal-Organic Framework Thin-Film Devices. *Science* **2014**, *343* (6166), 66–69.

(39) Schneider, C.; Ukaj, D.; Koerver, R.; Talin, A. A.; Kieslich, G.; Pujari, S. P.; Zuilhof, H.; Janek, J.; Allendorf, M. D.; Fischer, R. A. High Electrical Conductivity and High Porosity in a Guest@MOF Material: Evidence of TCNQ Ordering within Cu3BTC2 Micropores. *Chem. Sci.* **2018**, *9* (37), 7405–7412.

(40) Li, H.; Eddaoudi, M.; O'Keeffe, M.; Yaghi, O. M. Design and Synthesis of an Exceptionally Stable and Highly Porous Metal-Organic Framework. *Nature* **1999**, *402* (6759), 276–279.

(41) Bordiga, S.; Lamberti, C.; Ricchiardi, G.; Regli, L.; Bonino, F.; Damin, A.; Lillerud, K.-P.; Bjorgen, M.; Zecchina, A. Electronic and Vibrational Properties of a MOF-5 Metal–Organic Framework: ZnO Quantum Dot Behaviour. *Chem. Commun.* **2004**, No. 20, 2300–2301.

(42) Takaishi, S.; Hosoda, M.; Kajiwara, T.; Miyasaka, H.; Yamashita, M.; Nakanishi, Y.; Kitagawa, Y.; Yamaguchi, K.; Kobayashi, A.; Kitagawa, H. Electroconductive Porous Coordination Polymer Cu[Cu(Pdt)2] Composed of Donor and Acceptor Building Units. *Inorg. Chem.* **2009**, *48* (19), 9048–9050.

(43) Sheberla, D.; Sun, L.; Blood-Forsythe, M. A.; Er, S.; Wade, C. R.; Brozek, C. K.; Aspuru-Guzik, A.; Dincă, M. High Electrical Conductivity in Ni3(2,3,6,7,10,11-Hexaiminotriphenylene)2, a Semiconducting Metal–Organic Graphene Analogue. *J. Am. Chem. Soc.* **2014**, *136* (25), 8859–8862.

(44) Huang, X.; Sheng, P.; Tu, Z.; Zhang, F.; Wang, J.; Geng, H.; Zou, Y.; Di, C.; Yi, Y.; Sun, Y.; Xu, W.; Zhu, D. A Two-Dimensional π–d Conjugated Coordination Polymer with Extremely High Electrical Conductivity and Ambipolar Transport Behaviour. *Nat. Commun.* **2015**, *6* (1), 7408.

(45) Huang, X.; Zhang, S.; Liu, L.; Yu, L.; Chen, G.; Xu, W.; Zhu, D. Superconductivity in a Copper(II)-Based Coordination Polymer with Perfect Kagome Structure. *Angew. Chem. Int. Ed.* **2018**, *57* (1), 146–150.

(46) Day, R. W.; Bediako, D. K.; Rezaee, M.; Parent, L. R.; Skorupskii, G.; Arguilla, M. Q.; Hendon, C. H.; Stassen, I.; Gianneschi, N. C.; Kim, P.; Dincă, M. Single Crystals of Electrically Conductive Two-Dimensional Metal–Organic Frameworks: Structural and Electrical Transport Properties. *ACS Cent. Sci.* **2019**, *5* (12), 1959–1964.

(47) Xie, L. S.; Sun, L.; Wan, R.; Park, S. S.; DeGayner, J. A.; Hendon, C. H.; Dincă, M. Tunable Mixed-Valence Doping toward Record Electrical Conductivity in a Three-Dimensional Metal–Organic Framework. *J. Am. Chem. Soc.* **2018**, *140* (24), 7411–7414.

(48) Yan, Z.; Li, M.; Gao, H.-L.; Huang, X.-C.; Li, D. High-Spin versus Spin-Crossover versus Low-Spin: Geometry Intervention in Cooperativity in a 3D Polymorphic Iron(II)–Tetrazole MOFs System. *Chem. Commun.* **2012**, *48* (33), 3960–3962.

(49) Marshall, C. R.; Dvorak, J. P.; Twight, L. P.; Chen, L.; Kadota, K.; Andreeva, A. B.; Overland, A. E.; Ericson, T.; Cozzolino, A. F.; Brozek, C. K. Size-Dependent Properties of Solution-Processable Conductive MOF Nanocrystals. *J. Am. Chem. Soc.* **2022**, *144* (13), 5784–5794.

(50) Ghini, M.; Curreli, N.; Camellini, A.; Wang, M.; Asaithambi, A.; Kriegel, I. Photodoping of Metal Oxide Nanocrystals for Multi-Charge Accumulation and Light-Driven Energy Storage. *Nanoscale* **2021**, *13* (19), 8773–8783.

(51) Dan-Hardi, M.; Serre, C.; Frot, T.; Rozes, L.; Maurin, G.; Sanchez, C.; Férey, G. A New Photoactive Crystalline Highly Porous Titanium(IV) Dicarboxylate. *J. Am. Chem. Soc.* **2009**, *131* (31), 10857–10859.

(52) Saouma, C. T.; Tsou, C.-C.; Richard, S.; Ameloot, R.; Vermoortele, F.; Smolders, S.; Bueken, B.; DiPasquale, A. G.; Kaminsky, W.; Valdez, C. N.; Vos, D. E. D.; Mayer, J. M. Sodium-Coupled Electron Transfer Reactivity of Metal–Organic Frameworks Containing Titanium Clusters: The Importance of Cations in Redox Chemistry. *Chem. Sci.* **2019**, *10* (5), 1322–1331.

(53) Saouma, C. T.; Richard, S.; Smolders, S.; Delley, M. F.; Ameloot, R.; Vermoortele, F.; De Vos, D. E.; Mayer, J. M. Bulk-to-Surface Proton-Coupled Electron Transfer Reactivity of the Metal–Organic Framework MIL-125. *J. Am. Chem. Soc.* **2018**, *140* (47), 16184–16189.

(54) Altınçekiç, N. G.; Lander, C. W.; Roslend, A.; Yu, J.; Shao, Y.; Noh, H. Electrochemically Determined and Structurally Justified Thermochemistry of H Atom Transfer on Ti-Oxo Nodes of the Colloidal Metal–Organic Framework Ti-MIL-125. *J. Am. Chem. Soc.* **2024**, *146* (49), 33485–33498.

(55) Cotton, F. A.; Li, Z.; Liu, C. Y.; Murillo, C. A. Modulating Electronic Coupling Using O- and S-Donor Linkers. *Inorg. Chem.* **2007**, *46* (19), 7840–7847.

(56) Mortazavi, B.; Shahrokhi, M.; Hussain, T.; Zhuang, X.; Rabczuk, T. Theoretical Realization of Two-Dimensional M3(C6X6)2 (M = Co, Cr, Cu, Fe, Mn, Ni, Pd, Rh and X = O, S, Se) Metal–Organic Frameworks. *Appl. Mater. Today* **2019**, *15*, 405–415.

(57) Bader, R. F. W. Atoms in Molecules. *Acc. Chem. Res.* **1985**, *18* (1), 9–15.

(58) Poater, J.; Solà, M.; Duran, M.; Fradera, X. The Calculation of Electron Localization and Delocalization Indices at the Hartree–Fock, Density Functional and Post-Hartree–Fock Levels of Theory. *Theor. Chem. Acc.* **2002**, *107* (6), 362–371.

(59) Szabo, A.; Ostlund, N. S. *Modern Quantum Chemistry: Introduction to Advanced Electronic Structure Theory*; Dover Publications, 1996.

(60) Mayer, I. Charge, Bond Order and Valence in the AB Initio SCF Theory. *Chem. Phys. Lett.* **1983**, *97* (3), 270–274.

(61) Sun, Y.; Wang, T.; Luo, J.; Chen, J.; Huang, W.; Ding, J. Porous Semiconductor-Based Transistors and Their Applications. *Mater. Today Electron.* **2025**, *12*, 100151.

(62) Xie, L. S.; Skorupskii, G.; Dincă, M. Electrically Conductive Metal–Organic Frameworks. *Chem. Rev.* **2020**, *120* (16), 8536–8580. https://doi.org/10.1021/acs.chemrev.9b00766.

(63) Laeim, H.; Molahalli, V.; Prajongthat, P.; Pattanaporkratana, A.; Pathak, G.; Phettong, B.; Hongkarnjanakul, N.; Chattham, N. Porosity Tunable Metal-Organic Framework (MOF)-Based Composites for Energy Storage Applications: Recent Progress. *Polymers* **2025**, *17* (2), 130.

(64) Fritz, P. W.; Coskun, A. The Prospect of Dimensionality in Porous Semiconductors. *Chem. – Eur. J.* **2021**, *27* (27), 7489–7501.

(65) Xie, L. S.; Sun, L.; Wan, R.; Park, S. S.; DeGayner, J. A.; Hendon, C. H.; Dincă, M. Tunable Mixed-Valence Doping toward Record Electrical Conductivity in a Three-Dimensional Metal–Organic Framework. *J. Am. Chem. Soc.* **2018**, *140* (24), 7411–7414.

(66) Liu, W.-T.; Li, J.-Y.; Ni, Z.-P.; Bao, X.; Ou, Y.-C.; Leng, J.-D.; Liu, J.-L.; Tong, M.-L. Incomplete Spin Crossover versus Antiferromagnetic Behavior Exhibited in Three-Dimensional Porous Fe(II)-Bis(Tetrazolate) Frameworks. *Cryst. Growth Des.* **2012**, *12* (3), 1482–1488.

(67) Martinez-Martinez, A.; Resines-Urien, E.; Piñeiro-López, L.; Fernández-Blanco, A.; Lorenzo Mariano, A.; Albalad, J.; Maspoch, D.; Poloni, R.; Rodríguez-Velamazán, J. A.; Sañudo, E. C.; Burzurí, E.; Sánchez Costa, J. Spin Crossover-Assisted Modulation of Electron Transport in a Single-Crystal 3D Metal–Organic Framework. *Chem. Mater.* **2023**, *35* (15), 6012–6023.

(68) Davenport, A. M.; Marshall, C. R.; Nishiguchi, T.; Kadota, K.; Andreeva, A. B.; Horike, S.; Brozek, C. K. Size-Dependent Spin Crossover and Bond Flexibility in Metal–Organic Framework Nanoparticles. *J. Am. Chem. Soc.* **2024**, *146* (34), 23692–23698.

(69) Marshall, C. R.; Timmel, E. E.; Staudhammer, S. A.; Brozek, C. K. Experimental Evidence for a General Model of Modulated MOF Nanoparticle Growth. *Chem. Sci.* **2020**, *11* (42), 11539–11547.

(70) Majewski, M. B.; Noh, H.; Islamoglu, T.; Farha, O. K. NanoMOFs: Little Crystallites for Substantial Applications. *J. Mater. Chem. A* **2018**, *6* (17), 7338–7350.

(71) Ghorbanloo, M.; Safarifard, V.; Morsali, A. Heterogeneous Catalysis with a Coordination Modulation Synthesized MOF: Morphology-Dependent Catalytic Activity. *New J. Chem.* **2017**, *41* (10), 3957–3965.

(72) Webber, T. E.; Liu, W.-G.; Desai, S. P.; Lu, C. C.; Truhlar, D. G.; Penn, R. L. Role of a Modulator in the Synthesis of Phase-Pure NU-1000. *ACS Appl. Mater. Interfaces* **2017**, *9* (45), 39342–39346.

(73) Hu, Z.; Castano, I.; Wang, S.; Wang, Y.; Peng, Y.; Qian, Y.; Chi, C.; Wang, X.; Zhao, D. Modulator Effects on the Water-Based Synthesis of Zr/Hf Metal–Organic Frameworks: Quantitative Relationship Studies between Modulator, Synthetic Condition, and Performance. *Cryst. Growth Des.* **2016**, *16* (4), 2295–2301.

(74) Schaate, A.; Roy, P.; Godt, A.; Lippke, J.; Waltz, F.; Wiebcke, M.; Behrens, P. Modulated Synthesis of Zr-Based Metal–Organic Frameworks: From Nano to Single Crystals. *Chem. – Eur. J.* **2011**, *17* (24), 6643–6651.

(75) Hu, Z.; Peng, Y.; Kang, Z.; Qian, Y.; Zhao, D. A Modulated Hydrothermal (MHT) Approach for the Facile Synthesis of UiO-66-Type MOFs. *Inorg. Chem.* **2015**, *54* (10), 4862–4868.

(76) Morris, W.; Wang, S.; Cho, D.; Auyeung, E.; Li, P.; Farha, O. K.; Mirkin, C. A. Role of Modulators in Controlling the Colloidal Stability and Polydispersity of the UiO-66 Metal–Organic Framework. *ACS Appl. Mater. Interfaces* **2017**, *9* (39), 33413–33418.

(77) Garibay, S. J.; Iordanov, I.; Islamoglu, T.; DeCoste, J. B.; Farha, O. K. Synthesis and Functionalization of Phase-Pure NU-901 for Enhanced CO2 Adsorption: The Influence of a Zirconium Salt and Modulator on the Topology and Phase Purity. *CrystEngComm* **2018**, *20* (44), 7066–7070.

(78) Tajnšek, T. K.; Zabukovec Logar, N.; Mazaj, M. Tuning Size and Properties of Zinc Ascorbate Metal-Organic Framework via Acid Modulation. *Molecules* **2023**, *28* (1), 253.

(79) Schlesinger, H. I.; Valkenburgh, H. B. van. THE STRUCTURE OF FERRIC THIOCYANATE AND THE THIOCYANATE TEST FOR IRON. *J. Am. Chem. Soc.* **1931**, *53* (4), 1212–1216.

(80) Schimpf, A. M.; Knowles, K. E.; Carroll, G. M.; Gamelin, D. R. Electronic Doping and Redox-Potential Tuning in Colloidal Semiconductor Nanocrystals. *Acc. Chem. Res.* **2015**, *48* (7), 1929–1937.

(81) Carroll, G. M.; Schimpf, A. M.; Tsui, E. Y.; Gamelin, D. R. Redox Potentials of Colloidal N-Type ZnO Nanocrystals: Effects of Confinement, Electron Density, and Fermi-Level Pinning by Aldehyde Hydrogenation. *J. Am. Chem. Soc.* **2015**, *137* (34), 11163–11169.

(82) Valdez, C. N.; Schimpf, A. M.; Gamelin, D. R.; Mayer, J. M. Proton-Controlled Reduction of ZnO Nanocrystals: Effects of Molecular Reductants, Cations, and Thermodynamic Limitations. *J. Am. Chem. Soc.* **2016**, *138* (4), 1377–1385.

(83) Savateev, O. Photocharging of Semiconductor Materials: Database, Quantitative Data Analysis, and Application in Organic Synthesis. *Adv. Energy Mater.* **2022**, *12* (21), 2200352.

(84) Brozek, C. K.; Zhou, D.; Liu, H.; Li, X.; Kittilstved, K. R.; Gamelin, D. R. Soluble Supercapacitors: Large and Reversible Charge Storage in Colloidal Iron-Doped ZnO Nanocrystals. *Nano Lett.* **2018**, *18* (5), 3297–3302.

(85) Svensson Grape, E.; Brozek, C. K. Turn-On Conductivity with Proton-Coupled Electron Transport in Metal–Organic Frameworks. *J. Am. Chem. Soc.* **2025**, *147* (44), 40981–40991.

(86) Fabrizio, K.; Brozek, C. K. Size-Dependent Thermal Shifts to MOF Nanocrystal Optical Gaps Induced by Dynamic Bonding. *Nano Lett.* **2023**, *23* (3), 925–930.

(87) Mancuso, J. L.; Fabrizio, K.; Brozek, C. K.; Hendon, C. H. On the Limit of Proton-Coupled Electronic Doping in a Ti(IV)-Containing MOF. *Chem. Sci.* **2021**, *12* (35), 11779–11785.

(88) Fabrizio, K.; Gormley, E. L.; Davenport, A. M.; Hendon, C. H.; Brozek, C. K. Gram-Scale Synthesis of MIL-125 Nanoparticles and Their Solution Processability. *Chem. Sci.* **2023**, *14* (33), 8946–8955.

(89) Bueken, B.; Vermoortele, F.; Vanpoucke, D. E. P.; Reinsch, H.; Tsou, C.-C.; Valvekens, P.; De Baerdemaeker, T.; Ameloot, R.; Kirschhock, C. E. A.; Van Speybroeck, V.; Mayer, J. M.; De Vos, D. A Flexible Photoactive Titanium Metal–Organic Framework Based on a [TiIV3(M3-O)(O)2(COO)6] Cluster. *Angew. Chem. Int. Ed.* **2015**, *54* (47), 13912–13917.

(90) Zhang, Z.; Tian, Q.; Huo, S.; Meng, F.; Xie, Y.; Hu, X.; Pan, C.; Wu, E. Photodoping Strategies in Two-Dimensional Semiconductors: Mechanisms, Characterizations, and Emerging Applications. *InfoMat* **2025**, *n/a* (n/a), e70092.

(91) Shen, L.; Luo, M.; Huang, L.; Feng, P.; Wu, L. A Clean and General Strategy To Decorate a Titanium Metal–Organic Framework with Noble-Metal Nanoparticles for Versatile Photocatalytic Applications. *Inorg. Chem.* **2015**, *54* (4), 1191–1193.

(92) An, Y.; Xu, B.; Liu, Y.; Wang, Z.; Wang, P.; Dai, Y.; Qin, X.; Zhang, X.; Huang, B. Photocatalytic Overall Water Splitting over MIL-125(Ti) upon CoPi and Pt Co-Catalyst Deposition. *ChemistryOpen* **2017**, *6* (6), 701–705.

(93) Altınçekiç, N. G.; Achemire, M. A.; Noh, H. Crystal-Size-Dependent Optical Properties of H-Atoms on the Nodes of Ti-Based Metal-Organic Framework. *Chem. – Asian J. n/a* (n/a), e202401055.

(94) Carroll, G. M.; Brozek, C. K.; Hartstein, K. H.; Tsui, E. Y.; Gamelin, D. R. Potentiometric Measurements of Semiconductor Nanocrystal Redox Potentials. *J. Am. Chem. Soc.* **2016**, *138* (13), 4310–4313.

(95) Connelly, N. G.; Geiger, W. E. Chemical Redox Agents for Organometallic Chemistry. *Chem. Rev.* **1996**, *96* (2), 877–910.

(96) Paul, A.; Borrelli, R.; Bouyanfif, H.; Gottis, S.; Sauvage, F. Tunable Redox Potential, Optical Properties, and Enhanced Stability of Modified Ferrocene-Based Complexes. *ACS Omega* **2019**, *4* (12), 14780–14789.

(97) Fulmer, G. R.; Miller, A. J. M.; Sherden, N. H.; Gottlieb, H. E.; Nudelman, A.; Stoltz, B. M.; Bercaw, J. E.; Goldberg, K. I. NMR Chemical Shifts of Trace Impurities: Common Laboratory Solvents, Organics, and Gases in Deuterated Solvents Relevant to the Organometallic Chemist. *Organometallics* **2010**, *29* (9), 2176–2179.

(98) Gottlieb, H. E.; Kotlyar, V.; Nudelman, A. NMR Chemical Shifts of Common Laboratory Solvents as Trace Impurities. *J. Org. Chem.* **1997**, *62* (21), 7512–7515.

(99) Brunner, E. Solubility of Hydrogen in 10 Organic Solvents at 298.15, 323.15, and 373.15 K. *J. Chem. Eng. Data* **1985**, *30* (3), 269–273.

(100) Armarego, W. L. F. Chapter 3 - Purification of Organic Chemicals. In *Purification of Laboratory Chemicals (Eighth Edition)*; Armarego, W. L. F., Ed.; Butterworth-Heinemann, 2017; pp 95–634.

(101) Mendes, R. F.; Paz, F. A. A. Transforming Metal–Organic Frameworks into Functional Materials. *Inorg. Chem. Front.* **2015**, *2* (6), 495–509.

(102) Colón, Y. J.; Snurr, R. Q. High-Throughput Computational Screening of Metal–Organic Frameworks. *Chem. Soc. Rev.* **2014**, *43* (16), 5735–5749.

(103) Ghasempour, H.; Wang, K.-Y.; Powell, J. A.; ZareKarizi, F.; Lv, X.-L.; Morsali, A.; Zhou, H.-C. Metal–Organic Frameworks Based on Multicarboxylate Linkers. *Coord. Chem. Rev.* **2021**, *426*, 213542.

(104) Schneider, C.; Ukaj, D.; Koerver, R.; Talin, A. A.; Kieslich, G.; Pujari, S. P.; Zuilhof, H.; Janek, J.; Allendorf, M. D.; Fischer, R. A. High Electrical Conductivity and High Porosity in a Guest@MOF Material: Evidence of TCNQ Ordering within Cu3BTC2 Micropores. *Chem. Sci.* **2018**, *9* (37), 7405–7412.

(105) Svensson Grape, E.; Brozek, C. K. Turn-On Conductivity with Proton-Coupled Electron Transport in Metal–Organic Frameworks. *J. Am. Chem. Soc.* **2025**, *147* (44), 40981–40991.

(106) Xie, L. S.; Skorupskii, G.; Dincă, M. Electrically Conductive Metal–Organic Frameworks. *Chem. Rev.* **2020**, *120* (16), 8536–8580.

(107) Tao, S.; Wang, J.; Zhang, J. Conductive Metal–Organic Frameworks and Their Electrocatalysis Applications. *ACS Nano* **2025**, *19* (10), 9484–9512.

(108) Lin, Y.; Li, Y.; Cao, Y.; Wang, X. Two-Dimensional MOFs: Design & Synthesis and Applications. *Chem. – Asian J.* **2021**, *16* (21), 3281–3298.

(109) Huang, X.; Zhang, S.; Liu, L.; Yu, L.; Chen, G.; Xu, W.; Zhu, D. Superconductivity in a Copper(II)-Based Coordination Polymer with Perfect Kagome Structure. *Angew. Chem. Int. Ed.* **2018**, *57* (1), 146–150.

(110) Lu, C.; Clayville, B.; Choi, J. Y.; Park, J. 2D Metal-Organic Frameworks as an Emerging Platform with Tunable Electronic Structures. *Chem* **2023**, *9* (10), 2757–2770.

(111) Park, J.; Hinckley, A. C.; Huang, Z.; Feng, D.; Yakovenko, A. A.; Lee, M.; Chen, S.; Zou, X.; Bao, Z. Synthetic Routes for a 2D Semiconductive Copper Hexahydroxybenzene Metal–Organic Framework. *J. Am. Chem. Soc.* **2018**, *140* (44), 14533–14537.

(112) Kambe, T.; Sakamoto, R.; Hoshiko, K.; Takada, K.; Miyachi, M.; Ryu, J.-H.; Sasaki, S.; Kim, J.; Nakazato, K.; Takata, M.; Nishihara, H. π-Conjugated Nickel Bis(Dithiolene) Complex Nanosheet. *J. Am. Chem. Soc.* **2013**, *135* (7), 2462–2465.

(113) Lian, Y.; Yang, W.; Zhang, C.; Sun, H.; Deng, Z.; Xu, W.; Song, L.; Ouyang, Z.; Wang, Z.; Guo, J.; Peng, Y. Unpaired 3d Electrons on Atomically Dispersed Cobalt Centres in Coordination Polymers Regulate Both Oxygen Reduction Reaction (ORR) Activity and Selectivity for Use in Zinc–Air Batteries. *Angew. Chem. Int. Ed.* **2020**, *59* (1), 286–294.

(114) Park, J.; Lee, M.; Feng, D.; Huang, Z.; Hinckley, A. C.; Yakovenko, A.; Zou, X.; Cui, Y.; Bao, Z. Stabilization of Hexaaminobenzene in a 2D Conductive Metal–Organic Framework for High Power Sodium Storage. *J. Am. Chem. Soc.* **2018**, *140* (32), 10315–10323.

(115) Jin, Z.; Yan, J.; Huang, X.; Xu, W.; Yang, S.; Zhu, D.; Wang, J. Solution-Processed Transparent Coordination Polymer Electrode for Photovoltaic Solar Cells. *Nano Energy* **2017**, *40*, 376–381.

(116) Day, R. W.; Bediako, D. K.; Rezaee, M.; Parent, L. R.; Skorupskii, G.; Arguilla, M. Q.; Hendon, C. H.; Stassen, I.; Gianneschi, N. C.; Kim, P.; Dincă, M. Single Crystals of Electrically Conductive Two-Dimensional Metal–Organic Frameworks: Structural and Electrical Transport Properties. *ACS Cent. Sci.* **2019**, *5* (12), 1959–1964.

(117) Dou, J.-H.; Sun, L.; Ge, Y.; Li, W.; Hendon, C. H.; Li, J.; Gul, S.; Yano, J.; Stach, E. A.; Dincă, M. Signature of Metallic Behavior in the Metal–Organic Frameworks M3(Hexaiminobenzene)2 (M = Ni, Cu). *J. Am. Chem. Soc.* **2017**, *139* (39), 13608–13611.

(118) Kambe, T.; Sakamoto, R.; Kusamoto, T.; Pal, T.; Fukui, N.; Hoshiko, K.; Shimojima, T.; Wang, Z.; Hirahara, T.; Ishizaka, K.; Hasegawa, S.; Liu, F.; Nishihara, H. Redox Control and High Conductivity of Nickel Bis(Dithiolene) Complex π-Nanosheet: A Potential Organic Two-Dimensional Topological Insulator. *J. Am. Chem. Soc.* **2014**, *136* (41), 14357–14360.

(119) Mendecki, L.; Ko, M.; Zhang, X.; Meng, Z.; Mirica, K. A. Porous Scaffolds for Electrochemically Controlled Reversible Capture and Release of Ethylene. *J. Am. Chem. Soc.* **2017**, *139* (48), 17229–17232.

(120) Ko, M.; Aykanat, A.; Smith, M. K.; Mirica, K. A. Drawing Sensors with Ball-Milled Blends of Metal-Organic Frameworks and Graphite. *Sensors* **2017**, *17* (10), 2192.

(121) Cui, Y.; Yan, J.; Chen, Z.; Zhang, J.; Zou, Y.; Sun, Y.; Xu, W.; Zhu, D. [Cu3(C6Se6)] N : The First Highly Conductive 2D π-d Conjugated Coordination Polymer Based on Benzenehexaselenolate. *Adv. Sci. Weinh. Baden-Wurtt. Ger.* **2019**, *6* (9), 1802235.

(122) Wu, H.; Zhang, W.; Kandambeth, S.; Shekhah, O.; Eddaoudi, M.; Alshareef, H. N. Conductive Metal–Organic Frameworks Selectively Grown on Laser-Scribed Graphene for Electrochemical Microsupercapacitors. *Adv. Energy Mater.* **2019**, *9* (21), 1900482.

(123) Campbell, M. G.; Liu, S. F.; Swager, T. M.; Dincă, M. Chemiresistive Sensor Arrays from Conductive 2D Metal–Organic Frameworks. *J. Am. Chem. Soc.* **2015**, *137* (43), 13780–13783.

(124) Liu, J.; Song, X.; Zhang, T.; Liu, S.; Wen, H.; Chen, L. 2D Conductive Metal–Organic Frameworks: An Emerging Platform for Electrochemical Energy Storage. *Angew. Chem. Int. Ed.* **2021**, *60* (11), 5612–5624.

(125) Cotton, F. A.; Li, Z.; Liu, C. Y.; Murillo, C. A. Modulating Electronic Coupling Using O- and S-Donor Linkers. *Inorg. Chem.* **2007**, *46* (19), 7840–7847.

(126) Contreras-Pereda, N.; Pané, S.; Puigmartí-Luis, J.; Ruiz-Molina, D. Conductive Properties of Triphenylene MOFs and COFs. *Coord. Chem. Rev.* **2022**, *460*, 214459.

(127) Yang, J.; Feng, Z.; Wang, Y.; Huang, J.; Xu, C.; Li, H. Two-Dimensional π–d-Conjugated Cobalt-Based Metal–Organic Framework for Efficient Oxygen Evolution. *ACS Appl. Nano Mater.* **2024**, *7* (16), 18881–18888.

(128) Clough, A. J.; Yoo, J. W.; Mecklenburg, M. H.; Marinescu, S. C. Two-Dimensional Metal–Organic Surfaces for Efficient Hydrogen Evolution from Water. *J. Am. Chem. Soc.* **2015**, *137* (1), 118–121.

(129) Zhao, K.; Zhu, W.; Liu, S.; Wei, X.; Ye, G.; Su, Y.; He, Z. Two-Dimensional Metal–Organic Frameworks and Their Derivatives for Electrochemical Energy Storage and Electrocatalysis. *Nanoscale Adv.* **2020**, *2* (2), 536–562.

(130) Aust, M.; Herold, A. J.; Niederegger, L.; Schneider, C.; Mayer, D. C.; Drees, M.; Warnan, J.; Pöthig, A.; Fischer, R. A. Introducing Benzene-1,3,5-Tri(Dithiocarboxylate) as a Multidentate Linker in Coordination Chemistry. *Inorg. Chem.* **2021**, *60* (24), 19242–19252.

(131) Aust, M.; Schönherr, M. I.; Halter, D. P.; Schröck, L.; Pickl, T.; Deger, S. N.; Hussain, M. Z.; Jentys, A.; Bühler, R.; Zhang, Z.; Meyer, K.; Kuhl, M.; Eichhorn, J.; Medina, D. D.; Pöthig, A.; Fischer, R. A. Benzene-1,4-Di(Dithiocarboxylate) Linker-Based Coordination Polymers of Mn2+, Zn2+, and Mixed-Valence Fe2+/3+. *Inorg. Chem.* **2024**, *63* (1), 129–140.

(132) Liu, J.; Xing, G.; Chen, L. 2D Conjugated Metal–Organic Frameworks: Defined Synthesis and Tailor-Made Functions. *Acc. Chem. Res.* **2024**, *57* (7), 1032–1045.

(133) Xiong, D.; Deng, X.; Cao, Z.; Tao, S.; Song, Z.; Xiao, X.; Deng, W.; Hou, H.; Zou, G.; Ji, X. 2D Metal–Organic Frameworks for Electrochemical Energy Storage. *ENERGY Environ. Mater.* **2023**, *6* (6), e12521.

(134) Khan, M.; Qian, L.; Lin, Z.; Wang, Y.; Lin, H.; Wang, X.; Han, S.; Zhu, J. Next-Generation 2D Metal-Organic Framework Nanosheets: State-of-the-Art Synthesis Approaches and Their Integral Role in Energy Conversion and Storage. *Nano Energy* **2025**, *145*, 111423.

(135) Nobakht, N.; Etghani, S. A.; Hosseini, M.; Aboutalebi, S. H. Two-Dimensional MOF-Based Materials: Preparations and Applications as Electrodes in Li-Ion Batteries. *J. Energy Chem.* **2024**, *97*, 388–418.

(136) Wang, S.; Lu, J.; Liu, Q.; Cui, H.; Wang, H.; Feng, X.; Ge, K.; Yang, Y.; Zhao, Y. Photocatalytic Reduction of Hexavalent Chromium (Cr(VI)) in Water Using Two-Dimensional Fe/Cu-MOF-NH_2. *J. Environ. Chem. Eng.* **2025**, *13* (4), 117176.

(137) Kang, C.; Ahsan Iqbal, M.; Zhang, S.; Weng, X.; Sun, Y.; Qi, L.; Tang, W.; Ruan, S.; Zeng, Y.-J. Cu3(HHTP)2 c-MOF/ZnO Ultrafast Ultraviolet Photodetector for Wearable Optoelectronics. *Chem. – Eur. J.* **2022**, *28* (64), e202201705.

(138) Stanton, R.; Trivedi, D. J. Charge Carrier Dynamics at the Interface of 2D Metal–Organic Frameworks and Hybrid Perovskites for Solar Energy Harvesting. *Nano Lett.* **2023**, *23* (24), 11932–11939.

(139) Hu, W.-C.; Shi, Y.; Zhou, Y.; Wang, C.; Younis, M. R.; Pang, J.; Wang, C.; Xia, X.-H. Plasmonic Hot Charge Carriers Activated Ni Centres of Metal–Organic Frameworks for the Oxygen Evolution Reaction. *J. Mater. Chem. A* **2019**, *7* (17), 10601–10609.

(140) Gao, M.; Wang, Z.; Liu, Z.; Huang, Y.; Wang, F.; Wang, M.; Yang, S.; Li, J.; Liu, J.; Qi, H.; Zhang, P.; Lu, X.; Feng, X. 2D Conjugated Metal–Organic Frameworks Embedded with Iodine for High-Performance Ammonium-Ion Hybrid Supercapacitors. *Adv. Mater.* **2023**, *35* (41), 2305575.

(141) Neuba, A.; Ortmeyer, J.; Konieczna, D. D.; Weigel, G.; Flörke, U.; Henkel, G.; Wilhelm, R. Synthesis of New Copper(I) Based Linear 1-D-Coordination Polymers with Neutral Imidazolinium-Dithiocarboxylate Ligands. *RSC Adv.* **2015**, *5* (12), 9217–9220.

(142) Naeem, S.; Thompson, A. L.; Delaude, L.; Wilton-Ely, J. D. E. T. Non-Innocent Behaviour of Dithiocarboxylate Ligands Based on N-Heterocyclic Carbenes. *Chem. – Eur. J.* **2010**, *16* (36), 10971–10974.

(143) Delaude, L.; Demonceau, A.; Wouters, J. Assessing the Potential of Zwitterionic NHC·CS2 Adducts for Probing the Stereoelectronic Parameters of N-Heterocyclic Carbenes. *Eur. J. Inorg. Chem.* **2009**, *2009* (13), 1882–1891.

(144) Pérez-Ramos, P.; Mateo, M. A.; Elorriaga, D.; García-Vivó, D.; Soengas, R. G.; Rodríguez-Solla, H. Coordination of Azol(in)Ium Dithiocarboxylate Ligands to Au(III): Unexpected Formation of a Novel Family of Cyclometallated Au(III) Complexes, DFT Calculations and Catalytic Studies. *Dalton Trans.* **2024**, *53* (22), 9433–9440.

(145) Champion, M. J. D.; Solanki, R.; Delaude, L.; White, A. J. P.; Wilton-Ely, J. D. E. T. Synthesis and Catalytic Application of Palladium Imidazol(in)Ium-2-Dithiocarboxylate Complexes. *Dalton Trans.* **2012**, *41* (40), 12386–12394.

(146) Zain Aldin, M.; Zaragoza, G.; Deschamps, W.; Tomani, J.-C. D.; Souopgui, J.; Delaude, L. Synthesis, Characterization, and Biological Activity of Water-Soluble, Dual Anionic and Cationic Ruthenium–Arene Complexes Bearing Imidazol(in)Ium-2-Dithiocarboxylate Ligands. *Inorg. Chem.* **2021**, *60* (21), 16769–16781.

(147) Qin, X.-J.; Chen, Y.; Gao, F.-M. Studies of Iron-Sulfur Covalency in the Model System and Proteins. *Chin. J. Chem.* **2005**, *23* (9), 1203–1206.

(148) Harris, T. V.; Szilagyi, R. K. Protein Environmental Effects on Iron-Sulfur Clusters: A Set of Rules for Constructing Computational Models for Inner and Outer Coordination Spheres. *J. Comput. Chem.* **2016**, *37* (18), 1681–1696.

(149) Niu, S.; Ichiye, T. Probing Ligand Effects on the Redox Energies of [4Fe−4S] Clusters Using Broken-Symmetry Density Functional Theory. *J. Phys. Chem. A* **2009**, *113* (19), 5671–5676.

(150) Solomon, E. I.; Hedman, B.; Hodgson, K. O.; Dey, A.; Szilagyi, R. K. Ligand K-Edge X-Ray Absorption Spectroscopy: Covalency of Ligand–Metal Bonds. *Coord. Chem. Rev.* **2005**, *249* (1), 97–129.

(151) Harris, T. V.; Szilagyi, R. K. Iron–Sulfur Bond Covalency from Electronic Structure Calculations for Classical Iron–Sulfur Clusters. *J. Comput. Chem.* **2014**, *35* (7), 540–552.

(152) Kubas, A. Characterization of Charge Transfer Excited States in [2Fe–2S] Iron–Sulfur Clusters Using Conventional Configuration Interaction Techniques. *Theor. Chem. Acc.* **2020**, *139* (7), 120.

(153) Poater, J.; Solà, M.; Duran, M.; Fradera, X. The Calculation of Electron Localization and Delocalization Indices at the Hartree–Fock, Density Functional and Post-Hartree–Fock Levels of Theory. *Theor. Chem. Acc.* **2002**, *107* (6), 362–371.

(154) Nakaza, S.; Shi, Y.; Zhang, Z.; Akbar, S.; Shakib, F. A. Two-Dimensional Electrically Conductive Metal–Organic Frameworks: Insights and Guidelines from Theory. *Acc. Chem. Res.* **2025**, *58* (19), 3021–3032.

(155) Lu, Y.; Samorì, P.; Feng, X. Rational Construction of Two-Dimensional Conjugated Metal–Organic Frameworks (2D c-MOFs) for Electronics and Beyond. *Acc. Chem. Res.* **2024**, *57* (14), 1985–1996.

(156) Fradera, X.; Austen, M. A.; Bader, R. F. W. The Lewis Model and Beyond. *J. Phys. Chem. A* **1999**, *103* (2), 304–314.

(157) Bader, R. F. W.; Hernández-Trujillo, J.; Cortés-Guzmán, F. Chemical Bonding: From Lewis to Atoms in Molecules. *J. Comput. Chem.* **2007**, *28* (1), 4–14.

(158) Cortés-Guzmán, F.; Bader, R. F. W. Complementarity of QTAIM and MO Theory in the Study of Bonding in Donor–Acceptor Complexes. *Coord. Chem. Rev.* **2005**, *249* (5), 633–662.

(159) Bader, R. F. W. Atoms in Molecules. *Acc. Chem. Res.* **1985**, *18* (1), 9–15.

(160) Szabo, A.; Ostlund, N. S. *Modern Quantum Chemistry: Introduction to Advanced Electronic Structure Theory*; Courier Corporation, 1996.

(161) Schleyer, P. von R.; Maerker, C.; Dransfeld, A.; Jiao, H.; van Eikema Hommes, N. J. R. Nucleus-Independent Chemical Shifts: A Simple and Efficient Aromaticity Probe. *J. Am. Chem. Soc.* **1996**, *118* (26), 6317–6318.

(162) Stanger, A. Obtaining Relative Induced Ring Currents Quantitatively from NICS. *J. Org. Chem.* **2010**, *75* (7), 2281–2288.

(163) Kleinpeter, E.; Klod, S.; Koch, A. Visualization of through Space NMR Shieldings of Aromatic and Anti-Aromatic Molecules and a Simple Means to Compare and Estimate Aromaticity. *J. Mol. Struct. THEOCHEM* **2007**, *811* (1), 45–60.

(164) Bursch, M.; Mewes, J.-M.; Hansen, A.; Grimme, S. Best-Practice DFT Protocols for Basic Molecular Computational Chemistry. *Angew. Chem.* **2022**, *134* (42), e202205735.

(165) Kalisch, T.; Brehm, P. C.; Streubel, R. Tricyclic 1,4-Diphosphinines: Local vs. Global Aromaticity. *ChemPhysChem* **2024**, *25* (19), e202400417.

(166) Hanwell, M. D.; Curtis, D. E.; Lonie, D. C.; Vandermeersch, T.; Zurek, E.; Hutchison, G. R. Avogadro: An Advanced Semantic Chemical Editor, Visualization, and Analysis Platform. *J. Cheminformatics* **2012**, *4* (1), 17.

(167) Neese, F. Software Update: The ORCA Program System—Version 6.0. *WIREs Comput. Mol. Sci.* **2025**, *15* (2), e70019.

(168) Neese, F. An Improvement of the Resolution of the Identity Approximation for the Formation of the Coulomb Matrix. *J. Comput. Chem.* **2003**, *24* (14), 1740–1747.

(169) Neese, F. Definition of Corresponding Orbitals and the Diradical Character in Broken Symmetry DFT Calculations on Spin Coupled Systems. *J. Phys. Chem. Solids* **2004**, *65*

(170) Neese, F.; Wennmohs, F.; Hansen, A.; Becker, U. Efficient, Approximate and Parallel Hartree–Fock and Hybrid DFT Calculations. A 'Chain-of-Spheres' Algorithm for the Hartree–Fock Exchange. *Chem. Phys.* **2009**, *356* (1), 98–109.

(171) Helmich-Paris, B.; de Souza, B.; Neese, F.; Izsák, R. An Improved Chain of Spheres for Exchange Algorithm. *J. Chem. Phys.* **2021**, *155* (10), 104109.

(172) Neese, F. The SHARK Integral Generation and Digestion System. *J. Comput. Chem.* **2023**, *44* (3), 381–396.

(173) Izsák, R.; Neese, F. An Overlap Fitted Chain of Spheres Exchange Method. *J. Chem. Phys.* **2011**, *135* (14), 144105.

(174) Izsák, R.; Hansen, A.; Neese, F. The Resolution of Identity and Chain of Spheres Approximations for the LPNO-CCSD Singles Fock Term. *Mol. Phys.* **2012**, *110* (19–20), 2413–2417.

(175) Neese, F. The ORCA Program System. *WIREs Comput. Mol. Sci.* **2012**, *2* (1), 73–78.

(176) Izsák, R.; Neese, F.; Klopper, W. Robust Fitting Techniques in the Chain of Spheres Approximation to the Fock Exchange: The Role of the Complementary Space. *J. Chem. Phys.* **2013**, *139* (9), 094111.

(177) Neese, F. Approximate Second-Order SCF Convergence for Spin Unrestricted Wavefunctions. *Chem. Phys. Lett.* **2000**, *325* (1), 93–98.

(178) Lu, T. A Comprehensive Electron Wavefunction Analysis Toolbox for Chemists, Multiwfn. *J. Chem. Phys.* **2024**, *161* (8), 082503.

(179) Keith, T. A. AIMALL, 2019.

(180) Meng, E. C.; Goddard, T. D.; Pettersen, E. F.; Couch, G. S.; Pearson, Z. J.; Morris, J. H.; Ferrin, T. E. UCSF ChimeraX: Tools for Structure Building and Analysis. *Protein Sci.* **2023**, *32* (11), e4792.

(181) Pettersen, E. F.; Goddard, T. D.; Huang, C. C.; Meng, E. C.; Couch, G. S.; Croll, T. I.; Morris, J. H.; Ferrin, T. E. UCSF ChimeraX: Structure Visualization for Researchers, Educators, and Developers. *Protein Sci. Publ. Protein Soc.* **2021**, *30* (1), 70–82.

(182) Goddard, T. D.; Huang, C. C.; Meng, E. C.; Pettersen, E. F.; Couch, G. S.; Morris, J. H.; Ferrin, T. E. UCSF ChimeraX: Meeting Modern Challenges in Visualization and Analysis. *Protein Sci. Publ. Protein Soc.* **2018**, *27* (1), 14–25.

(183) Çetinkaya, E.; Hitchcock, P. B.; Küçükbay, H.; Lappert, M. F.; Al-Juaid, S. Carbene Complexes: XXIV22For Part XXIII, See Ref. 1. No Reprints Available.. Preparation and Characterization of Two Enetetramine-Derived Carbenerhodium(I) Chloride Complexes RhCl(LR)3 and [RhCl(COD)LR] and the Preparation and X-Ray Structures of the Enetetramine L2R and Its Salt [L2R][BF4]2. *J. Organomet. Chem.* **1994**, *481* (1), 89–95.

(184) Park, S.; Hwang, J.-Y.; Shin, J.; Kim, Y. N-Heterocyclic Carbene-Derived Carbon Disulfide Radical Ligands for Palladium Diradicals. *J. Am. Chem. Soc.* **2024**, *146* (41), 28508–28515.

(185) Luff, M. S.; Filipovic, T. M.; Corsei, C. S.; Oppel, K.; Krummenacher, I.; Bertermann, R.; Finze, M.; Braunschweig, H.; Radius, U. Azolium-2-Dithiocarboxylates as Redox Active Ligands in Nickel Chemistry. *Chem. Sci.* **2025**, *16* (12), 5142–5154.